Faculty of Engineering and Science

Identification of Saline Groundwater and the Hydrogeochemistry in Highland of Ba'kelalan Region Using Geophysical and Chemical Methods

Stephan Ongetta

This thesis is presented for the Degree of Master of Philosophy (Applied Geology) of Curtin University Malaysia

November 2020

DECLARATION

To the best of my knowledge and belief, this report contains no materials that were previously published by any other person except where due acknowledgement has been made.

This report contains no materials which have been accepted for the award of any other degree or diploma in any other university.

Signature :

Date : November 2020

ACKNOWLEDGEMENT

I would like to thank Associate Professor Dr. M. V. Prasanna, Dr. Sabarathinam Chidambaram and Professor Dr. Nagarajan Ramasamy as the thesis committee for their guidance during this study in the 24 months. It is a privilege to be under their supervision.

I wish to extend my special appreciation to the Curtin Malaysia Research Institute (CMRI) for their financial support.

My extended sincere thanks to Professor Clem Kuek, former Dean R&D and the Director of CMRI as a member of the research team who helped to find out and pinpoint the research gap and issues faced by the local community of the study area. Also, I would like to highly acknowledge his guidance and support to execute the project at various stages.

I would like to extend my gratitude to the internal assessors Professor Dr. Dominique Dodge-Wan and Dr. Zeinab for their guidance to improve the quality of the thesis. Also, I would like to add my thanks to Mrs. Illya Amalina for her teaching and supervision in conducting the geophysical methods.

I also gratefully acknowledge the National University of Malaysia (UKM) especially to Dr. Mohd Hariri Bin Arifin, Mr. Shahrizal Bin Deris and Mr. Muhammad Farid Bin Adnan for their teaching and advice for loaning and conducting geophysical equipment the 2D resistivity survey. And to Mr. Abdulmajid Muhammad Ali for his help and support in conducting the seismic refraction survey.

I intend my gratitude to Curtin University bio-valley and Faculty of Engineering and Science laboratory staffs for their teaching and assistance in completing the geochemical analysis throughout the 2 years.

ABSTRACT

The subsurface aqueous fluid in the saturated zone below the water table is referred as groundwater. Several factors could affect the chemistry and quality degradation of groundwater, which include natural and anthropogenic impacts. Saline groundwater plays an essential role in hydrocarbon migration, the formation of ore deposits, industrial application, irrigation for salt-tolerant crops, and desalinated for drinking water. The communities at highland of Ba'kelalan of Sarawak have been using saline groundwater for commercial salt production. Few saline water wells were discovered and were used for salt production for the past centuries. Salt production, along with paddy-planting and livestock rearing, is one of the main economic activities of the Lun Bawang community at Ba'kelalan. The production of salt is mainly by boiling the saline well water in metal vessels using firewood until salt crystals are formed. The entire process of deriving salts from the saline water with this method takes five days. Subsequently, the wet crystallized salt is dried in bamboo containers on fire embers, and finally, the salts are preserved either in bamboo or plastic packages. These salts are of commercial value and they are referred to as "Mountain salts". Considering the significance of this saline water, which serves as the lifeline for the people of Ba'kelalan, the current study aims to determine the evolution and source of these saline waters. Ba'kelalan is bounded between latitudes 3^0 57' and 4^0 04' N and longitudes 115^0 36' and 115^0 38' E, with an altitude of 910 meters above sea level (a.s.l) in an alluvium plateau surrounded by hills. This study aims to determine the major hydrochemical processes controlling the salinity in groundwater, to investigate the possible sources of saline groundwater, and to locate the potential new saline groundwater sources for extraction. In this context, five existing saline groundwater wells, one river water, and three rainwater samples were considered for investigation during the monsoon (MON) season in December 2018 and the post-monsoon (POM) season in April 2019.

The first phase of this research was to determine the hydrochemical quality and behaviour of physical (pH, EC, TDS, temperature, salinity, turbidity, and water level) and chemical (major ions, nutrients, and trace metals) parameters on hourly, daily and monthly basis of saline groundwater. Stable isotopes $\delta^{18}O$ and δD have conservative properties and provided information regarding the water recharge processes. Additionally, stable isotope of sulphur, boron and chloride ($\delta^{34}S$, $\delta^{11}B$ and $\delta^{37}Cl$) were mainly used to define salinity sources, water-rock interaction and evaporative environment. Cl^- and Na^+ are the dominant ions observed in the groundwater. The study infers that significant increase in TDS, EC and salinity is due to seasonal variation and fluctuation in water level which reflects the changes in groundwater recharge based on hourly, daily and monthly observation. The geochemical ratios and the statistical techniques revealed that the groundwater chemistry is inferred by the dissolution of marine evaporites as a dominant process, with other factors such as water-rock interaction, ion exchange and sulphate reduction. It is inferred from the isotopic signatures which indicated the origin of saline groundwater from high intense evaporation source of marine evaporites such as halite dissolution and oxidation of sulfide (pyrite). In the second phase of this study, 2D electrical resistivity and seismic refraction methods were used to identify the lithological variations, depth of potential sources of saline groundwater, and their subsurface structures. It is inferred that the probability of a conductive zone should be located at depth from 1 m to 14 m, in which the saline groundwater plume migrates from higher to lower elevation where the perched aquifer water table is intersected at a down valley. The seismic refraction inferred the presence of faults below the perched aquifer which facilitates the movement of brine groundwater from saturated zone to the surface. The 2D resistivity method is proven to be more significant to locate the saline groundwater region, whereas seismic refraction demonstrates subsurface fault structure. The outcomes of this research would enhance the local economy and commercial salt production as the results of the study could be used to manage the identified saline groundwater sources and to develop a sustainable management plan for the dependent community.

Table of Contents

LIST OF FIGURES

LIST OF TABLES

ABBREVIATIONS

A.s.l	Above Sea Level
Al	Aluminium
B	Boron
BDL	Below Detection Limit
Ba	Barium
Ca^{2+}	Calcium
Cd	Cadmium
Cl^{-}	Chloride
Co	Cobalt
CO_2	Carbon Dioxide
CO_3^{-2}	Carbonate
Cr	Chromium
Cu	Copper
EC	Electrical Conductivity
Fe	Iron
H^{+}	Hydrogen
$H_2CO_3^{-}$	Carbonic Acid
HCO_3^{-}	Bicarbonate
I	Iodine
K^{+}	Potassium

L	Litre
Li	Lithium
m/s	Meter/second (Seismic Refraction Unit)
ml	Millilitre
Mg^{2+}	Magnesium
mg/L	Milligram per Litre
mm	Millimetres (Water Column Unit)
Mn	Manganese
MON	Monsoon season
Na^{+}	Sodium
NH_3	Ammonia
NH_3N	Nitrogen
NH_4	Ammonium
NO_2^{-}	Nitrite
NO_3^{-}	Nitrate
O_2	Oxygen
Ω.m	Ohm.meter (2D Electrical Resistivity Unit)
P	Phosphorous
Pb	Lead
PO_4^{3-}	Phosphate
POM	Post-monsoon season
Rb	Rubidium

RW	Rainwater
SO_4^{2-}	Sulphate
Sc	Scandium
Sn	Tin
TDS	Total Dissolved Solid
UTM	Universal Transverse Mercator
WL	Water level
Zn	Zinc
µS	Micro-Siemen (Electrical Conductivity Unit)

CHAPTER 1. Introduction

Salinization is a worldwide environmental phenomenon that has significantly impacted our lives through the alternation of chemical compositions in our natural groundwater resources, degradation and increased cost of water supply for domestic agriculture, infrastructures, and industries, which caused severe health problems (Vengosh, 2014; Mateo-Sagasta et al., 2017; Walter et al., 2017; Mejri et al., 2018; Mgbenu and Egbueri, 2019). Salinization is a primary concern in managing water resources in many countries due to the importance of groundwater quantity and quality for daily usage (Grundmann et al., 2016). Nonetheless, saline groundwater possesses a vital role in various processes such as subsurface dolomitization, the formation of sediment-hosted ore deposits, and hydrocarbon migration (Grobe and Machel, 2002; Dezayes et al., 2015; Quattrini et al., 2016; Awaleh et al., 2020; Mirzavand et al., 2020a). Saline groundwater in Ba'kelalan has been used since unrecorded time for commercial salt production purposes due to its very high salinity. Based on Haile (1962), various salt springs occur in the mountainous highland from Lao Miatu, Bario, and Ba'kelalan, which are drained by the headwaters of the Baram and Trusan rivers. The Ba'kelalan salt is produced in the remote highlands of northern Sarawak by the isolated communities of Lun Bawang since undocumented history. The saltwater is extracted from nearby wells and poured into a tank above the fire stove fuelled by wood. Salt crystals will begin to appear slowly, and these crystals are continually stirred and turned over until the residual salt completely solidifies. The whole process requires an entire five-day period, with an average production of 40 kg of salt a week. When the salt forms pale patches and is white in colour, it is then collected from the bottom of the tank and dried entirely later on. Subsequently, the salts are preserved in a wrapped bamboo or plastic package. Nevertheless, the problem faced by Buduk Bui is the reduced commercial salt production due to the decline of water level in the existing wells in recent years. The depletion of existing wells happens especially during the POM season, where less rainwater recharge occurs in the studied area. Besides, the limited number of wells (3) in Buduk Bui is not sufficient to meet the commercial salt demand in the lowland, and there is a demand for new wells to be discovered (Sellato, 1993).

Groundwater hydrochemistry analysis provides researchers with all the vital information to understand the physical and chemical processes through which the groundwater undergoes, starting from rainfall, runoff and infiltration to the subsurface through the vadose zone to reach the saturated zone, hence recharging the aquifer (Auge, 2016; Aghazadeh et al., 2017). The weak acid formed during rainfall by the mixture of both rainwater and CO_2 from the atmosphere grants acceleration to the weathering of minerals available in the rocks and soils, thereby altering the chemical composition of the groundwater to reflect the types of geological materials in the area (Bartolino and Cole, 2002; Kura et al., 2018; Liu et al., 2019). Therefore, the groundwater chemistry depends on different hydrochemical processes over space and time such as water-rock interaction, ion exchange, evaporation, oxidation and anthropogenic activities (Narany et al., 2014; Liu et al., 2016; Barzegar et al., 2018; Han et al., 2018). Moreover, groundwater hydrochemistry is also influenced by other factors such as surrounding rock types, the residence time in the host rock, the original composition of groundwater and the flow path (Kumar et al., 2009; Redwan et al., 2016). Thus, understanding the hydrogeochemistry processes that control groundwater quality is essential for sustainable management of water resources and groundwater contamination (Kumar et al., 2009; Sun et al., 2016). The trace metal contamination is generally controlled by the geological and geochemical heterogeneity in the groundwater system (Islam et al., 2017). A high trace metal content in groundwater can generate hazardous effects for the people either from anthropogenic or natural sources (Madzin et al., 2016; Akoto at al., 2019). Furthermore, stable isotopes are valuable tracers in determining the source and mechanism of salinization of water due to their stability over time (Clark, 2015; Alexeev et al., 2020; Mirzavand et al., 2020b).

On the other hand, geophysical methods are established in groundwater resource evaluation and can be used to find solutions to other problems related to natural environments such as engineering, mining, hydrology, and natural hazard assessment (Akinbiyi et al., 2019). They have a massive potential for rapid, non-intrusive evaluation of the lateral and vertical extents of mapping for subsurface geological structures (Farid et al., 2017; Thapa et al., 2019; Glas et al., 2019). Various geophysical methods are available worldwide, such as electromagnetic,

electrical resistivity, seismic refraction and reflection, magnetic techniques, gravity techniques, and ground-penetrating radar, which are used to measure the physical properties of the Earth's subsurface with each technique utilized for specified application and the accommodated field conditions. The 2D resistivity and seismic refraction are the most suitable geophysical techniques for hydrological explorations (Mohamaden et al., 2016; Farid et al., 2017; Alhassan et al., 2018; Glas et al., 2019). The resistivity method employs an artificial source of current into the ground through steel electrodes, to measure the potentials in other electrodes in the vicinity of the current flow (Aizebeokhai et al., 2016; Khaki et al., 2016; Akinbiyi et al., 2019). Several parameters can influence the resistivity measurement, in which this could be due to variations in surface conductivity caused by weathering and moisture content (Islami et al., 2018). For instance, rugged topography would have related effects because the current flow is concentrated in valleys and dispersed beneath a hill (Giao et al., 2008; Thapa et al., 2019). The equipotential surface is misrepresented as a result and forming false anomalies due to topography. In the hydrological investigation, the seismic refraction method determines direct information on the water table level and quantifies the heterogeneity of aquifers. Hence, a significant increase in velocity causes an increase in water content (Kearey et al., 2013; Alhassan et al., 2018). Seismic refraction provides information to determine the subsurface structural and lithological framework by introducing seismic energy into the ground through striking a steel plate using a hammer (Alhassan et al., 2018; Glas et al., 2019). Subsequently, the generated seismic energy is detected by aligning 24 buried geophones on the ground and recorded in the seismograph (Chen and Zelt, 2016).

Unfortunately, there is little information and research about the origin of the salt and its geochemistry in this tropical region. Nevertheless, this study attempted to collect, analyse, and interpret the geochemistry of saline groundwater and perform a geophysical survey to determine the subsurface features as well as explore the potential source of the saline groundwater.

1.1 Problem Statements

The saline groundwater wells in Buduk Bui and Ba'kelalan region were discovered and extracted since unreported time. A total of 5 existing wells are accessible for commercial salt productions. The problem statements in this research study are:

1. The community of Buduk Bui, Ba'kelalan, mainly depends on the existing saline groundwater wells for their commercial salt production for many decades. Nonetheless, the number of existing wells is insufficient to fulfil the demand.
2. The Buduk Bui community is facing the problem of depletion of groundwater levels in the existing wells during the POM season.
3. The hydrogeochemical characteristics of this saline water are unknown so far.
4. The importance of geophysical methods in determining the subsurface lithological conditions, the flow of groundwater and the potential source of saline groundwater are unrevealed in this study area.

1.2 Research Questions/ Gaps

1. The application of geophysical methods (i.e. seismic refraction and 2D resistivity) has not been conducted to determine the potential sources for saline groundwater in the proposed study area.
2. The hydrogeochemical investigation has not been carried out to determine the physical and chemical characteristics of saline groundwater in the study area.
3. The studies of subsurface lithology and structures that control the saline groundwater characteristics have not been studied using the geophysical and chemical methods.

1.3 Aims and Objectives

The purposes of this research study are to help the community to analyse and identify the saline groundwater hydrochemistry and explore new saline groundwater potential. These are the objectives to be achieved:

1. To find the potential sources of saline groundwater by using the 2D resistivity method and seismic refraction method.
2. To identify the lithological and structural controls on saline groundwater.
3. To evaluate the hydrogeochemical characteristic of saline groundwater during different seasons.

1.4 Novelty, Outcomes and their Significance

There are no significant research studies on the saline groundwater in the study area. The originality of this proposed research is based on the detailed hydrochemistry analysis in relation to the geophysical methods. The 2D resistivity and seismic refraction methods are the most suitable geophysical techniques for groundwater exploration to locate new saline groundwater aquifer for the benefits of the Buduk Bui community, thus enhancing salt production with more wells being discovered.

CHAPTER 2. Literature Review

2.1 Background

Groundwater is found in spaces between soil particles and rocks or within cracks of the bedrock. It becomes one of the vital sources of potable water for human's sustenance, while ensuring a healthy ecosystem, besides boosting the global socio-economic development (Dillon and Simmers, 1989; Aghazadeh et al., 2017; Esmaeili et al., 2018). Groundwater is one of the primary sources of freshwater supply in many countries, and it constitutes approximately 20 % of the world's freshwater supply (Redwan et al., 2016). It is estimated that about 10% of Malaysia's freshwater resource is derived from groundwater, therefore, it plays a vital role in supplying the daily needs for both humans and the aquatic ecosystems (Abdul Razak and Abdul Karim, 2009; Nampak et al., 2014). It is spatially distributed throughout the country and can be found in 4 different aquifer types, such as volcanic and sedimentary rocks, alluvial, limestone, and crystalline igneous rocks (Kura et al., 2018). Manap et al. (2013) stated that Malaysia's groundwater storage in aquifers is predicted to be approximately 5,000 billion m^3, with an annual recharge rate of 64 – 120 billion m^3 and an annual rainfall of 2,420 mm. A geochemical assessment helps to obtain an insight into the contribution of natural processes and anthropogenic factors for groundwater quality (Okiongbo and Douglas, 2015; Vishwakarma et al., 2018; Mgbenu and Egbueri, 2019). Natural processes include water-rock interaction, mineral precipitation or dissolution, redox reaction, ion exchange, and local hydrogeology and anthropogenic factors such as mining, agriculture, and industry activities (Singh, 2012; Ehya and Marbouti, 2016; Barzegar et al., 2018; Mirzavand et al., 2020a).

Subsurface salinity processes leading to brine formation are complex due to various factors that occur either from natural processes or human activity (Lu et al., 2008; Sarikhani et al., 2015; Sun et al., 2016). Natural processes include the influences of geochemical process, hydrological system, the diagenetic formation of hydrous minerals (water-rock interaction, precipitation, and dissolution of evaporate deposits), interstitial seawater (connate waters) trapped during original sediment deposition, saline water flowing from adjacent or underlying

aquifers and membrane filtration of shales (Horita, 2005; Zarei et al., 2013; Farid et al., 2014; Mejri et al., 2018; Awaleh et al., 2020; Mirzavand et al., 2020a). Meanwhile, anthropogenic activities also contribute to groundwater salinization, such as massive-scale irrigation, discharge of brine, industrial waste, and over-exploitation of groundwater in the coastal zone (Aghazadeh et al., 2017; Jia et al., 2017). As a result of the chemical and biochemical interactions between groundwater and the geological material through which it flows, groundwater contains a wide variety of dissolved inorganic constituents at various concentration (Isawi et al., 2016). Electrical conductivity (EC) and total dissolved solids (TDS) are frequently used as water quality parameters and as indicators of salinity. Groundwater salinity could be classified based on either electrical conductivity (EC) or total dissolved solids (TDS) from freshwater, brackish, saline to hypersaline (Freeze and Cherry, 1979; Mondal et al., 2010). The widely used scheme for characterizing groundwater are based on TDS for instance freshwater (TDS > 1000 mg/L), brackish water (TDS = 1000 – 10,000 mg/L), saline water (TDS = 10,000 – 100,000 mg/L) and brine water (TDS > 100,000 mg/L) (Freeze and Cherry, 1979). The concentration of total dissolved solids (TDS) in groundwater is determined by weighing the solid residue consisting of inorganic constituent and organic matter. Electrical conductivity measures the liquid capacity to conduct an electric charge that is dependent on the ability of dissolved ions concentration, ionic strength, and temperature. This is expressed in terms of electrical resistivity and has a unit of measurement known as Siemens (S) or microSiemens (µS). The electrical conductivity (EC) measurement is a proxy for the salinity of which the relationship is dependent on the chemical composition of the water. For example, Na^+ and Cl^- ions exist in dilute (weaker) condition as single charged ions; Ca^{2+} and SO_4^{2-} tend to form complexes that decreased their ability to conduct electricity (Hem, 1985). The correlation between TDS and EC is not directly linear, however, it depends on the activity of specific dissolved ions in the liquid and ionic strength (Rusydi, 2018).

The crucial technique to trace salinity sources is the assumption that the chemical composition of the originated saline source is preserved during the salinization process (Richter and Keitler, 1993; Vengosh, 2014; Mejri et al., 2018). Usually, the sources might

have been derived from more than a single mechanism, for example, the Na^+/Cl^- ratio can be an excellent tracer to distinguish marine ($Na^+/Cl^- < 0.86$) from non-marine or anthropogenic sources ($Na/Cl \geq 1$) (Zarei et al., 2013; Vengosh, 2014; Liu et al., 2016). However, the reactivity of Na^+ in the unsaturated zone reduces the Na^+/Cl^- ratio even in non-marine settings (Vengosh, 2014; Isawi et al., 2016; Ammar et al., 2020). The origin of saline and brine groundwater in the aquifer is very controversial in geochemical studies (Sarikhani et al., 2015; Liu et al., 2019). The potential mechanism of a saline condition in a sedimentary aquifer can originate from (1) intrusion of marine water from the sea, (2) mixing of meteoric water with connate water trapped during the deposition of sediment in a marine environment, (3) the concentration of dissolved salt by evaporation or transpiration near the soil surface during slow diffuse recharged, (4) leaching of evaporitic salt deposit by water that is rapidly and continuously filtered by porous surface through the preferred pathway, (5) the chemical weathering of the aquifer materials, (6) oil and gas field brines, (7) natural saline groundwater, (8) halite dissolution or salt domes (Sami, 1991; Kloppmann et al., 2001; Aghazadeh et al., 2011; Zarei et al., 2013; Sarikhani et al., 2015; Mejri et al., 2018; Guseva, 2018; Liu et al., 2019; Awaleh et al., 2020; Mirzavand et al., 2020a). However, in a non-coastal area, the progressive increase of salinity and the chemical alteration controlled by chloride and sodium ions are derived from these possible processes: (a) dissolution and evaporation of soluble salts such as gypsum and halite minerals within the aquifer; and (b) advection and diffusion of saline fluids entrapped in impermeable zones in or outside the aquifer that is associated with an active permeable zone (Vengosh, 2003; Vengosh, 2014). Zarei et al. (2013) stated that the dissolution of halite mineral of the Konarshiah salt diapir, Iran, is attributed to the salinization in the adjacent aquifers. However, the result from molar ratios of Na^+/Cl^-, Li/Cl^-, Br/Cl^-, SO_4^{2+}/Cl^-, and isotopic signatures indicated mixing or dilution of freshwater with diapir brine. Nevertheless, other results indicated potential sources from deep fault intrusion brine and evaporation of shallow water table (Zarei et al., 2013). Commonly, halite dissolution of brines has Na^+/Cl^- molar ratio = 1; brines derived from halite dissolution in shallow fresh groundwater flow system reveal a similar ratio (Richter and Kreitler, 1993). As long as concentrations are high and not particularly affected by ion-exchange of calcium and magnesium for sodium on

clay mineral surfaces and alteration of feldspar, lower ratios could potentially be affected (Kumar et al., 2003; Zarei et al., 2013; Gil-Marquez, 2017). However, deep-basin brines exhibit Na^+/Cl^- molar ratios lower than 0.95 due to sodium reaction with the aquifer rock material by ion exchange or albitization processes with a high concentration of magnesium, potassium, and calcium (Richter and Kreitler, 1993). Compared with halite solution brine, the Na^+/Cl^- ratio for seawater is much lower = 0.85 (Richter and Kreitler, 1993; Mejri et al., 2018).

For halite dissolution, the requirements necessary for the processes are (1) a supply of water unsaturated with respect to halite, (2) a deposit of salt through which or against which the water flows, (3) an outlet that would accept the resultant brine and (4) energy to cause the flow of water through the system (such as the hydrostatic head) (Zarei et al., 2013; Sarikhani et al., 2015). For instance, discharge of brine in the shallow subsurface with local meteoric water infiltrates the ground and dissolves halite in the shallow subsurface on its way to the regional discharged area at topographically low areas. Halite occurs in the subsurface in the form of bedded or salt dome, depending on the depositional history and may be associated with other chloride salts (carnallite or sylvite), with sulphates (polyhalite, anhydrite or gypsum) or with carbonates (dolomite or limestone) which contribute to the overall salinity of groundwater in contact with halite (Richter and Kreiler, 1993). Meanwhile, salt domes are composed mainly of pure halite with a small amount of anhydrite, gypsum, and limestone (Kloppmann et al., 2001; Zarei et al., 2013). Salinization may enhance the mobilization of toxic trace metals in soil due to ion absorption in sites and formation, which leads to the chemical evolution and reactivity with the host surrounding solids and aquifer and consequently, their concentration in water resources (Vengosh, 2014).

The salinization of groundwater is one of the main factors of water quality degradation which alters the aspect of useable water supply and agriculture (Liu et al., 2016; Van Engelen et al., 2018; Ibrahim et al., 2019). In some cases, if there is an increase in residence time at a lower gradient, the water absorbs a higher amount of salt in solution due to an increase of contact time with the surrounding rock, which results in higher salinity content (Auge, 2016; Gil-Marquez et al., 2017). Based on Kura et al. (2018), groundwater's chemical characteristics

are typically influenced by 95 % of the major ions such as Ca^{2+}, Mg^{2+}, K^{+}, Na^{+}, HCO_3^{-}, Cl^{-} and SO_4^{2-}. Apart from this, ions have been significantly controlled by the physical parameters such as pH, temperature, turbidity, salinity, dissolved oxygen, total dissolved solids, and electrical conductivity. For instance, pH in water is essential to a chemical reaction, solubility, and mobility of minerals; thus, a change in pH means a change in composition in water (Samantara et al., 2017). For salinity, it is determined by the presence of Na^{+} and Cl^{-} ions in water, while Ca^{2+}, Mg^{2+}, and HCO_3^{-} concentration in groundwater are influenced by the lithology and dissolution of surrounding bedrocks such as limestone, dolomite, calcite, and magnesite (Auge 2016). Most importantly, the principal constituent and trace metals present in groundwater are vital for human metabolism and health (Grundmann et al., 2016; Samantara et al., 2017). On the contrary, the presence of heavy metals is a significant issue due to the perpetual of metals and the negative impact on human health and the well-being of living organisms in even low concentrations (Marcovecchio et al., 2007; Momondu and Anyakora, 2010). Humans can be susceptible to heavy metals from water by ingestion and dermal absorption through the skin. Heavy metal presents in water in the form of colloidal, particulate, and dissolved phases (Singh et al., 2014). Furthermore, it exist in groundwater from a variety of sources either from natural processes due to dissolution and weathering of parent rock, or through anthropogenic impacts such as the use of fertilizers, pesticides, and leachates (Isa et al., 2012; Zakhem and Hafez, 2015; Esmaeili et al., 2018).

Unfortunately, there is a lack of recent and available research for hydrogeochemistry and geophysics studies in the Ba'kelalan region. The hypersaline spring in Ba'kelalan probably originated from the salt-bearing beds of the underlying Meligan and Kelalan Formations, in which it rose to the surface from the depth along with steep fractures, bedding planes, faults, and joints (Haile, 1962). Adjacent to the highest peak of Sarawak (Mount Murud) towards the south-west, the Kelabit highland (Bario) is located on the northern of Sarawak, alike Ba'kelalan highland, has also produced commercial salt from the saline groundwater (Haile, 1962; Kessler et al., 2019). Kessler et al. (2019) found that the Bario salt is likely non-marine salt with unknown origin. However, it still contains a significant concentration of lithium,

borate, iodine, strontium, barium, and antimony. Sellato (1993) stated that natural highland salt is rich in iodine, which helps prevent goiter disease. Nevertheless, the recorded high concentration of iodine in Bario and Ba'kelalan's salt can probably be associated with a hydrocarbon-bearing reservoir (Haile, 1962; Sellatto, 1993; Boschetti et al., 2007; Dezayes et al., 2015; Ozdemir, 2018; Kessler et al., 2019). Furthermore, conservative elements such as bromine, boron, lithium, and iodine remain in the solution and can be a perfect ratio tool to determine salinization processes in groundwater (Dezayes et al., 2015; Barzegar et al., 2018). The ratio plots of Br/Cl^-, Li/Cl^-, and B/Cl^- can be an excellent indicator for water sources and rock water interaction as they are considered to be conservative tracer (Kloppmann et al., 2001; Boschetti, 2011; Vengosh, 2013; Zarei et al., 2013; Liu et al., 2016). Meanwhile, a stable isotope analysis could be an excellent indicator to reveal the origin of the brine and saline groundwater (Liu et al., 2016; Kessler et al., 2019). For instance, oxygen and hydrogen stable isotopes can be applied as an indicator to identify the effect of water-rock interaction and the origin of the water (Grobe and Machel, 2002; Boschetti et al., 2007; Zarei et al., 2013; Clark, 2015; Sun et al., 2016; Han et al., 2018; Lyu et al., 2019; Ammar et al., 2020).

The ionic ratios of the chemical compositions are useful devices for tracing the sources of salinity and its evolution (Liu et al., 2016; Bhandary et al., 2018). Moreover, interpretation of major ions' data in the Gibbs diagram, Durov diagram, Piper diagram, Chadhra diagram and Van Wirdum's diagram helps to explain the groundwater types and distinguish the influences of rock-water interaction, evaporation and precipitation on water chemistry (Gibss, 1970; Narany et al., 2014; Redwan et al., 2016; Isawi et al., 2016; Akota, 2019). Moreover, due to the large volume of hydrochemical data, most researchers used multivariate statistical analysis such as cluster analysis (CA), factor analysis (FA) and principal component analysis (PCA), which provided a reliable approach to recognize and interpret the complex system of water composition and the water quality (Kumar et al., 2009; Okiongbo and Douglas, 2015; Walter et al., 2017; Kura et al., 2018; Ibrahim et al., 2019).

Geophysical methods have been widely used for various hydrogeological exploration as they are relatively inexpensive, non-invasive, and efficient (Araffa et al., 2017; Farid et al.,

2017). Although there are numerous geophysical methods available globally, the conjunction of 2D resistivity and seismic refraction methods are most suitable for a hydrogeological investigation to minimize the ambiguity and limitation of each exploration methods (Moustafa et al., 2012; Al-Shuhail and Al-Shaibani, 2013; Aizebeokhai et al., 2016). In the 2D resistivity method, the measurement takes place on the subsurface by injecting current onto the Earth's surface through two current electrodes and measuring the voltage differences at two potential electrodes at a distance (Loke, 2004; Mainoo et al., 2019). However, the resistivity values are significantly affected by several parameters such as the presence of water or moisture, and pores spaces distribution that includes temperature (Farid et al., 2017). Studies by Dahlin and Zhou (2004), concluded that there are numerous common arrays used in the resistivity surveys, for instance, pole-pole, dipole-dipole, Wenner-Schlumberger, and gradient array. Wenner array provides well-resolved resistivity images, both horizontal and vertical, great depth penetration, and reduces fieldwork time significantly (Dahlin and Zhou, 2004; Loke, 2004). The choices of survey array depend on the site condition and target of the survey. The subsurface resistivity units vary over a wide range, for instance, massive granite gives a value of 106 ohm.m and clay bed saturated with brackish clay shows 1 ohm.m. Dry rocks or sediments have higher resistivity (>1,000 ohm.m), but if they are saturated, the resistivity decreases (7 to 15 ohm.m) because the current flow is conducted through the water (Auge 2016). Thus, the magnitude of resistivity depends on the degree of saturation, the porosity of the material, and the chemical composition of the saturating fluid. According to Hodlur et al. (2010), the resistivity of saline water aquifer is significantly lower than that of freshwater aquifer due to more dissolved salts (Na^+ and Cl^- ions) and high TDS concentration in the saline water, as well as greater conductors of current. For instance, clay/sand saturated with saline water has low resistivity <50 ohm.m; meanwhile, sandstone saturated with freshwater has slightly higher resistivity of 50 to 150 ohm.m (Hodlur et al., 2010). Samsudin (2012) stated that the subsurface resistivity distribution in the Melaka region of Peninsular Malaysia indicates that the saturated clay with water has an approximately low resistivity range of 7 to 10 ohm.m due to water trapped between the clay minerals and significant negative charge (Celico et al., 2008; Samsudin, 2008; Mhamdi et al., 2015). Meanwhile, higher resistivity

value of 1,100 to 2,600 ohm.m suggests an unsaturated zone. However, most researchers suggested that resistivity data interpretation in freshwater and saline water interface could be more reliable if better geophysical anomalies support it to identify water table through seismic refraction (Naidu et al., 2013; Aizebeokhai et al., 2016; Farid et al., 2017). The seismic refraction method is based on the measurement of propagation of elastic seismic waves velocity and amplitude through the subsurface medium (solids or fluids) (Patra et al. 2016; Alhassan et al., 2018). The seismic investigation, particularly P-waves (compressional body wave), can provide different prospects in the hydrogeological aspects, such as determining groundwater table and distinguishing bedrock depth (Pasquet et al., 2015). P-waves velocity depends on both matrix and pore fills with the rock, and P-waves are sensitive to rock porosity and fluid saturation with the highest rate of propagation, which is the perfect tool for groundwater exploration (Pasquet et al., 2015; Chen and Zelt, 2016). Based on Azwin et al. (2013), throughout the seismic propagation, the seismic waves are refracted once the elastic differences occur at boundaries between layer and different rock properties (velocities and densities). According to Araffa et al. (2017), the seismic refraction result of the Gulf of Suez indicated that the first soil layer (dry gravels and recent sand deposit) has velocity ranging from 253 to 375 m/s, while the second layer exhibited velocity ranging from 707 to 1,152 m/s which indicated sand and gravel. The third layer reflected velocity ranging from 1,445 to 2,410 m/s that corresponded to sandstone and shale with occurrences of fresh and saltwater overlying a bedrock of limestone (>2,450 m/s). Based on Al-Shuhail and Al-Shaibani (2013), the seismic investigation in Saudi Arabia, indicated that the first layer of sandy beds have an average velocity and thickness of 600 m/s and 15 m, respectively; the second layer have an average velocity of 2,400 m/s and 115 m and 'the bedrock layer distinctly has high velocity reading with values between 3,300 – 4,400 m/s. For pure halite, the seismic velocity is 4,500 m/s, whereas over 4,500 m/s of velocity, the salt unit interpreted this as impurities such as anhydrite with a velocity of 6,000 m/s (Ezersky, 2006). Nevertheless, P-wave velocity in a salt layer under the water table is varied between the value of 3,000 – 4,420 m/s due to the alternation of a layer with different elastic properties, porosity, weakening, and jointing (Ezersky, 2006).

2.2 Regional Tectonic Setting

Borneo is one of the largest islands in the world with an area of 743,330 km^2 with a region of rugged terrain. As such, this geological area is poorly studied due to the difficulties of accessing in the tropical rainforest (Hall and Nichols, 2002; Hutchison, 2005; Mathew, 2016; Wang et al., 2016; Saw et al., 2019). Borneo is the result of the Mesozoic and Cenozoic accretion of an ophiolitic, island arc, and a micro-continental fragment of south China and Gondwana origin (Hall and Nichols, 2002; Van Hattum et al., 2013). The tectonic evaluation of eastern Borneo has often been assumed to be the result of the SE subduction of the South China Sea lithosphere at the NW Borneo Trench. It includes predominantly turbiditic Late Cretaceous through Paleogene Rajang Group, deposited upon oceanic basement (Chert-Spilite-Formation), and the adjacent area which are underlain by continental crust (Hamilton, 1979; Hutchison, 2010). Subsequently, these sediments of Late Cretaceous to Early Miocene age were compressed between West Borneo Block and the Luconia Province continental block during the Late Miocene periods (Hutchison, 1996; Wang et al., 2016; Galin et al., 2017). The Rajang tectonostratigraphic unit consists of Cretaceous to Early Eocene flysch basin that progressed as an accretionary prism, resulting in sub-metamorphic to low-grade metamorphic which constitutes the basement rock in the study area as Kelalan Formation (Wannier, 2009).

Tectonically, most of the mountain ranges escarpment of western, central and northern Borneo are formed from a thick succession of Upper Cretaceous – Lower Miocene deep marine sediments of the Rajang group and the Crocker Formation (Hall and Nichols, 2002; Hutchison, 2010; Wang et al., 2016). During the Miocene age, the central mountain of Borneo became elevated, and the rapid removal of material by erosion in humid tropical settings generated significant sediments (Hall and Nichols, 2002). Van Hattum et al. (2013) stated the northern Borneo Cenozoic sedimentary deposits are divided by Top Crocker Unconformity (TCU) into deep marine deposit rock of the Upper Cretaceous to Eocene Rajang Group and the younger sedimentary rocks of Eocene to Lower Miocene Crocker Fan (Figure 2.1). The Top Crocker Unconformity (TCU) marks the termination of deep-marine sedimentation and a

change from deep water sediment to fluvial-deltaic and shallow marine sediments (Hutchison, 2010; Van Hattum et al., 2013; Wang et al., 2016).

The Middle Miocene Deep Regional Unconformity (DRU) divides the overlying of Belait Formation with Setap and Meligan Formation (Morley, 2008; Cullen, 2010). In the East Borneo Zone, it lies the major Rajang Group turbidite flysch (deep-water to shallow-water turbidity shales and sandstones) mobile belt basin that is developed as an accretionary prism along the southern margin of the Proto South China Sea. It has been folded, thrust, and uplifted into a NE trending orogeny and continues towards the SW as the Sibu Zone of Sarawak (Galin et al., 2017). This sub-metamorphic to low-grade metamorphic unit constitutes the basement rock in the area that is known as the Belaga, Mulu, and Kelalan Formations (mostly turbiditic siliciclastic) (Wannier, 2009; Wang et al., 2016).

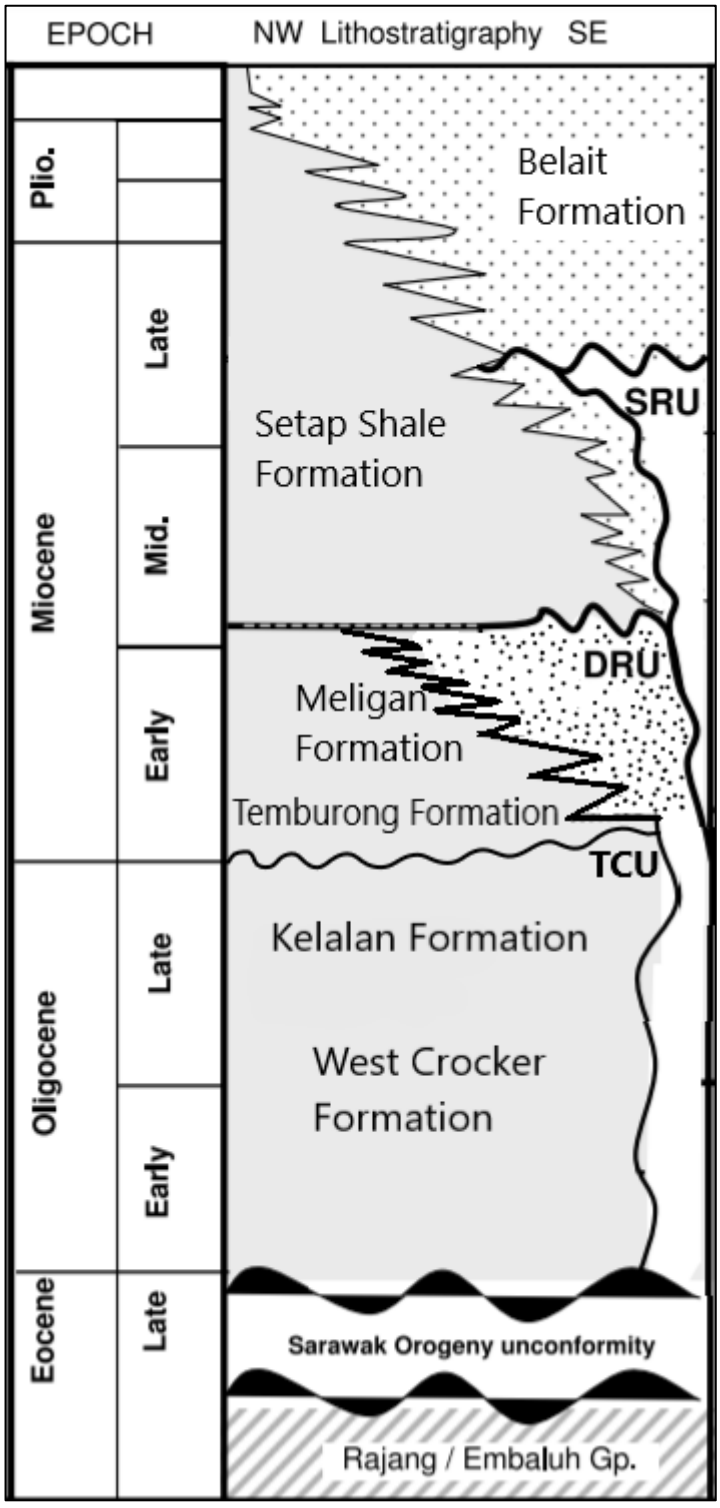

Figure 2. 1 Regional stratigraphy of Ba'kelalan. Adapted from Cullen, (2010).

2.3 Study Area

The study area, Ba'kelalan is situated in an enclosed mountain range in the northeast of Borneo and located between latitudes 3^0 57' and 4^0 04' N and longitudes 115^0 36' and 115^0 38' E, at altitude of 910 meters above sea level (a.s.l) and 4 km from the borders of Indonesia, Kalimantan. The Ba'kelalan (Figure 2.2) region stretches over approximately 14 km along the upper valley of the Kelalan river and is surrounded by mountainous landscapes as a result of sedimentation, tectonic activities and the subsequent weather of more than 50 million years (Haile, 1962; Hutchison, 2005). The mountain ranges are built up mainly by igneous and metamorphic rock of Mesozoic to Tertiary age, uplifted and intensely folded sedimentary rocks of the Paleogene age (Hutchison, 2005; Van Hattum et al., 2013). These Paleogene Formations are composed of deep-water thinly bedded turbidities of shale, slate, sandstone, calcareous sandstone, and rare limestone and had undergone regional metamorphism (Wang et al., 2016). The highlands are formed by an exceptional thickness of predominantly low grade regionally metamorphosed, turbiditic sediment of the Rajang Group, which belongs to the Belaga, Mulu, and Kelalan Formations (Hutchison, 2010; Wang et al., 2016; Galin et al., 2017).

The mountainous hinterland uplifted to over 1500 m above sea level divides Sarawak and Kalimantan, where the highest peak in Sarawak is Mount Murud at 2424 m, from which it flows the Baram, Limbang and Trusan rivers. The mountainous region in eastern Sarawak receives the highest rainfall in Malaysia with a warm and humid climate throughout the year. The annual average rainfall varied, ranging from 2,000 mm per year, often exceeding 4,000 mm (Manap et al., 2013). The rivers of Sarawak are of great importance to the state due to the significant role in the development, economic, and social system of the communities. The Kelalan river is the main drainage channel for the Ba'kelalan region, which flows through the valley from south to north direction (Figure 2.2).

The geology of the study area composed of Paleocene basement at the bottom which is made up of metamorphosed turbidites sediments, and subsequently overlain by fluvial-deltaic and shallow marine deposits of Neogene age. It is covered by the recent Quaternary alluvium

composed of sandy and clayey sediments with few gravels formed from river deposits (Haile, 1962; Hutchison, 2005). The Pliocene to Early Miocene aged Setap Shale Formation overlies the Meligan Formation, which is composed of a thick monotonous succession of grey shale and minor turbidities bed of sandstone that is deposited in a shallow marine environment (Morley, 2008; Wang et al., 2016). Meanwhile, the Meligan Formation is composed of massive sandstone with minor shale that forms prominent mountain ranges and are suggested as Oligocene to Late Miocene in age (Morley, 2008; Van Hattum et al., 2013; Abdullah et al., 2017). The sandstone is grey with medium to coarse-grained and, in general, quartzose, deposited from the fluviatile-deltaic-shallow environment (Wang et al., 2016). The Kelalan Formation underlies the Meligan Formation and the Setap Shale Formation, forming exceptional escarpments such as Mount Semadoh, Mount Murud, and Mount Batu Lawi (Liechti et al., 1960; Haile, 1962; Morley, 2008; Wang et al., 2016). The Kelalan Formation is a folded sandstone of turbiditic siliciclastic with grey slaty shale, siltstone, and rare limestone lenses, which are made up of fluvial sediments and is suggested as Paleocene in age (Haile 1962; Wannier, 2009). The sandstone is thinly bedded to massive slightly calcareous, fine to coarse-grained in grey colour. The Kelalan Formation outcrops are found to be exposed in the Ba'kelalan region due to the uplifted and overturned tectonic events (Haile, 1962; Hutchison, 2010).

The Ba'kelalan focal area consists of two main village clusters, Ba'kelalan and Long Semado, which are located 25 km apart and connected by a logging road. The road access has not been improved to a significant degree as the distance, expense, and difficulty are prohibitive. However, the area is still serviced by daily light aircraft with restricted, limited seats and bad weather factors that could cancel flights. The population of Ba'kelalan consisted of 13 villages (Punang Kelalan, Long Komap, Long Langai, Long Nawi, Pa'Tawing, Long Rusu, Long Ritan, Buduk Aru, Long Ubau, Long Rangat, Long Muda, Buduk Bui, Long Lemutut) with approximately 1,100 people (WWF, 2005). The villages in the Ba'kelalan are interlinked by footpaths that provide excellent trekking opportunities and pilgrimages to the church near the summit of Mount Murud (WWF, 2005).

The area is inhabited by the Lun Bawang tribe who practice sustainable wet rice irrigation systems, natural commercial salt, cattle, and buffalo rearing. Among the villages in Ba'kelalan region, only 3 communities (Buduk Bui, Pa'Komap and Punang Kelalan) have the privilege of saline groundwater extraction for commercial salt production. In the study area (Buduk Bui), it appeared to have a perched aquifer located adjacent to well (1,2 and 3) at a lower elevation in which it is the main target for geophysical exploration. The saline groundwater wells are located at Buduk Bui, Pa'Komap and Punang Kelalan with a total of 5 existing wells. Figure 2.3a, shows all the wells were designed using cement and concrete as casing and a PVC pipe to extract the saline groundwater to the surface. The measured ground level was approximately 5 m in depth with water level fluctuating between 0.5 m to 2 m. The existing wells are located near the foothills and between the valleys with bedding striking at NE-SW orientation (Figure 2.3c). A perched aquifer occurs in the unconfined zone when there is an impermeable layer of rock (aquiclude) or relatively impermeable layer (aquitard) above the water table but below the surface (Figure 2.3d). Therefore, where a perched aquifer intersects the ground surface, a perched aquifer can discharge water to springs (Figure 2.4) (Rains et al., 2006). However, there is no indication of connection between the perched aquifer with the existing wells intersected aquifer in the study area. The perched aquifer is located at the lowest elevation and in between the valleys with approximately 1 km adjacent to the Kelalan river.

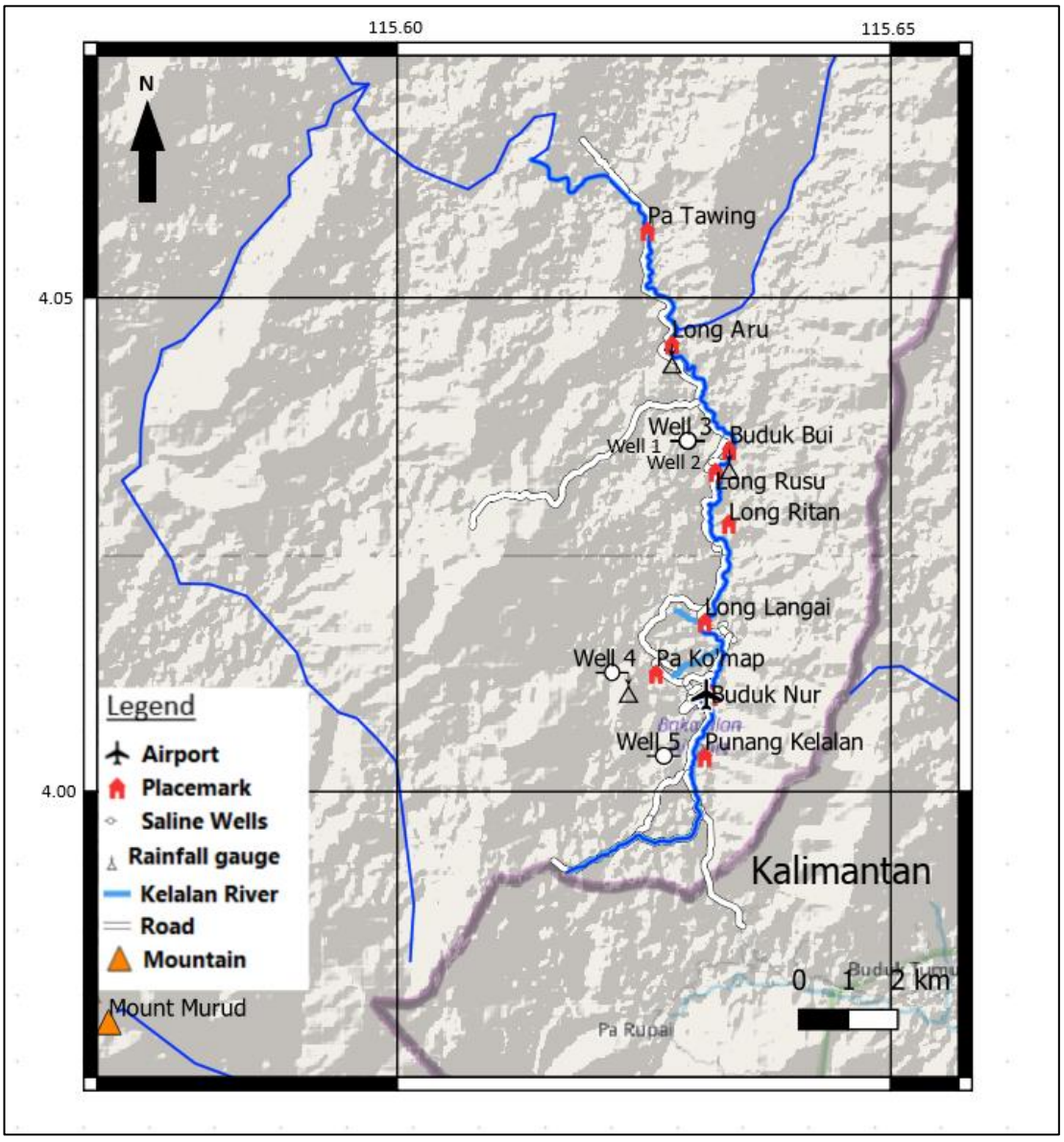

Figure 2. 2 Map of the study area, Ba'kelalan, Sarawak, Malaysia (QGIS).

Figure 2. 3 (A and B) The field photography of study area wells in Bang Main. (C) The field photography of well 1, 2 and 3 on the foothill of Buduk Bui. (D) The field photography of perched aquifer of the study area.

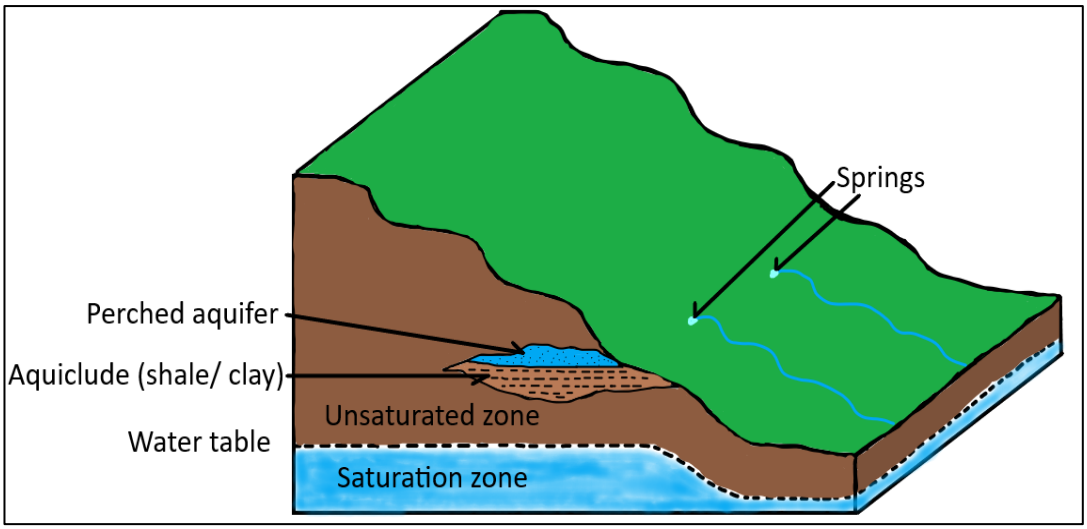

Figure 2. 4 The diagram illustrating the occurrence of the perched aquifer system (Rains et al., 2006).

2.4 Hydrogeochemistry

Based on Auge (2016), the typical change in hydrochemical facies along the regional groundwater flow path from the diluted rainwater at the recharged zone. With an HCO_3 water type and contained CO_2 entered the soil zone after which further CO_2 formed from the decay of organic matter and dissolved in the infiltrated water. In some cases, the application of agricultural chemicals such as fertilizers added further Na^+, Cl^- and K^+, NO_3, PO_4^{-3} into the groundwater. Meanwhile, within the soil and unsaturated zone, the dissolved CO_2 produces a weak acidic solution of carbonic acid, H_2CO_3, which separates and promotes the dissolution of calcium and magnesium carbonates that gives the Ca^{2+}-Mg^{2+}-HCO_3^- water type. Away from the reservoir of oxygen in the soil and unsaturated zone, the groundwater becomes increasingly anoxic (less O_2) below the water table with progressive reduction of oxygen, nitrate, and sulfate linked to bacterial respiration and mineralization of organic matter (Auge, 2016). Fe and Mn become mobilized under the increased reduced condition and then later precipitate as metal sulfides (Okiongbo and Douglas, 2015). In other cases, the existence of disseminated clay material within the aquifer, ion exchange takes place which caused Ca^{2+} to be replaced by Na^+ in the solution, where the water evolves to a Na^+-HCO_3^- water type. With deeper aquifer of a long flow path and increasing time, the groundwater chemistry tends to change from HCO_3^- type to Cl^- water type with increased salinity. A change in the dominant cation often accompanied by Ca^{2+} to Na^+, which produces a Na^+-Cl^- water type, where this typically occurs in the discharged zone (Sarikhani et al., 2015; Auge, 2016).

Besides, the chemical properties of groundwater depend upon the chemistry of water in the recharged zone as well as the occurrences of different geochemical processes in the subsurface (Kumar et al. 2009; Mattos et al., 2018b). Rainwater plays an essential role in collecting atmospheric soluble and insoluble components (Olivera et al., 2012). The chemical composition of rainwater provides information on atmospheric quality, which depends on emission sources, atmospheric chemistry, and metrological condition (Zunckel et al., 2003). The rainwater pH in a clean atmosphere is estimated to be around 5.6 due to the dissolution of CO_2 in rain droplets (Seinfeld and Pandis, 2016). Generally, rainwater is composed of natural

and anthropogenic species that often enriches sea salt (Na^+ and Cl^-), soil dust (Ca^{2+}, Mg^{2+} and K^+) and acidic constituent (SO_4^{2-} and NO_3^-) distributed over coastal, continental and urban areas, respectively (Huang et al., 2009). In a humid environment with well-drained regions, water selectively removed cations from weathered rocks and soils more rapidly (Hem, 1989).

In general, groundwater at the discharged zone tends to have higher mineral concentration than the recharged zone due to the longer residence time and prolonged contact with the aquifer matrix (Freeze and Cherry, 1979; Hem, 1989). The hydrogeochemical processes promote an understanding of anthropogenic and water-rock interactions, including ion exchange, dissolution, and precipitation (Liu et al., 2019). It plays a significant role and is responsible for the spatial-temporal variation, changes in the hydrogeochemical composition of the groundwater, and heavy metal migration (Kumar et al., 2006; Ibrahim et al., 2019; Mattos et al., 2018a). The ion-exchange reaction affects not only the exchanged ions but also the dissolution and precipitation reactions (Ibrahim et al., 2019). Ion exchange occurs when ions replace ions within the mineral lattices of solids in the aqueous solution, primarily on clays, soil organic matter, metal oxides and hydroxides (Zaidi et al. et al., 2015). Moreover, the mobility of an element is controlled by various factors such as contact between the solution and absorptive material, chemical reaction with organic matter, pH and Eh of the surrounding environment, and releasing of elements during weathering of parent rock (Prasanna et al., 2012).

The chemical composition of rainwater varies in the amount of major and minor ions as rainfall removes the atmospheric gaseous and particulate pollutants which are supplied from both natural (sea-salt aerosols, aeolian dust) and anthropogenic sources (biomass burning, agriculture activities, industries) (Carroll, 1962; Al-Obaidy and Joshi, 2004; Tripathy et al., 2019). In a humid environment, the essential quantity of major ions such as magnesium, calcium, sodium, and potassium added periodically by rainwater may be anticipated to influence the composition of the soil pore water. Thus, water selectively removes cations from weathering of rocks and soil, subsequently the possibility cations in the exchange positions of soil clay minerals. According to Radojevic and Tan (2000), rainwater acidity is dependent on

the source and ambient of atmospheric chemistry. Meanwhile, as runoff and percolation periodically flush materials from the surface into streams and groundwater after rain events. Rainwater contains certain constituents of local origin, and dry precipitation is added continually to the earth's crust to become part of the chemical weathering environment (Al-Obaidy and Joshi, 2004).

2.4.1 Rock-water Interaction

Groundwater chemistry is principally a function of mineral composition and the formations through which it flows due to rock-water interaction, which includes the nature of recharged water, hydrologic gradient, residence time, and anthropogenic activities (Redwan et al., 2016). Chiefly, rock-water interaction is an essential process due to the solid phase (inorganic and organic matter) which are the dominant sources and sink of dissolved constituents of groundwater. As a result, a variety of chemical constitutions and different chemical reactions with a solid phase take place during the movement of groundwater along its path from recharged to the discharged area. The magnitude of rock-water interaction and the chemical reaction such as dissolution/ precipitation, ion exchange processes, reduction, and oxidation, can be determined from the concentration of major ions (Elgano and Kannan, 2007). Redwan et al. (2016) have inferred that weathering, hydrolysis, and ion exchange are the dominant processes responsible for the groundwater chemistry in Southern Sohag, Egypt. Moreover, the evaporation and crystallization of gypsum and halite dissolution are accountable for the groundwater chemistry in the Northern, Sohag, Egypt. Thus, recognition of rock-water interaction that controls groundwater chemical evolution would lead to a better understanding of hydrogeochemistry. Chemical and isotopic analysis is proven to be a successful method to describe groundwater salinization processes, identification of the sources of salinity, and the origin of the water (Zarei et al., 2013; Liu et al., 2016; Banda et al., 2019). Additionally, oxygen and hydrogen isotopic ratios can provide information regarding the water source and effect of water-rock interaction (Grobe and Machel, 2002: Awaleh et al., 2020). Meanwhile, stable isotopes for chloride, boron, and sulphur are commonly used to define salinity sources,

water-rock interaction, and mixing of different waters (Liu et al., 2016; Han et al., 2017; Isawi et al., 2018).

2.4.2 Mineral Dissolution and Precipitation

Mineral dissolution and precipitation occur ubiquitously in natural systems as minerals in rocks are released into water, where this reduces solid mass, and increases aqueous concentrations (Liu et al., 2016). Most of the major ions are affected by precipitation or dissolution processes and by the diagenetic reaction. For example, acid stimulation accelerates mineral dissolution, therefore increases reservoir porosity, permeability, water storage, and the opposite occurs when mineral precipitates and clogs pore spaces (Devaraj et al., 2018).

Chemical weathering results from chemicals changing to minerals which becomes unstable when exposed to surface conditions. Chemical weathering and physical weathering (erosion) consume carbon dioxide and lock them into carbonate minerals, which regulate the atmospheric CO_2 level and sustain relatively element earth conditions (Okiongbo and Douglas, 2015). Some minerals, like quartz, are virtually unaffected by chemical weathering, while others, like feldspar, are easily altered. In general, the degree of chemical weathering is most significant in warm and humid climates and least in cold and dry climates (Auge, 2016). The significant characteristics of surface conditions that lead to chemical weathering are the presence of water, the abundance of oxygen, and the presence of carbon dioxide in the atmosphere, which produce weak carbonic acid when combined with water. The following equations can be expressed that processes:

$$H_2O + CO_2 \rightarrow H_2CO_3 \quad (1)$$

$$H_2CO_3 \leftarrow \rightarrow H^+ + HCO_3^- \quad (2)$$

$$HCO_3 \leftarrow \rightarrow H^+ + CO_3^{2-} \quad (3)$$

In reaction 1, when rainwater is combined with carbon dioxide in the atmosphere, it creates weak carbonic acid. Subsequently, the carbonic acid dissociates to form hydrogen and

carbonate ions (reaction 2). The carbonate acid in the water could be broken down based on reaction 3, and produces bicarbonate (HCO_3^-), and hydrogen (H^+) (Narany et al., 2014). However, the amount of carbon oxide in the air is only enough to produce weak carbonic acid, but there is much more carbon oxide in the soil, so water that percolates through the soil can become significantly more acidic. Other types of chemical weathering is hydrolysis, where some minerals are altered into other minerals for example, feldspar is altered to clay minerals. On the other hand, oxidation of iron in ferromagnesian silicate or pyrite starts with the dissolution of the iron (Hem, 1985).

The subsurface is composed of rocks, soils, and other forms of porous materials containing various types of minerals. Minerals dissolve and precipitate when interacting with water. As minerals dissolved, chemicals in the solid phase transform into ions in water, resulting in a decrease in mineral mass and volume. For example, calcite ($CaCO_3$) dissolve into carbonate species (H_2CO_3, HCO_3^-, CO_3^{2-}) and Ca^{2+} species in water. In contrast, mineral precipitation occurs when aqueous species is transformed into the solid phase, therefore leading to mass and volume increase in solid phases with a decrease in aqueous concentrations. In reduced condition, the dissolved organic matter can be another source of increased HCO_3^- in groundwater. It is estimated that over 95% of the Earth's carbon exists in carbonate minerals, the most common being calcite ($CaCO_3$). Dissolution is a simple and common weathering reaction in carbonate rocks. The dissolution of calcite's primary reaction mechanism is as follows:

$$CO_2(g) + H_2O \rightarrow H^+ + HCO_3^- \quad (4)$$

$$CaCO_3 + CO_2(g) + H_2O \rightarrow Ca^{2+} + 2HCO_3^- \quad (5)$$

Reaction (4) of carbon dioxide with water in the atmosphere, produces hydrogen ions (acidic conditions) that promotes the dissolution of calcite by the following reaction 5 (Narany et al., 2014):

$$CaCO_3 + H^+ \rightarrow Ca^{2+} + HCO_3^- \quad (6)$$

The first reaction (5) shows that calcite solubility is controlled by the amount of carbon dioxide presented; thus, the more CO_2, the more calcite would be dissolved. In the last reaction (6), it is shown that the calcite solubility is controlled by pH, thus lowering the pH (more hydrogen ions), the more calcite would be dissolved.

2.4.3 Ion-exchange

Soils and aquifers contain materials such as clay minerals, organic matter, and metal oxy-hydroxides, which absorbed chemicals (Ibrahim et al., 2018). Ion exchange reactions occur when ions in water is exchanged with those that are electrostatically bound to the solid phase. They commonly occur in iron oxides, organic matter, and clay minerals with a large surface area. Ion exchange reactions are important in determining the natural composition in surface water and groundwater (Liu et al., 2019). They would alter water composition and trigger other reactions, including mineral dissolution and precipitation. Due to the electrically charged ions in the water, both anions and cations have a tendency to be attracted onto a solid surface in ion exchange processes. The ions of the different elements have different tendencies to be absorbed or desorbed (Sarikhani et al., 2015). However, common minerals such as feldspar and quartz are less efficient than other minerals such as iron oxides and clay minerals. In particular, clays are effective at absorbing cations due to their surface that is consistently negatively charged. The tendency for absorption between the major cations in natural water from highest to lowest is as follows: $Ca^{2+} > Mg^{2+} > K^{+} > Na^{+}$ (Barzegar et al., 2018). It involves the replacement of one chemical Na^{+} ion exchange to another one at the solid surface, which may be clay mineral, organic matter, or metal oxy-hydroxide by other cations in the water, such as Ca^{2+} and Mg^{2+}, as expressed in equation 7. The reverse ion exchange is defined by the exchange of Ca^{2+} and Mg^{2+} ions on clay minerals by Na^{+} ions in the water as in equation 8 (Appelo and Postma, 2005):

$$2NaX + Ca^{2+} \rightarrow 2Na^{+} + CaX_2 \quad (7)$$

$$CaX_2 + 2Na^{+} \rightarrow Ca^{2+} + NaX \quad (8)$$

Ion exchange reaction underlies the desorption of Na^+ from the Na^+-Cl^- water based on equation (7), when freshwater (Ca^{2+}-HCO_3^-) infiltrates the ground and in contact the confining layers, Ca^{2+} is taken up from the freshwater replaced by Na^+, which released from the cation exchanger in the groundwater.

The changes in the chemical composition of groundwater along its flow path would be understood by calculating the Chloro-Alkaline Indices (CAI). Schoeller (1977), suggested the CAI 1 and 2 for the interpretation process of ion-exchanged between groundwater and host environment. Following equations are to calculate the Chloro-Alkaline Indices (CAI 1 and 2).

$$Cl^- - (Na^+ + K^+)/Cl^- \text{ (CAI 1)} \quad (9)$$

$$Cl^- - (Na^+ + K^+)/SO_4^{2-} + HCO_3^- + CO_3^{2-} + NO_3^- \text{ (CAI 2)} \quad (10)$$

When ion-exchange occur between Na^+ or K^+ in the groundwater with Mg^{2+} or Ca^{2+} attached to a solid surface, such as the clay of the aquifer material, both of the above equations (CAI 1 and 2) would be positive, and the concentration of Mg^{2+} and Ca^{2+} would be increased in the groundwater. On the other hand, if a reversed ion exchange occurs between Na^+ or K^+ attached to the aquifer material and Mg^{2+} or Ca^{2+} in the solution, then these equations (CAI 1 and 2) would be negative, and the concentration of Na^+ or K^+ would be increased (Kumar et al., 2009; Ibrahim et al., 2019; Liu et al., 2019).

For instance, when water passed through the system with calcium and magnesium ions in solution, they are conversely adsorbed onto a substrate (ion-exchange resin). A Na^+-Cl^- brine then passes through the system, and due to the overwhelmed amount of sodium in the solution, the calcium and magnesium on the exchanged site are replaced by sodium. Provided the reservoir of sodium ions is adsorbed onto clay minerals, calcium, and magnesium ions in the water prefer to be attached to the exchanged sites, and the sodium would be expelled and transferred into the water. This process is known as base-exchange softening (Montcoudiol and Lemieux, 2015).

Ion exchange and sorption processes control the transport of pollutants in groundwater and soils, and act as one of the most critical mechanisms responsible for the concentration of ions

in the aquifers (Appelo and Postma, 2005). Besides, ion-exchange is an essential process to trace metals, especially those that behave as cations. Iron-oxides minerals, clay-mineral bearing rocks, and sediments would naturally absorb heavy-metal cation from contaminated water (Hem, 1985; Martinez and Bocanegra, 2002; Ehya and Marbouti, 2016).

2.4.4 Redox Reaction

A chemical reaction involving the transfer of electrons from one ion to another between dissolved, gaseous or solid constituent is called an oxidation-reduction reaction or redox reactions (Freeze and Cherry, 1970; Singhal and Gupta, 2010). For any redox reactions to occur, it requires an electron donor and electron acceptor. The oxidation state of the electron donor increases during redox reactions, whereas that of the electron acceptor is decreased. Redox is an important solubility control that can enhance transport such as Fe, Mn, NO_3^- and SO_4^{2-} (Hiscock and Bense, 2014; Clark, 2015). In natural environments, organic carbon often serves as the electron donor in microbe-mediated reactions. It becomes oxidized from organic carbon to inorganic form (e.g., CO_2), while multiple electron acceptors often co-exist, including oxygen, nitrate, manganese, iron oxides, among others (Miao et al., 2012). There are typically multiple functioning microbial groups that use different electron acceptors. For instance, the decay of organic matter where the process uses oxygen and produces carbonic acid, as seen in equation 11:

$$CH_2O \text{ (carbohydrate)} + O_2 \rightarrow H_2O + CO_2 \quad (11)$$

The oxidation reaction of organic compounds occurs in soil or within aquifers, where organic matter is present. The supply of oxygen-depleted electron acceptors such as nitrite, iron, and sulphate might contemplate the oxidation of organic matter. The production of CO_2 as a result of organic matter oxidation may enhance the weathering of carbonate and silicate minerals and further reducing ferric iron to ferrous iron ($Fe^{3+} + e^- = Fe^{2+}$) (Appelo and Postma, 2005). Organic matters and sulphide minerals act as a reductant in the natural environment, where they consume oxygen and the condition leads to a bacterial reduction of carbon species

(Montety et al., 2008). Plenty of elements exist in more than one oxidation state where different oxidation states are more likely to have different solubilities under natural conditions. For example, ferrous iron (Fe^{2+}) is readily soluble in water, while ferric iron (Fe^{3+}) is quite insoluble. Ferrous iron would dissolve in groundwater that is sufficiently reduced, however when that water comes to the surface (a spring), the iron will oxidize to the ferrous state and precipitate as an iron mineral such as ferric hydroxide ($Fe(OH)_3$). For most of the other elements, the oxidized condition is more soluble than the reduced condition, such as copper, zinc, cadmium, lead, and uranium (Singhal and Gupta, 2010; Hiscock and Bense, 2014). The redox balance in a groundwater system is generally maintained by the relative rate of atmospheric O_2 and organic carbon input, carbon respiration and the oxidative weathering of reduced sulphur and iron minerals (Christensen et al., 2000).

In oxidation-reduction reaction, every oxidation is accompanied by a reduction and vice versa, which simultaneously maintains the electron balance. Redox comprises of two parts, a reduced half-reaction (gains e^-) and an oxidized half-reaction (loses e^-). For every redox half-reaction, the following equation can be written, where "n" is the number of electrons transferred:

Oxidized state + n e^- = reduced state

By description, reduction is the gain in electrons whereas, oxidation is the loss of electrons. For instance, the redox reaction for the oxidation of sodium chloride shown in the following equation in half-reactions:

$Na \rightarrow Na^+ + e^-$ (oxidation) (12)

$Cl + e^- \rightarrow Cl^-$ (reduction) (13)

$2Na + Cl_2 \rightarrow 2NaCl$ (balance reaction) (14)

The sodium atoms as reactants have to lose an electron to make the Na^+ ions, while the chlorine atoms as reactants have to each obtain an electron to become Cl^- ion. Another example, the redox reaction for the oxidation of iron illustrates the following equation in half-reactions:

$O_2 + 4H^+ + 4e = 2H_2O$ (reduction) (15)

$4Fe^{2+} = 4Fe^{3+} + 4e$ (oxidation) (16)

$O_2 + 4Fe^{2+} + 4H^+ = 4Fe^{3+} + 2H_2O$ (17)

In reaction (15), the oxidation state of oxygen went from 0 (oxygen as O_2) to -2 (oxygen in H_2O). Thus, four electrons are released due to 2 mol of H_2O forms from 1 mol of O_2 and 4 mol of H^+ (Freeze and Cherry, 1970; Hiscock and Bense, 2014). In equation (16), during the oxidation reaction, 4 mol of Fe^{2+} goes to 4 mol of Fe^{3+}, with a gain of four electron transfer (Freeze and Cherry, 1970). Equation (17), expresses the complete balance redox reaction of iron net effect of the electron transferred and therefore contained no free electrons.

Generally, the groundwater system tends to approach oxygen depletion and reducing condition due to the water circulated which is commonly isolated from the earth's atmosphere, and oxygen that is consumed by the hydrochemical and biochemical reaction is not replenished (Hem, 1989; Machel, 1989). Sulphate is ubiquitous in groundwater that occurs in both natural and anthropogenic water systems. The major natural sources of sulphate are, for instance, atmospheric deposition, sulphate mineral dissolution, and sulphide mineral oxidation (Halim et al., 2010). Meanwhile, anthropogenic sources include coal mines, power plants, phosphate refineries, and metallurgical refineries (Miao et al., 2012). For a reduction reaction of an inorganic constituents to happen, some other constituents must be oxidized and they are commonly organic matters. The reaction involved is catalysed by bacteria that derives energy by facilitating the process of electron transfer. For instance, bacterial sulphate reduction is a major mechanism of anoxic decomposition of organic matter in the sediment, when sulphate is available (Gavrieli et al., 2001). Based on Miao et al. (2012), sulphate reduction is significant for many subsurface systems due to the production of sulphide from sulphate reduction which can effectively precipitate heavy metals in the form of highly insoluble metal sulphides. Alternately, the oxidation of natural organic matter in an aquifer produces excess CO_2 and results in the dissolution of carbonate minerals (Langmuir, 1997; Snyder et al., 2004). Sulphate is the complete oxidized form of sulphur and the most stable aqueous form of sulphur

under aerobic condition. Sulphur occurs in different oxidation states from S^{2-} to S^{6+}, and geochemical behaviour such as sulphur's transport and fate is coupled to the aqueous redox conditions (Langmuir, 1997; Miao et al., 2012). The reduction of SO_4^{2-} to HS^- is a common feature in groundwater which takes place in the presence of bacteria, as shown in reaction 18:

$$SO_4^{2-} + CH_{4(bacterial)} \rightarrow HS^- + H_2O + HCO_3^- \quad (18)$$

Therefore, groundwater which has undergone sulphate reduction is characterized by the presence of HS^- and high content of HCO_3^- as carbonate precipitation is often a by-product of the process, as reported by several researchers (Bourg and Loch, 1995; Canfield, 2001; Gavrieli et al., 2001; De Montety et al., 2008; Singhal and Gupta, 2010). These bacteria are anaerobes that grow from the oxidation of organic matter that use sulphate as the terminal electron acceptor (Hao et al., 1996). The rate of reduction is influenced by a massive uncertainty, for instance, the decrease in sulphate concentration is caused by a factor other than sulphate reduction, such as hydraulic processes (e.g., dilution) and precipitation of sulphate-bearing minerals (e.g., gypsum) which result in the increase of sulphate concentration. However, it is often difficult to determine the concentration of H_2S when there is a significant amount of iron or other metal presence, as they can form metal sulphides that may be ambiguous to the actual amount of H_2S produced (Oyem et al., 2017). Besides, sulphate reduction occurs when hydrogen is released through the decomposition of organic matter by anaerobic bacteria (Singhal and Gupta, 2010). Bozau et al. (2015) stated that the Ba/ SO_4^{2-} ratio carried out in Western Europe and North America can be useful to determine the relationship between barite solubility and sulphate reduction process. Barium concentration in water is frequently related to barite solubility with increasing depth and TDS content (Blount, 1977). An increase in barium concentrations often correlates to sulphate reduction under an anoxic condition in deep reservoir attributed to bacterial or thermochemical processes. Conversely, due to the common ion effect, barium concentrations decrease when sulphate from the dissolution of celestite and anhydrite is released to the water (Bozau et al., 2015).

2.5 Trace Metals

Evaluation of trace metals concentrations in groundwater resources is significant to determine the water quality due to their toxicity, solubility, deposition, redox potential, recycling biogeochemical, absorption and desorption, as well as harmful to the environment and human body system (Zakhem and Hafez, 2015; Esmaeili et al., 2018). The origin of trace metals occurrences is either in the form of natural weathering of rocks (leaching) processes into groundwater or anthropogenic from industrial waste, mining and other human activities that have imported trace metals into groundwater sources (Belkhiri et al., 2017). For instance, groundwater quality would be contaminated from the surface water due to improper disposal of toxic substances from industrial or agriculture activities which replenish the groundwater system by movement through the soil, thus ending up in the groundwater system (Momodu and Anyakora, 2009; Akoto et al., 2019). Zakhem and Hafez (2013) stated that in the natural environment, usually the amount of trace metals concentration is very low since it is derived from the minerals, plants, volcanism, bedrock erosion and the weathered of the geological formation of that particular area (Prasanna et al., 2012). Meanwhile, the exposure of trace metals to humans is derived from direct intake, inhalation, and dermal absorption through the skin (Belkhiri et al., 2017). Long-term ingestion of trace metals in water may lead to dire health consequences and cause diseases such as bladder, lung and skin cancer by arsenic, neurotoxicity by Hg and immune system disorder by lead (Asante et al., 2007; Madzin et al., 2016; Akoto at al., 2019).

The toxicity level of trace metals depends on the physical and chemical parameters in the groundwater, for instance, the activity of pH that affects the solubility and mobility of trace metals in groundwater (Isa et al., 2014). Bourg and Loch (1995) found that pH and redox are related to the control of the solubility and behaviour of trace metals in natural water. For instance, in a decreased pH environment, trace metals cations tend to desorb or dissolve from solids; meanwhile, in increased pH, they absorb or precipitated until a certain degree where they regain solubility. Similarly, the organic matter in groundwater can combine with Fe and Mn to form stable organic complexes. Besides, high salinity in groundwater could enhance the

ionic strength and contributes to the solubility of Fe and Mn. In some conditions, Fe and Mn ions could form inorganic complexes with various anions and maintained stability (Lin et al., 2011). Meanwhile, redox condition has a direct and significant influence on the solubility of trace metal such as iron, manganese, or chromium (Bourg and Loch, 1995). High salinity influences the load and speciation of trace metals in groundwater such as boron, barium, cadmium, lead, etc. This is due to the increased availability of inorganic ligands (bonding of larger molecule to the metal atom) for complex formation with cations (Esmaeili et al., 2018), decrease in pH (Zahkem and Hafez, 2015), decrease in activity coefficient due to increase in ionic strength (Easley and Byrne, 2011) and cation exchange (Acosta et al., 2011; Monjerezi et al., 2012). Besides, the mixing between saline and fresh groundwater affects the desorption-absorption process of boron (Halim et al., 2010).

Nevertheless, in a minimal amount particular trace metals are useful to living organism, for instance, iron (Fe) is essential for plants' and animals' metabolism as well as a dietary requirement for human besides being used in part of multivitamin drugs and products (Singh et al., 2014; Akoto et al., 2019). Furthermore, iron is often associated with manganese which is essential element in plant metabolism and one of the most common and widely distributed elements in rocks and soils (Hem, 1985). However, over-consumption of iron is detrimental to human health as it could lead to nausea, vomiting, organ failure, coma, or even death. Groundwater with high salinity content influences the load amount and speciation of trace metals such as boron, barium, cadmium, lead, and mercury. Due to the increased availability of inorganic ligands (HCO_3, SO_4^{2-} and Cl^-) to bond with the metal atom to form complex formation, there is a decrease in pH, increase in ionic strength, and cation exchange process (Monjerezi et al., 2012; Karamouz et al., 2020). Also, the potential sources of these trace metals are related to natural processes or anthropogenic influences. In natural conditions, the dissolved ions in the water are attributed to the mineral aggregation in the rocks adjacent to the land surface (Isa et al., 2012; Akoto et al., 2019). Besides, heavy rainfall also plays an essential role in controlling the mobility of trace metals in the vadose zone (Liu et al. 2019). Likewise, rock composition, texture, porosity, nature of minerals, and regional structure affect

the composition of trace metals in groundwater (Hem, 1989; Esmaeili et al., 2019). Meanwhile, man-made factors such as agriculture return flow, usage of pesticides, installation of piping services, and dumping sites are other potential sources attributed to these elements (Isa et al., 2012; Belkhiri et al., 2018).

2.6 Stable Isotope

Isotopes form an exceptional diagnostic tool and has been applied in hydrological studies since the early 1950s to understand the infiltration and evaporation mechanism, biodegradation, water provenance, hydro-thermal processes, saltwater intrusion and paleo-hydrological evolution (Lavrushin, 2011; Musashi et al., 2015; Farid et al., 2015; Mirzavand et al., 2020b). Many elements exist in nature with different mass numbers also known as isotopes, for instance, hydrogen occurs in nature as a mixture of the isotopes ^{1}H and ^{2}H (deuterium) while oxygen is found as isotopes with the atomic masses ^{18}O, ^{17}O and ^{16}O (Awaleh et al., 2017). Isotopic tracer commonly used separately to delineate fluid origins and chemical modifications, for instance, oxygen and hydrogen isotopes are used for tracing the origin of waters, nature of the recharged fluids and the effect of water-rock interactions (Farid et al., 2015; Gil-Marquez et al., 2017; Banda et al., 2019). Boron isotope is used for identifying the impacts of anthropogenic sources (Han et al., 2018), while sulphate and strontium isotopes are used for evaluating water-rock interaction (Banner et al., 1988; Grobe and Machel, 2002; Lu et al., 2008). The studies of stable isotopes are commonly used to evaluate recharges input, to verify the effects of evaporation on groundwater systems and to evaluate advection/ diffusion rates in unsaturated/ saturated zones (Awaleh et al., 2020). The recharge process of groundwater is mainly replenished by precipitation where the absence of this process would lead the groundwater into depletion (Thivya et al., 2016). Therefore, recharge processes play a vital role in groundwater reserve. The ^{18}O and deuterium excess (d-excess) is used to identify the source of recharge water since their composition is not influenced by rock water exchanges at a lower temperature (Thivya et al., 2016; Gopinath et al., 2019). The δD - $\delta^{18}O$ relationships can be used for calculating the mixing ratio between freshwater and saline or brine,

investigation of seawater evaporation and up coning processes (Marandi and Vallner, 2010; Mirzavand et al., 2020b).

The integration of isotopic data for a variety of elements provides a better diagnostic tool in determining the origin of the salinity (Vengosh et al., 2000). The correlation between $\delta^{18}O$, $\delta^{2}H$, and salinity can be used to identify different salinization pathways (Liu et al., 2016). However, varieties of geochemical processes such as water-rock interaction, ion exchange, and mineral dissolution may influence the concentration of geochemical compositions in the process of groundwater salinization (Awaleh et al., 2017). Therefore, chloride stable isotopes are commonly used to define salinity sources, mixing of different waters, and water-rock interaction (Bagheri et al., 2014a; Awaleh et al., 2020). It is often challenging to differentiate the sources of salinity from major ions without the information of isotopes (Liu et al., 2016). According to Bagheri et al. (2014a), $\delta^{36}Cl$ isotope fractionation may be affected by the physical and chemical processes such as ion filtration, ion exchange, and diffusion (Du et al., 2016). Moreover, a stable Cl isotope ratio jointed with other geochemical parameters would be a useful tool to differentiate the sources of solute and to trace the transport mechanism of solute. Determination of the stable isotopic composition of saline water is a useful tool in discriminating the cause of salinity because due to evaporation, saline water would be isotopically more enriched (higher $\delta^{36}Cl$ values) than the source water, whereas water that is saline due to salt weathering would not significantly change the isotopic compositions (Thivya et al., 2016). For instance, meteoric chloride is recognized by a high $^{37}Cl/Cl$ signature that is conserved through evaporation concentration and salt recycling through precipitation-dissolution. Meanwhile, additional saline and brine sources are significantly reduced in the $^{37}Cl/Cl$ ratio (Bagheri et al., 2014b; Mirzavand et al., 2020b).

The tracer element boron and its isotopes $\delta^{11}B$ in saline groundwater can help to determine the formation environment of hydrothermal activities and the chemical sources (Han et al., 2018). Boron isotopes are widely used to identify the geological processes such as dehydration and metamorphism during tectonic events, the origin of saline groundwater, sedimentary environment, water-rock interaction, magmatism and the formation of hydrothermal ore

deposits and wastewater recharge (Vengosh et al., 2000; Musashi et al., 2015; Martin et al., 2016; Han et al., 2018). Additionally, stable isotopes such as sulfur and oxygen have been proven to be a powerful tracers in distinguishing its sources and the oxidation mechanism during water-rock interaction to determine whether it is abiotic or it involves bacteria (Taylor et al., 1984; Langmuir, 1997; Szynkiewicz et al., 2020). $\delta^{34}S$ is used in determining the origin of sulphate, salinization and usually, the sulphate reduction and oxidation leads to enrichment and depletion in $\delta^{34}S$, respectively (Mirzavand et al., 2020b).

2.7 X-Ray Diffraction

X-ray diffraction is a useful tool to determine phase, crystal structure and other structural parameters (Ragenspurg et al., 2016; Biyada et al., 2020). As each phase has a unique powder diffraction pattern, it is possible to distinguish between compounds as the diffraction method is sensitive to the crystal structure (Yalcin and Mutlu, 2011). X-ray diffraction is a multipurpose and non-destructive method to analyze material properties such as phase composition, structure, and texture from powder samples, solid samples, or liquid samples (Ladd et al., 2013; Aquilano et al., 2016; Pussi et al., 2020). X-ray diffraction is based on a monochromatic beam of electromagnetic radiation of short wavelength passing through a mineral grain, which is scattered by the atoms that compose the mineral (Mchenry et al., 2020). It is a valuable tool in determining the mineralogy composition of sedimentary rock, crystalline constituent, and structure of salt (Biyada et al., 2020; Chander et al., 2020). This phenomenon is known as diffraction, where at specific angles of incidence, the scattered X-rays are in phases that produce an intensified secondary beam as a reflection of the beams by planes of atoms (Bragg, 1913). The diffraction beam known as the first-order reflection occurs when, the distance travelled by one scattered beam is different by a length equal to the X-ray wavelength, and from the distance travelled by another beam scattered by an adjacent plant of the atom (Figure 2.5). Meanwhile, the resultant beam known as the second-order reflection occurs when the diffraction difference in distance travelled by X-ray is scattered from two

adjacent layers of atoms that is equals to two wavelengths (Bragg, 1913; Lindholm, 2012). The Bragg equation expressed the general relationship:

$$n\lambda = 2d \sin\theta \tag{19}$$

where n = a whole number (integer), λ = the X-ray wavelength, d = the distance between planes of atoms (Å), and θ = Bragg's angle of incidence. The direction of the primary x-ray remains constant as the subject rotates around an axis normal to the primary beam, in the diffractometer. Next, the peaks are recorded on a strip chart as the diffracted beams arrive at the detector tube attached to the goniometer. The angle recorded on the goniometer is due to the subject rotating through an angle of θ while, the detector tube rotates at an angle of 2θ. Different minerals have numerous sets of lattice parameters, where the x-ray diffraction produces its respective peak on the strip chart. This known as the diffractogram. The diffraction occurs for each angle of incidence satisfying the Bragg's equation related to a set of lattice planes with characteristic *d* spacing (Lindholm, 2012).

Electromagnetic radiation such as a beam of x-rays carries energy and the rate of flow through a unit area perpendicular to the direction of motion of the wave is called the intensity (*I*). All materials absorb x-rays and the transmitted intensity is attenuated based to an exponential law:

$$I = I_0 \exp(-\mu t) \tag{20}$$

where I_0 and I are the incidents and transmitted intensities, respectively, μ is the linear absorption coefficient of the material and t is the path length for x-ray through the material.

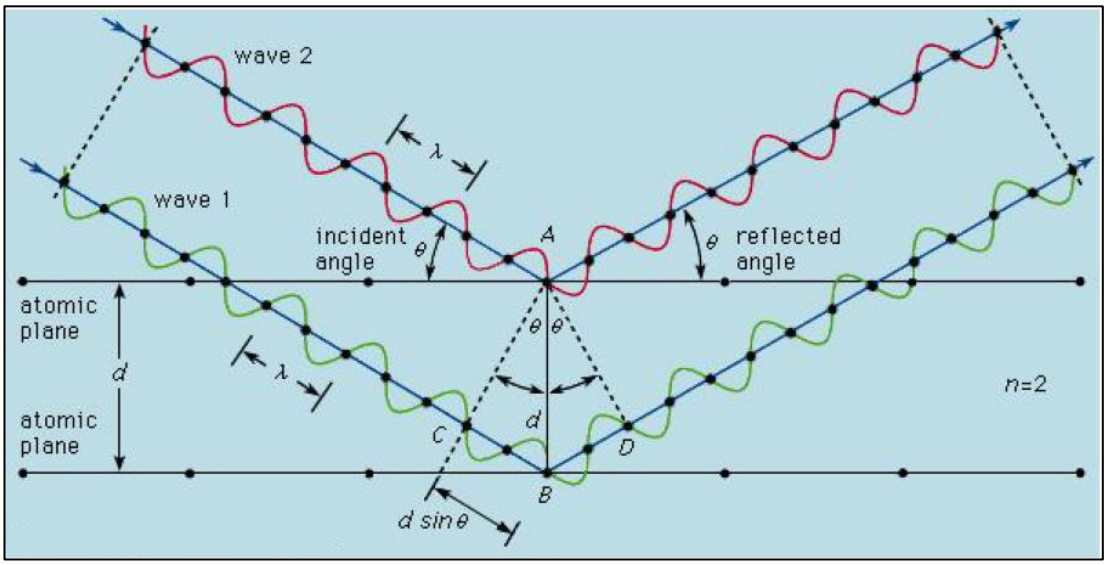

Figure 2. 5 Bragg's Law diagram: The incident X-rays are characterized by the two parallel waves from the top left corner. Adapted from Lindholm, (2012).

2.8 Geophysical Methods

Geophysical methods are based on the principle of physical properties that propagated through the Earth's interior (Saribudak and Hauwert, 2017; Nazaruddin et al., 2017; Oskooi et al., 2019). Analysis of these measurements unveiled how the physical properties of Earth's interior vary horizontally and vertically. Geophysical methods can be applied to a wide range of investigations from an exploration of minerals, hydrocarbon, hydrology, environmental, engineering, and other purposes (Kearey et al., 2013; Mahmoud and Ghoubachi, 2017). The most popular geophysical methods used are gravity, electromagnetic, seismic, resistivity, magnetic, and radar. Based on most researchers in hydrological exploration, the most suitable methods are seismic refraction and 2D resistivity used to locate the water table and map subsurface features (Rezaeia et al., 2013; Hamdan et al., 2010; Anomohanran et al., 2017; Alhassan et al., 2018).

Since it is impossible to verify the physical properties of subsurface materials directly, researchers and geophysicist depend on surface geophysical methods to determine their physical properties (Hodlur et al., 2010; Pasquet et al., 2015). Table 2.1 displays the physical properties of Earth's material for seismic refraction and 2D resistivity methods related to the hydrological aspect (Kearey et al., 2013; Kumar et al., 2014). There are several factors of ambiguity in the interpretation, for instance, the electrical properties of earth's material are controlled by clay content, porosity, total dissolved solids, salinity, temperature, and degree of saturation (Anomohanran et al., 2017; Farid et al. 2017). Similarly, the density properties of the earth's material are restricted to the degree of weathered rock, compaction, cementation, and porosity (Chen and Zelt, 2016; Oskooi et al., 2019). In hydrological exploration, common geophysical methods are combined with borehole log data for detailed geological and hydrological information for the area which significantly provides better interpretation for subsurface structures (Weight and Sonderegger, 2001; Kearey and Brooks, 2013; Anomohanran et al., 2017). Alternatively, combined geophysical methods such as seismic refraction and 2D resistivity are possible to distinguish the aquifer characteristic, and reduce some of the uncertainties attained from each geophysical method and allow better performance

for unambiguous interpretation (Hamdan et al., 2010; Moustafa, 2012; Rezaeia et al., 2013; Saribudak and Hauwert, 2017). Furthermore, the seismic refraction method has an advantage over the 2D resistivity method in interpreting complex geological structure with ease and minimizing ambiguity at the sites (Alhassan et al., 2018). Nevertheless, the 2D resistivity method provides a greater depth of investigation than the seismic refraction method (Ayolabi et al., 2009; Alhassan et al., 2018).

Table 2. 1 The physical properties of common earth's material adopted from Kearey et al., 2013; Kumar et al. 2014; Araffa et al. 2017

Material Type	Density	P-Wave Velocity (m/sec)	Resistivity (Ω.m)
Clay	1.1 – 2.4	1,000 – 2,600	1 – 100
Sand, gravel (dry)	1.3 – 2.2	200 – 1,000	100 – 10,000
Sand, gravel (wet)	1.3 – 2.2	1,500 – 2,000	50 – 3,000
Shale	2.1 – 2.75	2,000 – 4,000	5 – 40
Siltstone	2.2 – 2.75	2,000 – 4,000	30 – 100
Sandstone	2.15- 2.65	2,050 – 6,000	50 – 10,000
Limestone	2.44 – 2.71	2,600 – 6,000	100 – 100,000
Metamorphic	2.4 – 3.5	3,500 – 7,250	5 – 300,000
Water (fresh)	1.0	1,400 – 1,500	3 – 100
Water (saline)	1.01 – 1.05	1,400 – 1,500	0.2 - 1

2.8.1 2D Electrical Resistivity

The electrical resistivity method is non-invasive, low cost, field easy to operate, and portable, which is shown in the bulk resistivity value and a wide spectrum of resistivity range of subsurface with its significant aquifer properties (Kumar et al., 2016; Farid et al., 2017). This becomes the most suitable and useful geophysics method for groundwater exploration to determine the horizontal and vertical spatial of the aquifer, the depression structures and track groundwater flow (Thapa et al., 2019).

The electrical resistivity method measures potential differences in the subsurface when an induced current flow is injected at the surface. Generally, it can be achieved by deploying two electrodes as current electrodes (C1 and C2) and two electrodes as potential electrodes (P1 and P2), where the current (I) is then injected into the ground and the resulted voltage difference (ΔV) between the potential electrodes are measured (Figure 2.6) (Loke, 2004). The current and voltage measurement are then converted into an apparent resistivity (ρ_a) value, where k is the geometric factor that depends on the configuration of the current and potential electrodes from formula 21 (Loke et al., 2013):

$$pa = k\frac{\Delta V}{I} \tag{21}$$

Ahead of employed resistivity method survey, there are various types of arrays and features that are essential and need to be considered such as the depth of investigation, the sensitivity of the array to vertical and horizontal changes in subsurface resistivity, the horizontal data coverage and the signal strength (Loke et al., 2013). The applicable types of array configuration with different characteristics survey are Wenner, dipole-dipole, Wenner-Schlumberger, Schlumberger, pole-pole, pole-dipole, and multi-gradient (Loke et al., 2013).

For instance, the dipole-dipole array is very sensitive to horizontal changes in resistivity but insensitive to vertical changes, which is good in mapping vertical structures such dykes and cavities but poor in mapping horizontal structures such as sills or sedimentary layers. For groundwater investigation, the best and most suitable configuration is the Wenner array due

to the good sensitivity to vertical changes in the subsurface resistivity below the centre of the array (Figure 2.6). However, it is less sensitive to horizontal changes with moderate depth of investigation. The Wenner array has the highest signal strength compared to other arrays, which is important and a suitable factor if the survey is to be employed in areas with high background noise. Wenner array is the most commonly used array system worldwide, where the electrodes spread are uniformly spaced in a line. For depth exploration using the Wenner array (Figure 2.6), the electrodes are expanded about a fixed centre, increasing the spacing *a* in steps. The apparent resistivity equation can be expressed as follows:

$$\rho a = 2 \pi \Delta V/I \tag{22}$$

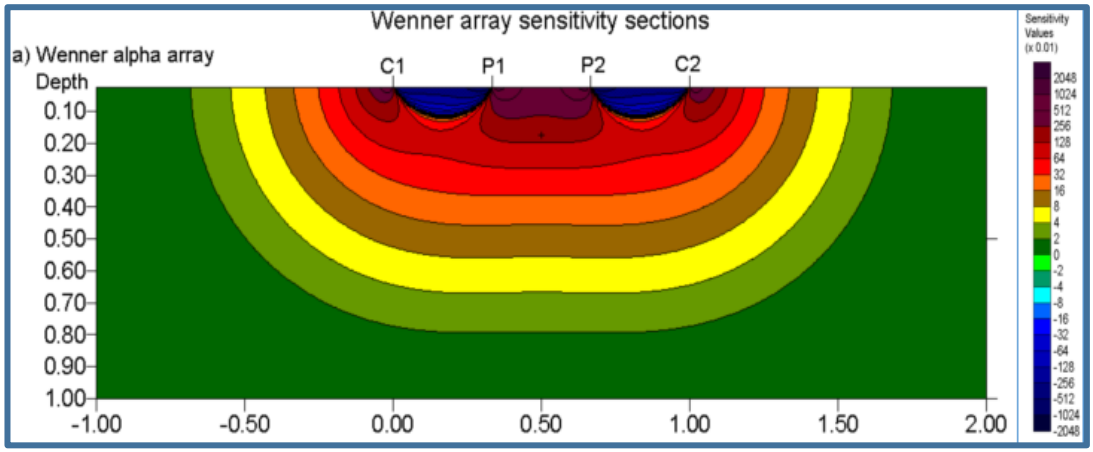

Figure 2. 6 The sensitivity section for the Wenner array. Adapted from Loke et al. (2013).

Generally, the resistivity meter measures the electrical resistivity by injecting current onto Earth's surface through two current electrodes and calculating the voltage differences at two potential electrodes at a distance. In the 1D survey, the resistivity meter has a current power source and voltage measuring circuit box that is connected to a cable to four electrodes. The resistivity meter method uses the sounding curves and profiling survey for the subsurface model. Meanwhile, for the 2D resistivity survey method, a multi-electrode system powered by a battery provides current flow via a multi-core cable which is coupled to 42 electrodes along a line, and is subsequently connected to the main circuit to run different types of the array configuration. A built-in internal automatic shift circuity is controlled by a programmable

microcomputer that automatically selects the most applicable 4 electrodes for each measurement (Loke et al., 2013). This enables almost any array configuration to be used. This data is conventionally presented as an apparent resistivity image, known as a pseudo-section (Figure 2.6).

The electrical resistivity of a geological formation is the physical characteristics, which determines the flow of electric current in the formation through the subsurface, depending on numerous site-dependent factors such as lithology, porosity, water content, burial compaction, the conductivity of electrolyte within the rock and groundwater salinity (Revil et al., 2012; Naidu et al., 2013; Rehman et al., 2016; Mohamaden et al., 2016; Farid et al., 2017). Fine sediment such as clay is a relatively good electrical conductor that produces a significant electrical contrast with more resistive coarse sediment like gravel when under fresh groundwater conditions (Farid et al., 2017). For instance, in groundwater exploration, the resistivity varies from 10 to 100 Ω.m depending on the concentration of dissolved salts. The low resistivity about 0 to 0.2 Ω.m of seawater or brine is due to a relatively high salt content (Ezersky, 2005; Chabaane et al., 2017). This made the resistivity method an ideal technique for mapping the saline and freshwater interface. For sedimentary rocks, which are usually more porous and have higher water content, they typically have a lower resistivity value, usually from 10 to 1000 Ω.m as compared to igneous or metamorphic rocks (>1000 Ω.m) (Patra, 2008; Mainoo et al., 2019). In the groundwater investigation, the conductivity of electrolyte in minerals plays a significant influence for instance, with clay having both electronic and electrolytic conductivities, it exhibits very low resistivity (Loke, 2011; Kearey et al., 2013). The main limitation of the 2D resistivity method is the assumption that the geological structure does not change in the direction perpendicular to the survey line. Therefore, it is a reasonable assumption when the survey line stretches out perpendicular to the strike of the structure. However, when there are significant offline variations or distortions in the model produced, it can result in misleading interpretation (Loke et al., 2013). The interpretation of the electrical resistivity that is inverse from the chargeability model would be ambiguous due to various factors influencing the values such as water content, resistivity, and

porosity (Khaki et al., 2016; Islami et al., 2018). For instance, low resistivity values are typical in saline, brackish water, leachate, and clay; intermediate resistivity is associated with freshwater, wet sand, sandstone, silt, gravel, limestone formation, while high resistivity corresponds to dry sand or granite bedrock (Guerin et al., 2004; Khaki et al., 2016).

Figure 2.7 shows the variation of electrical conductivity in Ω.m versus salinity (Na^+-Cl^-) in ppm, where the resistivity of the solution decreases distinctly with the increase of salinity. However, clay or shale layer and saline water-saturated aquifer in some areas might have similar values of resistivity. Therefore, researchers employ conjunction of 2D resistivity and Induced Polarization (IP) data to dismiss uncertainty of the similarity of clay or shale in which the IP method provides a measurement of membrane polarization across the cationic membrane to differentiate clay materials and contaminated saline aquifer (Abdulrahman et al., 2016; Kumar et al., 2016; Rehman et al., 2016).

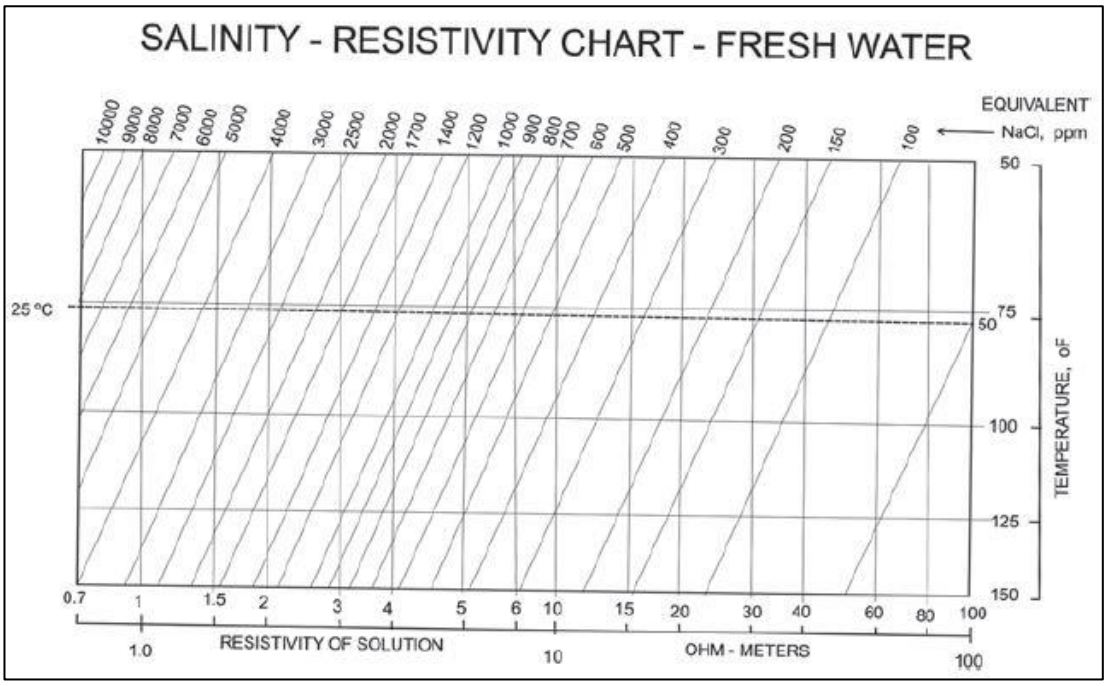

Figure 2. 7 Variation of electrical conductivity and salinity with resistivity value. Adapted from Scott Keys and MacCary, (1971).

2.8.2 Seismic Refraction

Seismic refraction is a non-intrusive geophysical method that provides the physical information on a larger volume of subsurface, but with significant potential of uncertainties (Pasquet et al., 2015). Seismic refraction is a popular geophysical method to determine the depth to bedrock, depth to the interface between unsaturated zoned and saturated zone (water table), thickness and geometry of subsurface unit, degree of weathered rock and location of fault zone (Haeni, 1986; Grelle and Guadagno, 2009; Alhassan et al., 2018; Oskooi et al., 2019). In general, the seismic refraction method employs artificial seismic energy that returns to the surface after propagation through the geological unit and calculation of the propagation velocities of elastic moduli and densities of the material which they pass through (Araffa et al., 2017). When seismic energy is released at a point (P) near the surface of the homogeneous medium, part of the energy propagates through the body of the medium as seismic body waves (Figure 2.8). The remaining part of the seismic energy is spread out over the surface as the seismic surface wave (Reynolds, 2011). The direction perpendicular to the wavefront is called the seismic ray path. Seismic body waves can be subdivided into two classes of waves, (a) P-waves, known as compressional and longitudinal waves. They are also called primary waves because they propagate through the medium faster than other wave types. In P-wave, particles constituting the medium are displaced in the same direction that wave propagates (radial direction), (b) S-waves, known as shear waves or secondary waves because they propagate through the medium slower than P-waves (Kearey et al., 2013).

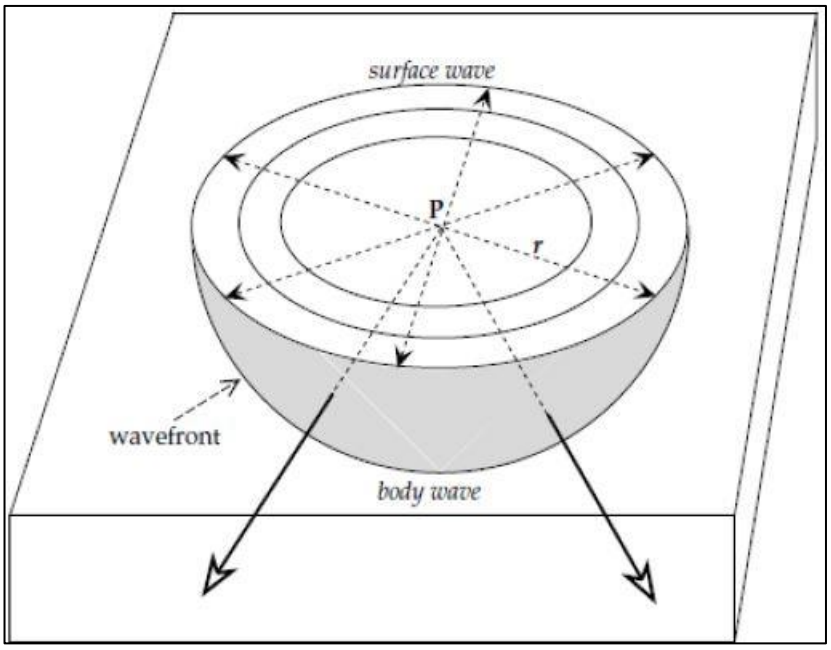

Figure 2. 8 Propagation of a seismic disturbance from a point source (P) near the surface of a homogeneous medium. Adapted from Kearey et al. (2013).

Seismic refraction method is based on the principle of Snell's law, which governs the seismic energy that returns to the surface of the Earth associated with angles of incidence through the subsurface and refraction of sound to locate refractors that separate the layer of different properties and velocities (Rezaeia et al., 2013; Alhassan et al., 2018). As sound waves travel from a medium of low seismic velocity into a higher velocity medium, some are refracted towards the lower velocity while some are reflected into the higher velocity. As the angle of incidence of the sound ray approaches the critical angle (angle from two media where the refracted ray contact meet at the surface), most of the compressional energy is transmitted along the surface of the second layer. Next, the energy propagates and generates new sound waves in the upper-medium which in turn propagates back to the surface at the critical angle and the seismic velocity of layer one (Rezaeia et al., 2013; Glas et al., 2019). For this phenomenon to work, the velocity of sound in each deeper layer must be greater than the layer above. Successively, when the condition is met, the refracted wave arrives at the Earth's surface where it could be detected by a geophone which generates an electrical signal and

sending the signals to a seismograph (Grelle and Guadagno, 2009). The mechanism is controlled by the seismic wave propagation that depends on the density and elasticity of the subsurface materials. As the wave propagates further downwards to the subsurface, some rays may be reflected and refracted at velocity interfaces (Patra et al., 2016).

The generalized form of Snell's Law states that, along any one ray, the ray parameter remains a constant, for the refracted P-waves ray shown in Figure 2.9, and therefore can be explained by the equation below:

$$\frac{\sin\theta_1}{V_1} = \frac{\sin\theta_2}{V_2} \tag{23}$$

Note that if $V_2 > V_1$ the ray is refracted away from the normal to the interface that is $\theta_2 > \theta_1$ (Kearey et al., 2013). Angle of incidence known as the critical angle (θ_c) is when the velocity is higher in the underlying layer which the angle of refraction is 90^0 (Reynolds, 2011). This gives rise to a critically refracted ray that travels along with the interface at the higher velocity V_2 and the critical angle formula is given as follows:

$$\frac{\sin\theta_c}{V_1} = \frac{\sin 90^0}{V_2} = \frac{1}{V_2} \text{ So, that } \theta_c = \sin^{-1}(V_1/V_2) \tag{24}$$

The seismic refraction method can be demonstrated for the case of the flat interface between two horizontal layers in Figure 2.10. Let the depth to the interface be (d) and the seismic velocities of the upper and lower layers be (V_1) and (V_2) respectively ($V_1 < V_2$). The geophone (G) at distance (x) on the surface after time (x/V_1) record the direct wave from the shot point at (S). The slope ($m_1 = 1/V_1$) indicate the travel-time curve for the direct ray in a straight line through the medium. The refracted ray velocity (V_1) of the upper layer travels along the path (SC) and impinges with critical angle (i_c) on the interface at (C). It goes by along the segment (CD) with velocity (V_2) of the lower layer and returns to the surface along (DG) with velocity (V_1). The segments for (SC) and (DG) are equal and the travel time for the refracted ray path can be written as:

$$t = \frac{x}{V_2} + \frac{2d}{V_1}\cos i_c \tag{25}$$

The first arrival recorded at (x_c) is regarded as both refracted and reflection rays while, the refracted rays are only recorded at distances greater than the critical distance (x_c). The refraction time-travel curve is found to intersect the time axis at the intercept time (t_i), given by:

$$t_i = \frac{2d}{V_i} cos\ i_c = 2d\ \frac{\sqrt{V_2^2 - V_1^2}}{V_1.V_2} \tag{26}$$

The first recorded wave close to the shot points is direct ray, however, refracted ray travels at a faster velocity of the lower layer, so when it will eventually overtake the direct ray and become the first arrival. The straight line for the direct and refracted rays cross each other at this distance is called the crossover distance (x_{cr}):

$$x_{cr} = 2d.\sqrt{\frac{V_2 + V_1}{V_2 - V_1}} \tag{27}$$

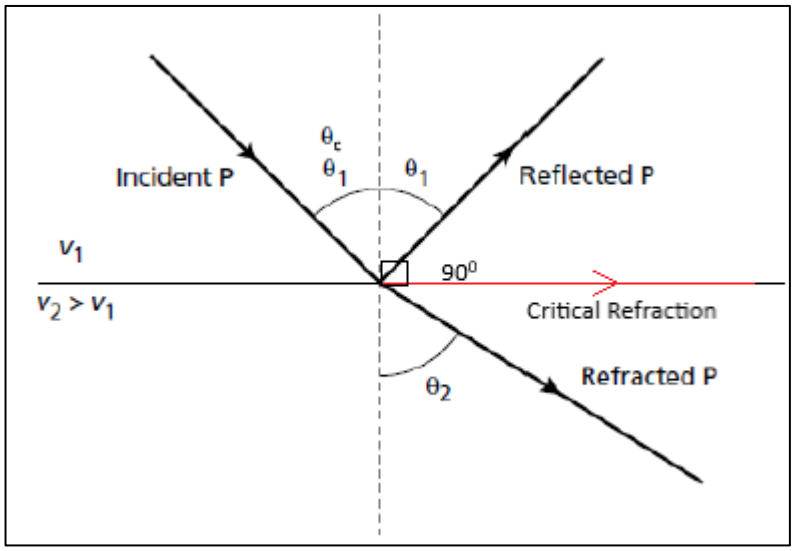

Figure 2. 9 Reflected, refracted, and critical refracted P-wave rays associated with a P-wave rays obliquely incident on the interface of acoustic impedance contrast. Adapted from Kearey et al. (2013).

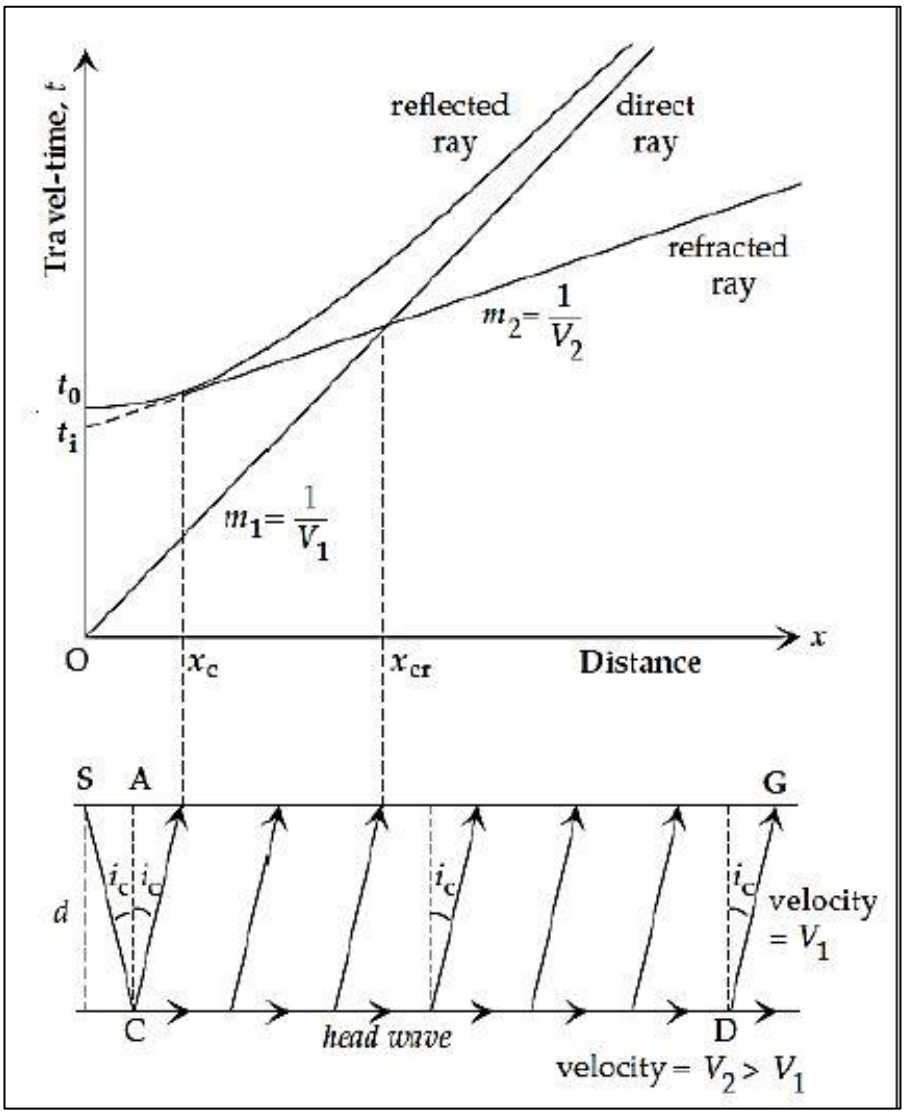

Figure 2. 10 Travel-time versus distance curves for the direct, reflected and refracted rays at a horizontal interface between two layers with seismic velocity V_1 and V_2. Adapted from Pasquet et al. (2015).

The water table depth can be determined by acquiring seismic P-wave travel times from refracted waves travelling at the interface between two layers of different velocities (Azhar et al., 2019). P-wave velocities depend on the signal wavelength and saturation stage of the rock-fluid system through which the wave travels (Fortin et al., 2014). The P-wave velocity values for groundwater saturated layers are typically ranging between 1,200 and 1,800 m/s, with an average of 1,500 m/s (Haeni, 1986; Kearey et al., 2002; Azhar et al., 2019). However,

velocities higher than 1,500 m/s to 2,000 m/s are possibly for deeper fully saturated layers (Araffa et al., 2017). Though, based on Desper et al. (2015), in the tropic areas, some saturated layers might have velocities lower than 1,500 m/s due to the rapid rising of water levels from heavy rainfalls causing air entrapment in the rock matrix or shallow water tables in unconsolidated sedimentary layers (Pasquet et al., 2015).

Nevertheless, the fundamental condition is, the overlying unit is obligated to have a lower propagation velocity than the underlying layer. Auspiciously, most of the time, unsaturated and unconsolidated layers such as alluvium had lower propagation velocity than the bedrock unit beneath it (Oskooi et al., 2019). In a hydrological investigation, the seismic refraction method provides direct information on the level of the water table, since an increase in water content caused an increase significantly in seismic velocity, specifically P-waves (Al-Shuhail and Al-Shaibani, 2013; Alhassan et al., 2018). By implication, the saturation zone (coarse-grained unconsolidated deposits) is, therefore, exceptional refractors and the upper layer or boundary can be determined with considerable accuracy. Furthermore, the seismic survey utilized would determine the structural, lithological framework and quantify the heterogeneity of the subsurface aquifer (Alhassan et al., 2018). The conjunction of resistivity and seismic refraction is ideal for hydrological exploration because they respond to differed physical properties of the subsurface and can minimize interpretive uncertainty associated with the method when used in confinement (Glas et al., 2019). Important rock characteristics are to be considered as they influenced wave velocities such as porosity, cementation, crystallinity, weathering, and discontinuities (bedding, joints, and faults) (Pasquet et al., 2015). Table 2.1 shows the general subsurface material P-wave velocity, for instance, compacted, massive, and low porosity rock which retains higher seismic wave velocity compared to the unconsolidated formation which possesses lower velocities.

CHAPTER 3. Methodology

3.1 Preliminary Survey, Sampling, and Physio-chemical Analysis

Reconnaissance investigation in the study area (Ba'kelalan, Limbang, Malaysia) was carried out to prepare the geology map, fixing the geophysical survey points using GPS, collection of groundwater samples from the wells, and allocation of rainfall gauges. Accurate and precise preparation for a geology map of the study area is vital to understand how geology (lithology and structures) influences and controls the groundwater system. QGIS software was adopted to map the study area with precise coordinates including the lithological identification, elevation, installed rainfall gauges, existed wells, villages, strike, and dip values of bedding planes of rock surfaces. A total of five wells and one river water (Kelalan river) were selected and sampled, 3 wells located in the downstream with an elevation of 913 m a.s.l (Buduk Bui) and 2 wells located in the upstream with an elevation of 948 m and 967 m a.s.l (Pa'komap and Punang Kelalan, respectively). The 5 existing wells are situated on the foothills and between the valleys with a distance of approximately 6.4 km between the downstream to the upstream. The distance for well 1, 2 and 3 are adjacent to each other with 3 m and 5 m apart, while, well 4 and 5's distance is approximately 2.2 km away. The average water level of the existing wells is shallow in depth ranging from 1 m to 2.5 m and drained using a PVC pipe or bucket into a storage tank and then into the fire stove. During sampling collections, the water level was measured from the top of the well down to the water surface using a measuring tape. The water samples were obtained by using a bucket to draw the groundwater from the well and were subsequently kept in polyethylene bottles of 100 ml, 500 ml and 5 L, which were rinsed with the water sample beforehand and were stored at a temperature of 4^0C until further analysis. The water sample collections were more frequented and detailed, including hourly (<24 hours), daily, and monthly information and samples were analysed from each season (MON and POM), for physical and chemical parameters. The physical parameters such as pH, salinity, temperature, turbidity, total dissolved solids (TDS), electric conductivity (EC) and water level (meter) were measured in situ using calibrated analyser probes (Thermo Scientific Orion Star and Turbidity meter) (Aris et al., 2009; Isa et al., 2012). Hourly measurements (< 24 hours), started from 8 am to 5 pm on the 11th December 2018 for well 1, 2, and 3, while, daily

measurements were taken from 12th until 18th December 2018 for well 1, 2, 3, 4, and 5. Furthermore, polyethylene bottles were kept for monthly collection from 18th December 2018 to 31st January 2019 and were measured for physical parameters such as well 1, 2, 3, and 4. Moreover, seasonal sampling of MON was taken in December 2018 and POM in April 2019 for complete chemical analysis for major ions, nutrients, and trace metals. Additionally, the hydrochemical result obtained from the laboratory in Canada (ActLab) is included the well 1 (2017) sample.

Secondary data of rainfall were obtained from NASA meteorology department station in Ba'kelalan airport (gpm.nasa.gov/data/directory) from 1st December 2018 to 31st April 2019. Three rainwater gauges were placed at Long Aru (RW LS), Buduk Bui (RW BB) and Pa'Komap (RW US). The rainwater samples were collected from December 2018 until the end of January 2019 and measured for physical parameters, major ions, and further chemical analysis.

3.2 Geochemical Analysis

Five saline groundwater and one river water samples were collected during December 2018 and April 2019 representing MON and POM season, respectively. Water samples were collected in 2L polyethylene bottles. The major ions such as CO_3, Cl^- and HCO_3^- were analysed by the titration method (chloride concentration using standard silver nitrate, while for carbonate and bicarbonate using a titration of sulfuric acid) (Ramesh and Anbu, 1996; APHA, 1998). Nutrients analysis, (NO_3^-, NO_2^-, SO_4^{2-}, NH_3, and PO_4^{3-}) were made through the Hach test kit/ Spectrophotometer powder pillow method. Subsequently, the collected water sample were filtered with a 0.45 µm filter membrane for further elemental analysis. The major ions (Na^+, Mg^{2+}, Ca^{2+}, K^+) and trace metals (Al, Co, Cu, Cd, Cr, Ba, Pb, Fe, Mn, Sc, Sn, Zn) were analysed using Atomic Absorption Spectrometer (Perkin Elmer, AAS) in Faculty of Engineering and Science laboratory, Curtin University, Malaysia. Besides, the trace metals such as lithium and boron were analysed using induced coupled plasma – optical emission spectrometry (Perkin Elmer, ICP-OES) facility in Bio Valley, Curtin University. The other

trace metal analysis was performed using acid digestion method (ADM) and liquid-liquid extraction method (LLE) due to the high salinity of the samples (Nickel et al., 1992). The analytical precision for measurements of ions was determined by calculating the ionic balance error of total cations (+) and total anions (-) (Freeze and Cherry, 1970; Clark, 2015). The geochemical analysis data were converted into their equivalent or milli equivalence units (meq/L = ppm x valence/ molar mass) for interpretation. Subsequently, calculations were made to find the difference between the sum of major cation (Σ cation) and anions (Σ anions), then divided with the sum of all major ions to provide the charge balance error (Clark, 2015):

$$\text{Charge balance error (\%)} = \frac{\Sigma\, cation - \Sigma\, anions}{\Sigma\, cation + \Sigma\, anions} x\ 100 \quad (28)$$

The acceptable error percentage for water analysis is ranged between ± 1 and ± 10 (Hem, 1985). The occurrence of errors in the chemical analysis of groundwater was possibly due to reagent, limitation of methods and instrument, the presence of impurities in distilled water or pure water, etc (Hem, 1985). Geochemical plots such as Piper, Durov and Gibbs diagram that determine the water type were calculated by first converting the result for the major cations and anions from mg/L to meq/L and mmol/L.

Consequently, the geochemical data interpretation used the ionic ratios, plotting diagram, and statistical analysis in IBM SPSS Statistic version 22 to determine the interrelationship between the ions and the controlling factor affecting the groundwater geochemistry (Isa et al., 2012; Van Engelen et al., 2018). Moreover, saturation indices (SI) were calculated using the program PHREEQC (Parkhurst and Appelo, 1999) with pitzer.dat as the appropriate database used for saline groundwater. While using individual tracers (Na^+/Cl^-, B/Cl^- and Na^+/Li), this could provide useful information on the saline source, it is, as it is insufficient to accurately identify the origin of the saline source. It is therefore essential to use isotopic tracers for accurate delineation of the salinity sources and provide robust and reliable clarification processes (Boschetti et al., 2011; Vengosh, 2014; Awaleh et al., 2017).

3.3 Stable Isotopes

Additional samples of untreated saline groundwater were collected in 2 L polyethylene bottles for analysis of stable isotopes (^{2}H, ^{18}O, ^{34}S, ^{11}B, ^{37}Cl). Oxygen and hydrogen (deuterium) isotopes were analysed at the Isotope Hydrology Division of the Center for Water Resource Development and Management (CWRDM), India using continuous-flow isotope ratio mass spectrometry (FINNIGAN DELTA^{PLUS} XP) and converted in per mil delta values (δ‰). CO_2 – H_20 equilibrium method was used to analyse the oxygen isotope ($\delta^{18}O$) and H_2 – H_2O equilibrium method using platinum catalyst support on a hydrophobic material was used to analyse the hydrogen isotope (δD). The value of stable isotopes is generally represented by δ (expressed in terms of parts per million, ‰) and is defined as (Craig, 1961; Coplen, 1994):

$$\delta\ (‰) = \left(\frac{R_{sample} - R_{std}}{R_{std}}\right) x\ 10^3 \quad (29)$$

where, R is *D/H* or $^{18}O/^{16}O$ and *SMOW* is the Standard Mean Ocean Water.

The stable isotopes analyses for ^{34}S, ^{11}B and ^{37}Cl were analysed at ActLabs in Ontario, Canada. For isotopic ^{34}S, the analysis was carried out using FINNIGAN MAT DELTA^{PLUS} XL IRMS coupled with Thermo Scientific TC/EA with unit symbol VCDT. Data was corrected and normalized using four international standards: USGS 32, NBS 127, IAEA SO5, IAEA SO6 and calibrated against International Atomic Energy Agency (IAEA). The ^{11}B isotope analysis was carried out using a single degassing filament technique on a Thermal Ionization Spectrometry (TIMS). The outcomes were corrected and calibrated against the International Standard NIST SRM 951a and seawater ($\delta^{11}B$ = 40±2). The ^{37}Cl stable isotope analysis was determined by a continuous-flow ratio mass spectrometry (CF-IRMS) and all the results were corrected and calibrated against the Standard Mean Ocean Bromide (SMOC). The $\delta^{18}O$ and δH^2 stable isotopes were analysed for well 1, 2 and 3 in the MON season. Whereas, $\delta^{34}S$, $\delta^{11}B$ and $\delta^{37}Cl$ were analysed for only well 1 in the POM season.

3.4 Graphical and Ionic Ratio Method

A variety of graphical techniques have been commonly used as hydrochemical tools to facilitate the classification of waters, with the utmost outcome of dividing a group of samples into similar homogeneous groups representing a hydrochemical facies. The prevailing graphical methods widely applied by most researchers include the Piper diagram, Gibbs diagram, Durov diagram, Stiff pattern diagram, Collins bar diagram, Pie diagram, Schoeller diagram, Langelier-Ludwig plot and Brine-Differentiation plot (Langelier and Ludwig, 1942; Piper, 1944; Gibbs, 1970; Zaporozec, 1972; Hounslow, 1995; Boschetti et al., 2011; Singh et al., 2012; Okiongbo and Douglas, 2015; Barzegar et al., 2018; Marandi and Shand, 2018; Liu et al., 2019; Awaleh et al., 2020). Nevertheless, this research project utilizes diagrams such as the Piper diagram, Durov diagram, Gibbs diagram, Van Wirdum's diagram, Langelier-Ludwig plot and Brine-Differentiation plot as they were recommended to be the best tool in helping to distinguish between small numbers of samples that have distinct chemical differences (Guler, 2002; Yu Lu et al., 2008; Isawi et al., 2016; Liu et al., 2019; Awaleh et al., 2020).

The Piper diagram is the most widely utilized graphical form which provides the relative concentration of major cations and anions on two separate trilinear plots, conjugate with a central diamond plot where the points from the two trilinear plots are projected. Subsequently, the central diamond is later used to show the overall chemical characteristic of the water (Piper, 1944). It helps to determine connections between different dissolved constituents and for classifying groundwater based on its chemical characteristics (Liu et al., 2019). Meanwhile, the Gibbs diagram is often applied in groundwater hydrochemistry represented by the boomerang contour, based on the main prevailing processes such as evaporation, precipitation, and water-rock interaction (Gibbs, 1970; Barzegar et al., 2018). The impact of these processes is defined in the boomerang contour: where $Na^+/(Ca^{2+} + Na^+)$ or $Cl^-/(Cl^- + HCO_3^-)$ ratios on the x-axis are plotted against the total dissolved solids (salinity) on the y-axis. According to Ravikumar et al. (2015), the Durov diagram has advantages over the Piper diagram in unveiling geochemical processes that are affecting groundwater genesis (Lloyd and Heathcoat, 1985).

In principle, the usage of various types of diagrams is associated with plotting ionic ratios and salinity to help to understand the groundwater chemistry and identify the key hydrochemical processes in groundwater. The ionic ratios are selected based on the characteristic composition of water, source of the ions, and expected chemical behaviour. For instance, the ionic ratio of calcium to magnesium may be useful in studying the water for carbonate rocks, the ionic ratio between sodium to total cations is useful to indicate cation exchange properties, and the ratio of chloride to other ions may be useful for studying salinization or brine contamination. Many research papers have suggested a variety of chemical constituents and ratios that could be used to identify possible tracers of the source of salinity to distinguish halite solution from other potential sources such as K^+/Na^+, $(Ca^{2+} + Mg^{2+})/ (Na^+ + K^+)$, Na^+/Cl^-, Ca^{2+}/Cl^-, Mg^{2+}/Cl^-, SO_4^{2-}/Cl^-, K^+/Cl^-, $(Ca^{2+} + Mg^{2+})/SO_4^{2-}$, $SO_4^{2-}/ (Na^+ + K^+)$ and SO_4^{2-}/TDS (Kloppmann et al., 2001; Mace et al., 2006; Zarei et al., 2013; Ehya and Marbouti, 2016; Sefie et al., 2018). Furthermore, ion ratios plot of Mg^{2+}/Ca^{2+} and Mg^{2+}/Na^+ used to delineate hydrochemical processes are usually linked with Gibbs diagram to determine evaporation and water-rock interaction that occurred in the groundwater system (Gibbs, 1970; Li et al., 2019a; Liu et al., 2019). Nonetheless, these ratios succeed best when few chemical processes occur after mixing of salt-water source and freshwater. However, investigators recommended the use of fewer trace metals, for instance, bromide, iodine, boron, lithium, and strontium, against chloride to elude changes of chemical constituent ratios by mechanisms other than mixing or dilution (Vengosh, 2003; Richter and Kreitler, 1993; Lu et al., 2008; Boschetti, 2011; Zarei et al., 2013).

3.5 Multivariate Statistical Technique

The IBM SPSS Statistic version 22, which is a commercial statistical software package was used for computing inter-elemental correlation and in the principal component analysis of the database. Multivariate statistical analysis is used simply as a numerical method to determine the variable that is more important than the other data to display parameter variation or to prove hydrochemical processes (Lu et al., 2008; Kumar et al., 2009; Barzegar et al., 2018).

The most widely used statistical approaches are hierarchical cluster analysis (HCA), discriminant analysis (DA), factor analysis (FA) and principal component analysis (PCA) to identify common patterns in data distribution, and to convert to the reduction of the initial dimension of data sets and simplified interpretation (Lu et al., 2008; Okiongbo and Douglas, 2015; Isawi et al., 2016; Islam et al., 2017). However, this research study used the hierarchical cluster analysis (HCA), principal component analysis (PCA) and factor analysis (FA), which are powerful statistical methods that have been used to verify the sources of chemical constituent and the factors that have influenced the groundwater quality (Singh et al., 2017; Liu et al., 2019; Maio et al., 2019). Parameters considered in this study include in situ measurements of TDS, EC, salinity, pH, temperature, turbidity, nutrients, major ions and trace metals. HCA and FA were conducted with the established algorithm that has been used and was shown to be appropriated for the classification of hydrochemical data (Daughney et al., 2012; Montcoudiol and Lemieux, 2015). Hierarchical cluster analysis (HCA) was used to cluster the geochemical variables according to their similarities using Ward Linkage method and squared Euclidean distance (Ward, 1963). In a hydrology study, different chemical constituents in groundwater are not independent and the correlation among different parameters is useful in exploring the sources of the groundwater (Usunoff and Guzman, 1989; Cloutier et al., 2008; Singh et al., 2010). The correlation coefficient is commonly used to measure and establish the relationship between two variables. It is simply a measurement to display how well one variable predicts the other variable (Singh et al., 2012).

3.6 Saturation Index

Mineral saturation indices have been used to identify mineral dissolution and precipitation processes in groundwater (Mejri et al., 2018). In other words, it is to evaluate the degree of equilibrium between water and minerals. Changes in the saturation state are useful to distinguish the stages of hydrochemical evolution and help to identify which geochemical reactions are important in that controlling the water chemistry (Coetsiers and Walraevens, 2006; Mossad et al., 2019). Geochemical modelling is a powerful technique for characterising

the geochemical phenomena and predicts their changes (Lu et al., 2008). One of the most adopted software for aqueous geochemical calculation is PHREEQC (Parkhurst and Appelo, 1999). PHREEQC simulates the mineral precipitation and the corresponding geochemical evolution of water evaporation using the PITZER database, which allows calculation of geochemical reaction in high ionic-strength brines (Pitzer, 1973). To calculate the saturation indices, the geochemical program PHREEQC was used to evaluate the hydrochemistry data of the groundwater (Parkhurst and Appelo, 1999; Banda et al., 2019). Saturation indices are computed from the following equation 30:

$$SI = Log (IAP/ Ks) \quad (30)$$

Where IAP is the ion activity product and Ks is the solubility product constant of the minerals. The saturation indices described quantitatively the deviation of water from equilibrium with respect to dissolved minerals. When the saturation indices (SI) of a mineral is positive (+) or equal to zero, the indication is that the mineral is saturated or supersaturated with respect to the solution or dissolved mineral. In that case, the mineral has precipitated. Such index values reflect groundwater discharged from an aquifer containing the amount of mineral with sufficient residence time to reach equilibrium. Nonetheless, supersaturation can also be produced by other factors such as incongruent dissolution, common ion effect, evaporation, rapidly increased in temperature, and CO_2 exsolution (Appelo and Postma, 1996; Langmui, 1997). Meanwhile, if the SI of the minerals is negative (-), it would suggest that the particular mineral was undersaturated with respect to that particular mineral or still undergoing dissolution in the system. Such value reflected the character of water from a formation with an insufficient amount of the mineral for the solution or short residence time. The saturation indices have identified few minerals based on their geochemical data such as carbonate minerals (calcite and dolomite), sulphate minerals (gypsum and anhydrite) and halides (halite).

3.7 X-Ray Diffraction Method

X-ray diffraction (XRD) of the powder sample provides one of the easiest and significant methods of identifying the minerals present in the rock samples. The wavelengths of x-rays are in the range of 0.01 nm to 10 nm (PANalytical, 2002). A representative powdered sample of salt extracted from the saline groundwater was subjected to X-ray diffraction with scan angle (2θ) ranging from 5 to 89^0, using a Philip X'Pert X-ray diffractometer. The XRD analysis and interpretation were using manual mineral phase identification based on the peak position (*d* spacing, 2θ and relative intensities) with the help of a reference book (Lindholm, 2012). The distinctive character was based on the position of each reflection as measured by 2θ and on the intensity of each reflection. The relative intensity equalled to the intensity of a particular reflection given as a ratio of the strongest reflection. Broadly, samples were subjected to an x-ray diffractometer through a range of 2θ from 2° or 3° to 40°. The 2θ of each major reflection was measured and compared with analyses of standards. The XRD samples were from the study area commercial salt, where the saline groundwater was the primary source. XDR studies were done to estimate the mineralogical composition of the commercial salt sample.

3.8 2D Electrical Resistivity Method

The 2D resistivity method was carried out using the Wenner array on a total of five traverse lines which consisted of 42 electrodes aligned collinearly. Each profile sited, the electrode spacing was chosen 2.5 m with a spread length of 105 m, laid perpendicular to the bed strike of NE-SW direction, and elevation varied from 820 m to 880 m above sea level. A total of 5 profiling was conducted across the study area site, where one profile was conducted on the operating wells, one profile on the old existing wells, and three profiles were on the perched aquifers on the lower elevation. The 2D resistivity profiling was conducted using ABEM Terrameter SAS1000 resistivity system, where the selected types of array could be transferred to an internal switching circuit that was controlled automatically and 4 appropriate electrodes were selected for each measurement (Loke et al., 2013; AL-Zubedi, 2014; Islami et al., 2018). The 2D resistivity survey array is commonly carried out using a computerized instrument that

combines the traditional VES and profiling methods. The raw data of resistivity soundings were presented as a plot of apparent resistivity versus current electrode spacing. The sounding curve was interpreted using inversion software to determine the individual layer thickness and convert apparent resistivity to true resistivity where these sections reflected both lateral and vertical variations (Chabaane et al., 2017; Nazaruddin et al., 2017). Precaution steps should be considered to ensure good contact at current electrodes, and the area around the electrodes should be moistened, if necessary. However, there are limitations with regards to the topographic effects, which generated errors to the reading with increased or decreased values depending on the feature.

3.8.1 2D Electrical Resistivity Software

RES2DINVx64 is a computer program that automatically determines a two-dimensional (2D) resistivity model for the subsurface data obtained from electrical imaging surveys (Dahlin and Zhou, 2004; Loke et al., 2013). Figure 3.1 illustrates an example of the electrodes arrangement and measurement sequence that can be used in a 2D electrical imaging survey. The multicore-cable has many different arrangements of cables and measurement strategies (Loke et al., 2013). The survey is usually carried out with a system where the electrodes are arranged along a line with a constant spacing between adjacent electrodes. The program automatically handles data sets with non-uniform electrodes spacing. The pseudo section is useful to demonstrate the measured apparent resistivity values in a pictorial form and as an initial guide for further quantitative interpretation. Moreover, the application of the pseudo section is suitable for segregating out poor apparent resistivity measurements that commonly stand out as unusually high or low values (Loke et al., 2013).

The 2D inversion of measured data was carried out by RES2DINV software developed by Loke (2001). The RES2DINV code was developed based on the nonlinear smoothness-constrained least-square optimization technique used to calculate the resistivity of the model blocks. Subsequently, finite-difference or finite-element modelling was used to calculate the apparent resistivity value, and a non-linear smoothness that constrained least-squares

optimization technique was used to calculate the resistivity of the model blocks (Loke et al., 2013). Many types of arrays such as Wenner, dipole-dipole, pole-dipole, Wenner-Schlumberger, and multi-gradient were considered suitable for the program. The Wenner array is a captivating selection for surveying in a noisy area and is also relatively sensitive to vertical changed below the centre of the array, however, it is less sensitive to horizontal changes in the subsurface resistivity (Abdulrahman et al., 2016; Kumar et al., 2016). The least-square optimization algorithm of the RES2DINV program attempted to minimize the mean-square errors between the model responded and the observed data which then produced a model with a smooth variation in the resistivity values as a function of depth (Loke et al., 2013). Since the resolution of the resistivity method decreased exponentially with depth, the inversion optimized the fit between the data and the model from the controlled damping parameter.

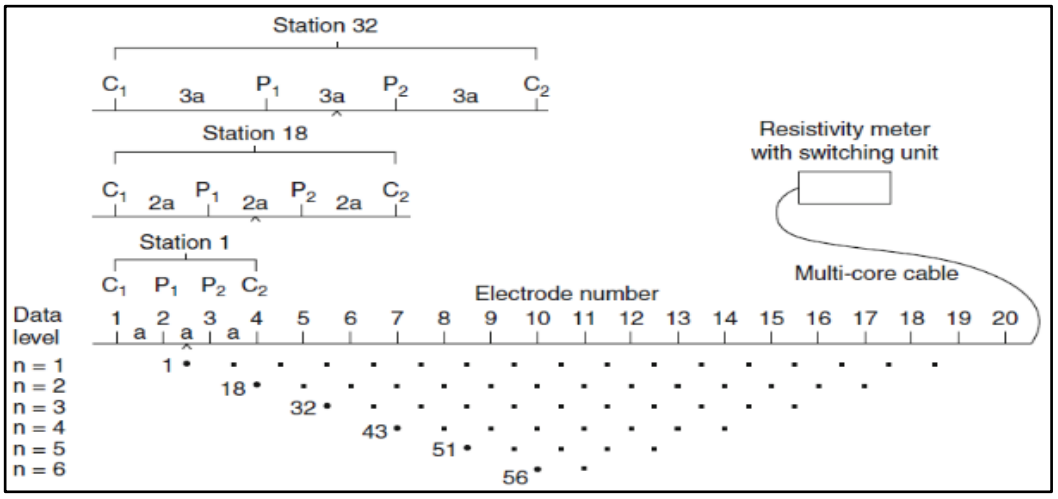

Figure 3. 1 Systematic diagram of the multi-electrode system and possible sequence of measurement to create a 2D pseudo section. Adapted from Loke et al., 2013).

3.8.2 2D Electrical Resistivity Data Acquisition

Figure 3.2 displays the list of 2D resistivity multi-electrode ABEM LUND Imaging System conducted to obtain resistivity data which consisted of an ABEM TERRAMETER SAS 1000, ELECTRODE SELECTOR, 200m cable rolls, 42 steel rods, external batteries, and connectors.

The selector allowed the automatic selection of the four active electrodes for each measurement using conventional configuration. The acquisition of the study area had 105 m spreading on each survey profiles. The resistivity survey used the Wenner array with 2.5 m electrode spacing and 42 electrodes on a straight line (Figure 3.3). An internal switching circuity controlled by a programmable microcomputer within the resistivity meter automatically selected the appropriate 4 electrodes for each measurement. In every different spacing measured at a different location along the cable. Subsequently, the data was entered manually to the RES2DINV software in preparation for processing and interpretation.

Table 3. 1 Survey parameter for each 2D resistivity survey line (profile 1 - 5)

Location	Profile 1	Profile 2	Profile 3	Profile 4	Profile 5
Electrode spacing	2.5 m	2.5 m	2.5 m	2.5 m	2.5 m
Survey length	105 m	105 m	105 m	105 m	105 m
RMS Error (%)	9.1	7.9	10.8	9.7	10.1

Figure 3. 2 List of geophysics equipment for 2D electrical resistivity ABEM LUND SAS 1000.

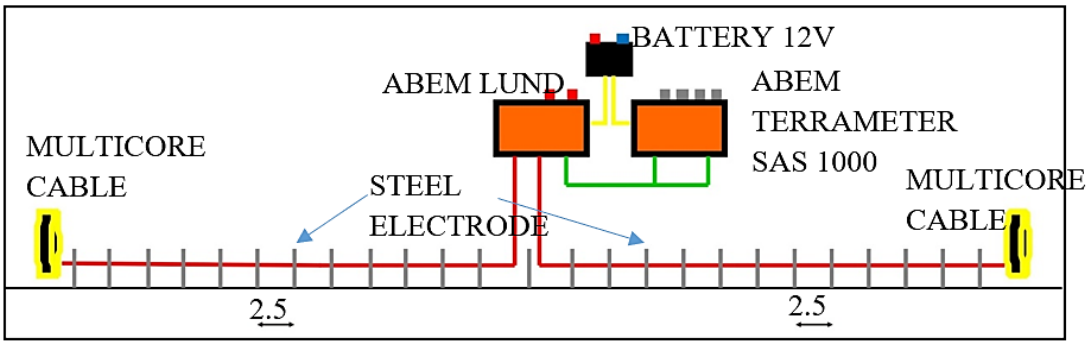

Figure 3. 3 The schematic image alignment for 2D resistivity profiling with 2.5 m electrode spacing and 105 m spreading length.

3.8.3 2D Electrical Resistivity Data Processing

The raw resistivity data was processed using the RES2DINV Geotomo software. The resistivity values measured were considered as apparent values since they represented a subsequent value of the resistivity and chargeability of a subsurface volume. To obtain a true section, an inversion procedure must be applied. The RES2DINV inversion program employed a fast technique for data inversion developed by Loke et al. (2013). It considered 2D subsurface models composed of rectangular block cells with each block with constant resistivity and chargeability. Starting from a simple initial model, an optimization method was used to iteratively change the resistivity of the model cells to minimized the difference between the measured and calculated apparent resistivity values. Then, a calculation was done based on finite element or finite difference methods. The finite-difference procedure was selected rather than the finite element for the forward modelling calculation. As a general rule, before carrying out the inversion of a data set, it is necessary to examine at the data as a pseudo section for poor data points. The poor data points with "systematic" noise showed up as spots with unusually low or high values by selecting exterminated poor datum points manually and continued with the trial inversion to identify any poor data and errors. After carrying out the trial inversion results, the "RMS error" statistics option that appeared displayed the distribution of the percentage difference between the logarithms of the measured and calculated with apparent resistivity values. The error distribution was displayed in the form of

a bar chart, where the highest bar was the one with the smallest error and the height of the bar should decrease gradually with increasing error values. The poor data points caused by problems such as poor ground contact at a small number of electrodes could influence neighbouring good data points. The acceptable percentage of "RMS error" should be < 10%.

The program offered two types of optimization procedures: a common least-square (L_2-norm) inversion and a robust (L_1-norm) inversion option in which the absolute values of data misfit were minimized (Loke, 2003; Dahlin et al., 2010). With regards to model constraint, it is necessary to stabilize the inversion processed, as the absolute variations of the resistivity/chargeability values can be minimized. The robust model constraint (L_1-norm) was used for blocky targets, while the standard model constraint (L_2-norm) was used for smooth changes in the subsurface properties (Loke et al., 2003). This investigation employed the L_1-norm, which allowed considerable variation in the inverted models and can address the high electrical resistivity contrast. As the significant resistivity contrast at the saline groundwater, the finest mesh with 4 nodes was chosen in the forward modelling. Values of 0.05 and 0.005 were selected for the robust data constraint cut off factor and the robust model constraint factor, respectively. The initial damping factor for the processing started at 0.15 with a minimum damping factor of 0.02.

3.9 Seismic Refraction Method

With regards to seismic refraction, the seismic energy transmitted from the source point through a stack of subsurface layers was partially refracted back to the earth's surface as head wave or first arrival. The elastic energy waves were generated by different energy sources from explosives, weight drop, or a sledgehammer. In this case, sledgehammer was used as the source where it was a stuck against a metal plate laid on the ground. However, the maximum depth expected to be explored is approximately 15 – 20 m. Spreading length, source-to-spread array and geophones spacing were to be appointed depending on the targeted depth, seismic velocity, wave type, and source as intended (Alhassan et al. 2018). Geophones used to record seismic waves typically use 40 Hz frequencies. The seismic refraction survey employed the

24-channel ABEM TERRALOC PRO 2 seismograph with a minimum of 7 shot points for each survey line with 5 m spacing between geophones and spans 120 m. To lower the effect of noise from wind and airwaves, the geophones that have short spikes were buried into the ground and positioned along straight profile lines for a 2D survey and connected to a seismograph (Alhassan et al., 2018; Araffa et al., 2017). The seismograph recorded the entire signal from individual geophones and was displayed as a seismic section to image the subsurface structures. An initial model was generated based on a travel time-distance graph to determine the velocity of each layer. Subsequently, the generalized reciprocal method was used for the data processing which was based on an iterative analysis of ray from forward and reverse seismic shots that display the refractor at the same point. It should be noted that the refraction method cannot identify subsurface layers where velocity decreased because these layers were not refracting back to the surface as the first arrival and head waves were considered as reading error or "blind spots" (Kearey et al., 2013).

3.9.1 Seismic Refraction Data Acquisition

The geophysical instrument seismic refraction was conducted to map the subsurface structures in the study area. Figure 3.4 shows the list of seismic refraction instruments that were acquired for each profile using ABEM TERRALOC PRO 2 seismograph, 24 geophones (40 Hz), trigger cable, steel plate, 200 m connector cables, external batteries and sledgehammer as the source. The seismic refraction survey was conducted with 5 m geophone spacing and 24 geophones on a straight line. There are 7 shot points located at minus (-) offset, 1st and 2nd geophones, 6th and 7th geophones, 12th and 13th geophones, 18th and 19th geophones, 23rd and 24th geophones and plus (+) offset (Figure 3.5). The survey lines stretched over between flat ground and sloping hillside of valley region, composed of alluvium loose soil and sand. Lines were shot in forward and reverse order, with a total length of 120 m interval on each survey profiles with a total of 5 profiles. To increase the signal-to-noise ratio, 3 shots were stacked using an 8 kg sledgehammer striking steel plate along with each profile. The parameter setup summary for each survey line is as shown in Table 3.2. Subsequently, the raw

data recorded by the seismograph was transferred for further processing using SeisImager software.

Table 3. 2 Survey parameter for each seismic survey line (profile 1 - 5)

Location	**Profile 1**	**Profile 2**	**Profile 3**	**Profile 4**	**Profile 5**
Geophone interval	5 m	5 m	5 m	5 m	5 m
Survey length (including offset shot, 5 m at both ends)	120 m	120 m	120 m	120 m	120 m
RMS Error (%)	0.4	1.2	0.8	1.0	1.3
Receiver	40 Hz geophone (24 channels)				
Sample interval	100 - 200 microsecond				
Number of samples	16,384				
Number of stacks	3 shots				
Record length	409.6 - 819.2 (millisecond)				

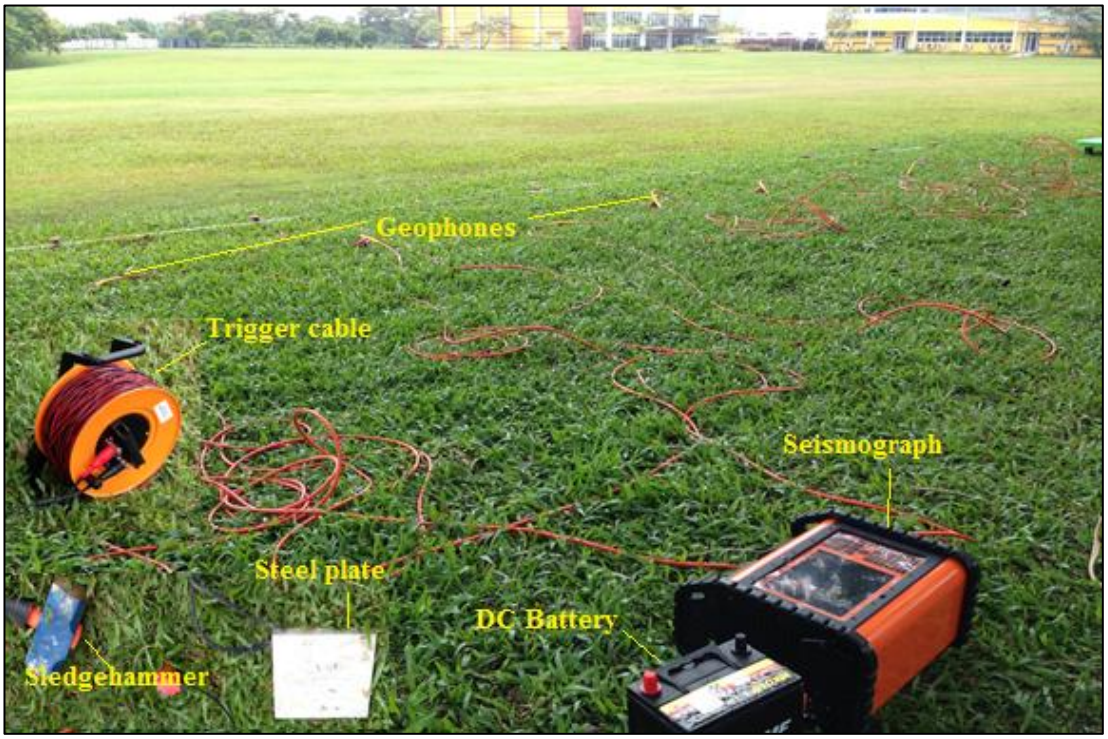

Figure 3. 4 List of geophysical equipment for seismic refraction, TERRALOC PRO 2.

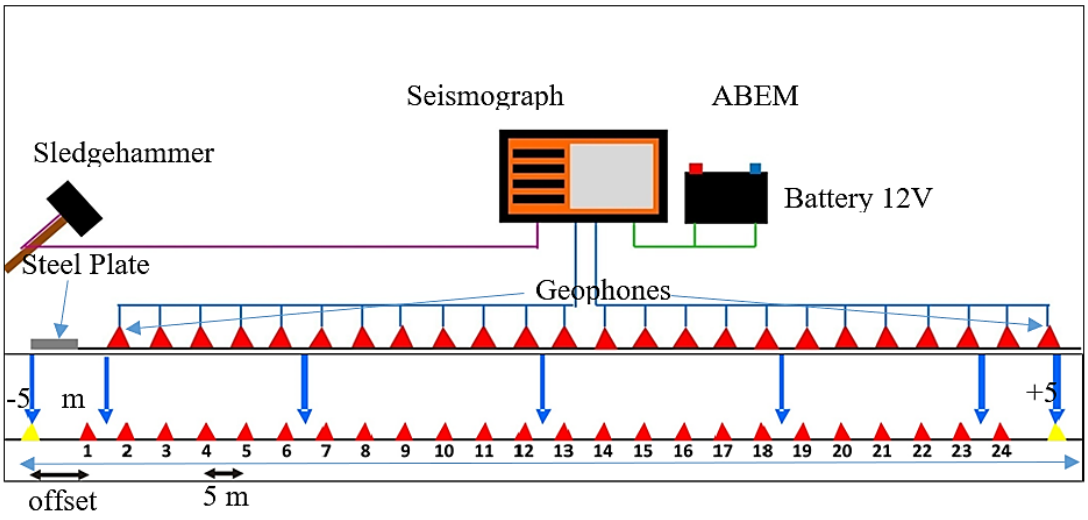

Figure 3. 5 The schematic image acquired for seismic refraction survey with 24 geophones and spacing of 5m stretched aligned over 120 m length.

3.9.2 Seismic Refraction Software

The initial step in processing first used PickWin software to pick the first arrival breaks for all the seismic survey lines. A plot called time-distance graph, showed the arrival times against distance between the shot and geophone positions. The Plotrefa software was used to carry out the time inversion to generate the seismic tomography section of the surveyed area. This inversion employed conjunction of the linear square and delay time analysis to invert the first arrival for a velocity section (Adelinet et al., 2018). The main focus in the seismic refraction method is the P-wave energy, which is a compressional body wave that has the highest rate of propagation of any seismic wave (Alhassan et al., 2018). The seismic refraction data was then transferred and processed using SeisImager software which utilized a ray-tracing algorithm for P-wave and the output was a seismic refraction tomography section that displayed the seismic velocity model of the subsurface such as lateral and vertical velocity and layer thickness.

In seismic refraction processing, the data was often based on the first arrival and the assumption lied on the value of the V1 (velocity of 1st layer) of the section above the refractor which were lower. However, heterogeneous composition near the surface deposits caused the overburden velocity to be rarely constant. Subsequently, the slope from time distance graph was used and calculated to obtain the average velocity of both 1st layer (V1) and refractor (V2) from the related equation for all shot points (7 shots). Lastly, by combining the general geology of the study area and standard approximate range of velocities of longitudinal seismic wave good insight into the subsurface geological structures was achieved. Subsequently, the first- and second-layer velocities were obtained from the graph. The depth of refractor (Z) was calculated using equation 31:

$$Z = \frac{Ti}{2}\frac{V_1V_2}{\sqrt{(V_2^2 - V_1^2)}} \tag{31}$$

Where Z is the depth of the refractor, V_1 is the velocity of the overburden layer, V_2 is the velocity of the refractor layer and T_i is the intercept time (Alhassan et al., 2018).

3.9.3 Seismic Refraction Data Processing

The raw data collected from the seismograph was transferred and seismic refraction models were created using two programs within SeisImager software. Pickwin was used to pick the first arrivals and dispersion curves, while Plotrefa was used for refraction velocity analyses. Pickwin used raw file .dat or .seg2 and plotted them to pick the first arrivals. A bandpass filter was applied to the data to remove excessive noise (airwave), using a 50-Hz high cut filter and a 15-Hz low cut filter to each field file (Geometrics Inc, 2009). The first step in seismic refraction processing was to identify and manually pick the first break seismic arrivals. A first break is the first arrival of the direct or refracted seismic signal within the seismic trace (Saribudak and Hauwert, 2017). To create an accurate velocity model, a precise picking of the first arrival is vital. The first arrivals could be identified by the first noticeably different spikes in the signal. After the first arrival is picked, the file containing the pick files was loaded into the Plotrefa software and converted to travel-time curves. A topography file can be imported for each survey profile. Furthermore, using the generalized reciprocal method, a 2D velocity model can be generated. The general reciprocal method (GRM) is a useful technique for solving lateral variation in the refractor velocity and effective determining bedrock depth (Palmer, 1980). It starts with an initial velocity model using a time-term inversion algorithm. The reciprocal method allows a two- or three-layer interpretation and once all of the layers have been assigned, the data is ready for inversion to the velocity section. With the creation of an initial velocity model, the reciprocal method involves tracing rays through the model with the primary purpose of reducing RMS error between the observed and calculated travel-time. The process is repeated and the model is modified until the difference between calculated and measured times is minimized (Azhar et al., 2019). The inversion error will be displayed based on the least-square inversion with root-mean-square (RMS) error between the observed and actual travel time versus distance which will be calculated then. The RMS error should not exceed 1.5 %, if it is larger, examining the first arrival or layer assignment is recommended (Geometric Inc, 2009).

Analysis of seismic refraction data depends upon the complexity of the subsurface velocity structure, where the types of method in interpretation techniques are time-term inversion method (ITM), generalized reciprocal method (GRM) and refraction tomography (RT) (Palmer, 1980; Geometric Inc, 2009). The time-term inversion technique employs a combination of linear least squares and delays time analysis to invert the first arrivals into the velocity model section (Azhar et al., 2019). The generalized reciprocal method simplifies the velocity structure with near-surface attributes such as heterogeneity, lateral discontinuities, and gradient (Palmer, 1980). Furthermore, the refraction tomography (RT) is proven to resolve velocity gradients and lateral velocity changes and is therefore perfect to be applied in complex subsurface velocity settings such as compaction, karst, and fault zone (Zhang and Toksov, 1998; Azhar et al., 2019).

CHAPTER 4. Preliminary Survey

4.1 Results

4.1.1 Geological Survey

The outcome of conducting a preliminary geological survey during December 2018 to map the study area yielded important information on the regional geology. The excursion resulted in a total of 36 exposed outcrops that were discovered across the Ba'kelalan region in approximately 9 villages from the lower stream to the upstream of Pa Tawing, Long Aru, Buduk Bui, Long Rusu, Long Ritan, Long Langai, Pa'Komap, Buduk Nur and Punang Kelalan, respectively (Figure 4.1). The distance achieved across the study area region was estimated to be 12.3 km from Pa Tawing village on the downstream to the upstream of Punang Kelalan village. The preliminary investigation yielded 5 operated salt wells discovery around the Ba'kelalan region, in which three were located in Buduk Bui on the lower stream with an elevation of 913 m a.s.l and 5 m distance to each well. Whereas on the upstream, one well was located in Pa'komap with an elevation of 967 m a.s.l and another well was located in Punang Kelalan with an elevation of 948 m a.s.l. All the 5 wells exhibited a shallow water table with a depth ranged from 2 m to 3 m and at a distance of 8 km to 10 km from the lower stream to the upstream. The existing wells were established and exploited since unrecorded time and are still actively producing commercial highland salt until today. The Kelalan river displayed on the map flows pass through the study area from SE to NW direction in Figure 4.1. During the preliminary survey, the GPS coordinates for discovered outcrops, elevation and orientation of beds from the formation of the surrounding area are illustrated in Table 4.1. Table 4.2 shows the coordinates of the villages, the elevation, existing wells, and installed rainfall gauges in the study area. The rainfall gauges were installed in three respective places: Long Aru on the lower stream, Buduk Bui on the mid-stream, and Pa Ko'map on the upstream.

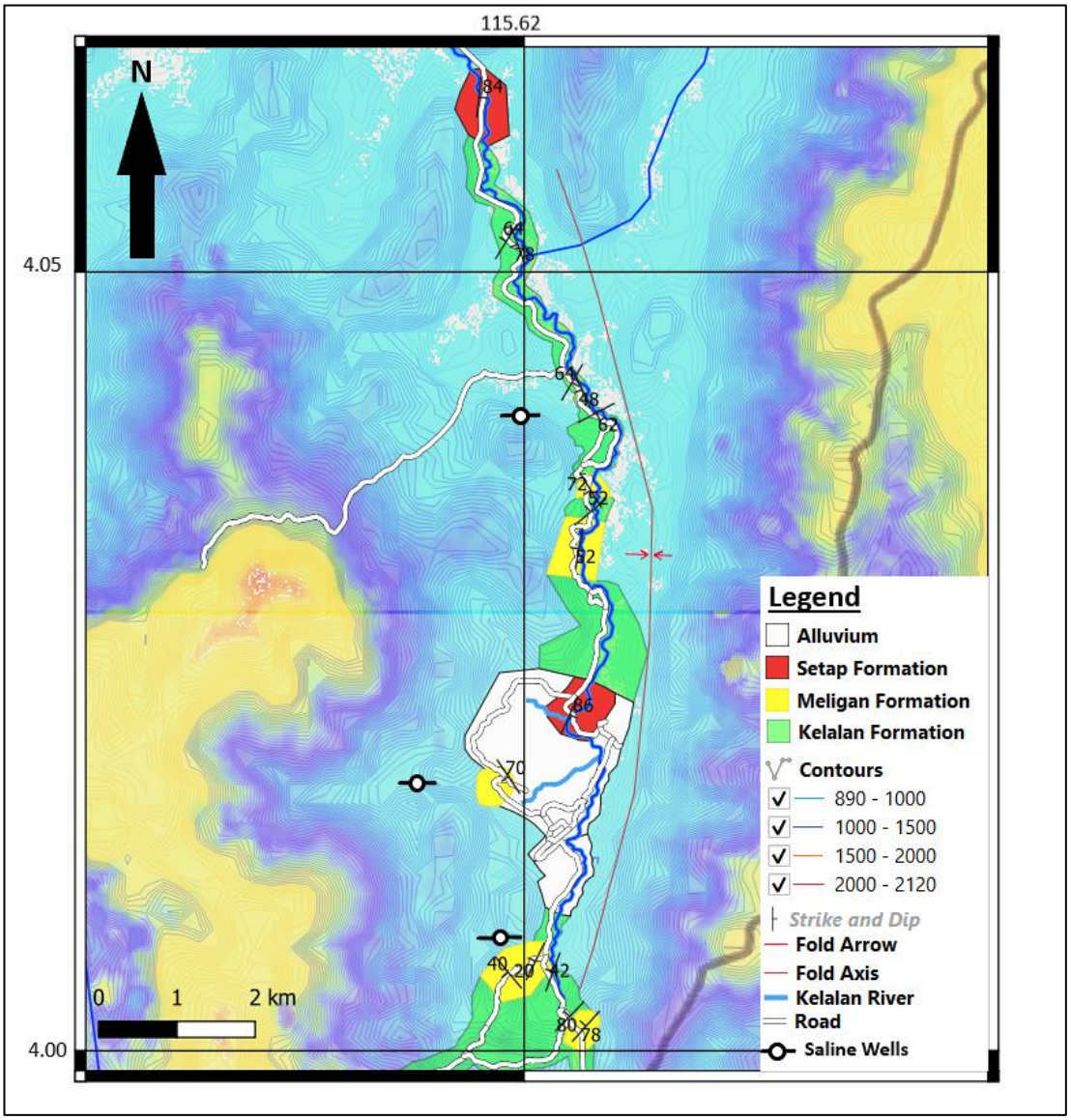

Figure 4. 1 The geology map of the study area, displayed the orientation of formation elevation in meters.

Table 4. 1 Outcrops details during preliminary field survey

Outcrop name	UTM Northing	UTM Easting	Elevation (m)	Orientation	Formation	Geology
Outcrop 1 Buduk Bui	4.02348	115.62041	908	076/50 SE	Kelalan Formation	Gently folded sandstone interbedded with mudstone and siltstone
Outcrop 2 Buduk Bui	4.02506	115.61957	906	014/58 NW	Kelalan Formation	Unconsolidated sandstone interbedded mudstone and siltstone
Outcrop 3 Buduk Bui	4.02544	115.61951	909	002/40 NW	Kelalan Formation	Sandstone 80 %; Mudstone 20 %
Outcrop 4 Buduk Bui	4.02622	115.61912	910	030/64 SE	Meligan Formation	Unconsolidated massive sandstone 90 % - mudstone 10 %
Outcrop 5 Buduk Bui	4.02254	115.62173	916	358/ 78 NW	Meligan Formation	Massive sandstone 70% interbedded 30% mudstone
Outcrop 6 Buduk Bui	4.02221	115.62215	923	062/62 SE	Kelalan Formation	Sandstone 70% interbedded 30% shale

Outcrop 7 Long Rusu	4.00510	115.61875	930	072/ 48 NW	Meligan Formation	Massive sandstone with minor mudstone beds 90%-10%
Long Rusu Boulders sites	4.00553	115.62270	902		Kelalan Formation	Consolidated sandstone and siltstone like meta-sedimentary boulders
Outcrop 8 Lg Rusu - 168 m	4.00555	115.61886	935	008/56 W & 028/72 W	Meligan Formation	Interbedded sandstone 70%; mudstone 30%
Outcrop 9 Lg Rusu - sandstone quarry	4.00679	115.61927	936	118/48 SW	Meligan Formation	Massive sandstone highly fractured and jointed
Outcrop 10 sandstone quarry	4.00734	115.61913	937	010/52 W & 020/70 W	Meligan and Kelalan Formation	Massive sandstone on top with minor hard meta-sandstone on bottom with grey, red and black clay
Outcrop 11	4.01022	115.62070	943	042/78 SE	Meligan Formation	Unconsolidated sandstone highly disturbed tilted beddings

Outcrop 12	4.01185	115.62060	945	050/52 NW	Meligan Formation	Sandstone beds dominantly shale, ratio 70%-30%
Outcrop 13	4.01212	115.62061	947	023/72 NW & 028/68 NW	Meligan and Kelalan Formation	Massive outcrop on top with sandstone interbedded shale 60%-40% and highly folded low meta-sandstone bed on bottom
Outcrop 14	4.01310	115.62026	946	150/48 W	Kelalan Formation	Highly disturbed outcrop with jointed features and covered with boulders meta-sedimentary like - sandstone 80% shale 20%
Outcrop 15	4.01379	115.62054	947	148/72 W	Kelalan Formation	Sandstone interbedded mudstone 50%-50%, laminated and cross-bedded with mud clast
Outcrop 16	4.01449	115.62061	944	110/62 SW & 142/68 SW	Kelalan Formation	Long stretch outcrop - Massive sandstone interbedded mudstone 70-30, laminated and cross-bedded

Outcrop 17	3.95824	115.61108	1092	140/40 W	Meligan Formation	Highly weathered heterogeneous sandstone with shale 80%-20%
Outcrop 18	3.95851	115.61305	1069	166/82 NE	Meligan Formation	Highly weathered, disturbed and jointed features for massive sandstone
Outcrop 19	3.95898	115.61362	1059	020/18 W	Kelalan Formation	Highly weathered, disturbed sandstone beds
Outcrop 20	3.95997	115.61414	1035	026/20 W	Kelalan Formation	Highly weathered, disturbed sandstone beds with minor shale
Outcrop 21	3.96021	115.61509	1013	030/60 W	Meligan Formation	Highly weathered and disturbed sandstone bed with minor shale
Outcrop 22 Long Langai River Tributary	3.98800	115.61887	906	024/86 SE & 022/82 SE	Setap Shale Formation	Thick monotonous tilted shale up to 50 m covering the whole river bottom - river flows towards NE
Outcrop 23	3.95871	115.61614	966	020/42 NW	Kelalan Formation	Unconsolidated highly weathered sandstone on

						top with interbedded shale and sandstone at the bottom with coal lamination.
Outcrop 24 - 50 m height	3.95260	115.62003	975	042/78 NW	Kelalan Formation	Massive outcrop composed of recent topsoil with the bottom showing tilted and folded sandstone interbedded with siltstone and pyrite mineral present.
Outcrop 25	3.95166	115.61954	973	016/76 NW	Kelalan Formation	Outcrop covered by topsoil, at the bottom-tilted beds of sandstone interbedded shale
Outcrop 26	3.95374	115.61817	980	024/80 NW	Kelalan Formation	Highly weathered sandstone with minor shale and siltstone
Outcrop 27	3.95418	115.61788	977	042/74 NW	Kelalan Formation	Highly weathered sandstone 60% with minor shale and siltstone 40%

Outcrop 28	3.98058	115.60998	961	176/76 W & 172/74 W	Kelalan Formation	Weathered reddish sandstone interbedded shale 70%-30%
Outcrop 29	3.98081	115.61107	983	146/70 W	Kelalan Formation	Highly disturbed sandstone and weathered with interbedded shale; observed crossbedding sedimentary structure on the drainage system
Outcrop 30	3.98179	115.61033	1003	140/40 SW	Kelalan Formation	Sandstone 50 % interbedded shale 50%
Outcrop 31	3.98189	115.61024	1006	060/50 NW	Kelalan Formation	Sandstone 60% interbedded shale 40%
Outcrop 32	3.98231	115.60952	1011	160/54 SW	Kelalan Formation	Sandstone 70% interbedded shale 30%
Outcrop 33 Downstream	4.04290	115.61082	922	032/64 NW	Kelalan Formation	Weathered sandstone interbedded grey mudstones with coal lamination

Outcrop 34	4.04255	115.61110	928	038/52 NW	Kelalan Formation	Highly weathered sandstone interbedded with mudstones
Outcrop 35	4.04216	115.61209	924	160/78 NW	Kelalan Formation	Sandstone interbedded with shale 60%-40 %
Outcrop 36 Kelalan River Downstream	4.05924	115.60845	890	006/84 SE	Setap Shale Formation	Massive weathered sandstone beds with monotonous thick shale bed on bottom
Outcrop 36	4.02214	115.61997	931	126/49 SW	Meligan Formation	Highly fractured and jointed sandstone with minor shale in Buduk Bui salt spring

Table 4. 2 Details of existing wells and installed rainfall gauges station in the study area

UTM Northing	UTM Easting	Elevation above sea level (m)	Location remarks
4.03855	115.61291	897	Long Aru village - Rainfall gauges installed for downstream
4.01932	115.62335	909	Buduk Bui village – Rainfall gauges installed for mid-stream
4.02074	115.61885	913	Bang Main Well 1
4.02082	115.61890	913	Bang Main Well 2
4.02084	115.61886	914	Bang Main Well 3
3.97864	115.60497	967	Pa Ko'map village and salt spring well 4 - Rainfall gauges installed for upstream
3.96345	115.61453	948	Punang Kelalan village and salt spring well 5

The lithological information described and gathered from the survey was mapped and generated via QGIS mapping software. There are three main formations exposed in the study area: (1) the recent Quaternary alluvium terrace found near the airport and Buduk Nur village (873 m above sea level), composed of sand, clay, clayey sand and gravels. The Setap Shale Formation (2) was observed at the river bottom near Long Langai village on the upstream and Pa Tawing on the lower stream. It consisted of a massive monotonous succession of shale approximately 50 m thick with tiny alternating sandstone beds. The Setap Shale Formation strikes towards NE-SW direction and steeply tilted beds with dip values were found from 80° to 85° towards SE direction. The Meligan Formation (3) underlying the Setap Shale Formation which was well-exposed in few places across the study area with characteristics of predominantly sandstone with minor shale beds were highly weathered, jointed, and fractured. The Meligan Formation is oriented in the NE-SW direction; dipping either NW or SE direction, it formed a syncline fold structure in the valley. The Meligan Formation was assumed as a relatively potential aquifer reservoir for the saline groundwater in Ba'kelalan due to the high porosity and permeability features that existed in the sandstone. The sandstone was yellow to grey colour, coarse-grained, well-sorted, and classified as quartzose sandstone. Additionally, the abundance of available massive sandstone in the study area was used for sand quarry by the locals to repair roads and cement mixtures. The oldest formation observed in the study area was the Kelalan Formation (4), which comprised of steeply tilted and folded turbiditic heterogenous shale, siltstone, and low-metamorphosed sandstone beds with pyrite mineral present (Nagarajan et al., 2020). The meta-sandstone was grey to yellow colour, fine-grained, well-sorted with thinly bedded with sedimentary lamination of coal seams, meanwhile, the siltstone was dark grey, very fine-grained and with pyrite mineral present (Figure 4.3c). The Kelalan Formation strikes the NE-SW trend with steep dipping beds of 70^0 to 86^0 towards NW. The intense tectonic activities that formed the mountainous ranges had uplifted, folded, tilted, and overturned the formations, hence, the oldest formation was well-exposed at the top in the study area (Haile, 1962).

In Figure 4.2a the tilted Setap Shale Formation beds observed parallel striking to the Kelalan River tributary flow near to Long Langai village covering the whole river bottom and stretched approximately 20 to 40 m in length. The Kelalan river flowing from SE to NW direction, while the Setap Shale Formation strike trending to NE-SW.

The Meligan Formation (outcrop 7) was exposed throughout the study area with distinctive features of highly weathered and fractured massive sandstone beds (< 3 m thick) with minor thin shale beds. Figure 4.2b shows that the sandstone beds are highly jointed and fractured with mildly steeping beds. Outcrop 10 displayed the disturbed and the excavated massive sandstone bed that was highly fractured and outcrop 36 which was located in Buduk Bui salt spring with sandstone beds jointed, fractured, and covered by the topsoil (Figure 4.2c). The Meligan sandstone was believed to be a good reservoir aquifer for the saline groundwater with a highly fractured feature (Haile, 1962).

The Kelalan Formation is well exposed in Ba'kelalan region and was characterized by tilted folded turbiditic sandstones alternating with shale and siltstone and traces of pyrite. In outcrop 15, the Kelalan Formation was composed of steeply tilted thin beds of sandstone interbedded with a thin bed of shale (Figure 4.2d). Outcrop 13 belong to the Kelalan Formation displayed sandstone beds which are symmetrical anticlinal folds where the oldest rocks are located in the centre of the folds, and the strata are progressively younging outwards (Bhattacharya, 2005). In contrast, the syncline folding on Ba'kelalan valley indicates that the core/centre of the syncline fold consists of the youngest strata and the strata were progressively older outwards (Figure 4.3a). Meanwhile, in Figure 4.3b, the sandstone bed with a recumbent fold that has a horizontal axial plane (Bhattacharya, 2005).

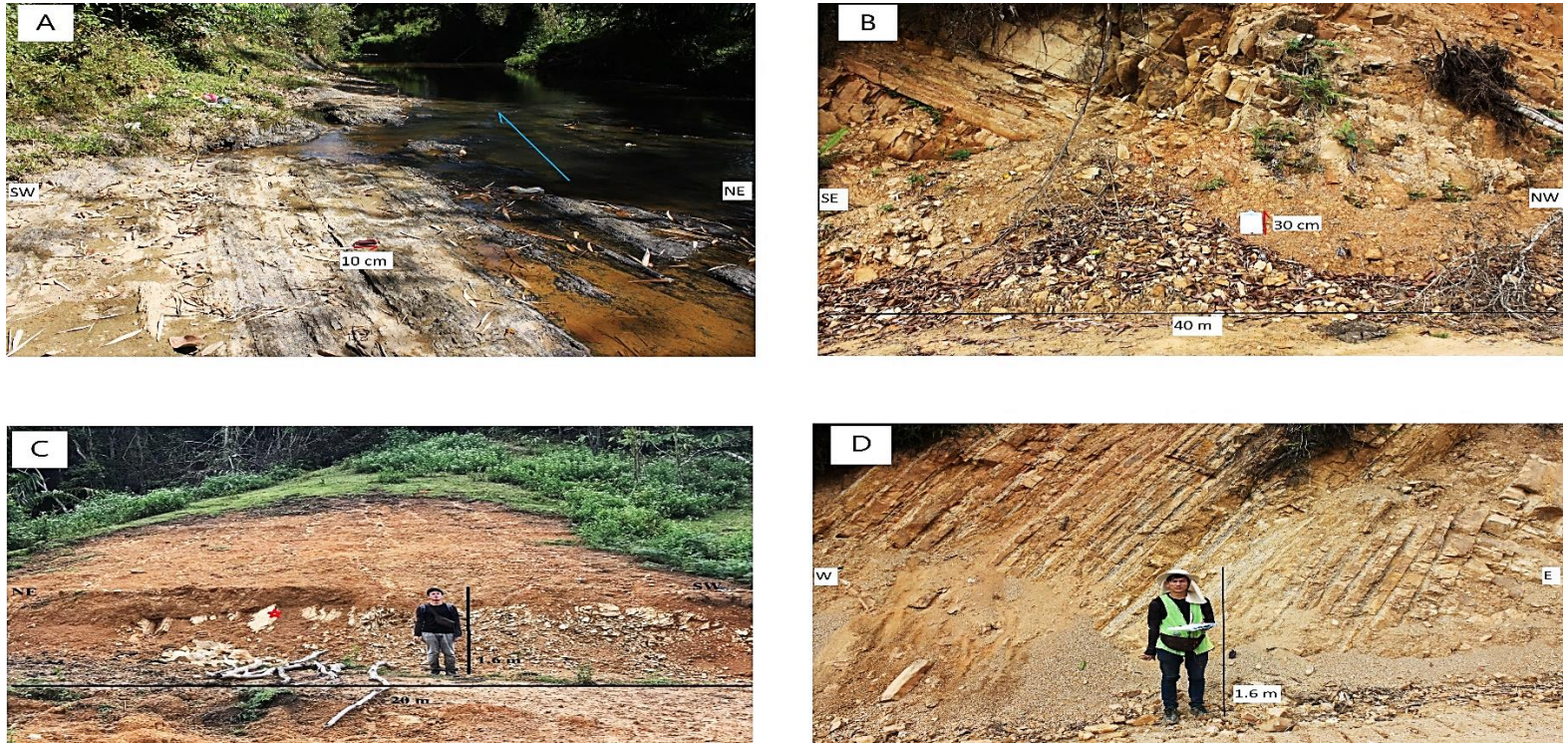

Figure 4. 2 (A) Outcrop 22, the Setap Shale Formation composed of monotonous thick shale beds that are steeply dipping sub-vertical and striking parallel to the river flow. (B) Outcrop 7, the Meligan formation composed of highly weathered and fractured sandstone approximately 20 m height and stretched to 40 m wide. (C) Outcrop 36, the Meligan Formation consisted of 1 – 2 m thick of predominantly sandstone beds (red star) covered by topsoil in Buduk Bui salt spring. (D) Outcrop 15, observed the cyclic sedimentation of weathered and tilted Kelalan Formation composed of heterogenous alternating sandstone and shale beds.

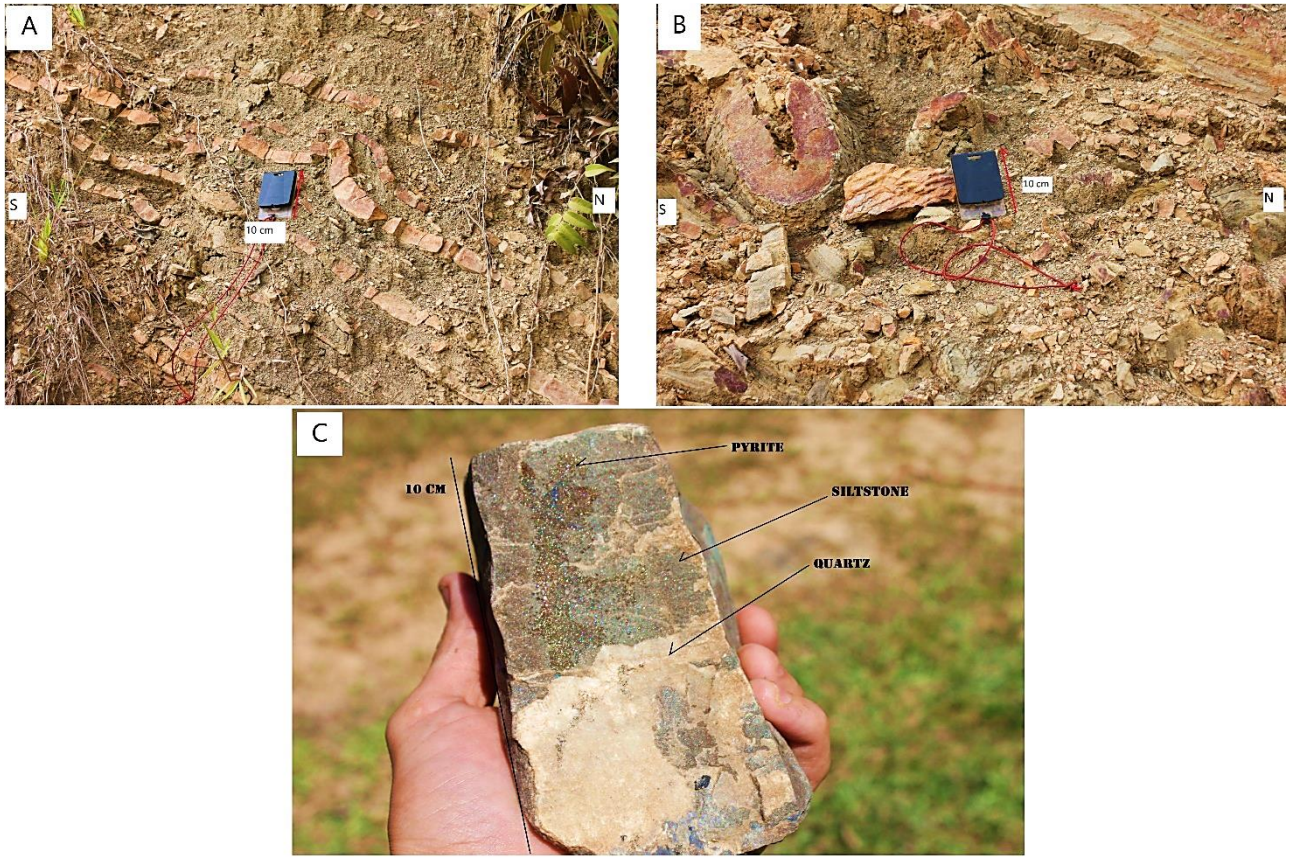

Figure 4. 3 (A) Outcrop 13, the Kelalan Formation sandstone beds were found steeply tilted and folded. (B) The sandstone bed was found to be intensively folded and could be described as recumbent fold. (C) Hand rock sample of grey siltstone with pyrite and quartz mineral found from outcrop 24.

4.1.2 X-Ray Diffraction

Figure 4.4 shows the X-ray diffractogram of the commercial salt sample that indicates several peaks spread over the range 2Θ from 20^0 to 45^0, with the highest score/ count for the peak of $2\Theta = 45.359^0$. The XRD revealed the presence of NaCl halite in the sample along with minor composition of aragonite and orthoclase minerals (Table 4.3), where halite mineral has the highest peak and is the dominant mineral present in the sample (Figure 4.5).

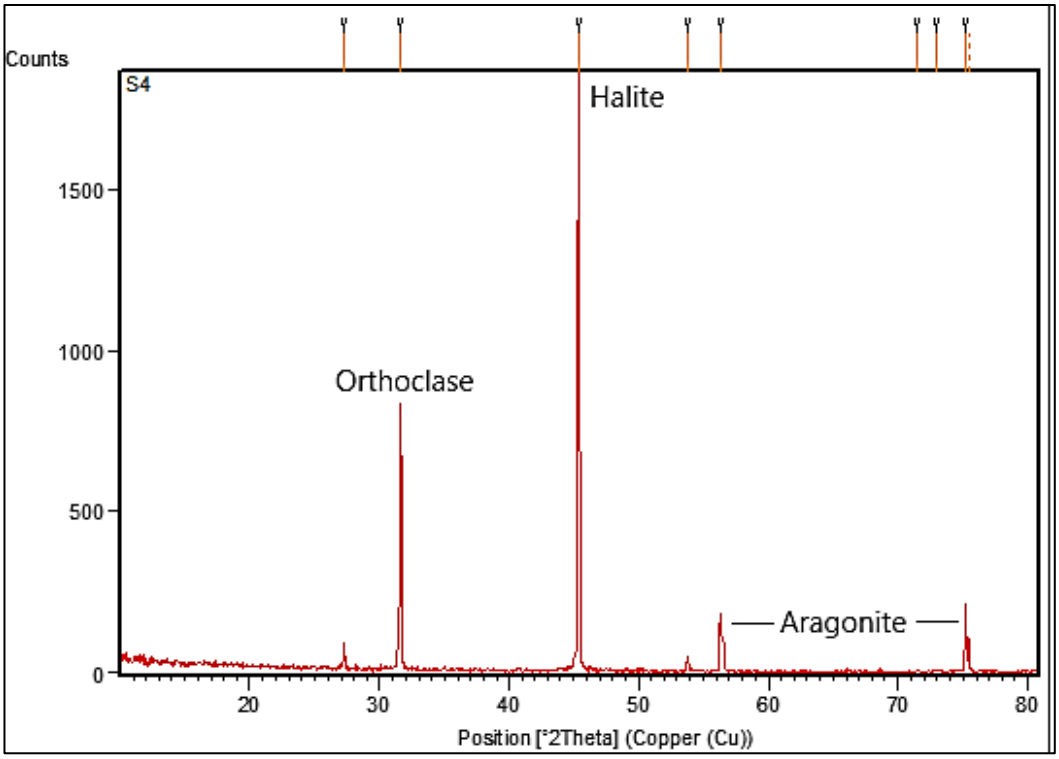

Figure 4. 4 The X-ray diffractogram of the commercial salt of the study area.

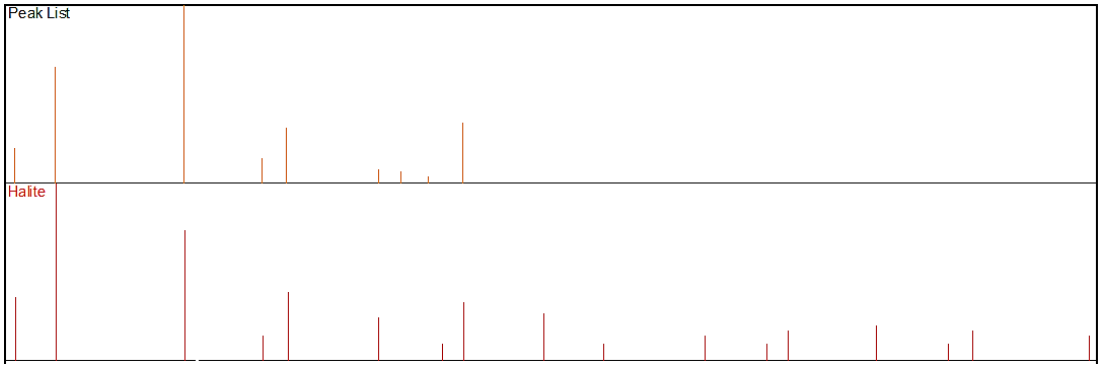

Figure 4. 5 The highest peak match with halite mineral of the commercial salt sample.

Table 4. 3 Major minerals identified in the XRD data

Pos. [°2Th.]	Height [cts]	FWHM Left [°2Th.]	d-spacing [Å]	Rel. Int. [%]	Sources
27.2422	77.05	0.1476	3.27362	4.00	Aragonite
31.6187	785.82	0.1476	2.82977	40.84	Orthoclase
45.3597	1924.10	0.1968	1.99941	100.00	Halite

4.1.3 Saline Groundwater Physico-chemical Analysis

4.1.3.1 < 24 Hours Measurement

The purpose of the hourly measurement was to observe the short-term variation in each parameter and study the characteristic of the saline groundwater at an hourly rate from 8 am to 5 pm during MON season (11th December 2018). Well 1, 2 and 3 were located adjacent to each other in the study area Buduk Bui and it was found that well 1 has the highest value for most of the physical parameter (TDS, EC and salinity) compared with the rest of the wells (Table 4.4).

The pH is an important factor and provides vital information in geochemical equilibrium, the solubility of trace metals and organic compound content (Bourg and Loch, 1995; Gao et al., 1998). From the < 24 hours observation, the pH value average for well 1, 2, and 3 were measured at 6.6, 7.04, and 7.55 respectively. This indicates that the saline groundwater wells

were slightly acidic to alkaline in nature. From the graph (Figure 4.6a), it was found that the pH value in well 1 was constant (6.6) from 8 am to 1 pm and increased to 7 at 2 pm. The pH value for well 2 was observed to have slightly decreased at 9 am from 6.9 to 6.5 and significantly increased from 2 pm to 5 pm with the highest peak reading of 7.6. Well 3 was found to be constant from 8 am to 5 pm with the highest pH value 7.6 among the other wells.

In Figure 4.6b, the TDS average values for well 1, 2, and 3 were ranged from 33,380, 30,550, and 27,440 mg/L, respectively. Freeze and Cherry (1979) stated that the water classification was based on the total dissolved solids in Table 4.6, where well 1, 2, and 3 were classified as saline water ranging from 10,000 to 100,000 mg/L. Meanwhile, the average value of EC for well 1, 2, and 3 were 52,370, 48,720, and 44,115 µS/cm accordingly. Based on the water classification in Table 4.7, well 1 and 2 are classified as brine water (> 45,000 µS/cm) whereas well 3 is classified as highly saline (10,000 – 25,000 µS/cm). It was found that the TDS for well 2 was peaking at 9 am, however, from 2 pm to 4 pm the TDS and EC values were significantly decreased and raised back at 5 pm. For well 1 and well 3, the TDS and EC were relatively constant from 8 am to 4 pm but a significant increase in EC in well 1 was detected at 5 pm.

The average temperature for well 1, 2, and 3 were ranged from 27.1. 27.4 and 27.4 ^{0}C, respectively (Figure 4.6c). From the hourly measurements, it was observed that the temperatures for well 1, 2 and 3 were consistent from 8 am to 12 pm, subsequently decreased at 1 pm to 2 pm and increased at 3 pm but substantially decreasing again at 4 pm to 5 pm. The average values for salinity in well 1, 2, and 3 were found ranging from 34.5, 31.8, and 28.4 ($^{0}/_{00}$), respectively (Figure 4.6c). The hourly rate for the salinity content slightly varied throughout the day, indicating that well 1 has the highest salinity content compared to well 2 and well 3.

The turbidity average values for well 1, 2, and 3 ranged from 18.7, 18.2, and 9.6 nephelometric turbidity unit (NTU) respectively. In Figure 4.6d, the increase of turbidity and water level were observed from 12 pm and 4 pm for well 1, however the turbidity and water level reading for well 2 decreased from 12 pm to 4 pm but increased at 5 pm. For well 3, a

significant decrease was observed in turbidity and water level value from 9 am and 11 am, respectively. From the hourly measurement, all three wells at 10 am (2.2 m) to 11 am (1.4 m) illustrated significant changes in water level.

Table 4. 4 Minimum, maximum, and average values for physical parameters for saline groundwater from 8 am to 5 pm

Well 1							
Time	pH	Temperature (^{0}C)	TDS (mg/L)	EC (µS/cm)	Salinity (‰)	Turbidity (NTU)	Water level (m)
8am	6.6	28.1	33600	53100	35	16.2	1.7
9am	6.6	27.9	33400	52600	34.7	17	1.7
10am	6.5	28.0	33200	52700	34.8	15.3	1.8
11am	6.5	28.3	33300	52600	34.6	16.5	1.7
12pm	6.5	27.5	33000	52300	34.5	21.3	1.8
1pm	6.5	27.5	33100	52300	34.5	19.7	1.9
2pm	6.9	26.6	33100	52400	34.6	18.9	1.6
3pm	6.5	28.0	33000	52500	34.4	19.3	1.9
4pm	6.5	25.3	32500	51600	34	22.1	2
5pm	6.5	24.3	35600	51600	34	21.5	1.5
Mean	6.6	27.1	33800	52370	34.5	18.8	1.7
Min	6.5	24.3	32500	51600	34	15.3	1.5
Max	6.9	28.3	35600	53100	35	22.1	2.0
Well 2							
Time	pH	Temperature (^{0}C)	TDS (mg/L)	EC (µS/cm)	Salinity (‰)	Turbidity (NTU)	Water level (m)
8am	6.8	28.3	31400	50000	32.8	20.3	1.8
9am	6.5	27.8	34600	50300	33.1	19.1	1.6

10am	6.9	27.8	31700	50300	32.9	20.5	1.6
11am	6.9	28.3	31500	50200	33.1	19.4	1.5
12pm	7.0	28.8	31500	50100	32.8	21.0	1.4
1pm	6.9	28.0	31400	50100	32.9	20.2	1.5
2pm	7.4	27.0	29200	46700	30.3	14.7	1.5
3pm	7.5	28.6	27500	44400	28.7	10.1	1.5
4pm	7.1	25.1	28400	45500	29.5	11.9	1.5
5pm	6.9	25.1	31300	49700	32.5	25.5	1.4
Mean	7	27.4	30550	48720	31.8	18.2	1.5
Min	6.5	25.1	27500	44400	28.7	10.1	1.4
Max	7.5	28.8	31700	50300	33.1	25.5	1.8
Well 3							
Time	pH	Temperature (^{0}C)	TDS (mg/L)	EC (µS/cm)	Salinity (‰)	Turbidity (NTU)	Water level (m)
8am	7.4	27.7	27700	44450	28.8	12.7	2.4
9am	7.5	28.2	27600	44400	28.6	7.5	2.3
10am	7.6	28.3	27600	44400	28.7	6.9	2.2
11am	7.5	28.4	27700	44400	28.7	8.2	1.4
12pm	7.5	28.2	27500	44200	28.6	10.2	1.4
1pm	7.5	27.3	27400	44100	28.5	10.2	1.3
2pm	7.5	26.6	27200	43800	28.3	10.1	1.4
3pm	7.5	28.5	27400	44000	28.3	8.8	1.3
4pm	7.5	25.7	27200	43800	28.2	11.7	1.2
5pm	7.6	25.1	27100	43600	28.1	9.6	1.4
Mean	7.5	27.4	27440	44115	28.4	9.6	1.6
Min	7.4	25.1	28100	43600	28.1	6.9	1.2
Max	7.6	28.5	27700	44450	28.2	12.7	2.4

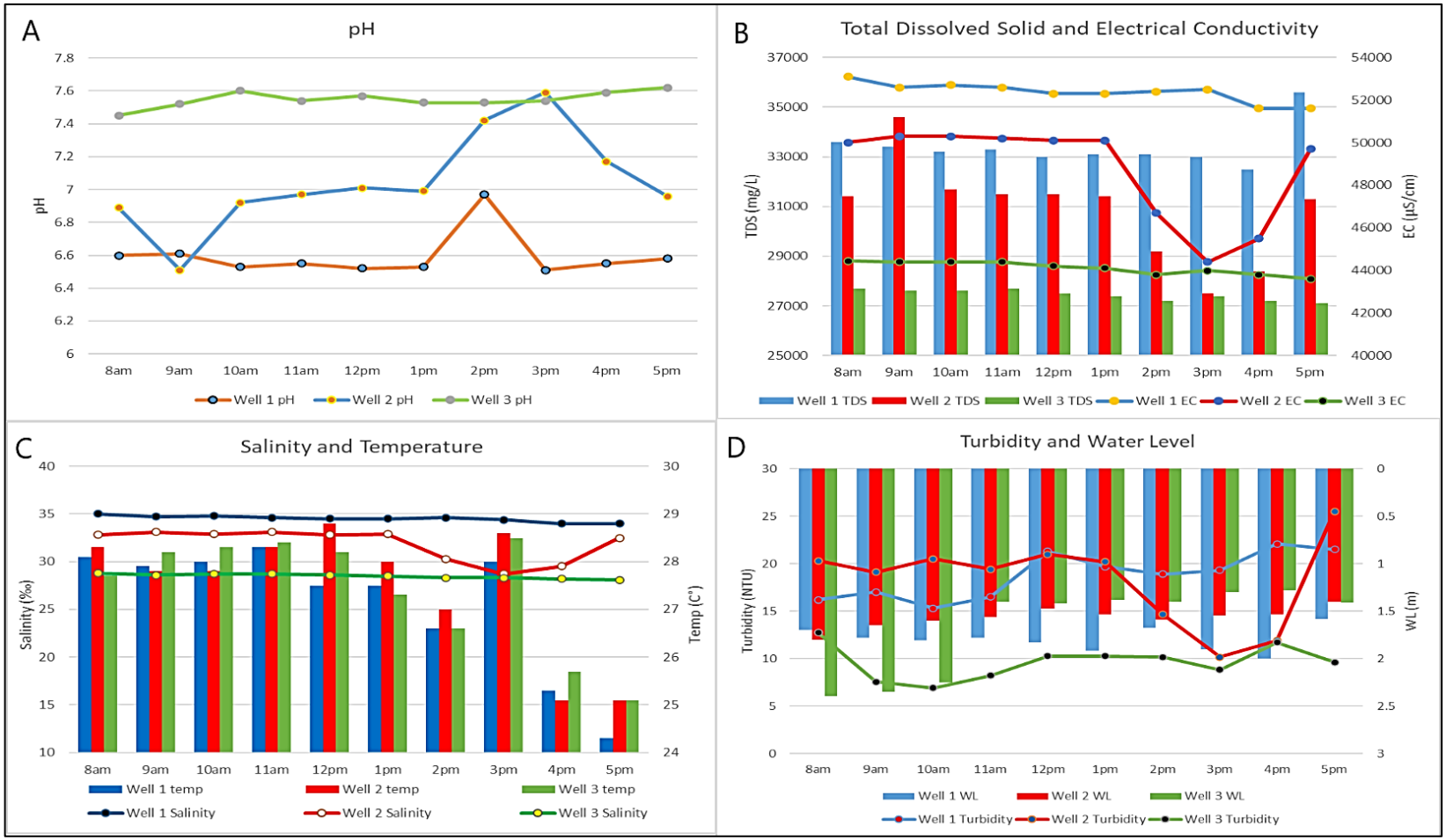

Figure 4. 6 (A, B, C and D) The hourly measurement graph for pH, TDS, EC, salinity, temperature, turbidity and water level.

4.1.3.2 Daily Measurement

Table 4.5 shows the daily (7 days) maximum, minimum, and average values of the physical parameters such as pH, EC, TDS, turbidity, water level, and salinity. In Figure 4.7a, all five wells appeared to have a slight fluctuation value of pH especially for well 2 on 17/12/2018 where a significant increase in pH was observed, with the highest value at 9.8. Meanwhile, well 3 appeared to have a slight increase in pH value throughout the daily measurement starting from 7.2 to a peak of 7.7. Based on Freeze and Cherry's (1979) classification for TDS values, well 1, 2, 3, 4 and 5 falls under saline water type (10,000 – 100,000 mg/L), whereas, the EC values for well 1, 2 and 3 were suggested as brine water type (<45,000 µS/cm) compared to well 4 and 5 which were represented as saline water type (2,000 – 45,000 µS/cm). The TDS and EC values were found in well 1 as the most constant and have the highest value compared to the rest of the wells. It shows that in well 5, the TDS and EC values are decreasing with time and indicated the lowest value on 18/12/2018. Figure 4.7b shows a significant decrease of TDS and EC for well 5, meanwhile, TDS value for well 4 was slightly decreased on 18/12/2018 and a significant increase of EC was seen. It was noticed that TDS, EC, and salinity were strongly correlated and decreasing values in TDS and EC for well 2 were observed on 14/12/2018 which corresponded to the decrease in salinity (Figure 4.7). For the salinity value, well 1 possessed the highest reading while in well 4 and 5 recorded the lowest (Figure 4.7c). The salinity value for well 4 and 5 throughout the week shows that well 4 was slightly increasing while well 5 was slightly decreasing. For turbidity values, well 2 possessed the highest value followed by well 5 > well 4 > well 3 > well 1 (Figure 4.7d). Similarly, well 2 dominated the peak value for the water level (Figure 4.7d). Meanwhile, the temperatures for all the wells were constant with values ranging from 21.5 to 25.2 ^{0}C.

Table 4. 5 Minimum, maximum and average daily basis physical parameters for saline groundwater well 1, 2, 3, 4 and 4 on daily basis

Well 1							
Time	pH	Temperature (^{0}C)	TDS (mg/L)	EC (µS/cm)	Salinity (‰)	Turbidity (NTU)	Water level (m)
Mean	6.7	22.6	33,000	51,242	34.3	2.8	1.5
Min	6.6	21.5	32,700	51,800	34.1	1.7	1.3
Max	6.8	25.2	33,200	52,500	34.6	4.5	1.7
Well 2							
Time	pH	Temperature (^{0}C)	TDS (mg/L)	EC (µS/cm)	Salinity (‰)	Turbidity (NTU)	Water level (m)
Mean	7.4	22.4	30,414	48,742	31.8	14.1	2.1
Min	6.7	21.6	27,200	43,700	28.2	1.5	1.6
Max	9.8	23.7	32,000	50,800	33.4	42.8	2.5
Well 3							
Time	pH	Temperature (^{0}C)	TDS (mg/L)	EC (µS/cm)	Salinity (‰)	Turbidity (NTU)	Water level (m)
Mean	7.5	22.3	27,500	44,485	28.7	2.5	1.6
Min	7.2	21.6	27,000	43,400	28.0	1.6	1.5
Max	7.7	23.7	30,000	47,800	31.2	5.0	1.7
Well 4							
Time	pH	Temperature (^{0}C)	TDS (mg/L)	EC (µS/cm)	Salinity (‰)	Turbidity (NTU)	Water level (m)
Mean	7.1	23.6	18,860	31,300	19.3	8.1	1.1
Min	6.9	22	18,770	31,100	19.2	3.8	0.8
Max	7.2	25.2	18,960	31,500	19.5	12.3	1.4

Well 5							
Time	pH	Temperature (^{0}C)	TDS (mg/L)	EC (µS/cm)	Salinity (‰)	Turbidity (NTU)	Water level (m)
Mean	6.9	23.4	20,860	34,350	21.6	14.8	2.1
Min	6.8	23.3	17,120	28,800	17.7	10.9	2.0
Max	6.9	23.8	24,600	39,900	25.5	18.8	2.1

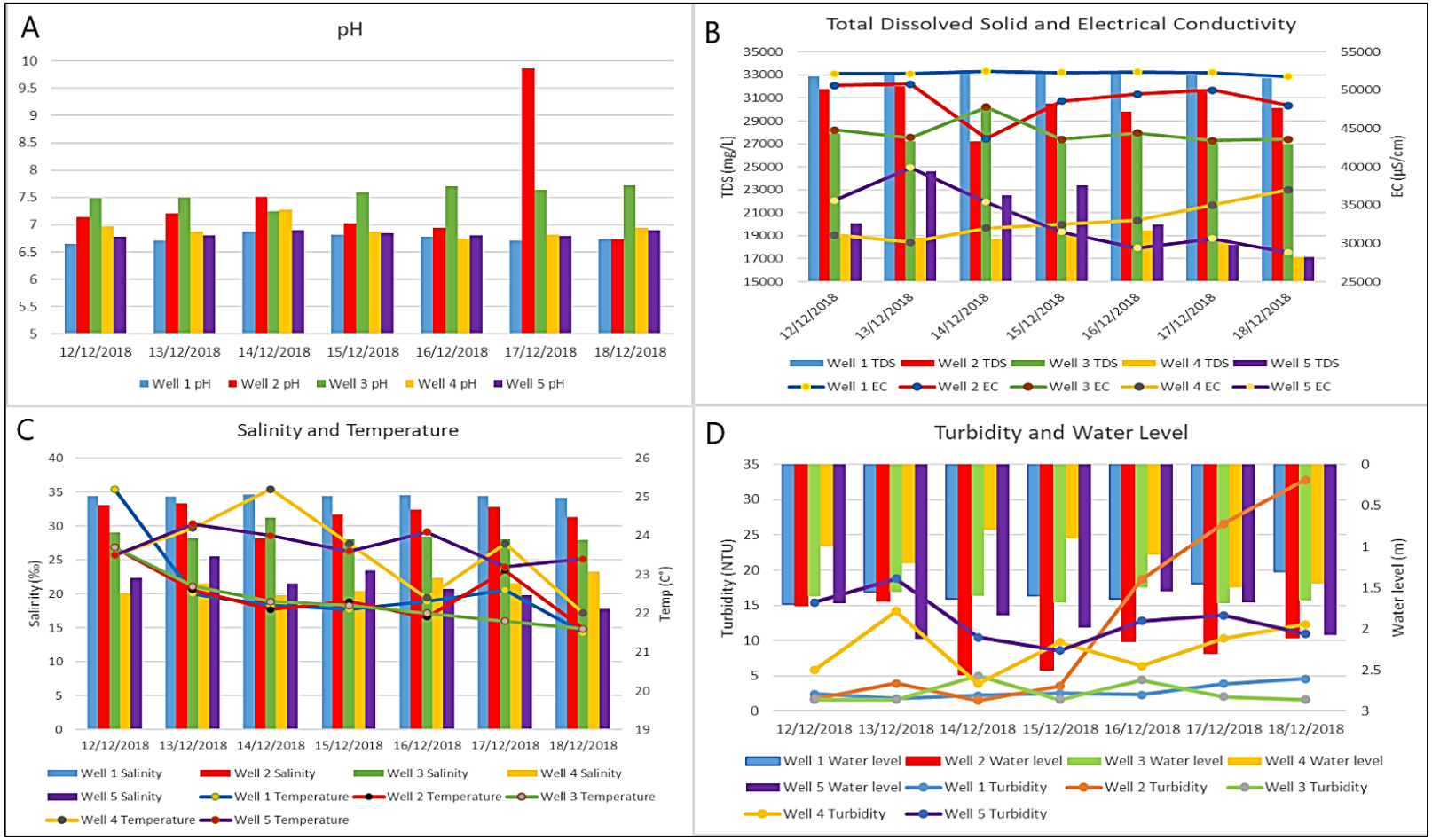

Figure 4. 7 (A, B, C and D) The daily measurement graph for pH, TDS, EC, salinity, temperature, turbidity and water level.

4.1.3.3 Monthly Measurement

Table 4.6 illustrates the minimum, maximum, and average physical parameter statistic for monthly measurements. In Figure 4.8a, the pH value for well 4 was found to have significantly increased from 22nd December 2018 to 30th December 2018, from 7.6 to 8.4 as the highest pH value followed by well 3 > well 2 > well 1. Furthermore, the TDS, EC, and salinity values were recorded where well 1 and 2 were the highest followed by well 3 then well 4 (Figure 4.8).

Table 4. 6 The statistic of minimum, maximum and average values of monthly basis physical parameters for saline groundwater from December 2018 to the end of January 2019

Well 1							
Time	pH	Temperature (^{0}C)	TDS (mg/L)	EC (µS/cm)	Salinity (‰)	Turbidity (NTU)	Water level (m)
Mean	7.4	23.4	34,448	68,997	47.1	15.6	1.8
Min	7.3	22.1	33,500	67,100	45.6	10.8	1.6
Max	7.7	24.8	35,000	69,900	47.8	24.4	2.1
Well 2							
Time	pH	Temperature (^{0}C)	TDS (mg/L)	EC (µS/cm)	Salinity (‰)	Turbidity (NTU)	Water level (m)
Mean	7.5	23.3	34,264	68,797	47.1	20.7	1.6
Min	7.4	22.5	33,300	66,600	45.3	5.8	1.3
Max	7.6	24.2	34,800	69,900	47.8	35.7	1.9
Well 3							
Time	pH	Temperature (^{0}C)	TDS (mg/L)	EC (µS/cm)	Salinity (‰)	Turbidity (NTU)	Water level (m)
Mean	7.8	22.8	30,737	61,397	41.1	4.9	2.1
Min	7.7	24.3	29,000	58,400	39.3	2.8	1.4
Max	8.0	25.4	32,500	66,500	44.7	6.9	2.6

Well 4							
Time	pH	Temperature (^{0}C)	TDS (mg/L)	EC (µS/cm)	Salinity (‰)	Turbidity (NTU)	Water level (m)
Mean	8.1	24.2	21,548	43,240	27.8	7.2	1.3
Min	7.5	22.8	21,100	43,000	27.5	4.5	0.7
Max	8.4	25.6	21,900	43,700	27.9	9.8	1.8

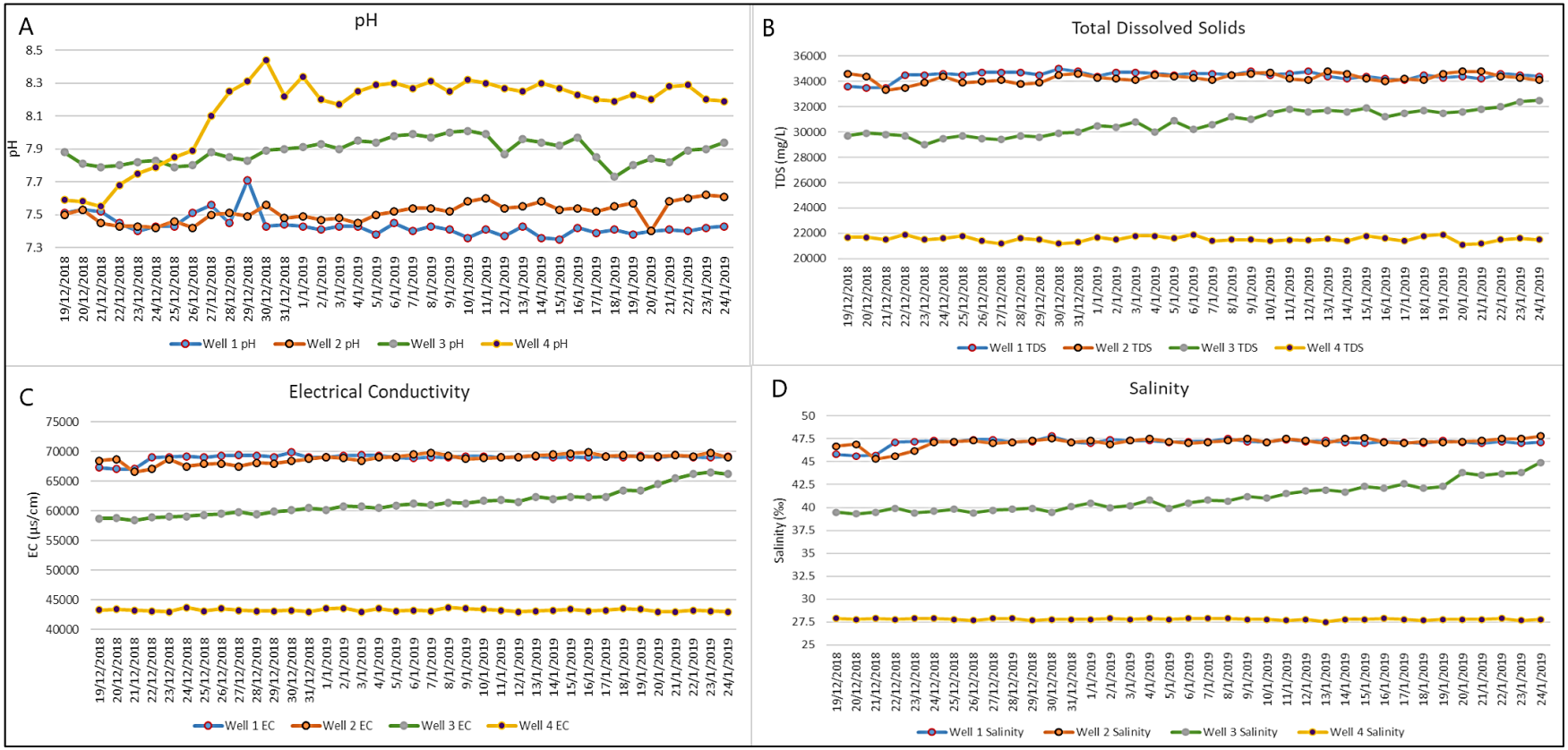

Figure 4. 8 (A, B, C and D) The monthly measurement graph for pH, TDS, EC and salinity.

Table 4. 7 Water classification based on electrical conductivity and total dissolved solids by Freeze and Cherry, (1979)

Water Class	Total Dissolved Solids (TDS) (mg/L)	Water Class	Electrical Conductivity (EC) (µS/cm)
Fresh	0 – 1,000	Non-saline	< 700
Brackish	1,000 – 10,000	Slightly Saline	700 – 2,000
Saline	10,000 – 100,000	Moderately Saline	2,000 – 10,000
Brine	> 100,000	Highly Saline	10,000 – 25,000
		Brine	> 45,000
Well 1	33,800 – 34,448	Saline - Brine	52,370 – 68,997
Well 2	30,550 – 34,264	Saline - Brine	48,720 – 68,797
Well 3	27,440 – 30,737	Saline - Brine	44,115 – 61,397
Well 4	18,860 – 24,548	Saline – highly saline	31,300 – 43,240
Well 5	20,860	Saline – highly saline	34,350

4.2 Discussion

4.2.1 Saline Groundwater Physico-chemical during Preliminary Survey

Well 1, 2 and 3 were located adjacent to each other in the study area Buduk Bui and it was found that well 1 has the highest value for most of the physical parameter (TDS, EC and salinity) compared with the rest of the wells. From the daily measurement, the acidic nature (pH 6.5) in well 1 causes more dissolution during water-rock interaction which gave more ionic concentration. Meanwhile, the change in TDS and EC values indicated that both parameters are strongly correlated and relatable to the recharge in the study area (Rusydi, 2018). Additionally, from the hourly measurement, all three wells at 10 am (2.2 m) to 11 am (1.4 m) illustrated significant changes in water level that possibly indicate the groundwater recharge. Based on Freeze and Cherry's (1979) water classification based on the TDS values in Table 4.7 indicate well 1, 2, 3, 4 and 5 were classified as saline water (10,000 – 100,000

mg/L). Meanwhile, based on the EC values in Table 4.7, well 1, 2 and 3 were classified as brine water (<45,000 µS/cm) whereas, well 4 and 5 which were represented as saline water (2,000 – 45,000 µS/cm). Well 1, 2 and 3 were located adjacent to each other in the study area Buduk Bui and it was found that well 1 has the highest value for most of the physical parameter (TDS, EC and salinity) compared with the rest of the wells.

CHAPTER 5. Water Chemistry

5.1 Results

5.1.1 Saline Groundwater Physico-chemical Parameters

The results of hydrochemical analyses for well 1, 2, 3, 4 and 5 samples are summarized in Table 5.1 and 5.2 for the monsoon (MON) and post-monsoon season (POM), respectively. The pH values for saline groundwater suggested a slightly acidic to alkaline in nature which varies from 6.7 to 7.7 for MON and 6.5 to 7.7 for POM. Saline groundwater wells in Ba'kelalan have high salinity content with the EC value varying between the seasons with 28,800 to 51,800 µS/cm for MON and 40,500 to 66,500 µS/cm for POM. According to Freeze and Cherry (1970), well 1 and 2 were categorized as brine water, while well 3, 4 and 5 were considered as saline water based on EC values. However, based on TDS values, all groundwater samples were categorized as saline water, with the range of 17,120 to 32,700 mg/L for MON and 10,300 to 33,300 mg/L for POM. It was found that the salinity increased significantly in the POM, ranging from 17.7 to 34.1 ‰ in MON and 25.9 to 45.2 ‰ in the POM.

5.1.2 Major Ions (Na+, Ca2+, Mg2+, K+, Cl- and HCO3-)

Sodium is the most abundant member of the alkali-metal group and is retained by adsorption on mineral surfaces, especially clays, due to high cation exchange capacities (Ibrahim et al., 2019). For the hydrochemical data in the saline groundwater (well 1, 2, 3, 4, 5), the concentration of Na^+ ranged from 2,976 to 4,536 mg/L for MON and 6,740 to 14,184 mg/L for POM, respectively. Na^+ is the dominant cation in all saline groundwater samples for both seasons (Table 5.1 and 5.2). Meanwhile, potassium is an essential plant nutrient and is present in the ash of plants (Karamouz et al., 2020). For all the saline groundwater samples, the K^+ concentration ranged between the seasons with 10.4 to 28.8 mg/L for MON and 24.3 to 31.7 mg/L for POM, respectively. A slight increase was observed in potassium's concentration in the POM season for all the saline groundwater samples. In most natural freshwater, calcium is the principal cation and it is an important element to develop proper

bone growth for human and animals (Hem, 1989). The Ca^{2+} concentration vary between the seasons as 225.2 to 378.6 mg/L for MON and 138 to 245.2 mg/L for POM. The saline groundwater analysis results for Mg^{2+} concentration vary between the seasons with 54.80 to 138.6 mg/L for MON and 62.8 to 138.6 mg/L for POM. Chloride is often present in natural waters but generally in low concentration. However, chloride is present in great abundance in ocean water, as a predominant anion (Hem, 1985). Cl^- is the dominant anion in all groundwater samples, where it has a value ranging from 6,534.4 to 8,175 mg/L for MON and 11,547 to 25,450 mg/L for POM. In natural water, bicarbonate concentration is generally held within a moderate range by the effects of carbonate equilibria where it is common to have a high concentration in groundwaters. The HCO_3^- concentration varies between season with 548 to 875.55 mg/L for MON, while for the POM, it ranged between 1,085.8 to 1,708 mg/L. However, the concentration of CO_3^- is absent or below the detection limit in both the seasons. The order of major ions in both seasons for the saline groundwater samples is as follows: $Na^+ > Ca^{2+} > Mg^{2+} > K^+ = Cl^- > HCO_3^- > NO_3^- > SO_4^{2-}$.

5.1.3 Nutrients (SO_4^{2-}. NO_3^-, NO_2^-, NH_3, NH_3N, $NH4^+$, P, PO_4^{3-})

Sulphate is a typical anion in water and neglected as pollution in groundwater. It is usually discharged into water from domestic wastewater, industrial wastes, seawater intrusion, geothermal processes and atmospheric deposition (Torres-Martinez et al., 2020). The SO_4^{2-} concentration in the saline groundwater samples ranged from 1 mg/L to 2 mg/L in MON and 1 mg/L in POM. The element nitrogen is present in small quantities in rocks but is concentrated to a greater extent in soil and biological materials. The greater portion of gas present in the Earth's atmosphere is nitrogen gas (Margat and Van der Gun, 2013). NO_3^- concentration in saline groundwater ranged between 0.1 to 19 mg/L for MON and 0.1 to 1.1 mg/L for POM, respectively. Whereas, the concentration for NO_2^- in saline groundwater ranged as 0.1 to 4.3 mg/L for MON and BDL for POM. For NH_4^+, NH_3 and NH_3N, the concentration exhibited similar values, however, ammonia ion (NH_4^+) was the major N-species, where it varied from 0.5 to 24.5 mg/L for MON and 0.3 to 16.7 mg/L for POM. Phosphorous is an essential element

in the growth of plants and animals, and some contribute nitrates such as organic wastes and leaching of soils (Domagalski and Johnson, 2011). The phosphorous found is normally identified as orthophosphate (PO_4^{3-}), where the water samples exhibited low concentration in both phosphate and phosphorous, with the PO_4^{3-} value varying between 0.3 to 0.7 mg/L for MON and 0.2 to 0.7 mg/L for POM. Meanwhile, the phosphorous concentration was ranged between 0.1 to 0.2 mg/L for MON and 0.2 to 0.3 mg/L for POM.

5.1.4 Trace Metals Concentration

In Figure 5.2, the order for trace metal concentration present in the saline groundwater samples for MON season is as follows: Sn > Ba > B > Sc > Fe > Cu > Li > Cr > Co > Rb > Zn; meanwhile, for POM season, the order is as follows: Ba > B > Sc > Sn > Fe > Li > Zn > Co (Figure 5.2). The concentration of tin in groundwater samples indicated that the highest loading in MON ranged from 16.56 to 23.6 mg/L. However, in POM, the concentration is reduced to 2.3 to 5.3 mg/L. The groundwater samples for boron has values ranging from 0.1 to 5 mg/L for MON and 0.2 to 5.3 mg/L for POM. While ocean water has an average of 4.6 mg/L (Han et al., 2018). Barium concentration was observed in the range of 8.5 to 14.2 mg/L in MON and 3.3 to 7.3 mg/L in POM. The concentration for scandium in groundwater samples varied between 2.41 to 3.95 mg/L for MON and 2.31 to 5.42 mg/L for POM. The iron concentration for groundwater samples varied between 1.3 to 7.2 mg/L for MON and 1 to 1.2 mg/L, for POM.

The concentration of copper varied between 0.47 to 0.6 mg/L for MON and 0.02 to 0.06 mg/L for POM. The lithium concentration in the saline groundwater ranged from 0.1 to 0.3 mg/L. Meanwhile, the chromium concentration ranged between 0.1 to 0.42 mg/L for MON and 0.03 to 0.06 mg/L for POM. Cobalt concentration ranged between 0.10 to 0.13 mg/L for MON and 0.18 to 0.13 for POM. The concentration of zinc in the saline groundwater samples ranged between 0.1 to 0.17 mg/L for MON and 0.1 to 0.2 mg/L for POM. The concentration for Rb and Mn were very low with an average value of 0.02 mg/L and 0.01 mg/L, respectively. Whereas, the analysis results for Al and Pb showed that they were below the detection limit.

5.1.5 River Water Analysis

The result of hydrochemical analysis for river water samples are summarized in Table 5.1 and 5.2 for the MON and POM, respectively. The pH value suggests that alkaline in nature varies between 7.45 for MON and 7 for POM. For the EC value ranged between 80 µS/cm for MON and 60 µS/cm for POM, whereas, the TDS value ranged between 40 mg/L for MON and 30 mg/L for POM, respectively. The order of major ions for river sample is as follows: $Na^+ > Mg^{2+} > Ca^{2+} > K^+ = HCO_3^- > Cl^- > NO_3^- > SO_4^{2-}$. Whereas, the order of trace metal (Figure 5.2) is as follows: Sn > Ba > Fe > Sc > Cu > B > Co > Rb > Zn > Cd > Li for MON and for POM, the order is as follows: Ba > Sn > Sc > Fe > B > Zn > Co > Cr > Cd > Rb.

Table 5. 1 The statistical summary of hydrogeochemical parameters for monsoon season (MON) of saline groundwater and river samples of Ba'Kelalan region

Parameter	Monsoon 18/12/2018							
	Well 1	Well 2	Well 3	Well 4	Well 5	River	Mean	Well 1 2017
pH	6.7	6.8	7.7	6.9	6.7	7.4	7	7.4
Temperature (^{0}C)	21.5	21.6	21.6	22.0	23.4	24.5	22.4	23
TDS (mg/L)	32,700	30,100	27,000	18,770	17,120	40	20,955.2	23,800
EC (µS/cm)	51,800	48,000	43,600	31,100	28,800	80	33,897.1	48,800
Salinity (‰)	34.1	31.3	28.0	19.2	17.7	0.04	21.7	31.7
Turbidity (NTU)	4.5	42.8	1.6	12.3	10.9	9.8	13.6	-
SO_4^{2-} (mg/L)	1	2	1	1	1	1	0.5	1

PO_4^{3-} (mg/L)	0.7	0.5	0.1	0.4	0.4	0.3	0.4	-
P (mg/L)	0.2	0.1	0.1	0.1	0.1	0.1	0.1	-
NO_3^- (mg/L)	0.6	0.6	19	0.1	0.1	BDL	0.3	0.5
NO_2 (mg/L)	0.1	0.1	4.3	BDL	BDL	BDL	0.7	-
NH_4 (mg/L)	3.7	24.5	0.5	12.5	12	0.5	8.9	-
NH_3 (mg/L)	3.5	23	0.5	11.7	11.2	0.5	8.4	-
NH_3N (mg/L)	3.1	19	0.4	9.7	9.2	0.4	6	-
Na^+ (mg/L)	4,512	4,536	4,308	3,875	3,575	24.3	3,069.7	9,750
K^+ (mg/L)	18.6	24.9	10.4	29.8	25.6	1	18.4	49.3
Ca^{2+} (mg/L)	378.6	430.2	325.2	285.4	251.2	2.6	265.8	155
Mg^{2+} (mg/L)	126.6	138.6	54.8	74.6	100.4	6.	83.6	172.8
Cl^- (mg/L)	8,175	8,075.5	7,856.9	6,875.5	6,534.4	31.5	7503.4	17,503.4
HCO_3^- (mg/L)	875.5	762.5	603.9	548	578.9	51.5	570	1311.5
CO_3 (mg/L)	BDL	BDL	BDL	BDL	BDL	BDL	-	BDL
Mn (mg/L)	BDL	BDL	BDL	BDL	BDL	BDL	-	-
Fe (mg/L)	2.8	7.2	1.3	1.6	2	3.3	3	0.50
Ba (mg/L)	8.5	9.6	11.2	11.7	12.8	14.2	11.3	21.3
Zn (mg/L)	BDL	BDL	0.17	0.1	BDL	BDL	0.1	0.1
Sc (mg/L)	3.9	2.4	2.6	2.4	3.9	2.5	2.9	-
Pb (mg/L)	BDL	BDL	BDL	BDL	BDL	BDL	-	-

Al (mg/L)	BDL	BDL	BDL	BDL	BDL	BDL	-	-
Co (mg/L)	0.1	0.1	0.1	0.1	0.1	0.1	0.1	-
Cd (mg/L)	BDL	BDL	BDL	BDL	BDL	BDL	-	-
Cu (mg/L)	0.4	0.6	0.4	1.6	0.6	0.2	0.5	-
Cr (mg/L)	0.1	0.1	0.2	1	0.4	BDL	0.1	-
Rb (mg/L)	0.03	0.03	0.03	0.03	0.03	0.02	0.02	0.1
Sn (mg/L)	16.5	18.1	19.8	21.5	22.6	23.6	20.3	-
B (mg/L)	4.1	3.6	5	2	2	0.1	2.8	-
Li (mg/L)	0.2	0.2	0.3	0.1	0.1	BDL	0.1	14.2
Sr (mg/L)	-	-	-	-	-	-	-	48.2

Table 5. 2 The statistical summary of hydrogeochemical parameters for post-monsoon season (POM) of saline groundwater and river samples of Ba'Kelalan region

Parameter	Post-monsoon 10/4/2019							
	Well 1	Well 2	Well 3	Well 4	Well 5	River	Mean	Std. Deviation
pH	6.5	6.7	6.8	7.1	7.3	7	6.9	0.2
Temperature (^{0}C)	25	24.9	24.0	23.2	23.9	25	24.3	0.7
TDS (mg/L)	33,300	28,100	25,100	10,800	10,300	30	19,605.5	12,336.87
EC (µS/cm)	66,500	56,300	58,900	41,700	40,500	60	43,994.3	23,779.42
Salinity (‰)	45.2	37.4	33.1	26.7	25.9	0	28	15
Turbidity (NTU)	14.5	12.8	8.7	29.7	2.1	5.7	12.2	9.6
SO_4^{2-} (mg/L)	1	1	1	1	1	2	0.5	0.8
PO_4^{3-} (mg/L)	0.7	0.7	0.4	0.9	0.2	0.0	05	0.3

P (mg/L)	0.2	0.2	0.2	0.3	0.08	0.0	0.1	0.1
NO_3^- (mg/L)	0.1	0.2	0.1	1.1	0.2	0.3	0.3	0.3
NO_2 (mg/L)	0	0	0	0	0	0	0	0
NH_4 (mg/L)	16.7	14.7	4.2	9	4.7	0.3	8.3	6.4
NH_3 (mg/L)	15.75	14	4	8.5	5.7	0.3	8	5.9
NH_3N (mg/L)	13	11.5	3.7	1	5.7	0.2	6.8	4
Na^+ (mg/L)	14,184	12,064	10,248	7,736	6,740	1.3	8,366.8	3,073.5
K^+ (mg/L)	28.6	31.7	24.8	26.4	24.3	2.5	23.1	10.4
Ca^{2+} (mg/L)	240	245.2	204.4	138.0	148.2	0	162.7	91.2
Mg^{2+} (mg/L)	138.6	120	106.8	82.2	62.8	6	86	47
Cl^- (mg/L)	25,450	21,584	17,859	13,458	11,547	17.5	17,979.6	5,714.81
HCO_3^- (mg/L)	1,708	1,500.6	1,256.6	1,195.6	1,085.8	15.5	1,127	589.1
CO_3 (mg/L)	BDL	BDL	BDL	BDL	BDL	BDL	-	-
Mn (mg/L)	BDL	BDL	BDL	BDL	BDL	BDL	-	-
Fe (mg/L)	1.1	1.1	1	1.1	1.2	0.6	5.7	1.2
Ba (mg/L)	3.3	5.9	5.5	6.1	7.3	5.8	0.2	0.8
Zn (mg/L)	0.1	0.2	0.2	0.3	0.1	0.1	3.5	1
Sc (mg/L)	3.7	5.4	2.3	2.9	3.2	3.7	0.1	0.1
Pb (mg/L)	BDL	BDL	BDL	BDL	BDL	BDL	-	-
Al (mg/L)	BDL	BDL	BDL	BDL	BDL	BDL	-	-
Co (mg/L)	0.1	0.1	0.1	0.1	0.1	0.1	0.1	0.1

Cd (mg/L)	BDL	BDL	BDL	BDL	BDL	BDL	-	-
Cu (mg/L)	BDL	BDL	BDL	BDL	BDL	BDL	-	-
Cr (mg/L)	BDL	BDL	BDL	BDL	BDL	BDL	-	-
Rb (mg/L)	BDL	BDL	BDL	BDL	BDL	BDL	-	-
Sn (mg/L)	2.2	2.4	3.3	3.8	4.9	5.3	3.6	1.2
B (mg/L)	5.2	5.3	3.6	1.4	2.5	0.2	3	2
Li (mg/L)	0.3	0.3	0.2	0.1	0.2	0	0.1	0.1

5.1.6 Rainwater Analysis

Allocation of rain gauges for collection of rainwater was fixed from the lower stream at Long Aru (RW LS), middle stream at Buduk Bui (RW BB), and upstream at Pa'Komap (RW US) to determine the quantity and quality of recharge to the groundwater wells in the region. Table 5.3 shows that the data from upstream received more amount of rainwater especially during the early month of January 2019 compared to Buduk Bui and the lower stream. In Figure 5.1, the TDS and EC values observed in the lower stream have slightly higher concentration compared to Buduk Bui and the upstream. Also, TDS and EC values for all locations exhibited higher values in December 2018 compared to January 2019. The TDS and EC values varied for RW LS, RW BB and RW US, ranging from 27.8, 11.4, 18.5, 11.2, 18.5, 10.9 mg/L and 54.3, 22.01, 34.8, 80.1, 34.46, 19.9 µS/cm, respectively. According to Freeze and Cherry (1979), the rainwater samples were classified based on TDS and EC values as freshwater and non-saline water type. It is expected that the salinity in rainwater is very low with a value ranging from 0.01 to 0.03 ‰. The density and quantity of collected rainwater showed that higher elevation station received more amount of rainwater and are more frequent with 2,290 mm at RW US, followed by RW BB station with 1,345 mm and 840 mm at RW LS. The pH values showed the rainwater is acidic to slightly acidic, with the average pH for RW US, RW BB and RW US ranging from 5.8 to 6.1, 6.0 to 6.2, 4.6 to 5.8, respectively. Figure 5.1d shows the quantity of rainwater collection from Ba'kelalan airport, indicating a

more frequent amount of rainfall in the MON, especially during January 2019, compared to POM in April 2019 (gpm.nasa.gov/data/directory).

Table 5.4 shows the average for the physical parameters, major ions and trace metals for each month in designated locations from lower stream to upstream in Ba'kelalan. The dominant orders for major ions are as follows: in RW LS December 2018 and January 2019 ($K^+ > Ca^{2+} > Na^+ > Mg^{2+} = HCO_3^- > Cl^- > NO_3^- > SO_4^{2-}$); in RW BB December 2018 ($Ca^{2+} > Na^+ > K^+ > Mg^{2+} = HCO_3^- > Cl^- > SO_4 > NO_3^-$); in RW BB January 2019 and RW US December 2018 ($Ca^{2+} > K^+ > Na^+ > Mg^{2+} = HCO_3^- > Cl^- > NO_3^- > SO_4^{2-}$); in RW US January 2019 ($Ca^{2+} > Na^+ > K^+ > Mg^{2+} = HCO_3^- > Cl^- > NO_3^- > SO_4^{2-}$). The concentration of acidic species (SO_4^{2-} and NO_3^-) at RW US, BB and US were observed to be very low. Meanwhile, Na^+ and Cl^- concentration observed a decreased concentration in the following month for all rainwater locations. The concentration of trace metals in the Buduk Bui rainwater samples is illustrated in Table 5.4 and Figure 5.2. From the results, the RW concentration of trace metals decreases in the following order: Ba > Sn > Sc > Fe > Co > Zn > Cr.

Table 5. 3 The physical parameters and quantity of rainwater from 3 locations

RW LS	Date	Quantity (mL)	pH	Temperature (^{0}C)	TDS (mg/L)	EC (µs/cm)	Salinity (‰)
	19/12/2018	60	5.6	24.1	38.5	76.2	0.04
	20/12/2018	60	6	24.5	17.2	32.4	0.02
	3/1/2019	120	5.9	24.3	15.7	31.2	0.02
	4/1/2019	120	5.9	24.2	11	21.8	0.02
	12/1/2019	120	6.4	24	17	33.6	0.02
	13/1/2019	120	6.2	24.8	18.4	36.5	0.02
	14/1/2019	40	6.4	24.7	11.6	20.6	0.02
	15/1/2019	100	5.9	24.5	2.6	4.6	0.01
	31/1/2019	100	5.9	24.6	3.6	5.7	0.01

Total amount of rainwater (mL)		840					
RW BB	Date	Quantity (mL)	pH	Temperature (^{0}C)	TDS (mg/L)	EC (µs/cm)	Salinity (‰)
	19/12/2018	120	6.1	23.5	20.5	65.4	0.03
	21/12/2018	65	5.9	23.4	35.7	70.6	0.04
	22/12/2018	120	6.1	23.2	6.4	1.2	0.02
	27/12/2018	120	6	23.4	11.6	2.3	0.02
	2/1/2019	120	6.1	23.1	5	9.4	0.01
	3/1/2019	100	5.9	23	4.2	7.5	0.01
	4/1/2019	120	6.2	23.6	3.7	6.9	0.01
	12/1/2019	120	6.8	23.4	5.5	10.1	0.01
	13/1/2019	100	6.1	23.2	4.6	8.2	0.01
	14/1/2019	120	6.4	23.1	3.9	7	0.01
	16/1/2019	120	6.3	23	6.5	6.2	0.01
	20/1/2019	120	6.2	23.5	4.7	8.5	0.01
Total amount of rainwater (mL)		1,345					
RW US	Date	Quantity (mL)	pH	Temperature (^{0}C)	TDS (mg/L)	EC (µs/cm)	Salinity (‰)
	19/12/2018	120	5.29	23.2	16	31.7	0.02
	20/12/2018	120	4.91	24.5	15.2	30.3	0.02
	21/12/2018	120	4.18	23.5	23.6	46.9	0.03
	22/12/2018	120	4.17	23	24.4	46.1	0.03
	23/12/2018	120	4.3	24.2	19.2	38.2	0.03
	27/12/2018	70	4.85	24	12.9	25.6	0.02
	1/1/2019	120	5.51	23.9	11.5	21.7	0.02
	2/1/2019	120	5.84	24	17.6	35.6	0.02
	3/1/2019	120	5.88	23.6	6.7	17.9	0.02

	4/1/2019	120	5.99	24.1	10.1	20.4	0.02
	5/1/2019	120	5.77	24.3	3.3	6.7	0.01
	8/1/2019	120	5.7	24.1	7.2	14.5	0.02
	9/1/2019	120	6.37	24.2	41	52.1	0.04
	12/1/2019	120	6.09	24	11.2	22	0.02
	13/1/2019	120	5.84	24.5	8	16	0.02
	14/1/2019	120	5.81	24.3	5.3	10.6	0.01
	15/1/2019	120	5.69	24.1	7.2	14.4	0.02
	16/1/2019	120	5.73	24.2	4.8	9.6	0.01
	20/1/2019	60	5.75	24	4.4	8.8	0.01
	26/1/2019	120	6.5	24.5	13.9	27.8	0.02
Total amount of rainwater (mL)		2,290					

Table 5. 4 The hydrogeochemical data for rainwater

Parameter (ppm)	Monsoon December 2018 – January 2019					
	RW LS December	RW LS January	RW BB December	RW BB January	RW US December	RW US January
pH	5.8	6.1	6.0	6.2	4.6	5.8
Temperature (^{0}C)	24.1	24.2	23.3	23.2	23.5	23.4
TDS (mg/L)	27.8	11.4	18.5	11.2	18.5	10.9
EC (µS/cm)	54.3	22.0	34.8	80.1	36.4	19.9
Salinity (‰)	0.03	0.02	0.03	0.01	0.03	0.02
Na^+ (mg/L)	2	2.4	2.3	1	1.3	1.5
K^+ (mg/L)	5.9	4.7	3.9	2.5	2.7	1.5
Ca^{2+} (mg/L)	2.6	1.3	4.9	1.4	1.7	1.3
Mg^{2+} (mg/L)	0.2	0.1	0.4	0.01	0.2	0.1

Cl^- (mg/L)	3.5	2.7	2.8	3.8	2.3	1.8
HCO_3^- (mg/L)	10.8	9.4	10.2	8.7	9.3	8.1
CO_3 (mg/L)	BDL	BDL	BDL	BDL	BDL	BDL
Mn (mg/L)	BDL	BDL	BDL	BDL	BDL	BDL
Fe (mg/L)	0.37	0.39	0.35	0.34	0.49	0.5
Ba (mg/L)	9.36	11.45	14.04	16.52	20.49	28
Zn (mg/L)	0.25	0.11	0.21	0.31	0.17	0.2
Sc (mg/L)	3.28	2.72	3.27	4.97	3.50	3.2
Pb (mg/L)	BDL	BDL	BDL	BDL	BDL	BDL
Al (mg/L)	BDL	BDL	BDL	BDL	BDL	BDL
Co (mg/L)	0.2	0.2	0.2	0.2	0.2	0.3
Cd (mg/L)	BDL	BDL	BDL	BDL	BDL	BDL
Cu (mg/L)	BDL	BDL	BDL	BDL	BDL	BDL
Cr (mg/L)	BDL	BDL	BDL	BDL	BDL	BDL
Rb (mg/L)	BDL	BDL	BDL	BDL	BDL	BDL
Sn (mg/L)	8.3	8.8	9.2	10.3	11.5	12.2

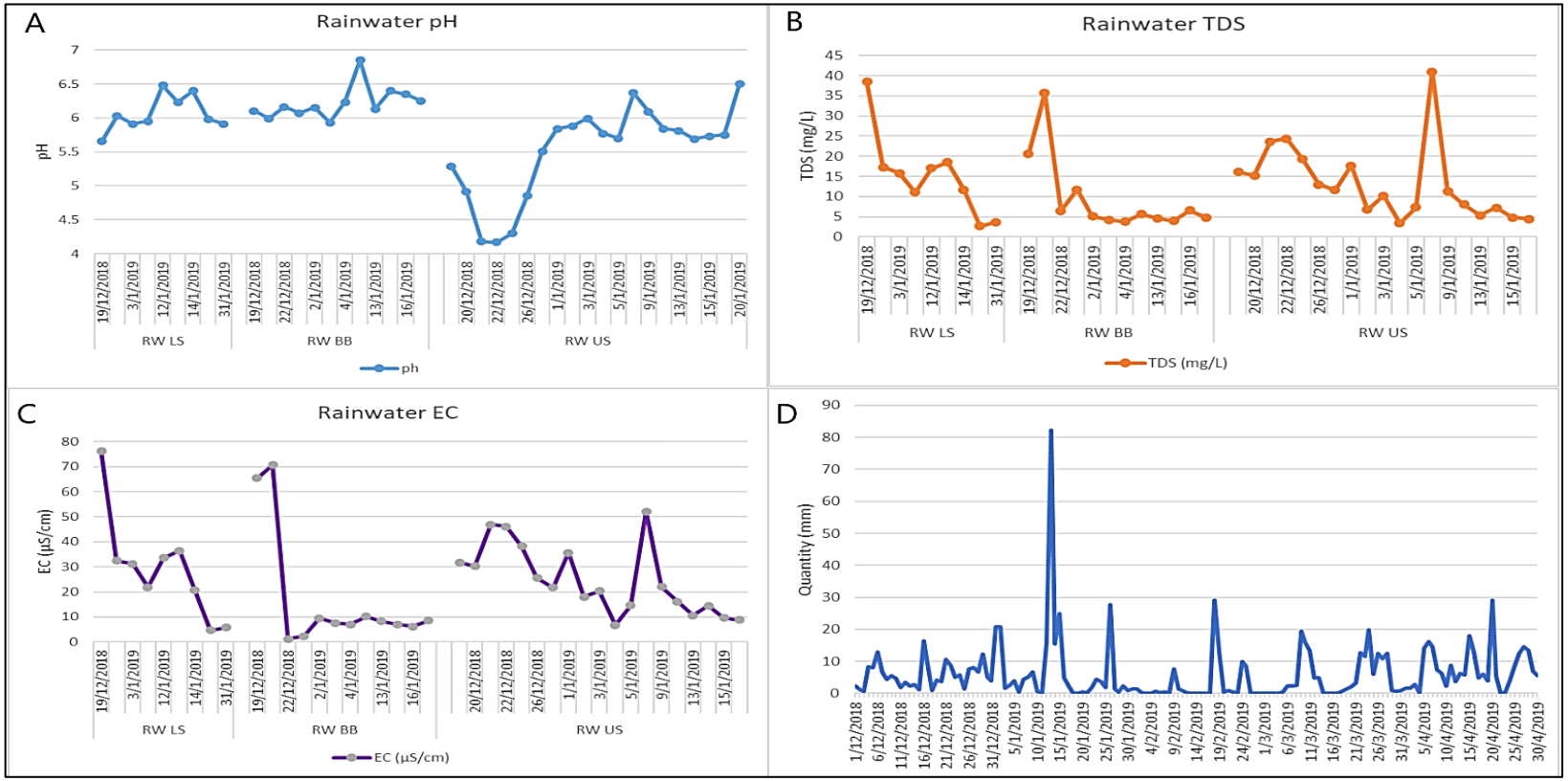

Figure 5. 1 (A) The graph for rainwater TDS. (B) The graph for rainwater pH. (C) The graph for rainwater EC. (D) The graph of rainfall data in Ba'kelalan airport (gpm.nasa.gov/data/directory).

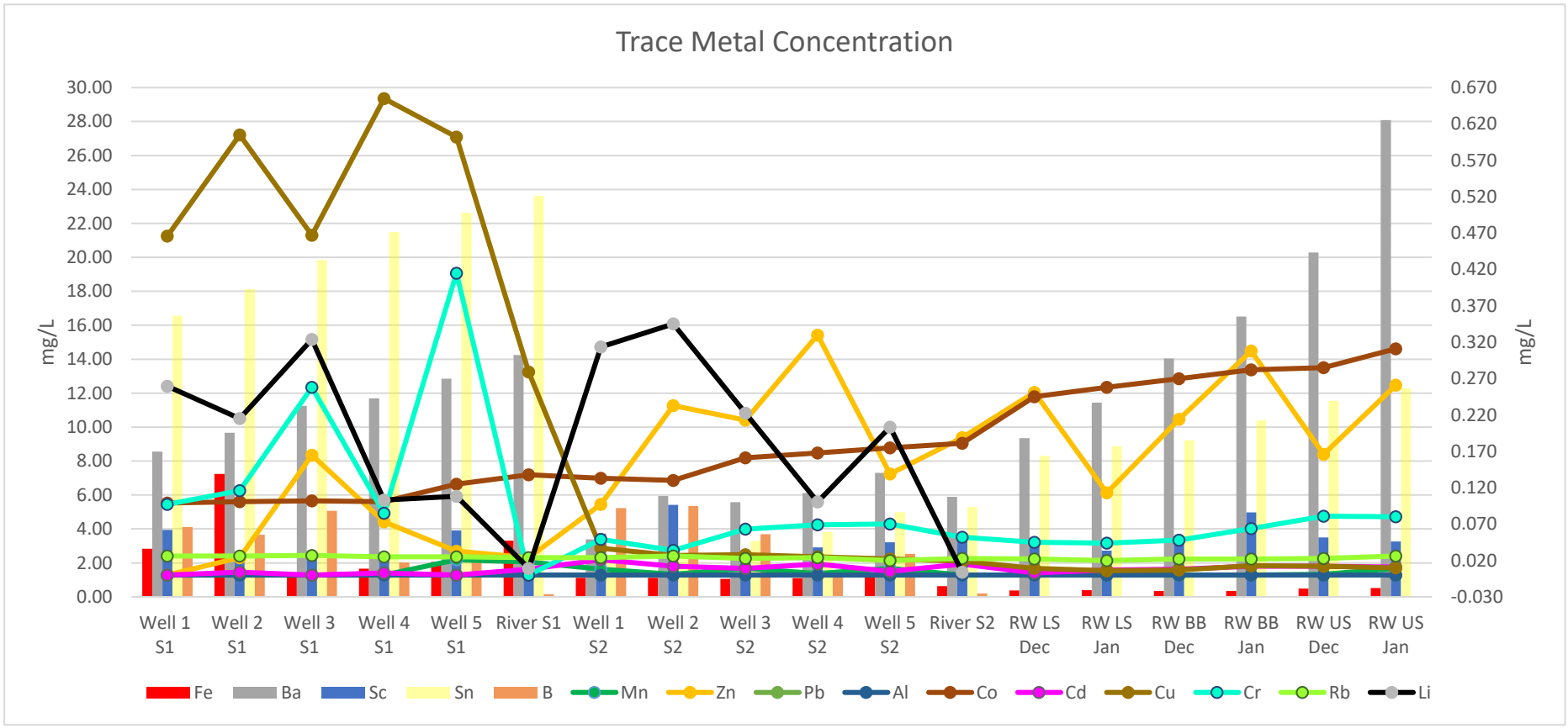

Figure 5. 2 The graph for trace metal concentration for saline groundwater, river and rainwater samples for MON and POM seasons. From left to right (Iron, Barium, Scandium, Tin, Boron, Manganese, Zinc, Lead, Aluminium, Cobalt, Cadmium, Copper, Chromium, Rubidium and Lithium).

5.2 Discussion

5.2.1 Water Physico-chemical Interpretation

From the initial physical parameter measurement for saline groundwater made from 11th December 2018 to 24th January 2019, a significant increase was observed especially for TDS, EC, and salinity for all the wells. This due to the change from MON season to POM season, with various recharge resulting in the increase in EC, TDS, and salinity values. The significant increase in EC and salinity in the groundwater was perhaps due to the seasonal change with dilution effect from the recharge in the region. Large variation of TDS and EC values were majorly attributed to geochemical processes such as ion exchange, evaporation, mineral dissolution and rainwater infiltration (Ehya and Marbouti, 2016; Aghazadeh et al., 2017). The physical parameter values in Table 5.1 and 5.2 show an increasing to decreasing concentration in TDS, EC and salinity values with a trend along the topography gradient from downstream to upstream: well 1 (913 m) > well 2 (913 m) > well 3 (914 m) > well 5 (948 m) > well 4 (967 m).

The less amount of rainfall in the POM season resulted in water level falling and perhaps the groundwater has a higher dissolved fraction that is diluted when there is more recharge in the MON season. This explains that the amount of recharge during the MON season compared to POM that shows a high contrast in the ionic variation in rainwater. The pH values for rainwater were found to increase slightly towards the end of January 2019. Tripathy et al. (2019) stated that higher pH values in rainwater are due to a higher concentration of alkaline species that result in basic rainwater. In a natural atmosphere, the rainwater pH values are approximately 5.6 due to the dissolution of atmospheric CO_2 in rain droplets. Hence, in this study area (Figure 5.1), on the upstream in December 2018, the pH value was less than 5.6, therefore classified as acidic rain (Al-Obaidy and Joshi, 2004; Oliveira et al., 2012). Naturally, rainwater is slightly acidic because of the reaction with carbon dioxide in the atmosphere, thus making the rainwater slightly acidic according to the following reaction:

$$H_2O + CO_2 = H_2CO_3 \text{ (Carbonic Acid)} \quad (32)$$

The carbonic acid in the water could be broken down based on the following reaction which produces bicarbonate and hydrogen ions:

$$H_2CO_3 \leftrightarrow HCO_3^- + H^+ \quad (33)$$

$$HCO_3^- \leftrightarrow H^+ + CO_3^{2-} \quad (34)$$

5.2.2 Saline Groundwater Chemistry

Cl^- is the dominant anion in all saline groundwater samples for both seasons. Notice that the high concentration increased in the POM season, indicating intense supply source into the aquifer system. Chloride may be present in the inclusion of connate brine, leached deposits, or evaporites sedimentary rock (Beaty, 2002; Sarikhani et al., 2015). When porous rocks are submerged in the sea after their formation, they become impregnated with soluble salts. Fine-grained marine shale might retain some of this chloride for very long periods of time and the chloride ions could be expected to be held back in interstitial or pore water in clay and shale while the water itself is transmitted. In all these rock types, chloride is mostly present as sodium chloride or solution of sodium and chloride ions (Hem, 1985). Therefore, in residual brines, chloride would be in high concentration due to chloride characteristically retained in solution through most of the processes.

Na^+ is the dominant cation in all saline groundwater samples for both seasons (Table 5.1 and 5.2). The source of sodium that is readily available in a solution of water is the evaporates such as halite (NaCl) and mirabilite ($Na_2SO_4.10H_2O$) (Hem, 1989; Dillon and Simmers, 1989). Moreover, sodium is a commonly encountered cation in water, where it was found that there is a significant increase in concentration during the POM season which was probably due to mineral dissolution or ion exchange processes (Shamsuddin et al., 2019). However, potassium ion is substantially larger than sodium ion and is expected to absorb less strongly than sodium (Hem, 1989). A slight increase in potassium concentration was observed in the POM season for all the saline water samples.

The significant increase of bicarbonate in the POM season suggested that the groundwater system is open to soil CO_2, resulting from the decay of organic matter and root respiration, which in turn, combines with rainwater to form HCO_3^-. The higher concentration of HCO_3^- in the water is supposedly to indicate the dominance of carbonate mineral dissolution or oxidation of organic carbon (Rao et al., 2012; Liu et al., 2013). In some cases, a high concentration of bicarbonate over 1,000 mg/L occurs in water with a low level of calcium and magnesium and especially where redox reaction processes occur, such as sulphate reduction (Hem, 1989). However, the concentration of CO_3^- is absent or below the detection limit (BDL) in both seasons. This indicates that HCO_3^- can consume protons or produce protons depending upon the variation of pH value (Devaraj et al., 2018). The following equation explains the reactions:

$$HCO_3^- \rightarrow H^+ + CO_3^- \quad (35)$$

$$HCO_3^- + H^+ \rightarrow H_2CO_3 \quad (36)$$

The cations Ca^{2+} and Mg^{2+} often come from carbonate minerals released in groundwater from carbonate minerals dissolution and enhanced by respiration of CO_2 from oxic and anoxic organic matter degradation (Halim et al., 2010). There is also CO_2 in rainwater which can enhance carbonate mineral dissolution, resulting in high Ca^{2+}, Mg^{2+} and HCO_3^- concentration present in groundwater (Oliveira et al., 2012; Gautam et al., 2017). The following equation explains the oxidation reaction of organic matter that produces CO_2 followed by dolomite and calcite dissolution reaction:

$$CH_2O \text{ (organic matter)} + O_2 \rightarrow H_2O + CO_2 \quad (37)$$

$$CaMg(CO_3)_2 + CO_2 + H_2O \rightarrow Mg^{2+} + 2HCO_3^- + CaCO_3 \text{ (Dolomite dissolution)} \quad (38)$$

$$CaCO_3 + CO^2 + H_2O \rightarrow Ca^{2+} + 2HCO_3^- \text{ (Calcite dissolution)} \quad (39)$$

The SO_4^{2-} that was present in all saline groundwater samples exhibited low concentration and was below detection limits in both seasons. This probability is caused by sulphate reduction process involving micro-bacterial action that consumes sulphate present in

groundwater as they run of out nutrients (Machel, 1989; Miao et al., 2012). Under reducing low-oxygen conditions, sulfide (S^{-2}) may be the dominant species of sulfur in groundwater, influenced by anaerobic bacteria (Halim et al., 2010). In general, some brines associated with petroleum may contain significant dissolved H_2S and the process of sulfate reduction requires the presence of bacteria and organic matter. Furthermore, sulphate reduction is a typical reaction in some saltwater/ freshwater mixing (Martinez and Bocanegra, 2002). The reaction may be explained as:

$$SO_4^{2-} + CH_4 = HS^- + HCO_3^- + H_2O \quad (40)$$

This results in hydrogen to be consumed and bicarbonate to be released and subsequently, increases the pH value. However, a decrease in sulphate concentration can be potentially caused by other factors such as precipitation of sulfate-bearing mineral (gypsum and anhydrite) or dilution processes (Karamouz et al., 2020). In near to alkaline solution or pH 7 in reducing environments, the sulphate species is most likely to form as undissociated H_2S or HS^-, in which the ion sulfur requires a very high pH (Miao et al., 2012). Based on Hem (1989), groundwater that is low in sulphate is presumably due to sulphate reduction or brine that may be associated with hydrocarbon/ petroleum.

5.2.3 Hydrogeochemical Facies and Classification

The hydrochemical facies are used to describe the bodies of groundwater in an aquifer that differ in their chemical composition. The facies are the purpose of the lithology, solution and flow patterns of the aquifer (Aghazadeh et al., 2011; Barzegar et al., 2018). One of the common and recommended diagrams is the Piper diagram (Piper, 1944) which provides a convenient method to classify and compare water types based on the ionic composition of different water samples (Kumar et al., 2009; Aghazadeh et al., 2011). Classification methods are used for basic characterization of the chemical composition of groundwater by differentiating the chemical type of water and helping in identifying the dominant types.

5.2.3.1 Piper Diagram

Hydrochemical classification and interpretation are mostly based on the calculation of ratios of major ions, with a classification of water type, according to the Piper plot (Piper, 1944) which was designed to delineate the variability to understand groundwater flow and geochemistry (Okiongbo and Douglas, 2015; Dinka, 2017). Piper diagram consists of cations and anions triangles that occupy the position at lower left and lower right, respectively, with bases aligned vertically, with vertices pointing towards each other. The points plotted in the central diamond-shape field may have areas proportionate to total concentrations and are located by extending the points in the anion and cation triangles to the point of intersection. The Piper diagram (Figure 5.3) shows that the chemical composition of the saline groundwater was classified as Na^{+}-Cl^{-} water type in both seasons including well 1 (2017). The river sample is classified as mixed Ca^{2+}-Mg^{2+}-Cl^{-} water type in MON season, while in the POM season, the river sample was classified as Na^{+}-Cl^{-} type. Possibly due to the fact of a large amount of heavy rainfall during the MON season, the river exhibited discharge zone characterized as Na^{+}-Cl^{-} endmember water type. Na^{+}-Cl^{-} facies generally indicate the characteristic of discharge zone, ion exchange process or the residence time of water in rock matrix (Sami, 1991; Devaraj et al., 2018; Mossad et al., 2019). Meanwhile, the rainwater sample is classified as mixed water type of Ca^{2+}-HCO_3^{-} which showed the interaction of atmospheric composition.

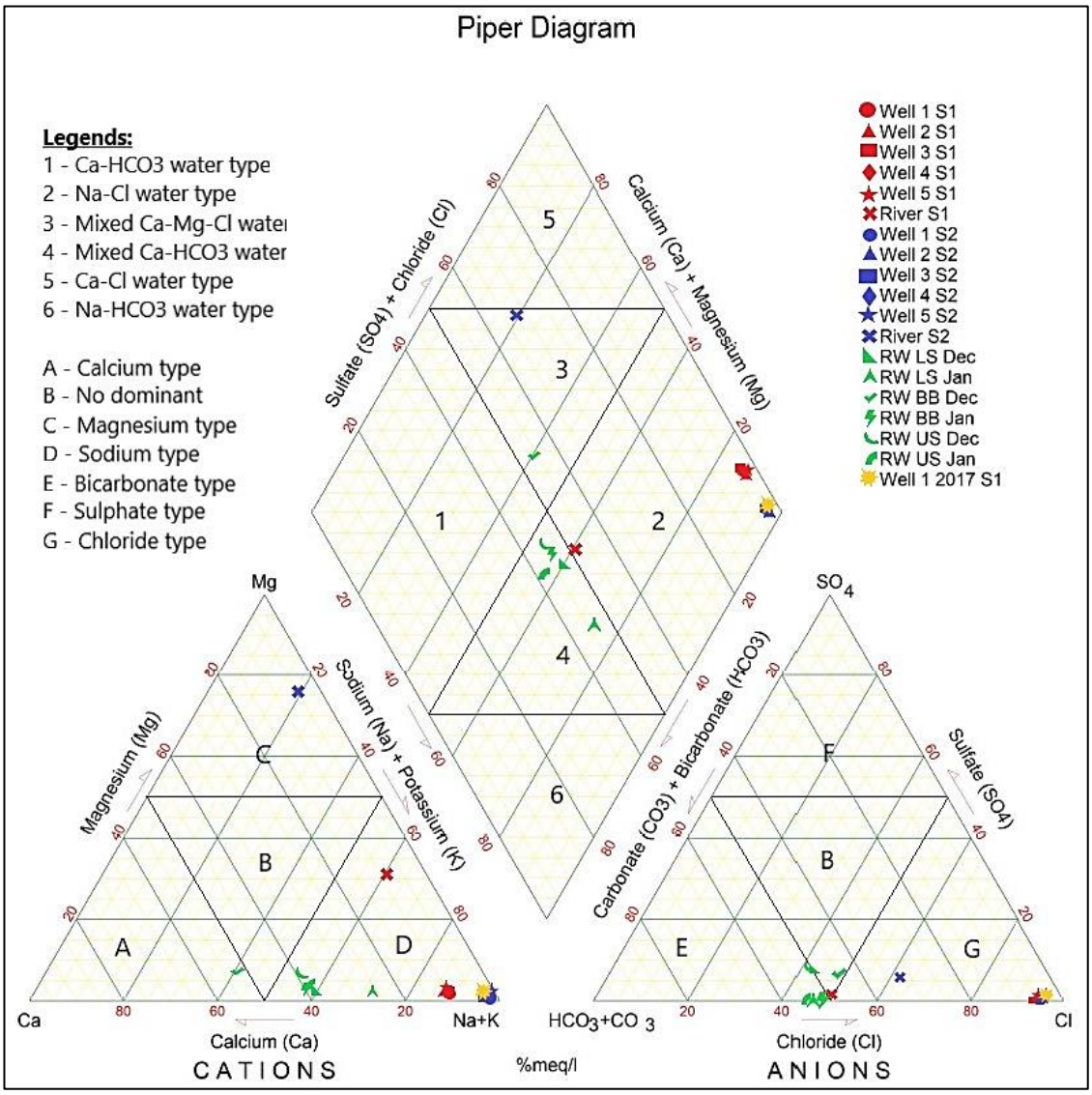

Figure 5. 3 Piper diagram for saline groundwater and river sample.

5.2.3.2 Durov Diagram

Other classification diagrams could be used to aid or compare the results from the Piper diagram such as the Durov diagram. Durov diagram is a useful graphical representation of hydrochemical data by determining the hydrochemical facies of groundwater that reflect the effect of hydrochemical processes and types of ion exchange relative to pH and TDS (Durov, 1948; Mossad et al., 2019). Compared to the Piper diagram, Durov diagram is more advantageous as it exhibits possible geochemical processes that could probably affect the

water origin, such as mixing of different water-type, ion exchange and reverse ion exchange (Durov, 1948; Llyod and Heathcote, 1985). Based on Durov diagram in Figure 5.4, the trend of all the groundwater samples can be classified as Na^+ and Cl^- as dominant anion and cation, which indicates that ion exchange is the dominant process in groundwater, meanwhile river water and rainwater samples data plot indicate mixing processes (Llyod and Heathcote, 1985; Mossad et al. 2019).

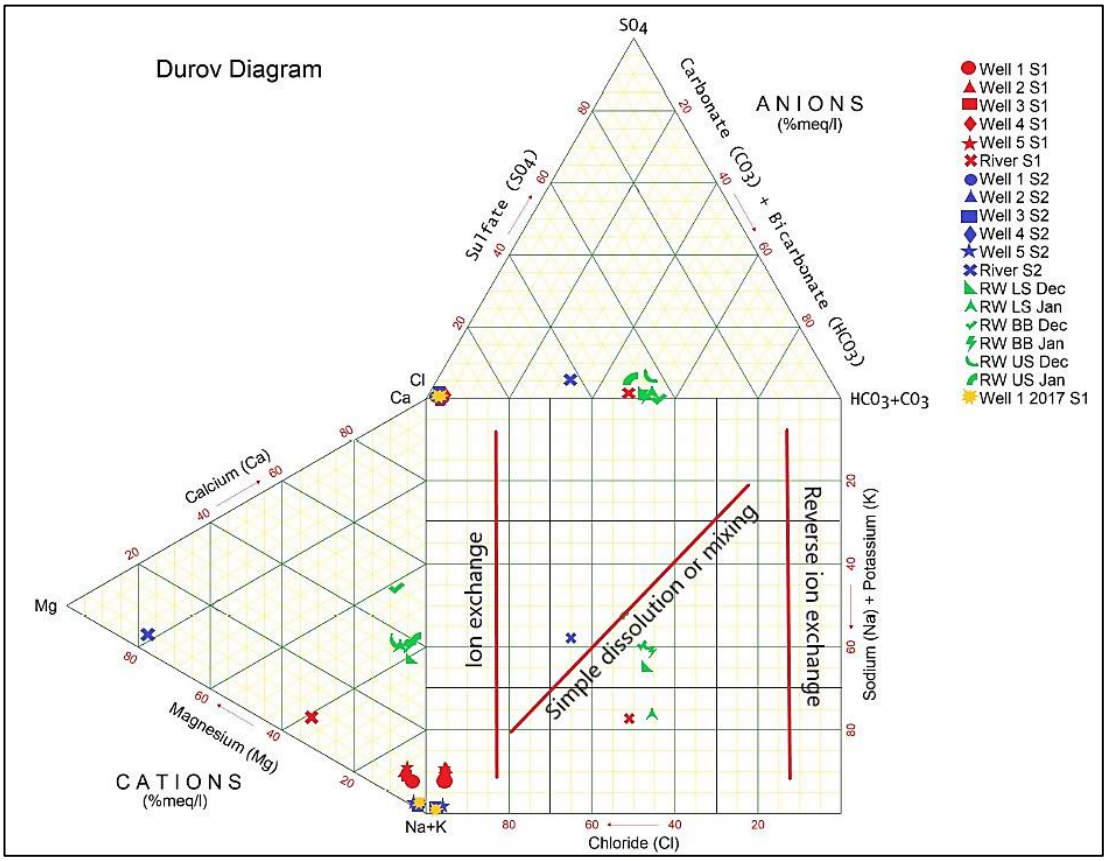

Figure 5. 4 Durov diagram classification for groundwater and river samples.

5.2.3.3 Van Wirdum's Diagram

Van Wirdum's diagram provides a different approach to the impact of water-rock interaction on groundwater mineralization and salinization source origins (Isawi et al., 2016). Van Wirdum's diagram relating to the ionic ratio (IR) is plotted against the electrical

conductivity (EC) or total dissolved solids (TDS), where IR (in %) = (Ca^{2+}/ (Ca^{2+} + Cl^{-}) with concentration expressed in meq/L. The EC can be seen as a measurement of the salinity, and IR as a measure of the prevalence of calcium among the cations and chloride among the anions (Van Wirdum, 1980). This prevalence is a result of geochemical processes that occurred within the aquifer system. Based on the position in the diagram (Figure 5.5), the groundwater can be classified as atmospheric (At = rainwater), lithotrophic (Li = calcium-rich freshwater), thalassotrophic (Th = seawater) or mixing water in between. The water samples were distributed among the two references water type from the hydrological cycle. All the saline groundwater was situated in the seawater type (Th), meanwhile collected rainwater samples were located in atmospheric water (At) and river samples were placed in mixing water in between, which matched with the inferences made by Piper and Durov diagrams.

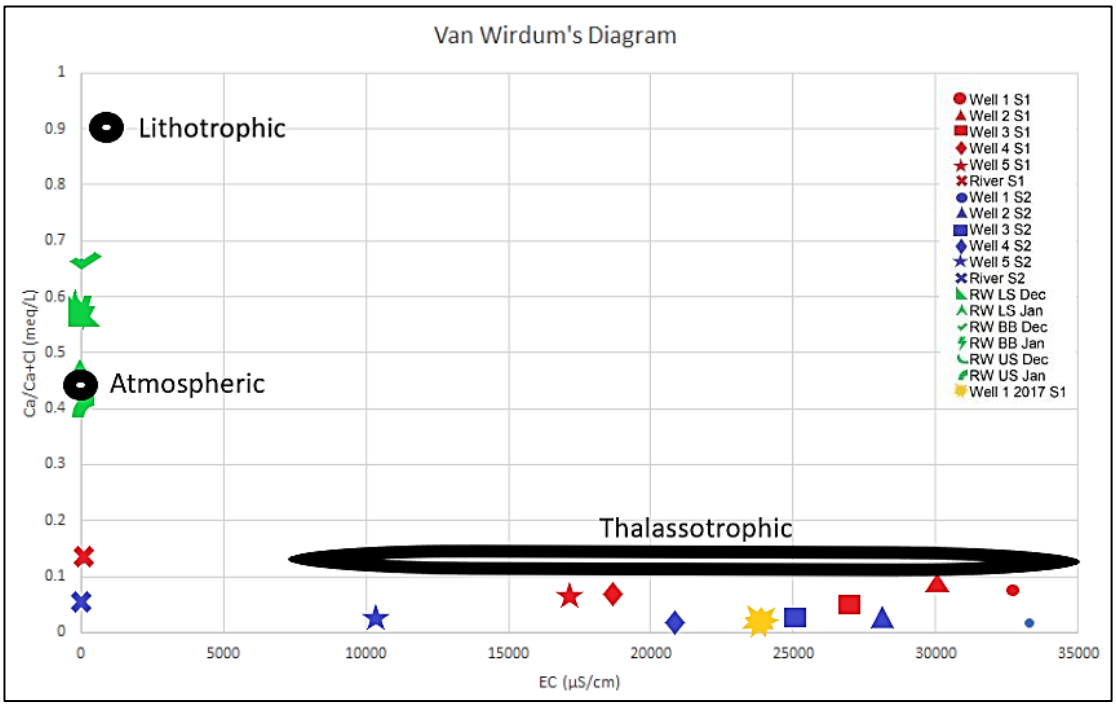

Figure 5. 5 Van Wirdum's diagram for saline groundwater, river water and rainwater samples.

5.3 Geochemistry of Ba'kelalan Saline Groundwater during the MON Season

In order to understand the geochemical processes occurring in the groundwater, correlation coefficient, hierarchical cluster and factor analysis were carried out. The correlation coefficients are summarized in Table 5.5 and Table 5.6, for MON and POM season, respectively. The green marker highlights the moderate and strong positive correlation, while the red marker highlights the moderate and strong negative correlation. In MON season's (Table 5.5) correlation coefficient, the pH strongly correlates with NO_3^- (r = 0.96), NO_2 (r = 0.96), Zn (r = 0.97) and moderately correlates with Rb (r = 0.64), B (r = 0.52) and Li (r = 0.51) for MON season. This illustrates that the pH variation affects the nitrate and nitrite present in the groundwater or involving nitrification processes while slightly affecting the mobility of trace metal Rb, B and Li (Hantzsche and Finnemore, 1992). There is a significant correlation between TDS, EC and salinity with HCO_3^- (r = 0.88), Na (r= 0.97), Cl^- (r = 0.98), B (r = 0.81), Li (r = 0.81) and Rb (r = 0.7) while being moderately correlated with PO_4 (r = 0.68), P (r = 0.70) and Ca (r = 0.66). The strong correlation between these ions indicates (Na^+, Cl^-, HCO_3^-) that they were most likely to be derived from the same source and were a major contribution for salinization in the groundwater (Rusydi et al., 2018). The major ions showed significant to moderate correlation between one another, for instances Na-Cl^-, Na-Mg, Na-Ca, Na-K, Na-HCO_3^-, r = 0.68, 0.92, 0.94, 0.89, 0.83, respectively. Additionally, trace metal such as B, Li, Rb and Cu showed a significant correlation with the major ions. The temperature showed strong correlation with Mn (r = 0.97), Co (r = 0.97), Cr (r = 0.81), Sn (r = 0.79) and Ba (r = 0.78). This could indicate that the mobility of these trace metals is highly regulated by the temperature as well. The SO_4 showed a strong correlation with NH_4 (r = 0.84), NH_3 (r = 0.84), NH_3N (r = 0.85) and Fe (r = 0.97) while being moderately correlated with Cd (r = 0.83), Ca (r = 0.74) and Mg (r = 0.63). Furthermore, the moderate correlation coefficient of phosphate and phosphorus with TDS and HCO_3 may indicate the possibility of source contribution from leaching into groundwater via rainfall-runoff although phosphate is not as soluble compared to other nutrients such nitrate and ammonia. Nevertheless, it gets absorbed into soil material and infiltrates into the groundwater system through soil erosion (Mateo-Sagasta et al. 2017). Inorganic phosphorus in groundwater generally occurs as orthophosphate and carries a

negative charge, therefore, a moderate correlation coefficient with electrical conductivity (EC) is observed. Besides, clays and iron oxide minerals are accountable for the adsorption of orthophosphate in the soil subsurface (Domagalski and Johnson, 2011). The samples nutrients, for instance phosphate and phosphorus, showed moderate correlation with Na, Ca, Mg and HCO_3, r = 0.71, 0.74, 0.77 and 0.71, correspondingly. Furthermore, the moderate correlation between PO_4, P and Cl and Ca were possibly sourced from apatite as a group of phosphate minerals containing calcium and chloride ($Ca_{10}(PO_4)_6(Cl)_2$) (Rajmohan and Elango, 2005; Mateo-Sagasta et al., 2017). Meanwhile, trace metal (B, Rb, Li) and nutrient element (P and PO_4) correlated significantly with the groundwater's TDS, EC and salinity. For nitrate and nitrite, the correlation coefficient showed significant to moderate relationship with pH (r = 0.74) and trace metals for instance, Zn (r = 0.90), Rb (r = 0.72), B (r = 0.63 and Li (r = 0.65). Organic nitrogen can be easily converted to the ammonium ion through the process of ammonification, subsequently oxidized to nitrate by nitrification (Ehya and Marbouti, 2016). For turbidity, there was a strong correlation with Fe (r = 0.92), SO_4 (r = 0.87) and nutrients such as NH_3 (r = 0.90), NH_3N (r = 0.89) and NH_4 (r = 0.90). Moreover, ammonium, ammonia and nitrogen showed strong correlation with turbidity (r = 0.90), subsequently, indicating moderate relationship with few major ions, Na (r = 0.78), K (r = 0.74), Ca (r = 0.65) and Mg (r = 0.67).

The results of the Hierarchical Cluster Analysis (HCA) are displayed as a dendrogram, from which related chemical groups can be identified (Figure 5.6). The water geochemical variables were divided and classified by HCA into four clusters for MON (S1) and POM (S2) season, respectively, according to their dominant geochemical composition and processes. The MON cluster 1 comprised of the nutrient's element (NO_2^- and NO_3^-) and trace metal Zn, which appeared to correlate with the pH of the groundwater, where most probably pH controlled the nitrification processes and released Zn into the water. Cluster 2 is dominated by various trace metals such as Ba, Cd, Co, Cr, Sc, Mn and Sn and showed a correlation with groundwater temperature, indicating that the mobility and concentration of these trace metals were controlled by the temperature. Cluster 3 consisted of groundwater turbidity, Fe, SO_4^{-2}, K^+, Cu,

Cd and nitrogen species (NH_4, NH_3 and NH_3N) and showed that the cluster was controlled by the physical parameter of turbidity, indicating that the groundwater cloudy display was defined by the iron, copper and sulphate content in the water while the nitrogen species was affected by the degree of turbidity of the water (Oyem et al., 2017). Cluster 4 can be divided into two subgroups (C4-a and C4-b), with C4-a comprising of Ca^{2+}, Mg^{2+}, PO_4^{-3}, P and HCO_3^- while C4-b comprising of the groundwater salinization parameter (TDS, EC, salinity) which was defined by the Na^+ and Cl^- concentration in the groundwater and trace metal (B, Li and Rb). This indicates that the presence of trace metals and mobility were influenced and controlled by the salinity and EC of the groundwater.

The results of Principal Component Analysis (PCA) are presented in Table 5.7. For the factor loadings, a high loading is defined as greater than 0.75, moderate loading as 0.50 – 0.75 and loading with less than 0.50 is considered as insignificant (Ibrahim et al., 2019). Principal component analysis for the MON season showed that four factors (PC1, PC2, PC3 and PC4) explained 43.5, 34.8, 14.3 and 7.3 % for the variance, respectively. The PC1 has the highest factor loadings for most major ions (Na^+, Cl^- and HCO_3^-), nutrients (PO_4^{-3} and P) and the physical parameters, indicating that TDS, EC and salinity were mainly controlled by these elements and most likely to be derived from the same source. PC1 has high factor loading for Na^+, Cl^-, TDS and EC, suggesting the most important role of these two ions (Na^+ and Cl^-) in the salinization or mineralization process. Trace metal of rubidium, boron and lithium showed that it has the highest loading among other trace metal, possibly indicating that the occurrences were from a common source such as clays or shale (Lavrushin et al., 2003; Han et al., 2018). Besides, the level of salinity of the groundwater influenced the concentration and mobility of these trace metals. Meanwhile, the high negative loadings of temperature, potassium and trace metal such as manganese, barium, cobalt, cadmium and tin, indicated that temperature plays a significant role and is controlled upon the presence of trace metal (Singh et al., 2014). From the factor score in which sample contributes more, well 1 was shown to be contributing the most (+). Furthermore, PC2's highest factor (well 1) loading showed nutrient ions (PO_4^{-3} and P), K^+, Ca^{2+}, Mg^{2+} and HCO_3^- and trace metal (Sc). This may indicate that P and PO_4 were

associated with scandium which may be due to leaching or dissolution from common source rocks such as shale or mudstone. On the other hand, PC3 was less defined, which explains the 9% of the variability of data for well 2 while the highest loading showed the turbidity, the nutrients (NH_4, NH_3, NH_3N and SO_4^{-2}), Ca^{2+}, Fe, Cd and Cu, indicating that the association of iron, copper and cadmium was probably dependent on the availability of nutrients' present in the groundwater and commonly, found in chalcopyrite in an oxygen-poor environment (Samantara et al., 2017). The turbidity of the groundwater samples plays an essential role in controlling most of the nutrients ions especially sulphate and is associated with iron. Organic matter, iron (Fe^2) and pyrite (FeS_2) are important substitution donors for nitrate reduction (Tesoriero et al., 2000; Appelo and Postma, 2005). In PC4, the result for well 5 has the lowest variance, and the temperature indicated the role in controlling the mobility of trace metal (Mn, Sc, Co and Cr) in the groundwater (Samantara et al., 2017).

Table 5. 5 The correlation coefficient for saline groundwater sample in MON season

		pH	Temp	TDS	EC	Salinity	Turbidity	SO4	PO4	P	NO3	NO2	NH4	NH3	NH3N	Na	K	Ca	Mg	Cl	HCO3	Mn	Fe	Ba	Zn	Sc	Co	Cd	Cu	Cr	Rb	Sn	B	Li
Correlation	pH	1.000																															
	Temp	-.150	1.000																														
	TDS	-.071	-.809	1.000																													
	EC	-.061	-.808	1.000																													
	Salinity	-.075	-.799	1.000	1.000	1.000																											
	Turbidity	-.506	-.118	.185	.181	.184	1.000																										
	SO4	-.370	-.295	.402	.401	.402	.963	1.000																									
	PO4	-.716	-.456	.684	.677	.686	.232	.274	1.000																								
	P	-.704	-.463	.700	.692	.702	.230	.278	1.000	1.000																							
	NO3	.966	-.316	.180	.189	.177	-.424	-.233	-.550	-.533	1.000																						
	NO2	.966	-.315	.179	.189	.176	-.423	-.232	-.551	-.534	1.000	1.000																					
	NH4	-.613	.130	-.097	-.101	-.097	.949	.831	.147	.138	-.604	-.603	1.000																				
	NH3	-.612	.129	-.097	-.102	-.098	.949	.831	.147	.137	-.603	-.602	1.000	1.000																			
	NH3N	-.622	.122	-.089	-.093	-.089	.950	.832	.160	.151	-.610	-.610	1.000	1.000	1.000																		
	Na	-.015	-.899	.973	.973	.970	.286	.497	.607	.620	.222	.222	-.002	-.002	.005	1.000																	
	K	-.724	.426	-.538	-.546	-.540	.471	.222	.116	.094	-.857	-.857	.710	.710	.712	-.485	1.000																
	Ca	-.727	-.474	.660	.654	.660	.711	.745	.842	.842	-.548	-.548	.593	.593	.603	.669	.262	1.000															
	Mg	-.846	-.090	.485	.479	.492	.637	.634	.800	.800	-.687	-.688	.585	.584	.593	.411	.326	.898	1.000														
	Cl	.049	-.867	.987	.987	.985	.199	.428	.580	.596	.292	.291	-.099	-.099	-.092	.991	-.582	.604	.378	1.000													
	HCO3	-.483	-.549	.889	.886	.893	.272	.410	.906	.916	-.248	-.249	.081	.080	.092	.802	-.220	.825	.790	.807	1.000												
	Mn	-.151	.970	-.650	-.648	-.638	-.119	-.250	-.368	-.370	-.265	-.265	.081	.080	.073	-.777	.276	-.404	.022	-.724	-.384	1.000											
	Fe	-.524	-.298	.493	.491	.495	.937	.974	.466	.469	-.362	-.362	.806	.806	.810	.548	.241	.860	.789	.484	.576	-.226	1.000										
	Ba	.345	.789	-.937	-.933	-.936	-.223	-.375	-.877	-.885	.121	.122	-.006	-.006	-.018	-.909	.265	-.797	-.615	-.895	-.939	.673	-.506	1.000									
	Zn	.970	-.171	-.170	-.161	-.177	-.400	-.302	-.771	-.763	.904	.904	-.480	-.479	-.489	-.064	-.565	-.711	-.892	-.030	-.595	-.224	-.486	.408	1.000								
	Sc	-.339	.468	-.007	-.008	.006	-.441	-.459	.341	.344	-.318	-.318	-.358	-.359	-.355	-.236	-.065	-.049	.316	-.153	.303	.595	-.279	-.053	-.525	1.000							
	Co	-.078	.973	-.684	-.682	-.673	-.107	-.236	-.453	-.456	-.201	-.200	.088	.088	.080	-.796	.257	-.455	-.043	-.744	-.453	.995	-.235	.730	-.142	.522	1.000						
	Cd	-.396	-.281	.014	.009	.005	.834	.746	.139	.127	-.398	-.397	.839	.839	.841	.195	.611	.557	.313	.069	.020	-.401	.675	-.142	-.194	-.725	-.379	1.000					
	Cu	-.445	.452	-.668	-.673	-.672	.532	.295	-.223	-.243	-.606	-.606	.754	.755	.751	-.556	.922	.068	.085	-.655	-.480	.276	.227	.489	-.250	-.342	.297	.696	1.000				
	Cr	.324	.807	-.532	-.525	-.521	-.280	-.309	-.637	-.630	.238	.239	-.182	-.183	-.193	-.637	-.162	-.644	-.284	-.549	-.482	.871	-.351	.717	.217	.425	.900	-.580	-.029	1.000			
	Rb	.645	-.669	.704	.711	.703	-.131	.134	-.022	.000	.819	.819	-.427	-.427	-.428	.723	-.916	.009	-.181	.779	.335	-.535	.086	-.437	.544	-.252	-.504	-.245	-.793	-.101	1.000		
	Sn	.236	.799	-.977	-.974	-.976	-.182	-.365	-.816	-.828	-.002	-.001	.062	.063	.052	-.942	.393	-.741	-.568	-.942	-.937	.660	-.487	.989	.321	-.060	.710	-.059	.590	.638	-.553	1.000	
	B	.528	-.719	.804	.810	.803	-.152	.118	.150	.172	.726	.725	-.454	-.455	-.453	.797	-.910	.118	-.063	.855	.483	-.567	.111	-.574	.408	-.137	-.555	-.282	-.859	-.182	.983	-.680	1.000	
	Li	.510	-.699	.811	.817	.810	-.165	.105	.169	.191	.711	.711	-.466	-.466	-.464	.792	-.916	.122	-.041	.855	.503	-.539	.107	-.581	.380	-.091	-.530	-.314	-.877	-.161	.976	-.688	.999	1.000

5.4 Geochemistry of Ba'kelalan Saline Groundwater during the POM Season

In POM season (Table 5.6), the correlation coefficient for pH showed strong correlation with Ba (*r* = 0.88), Co (*r* = 0.92), Sn (*r* = 0.97) and Cr (*r* = 0.78), probably indicating that pH controls the trace metal mobility in the groundwater (Bourg and Loch, 1995). There is a strong correlation coefficient for TDS, EC and salinity with major ions, Na (r = 0.97), K (r = 0.92), Ca (r = 0.93), Mg (r = 0.97), Cl (r = 0.98), HCO_3 (r = 0.97), with trace metal such as B (r = 0.90), Cu (r = 0.86), Li (r = 0.87), Fe (r = 0.75), Mn (r = 0.51), and moderately corresponds with nutrient ions, P (r = 0.56), PO_4 (r = 0.57), NH_4 (r = 0.76), NH_3 (r= 0.74), NH_3N (r= 0.78). This correlation might indicate that the groundwater TDS, EC and salinity control the nutrients cycles, the major ions (Na^+, K^+, Ca^{2+}, Mg^{2+}, Cl^-, HCO_3) that made up the groundwater chemistry and is likely to be accounted for groundwater salinization (Na-Cl), dissolution or leaching processes. The turbidity of the groundwater showed a good correlation with nutrient ions, P (r = 0.88), PO_4 (r = 0.91), NO_2 (r = 0.89), NO_3 (r = 0.88) and was moderately correlated with Zn (r = 0.71), Cd (r = 0.61) and Rb (r = 0.55). The temperature showed a strong relation with trace metal, B (r = 0.97), Li (r = 0.97), major ions Ca (r = 0.93), Cl (r = 0.87), Na (r = 0.88), K (r = 0.70), Mg (r = 0.80), HCO_3 (r = 0.85) and nutrients NH_4 (r = 0.72), NH_3 (r = 0.74), NH_3N (r = 0.76) and SO_4 (r = 0.52). The sodium ions were highly correlated with other major ions (K, Ca, Cl, Mg, HCO_3) with the strongest correlation between Na-Cl (r = 0.99), Na-HCO_3 (r = 0.99), Na-Mg (r = 0.97), Na-Ca (r = 0.92), Na-K (r = 0.73) and few trace metals B (r = 0.90), Cu (r = 0.89), Li (r = 0.81), Cd (r = 0.74) and Rb (r = 0.66). The major ions (Na, K, Ca, Cl, Mg, HCO_3) showed a significant correlation with the nutrients (NH_4, NH_3 and NH_3N).

The POM cluster 1 (Figure 5.6) consisted of turbidity, the nutrients species (NO_3^-, NO_2^-, PO_4^{-3} and P) and trace metal (Zn and Rb). This indicated that the groundwater turbidity is defined and controlled by the composition and mobility of the nutrients (NO_3^-, NO_2^-, PO_4 and P) and trace metal (Zn and Rb). Cluster 2 was dominated by pH and trace metal (Co, Cr, Sn, Ba, Fe and Mn), showing that the groundwater pH controlled the mobility and presence of the trace metal in the groundwater. Cluster 3 can be divided into two subgroups (C3-a and C3-b),

with C3-a comprising of temperature, Ca^{2+}, B and Li, while C3-b consisted of EC, TDS, salinity, Na^{+}, Cl^{-}, Mg^{2+}, HCO_3^{-} and Cu. This suggests temperature as the main control of the trace metal's (B, Li and Cu) mobility and presence in the groundwater. The high TDS, EC and salinity may influence the mobility or attributes of trace metals such as boron, lithium, copper, manganese, iron and is similar to PC1's result (Acosta et al., 2011). The groundwater (TDS, EC and salinity) indicated that the major ion Na, Cl, Mg and HCO_3 were responsible for the high salinity in the groundwater. Cluster 4 was composed of SO_4^{-2}, K^{+}, NH_3, NH_3N, NH_4 and trace metal (Sc and Cd), indicating that SO_4^{-2} and K^{+} were controlling the mobility of scandium concentration in the groundwater. Moreover, the nutrients species (NH_3, NH_3N, NH_4) controlled the mobility of cadmium in the groundwater.

Principal component analysis for the POM season showed that four factors (PC1, PC2, PC3 and PC4) explained the 60.9, 22.01, 11.56 and 5.49 % of the variance respectively (Table 5.7). PC1 showed the highest positive loading with 60.9 % of variability for the physical parameters (TDS, EC, salinity and temperature), major ions (Na^{+}, Cl^{-}, Ca^{2+}, Mg^{2+} and HCO_3^{-}), nutrient ions (NH_4, NH_3 and NH_3N) and trace metals (Cd, Cu, Rb, B and Li). The samples with high contribution to PC1 were from well 1, indicating a progression of mineralization towards the high salinization processes in groundwater, which is the Na^{+}-Cl^{-} water type. It has the highest positive loadings for most variables, especially Na^{+}, Cl^{-}, TDS and EC, which may indicate salinization by mineral dissolution. Besides, the high loading for Na^{+}, Mg^{2+} and Ca^{2+} indicated potential ion-exchange processes (Zaidi et al., 2015; Ibrahim et al., 2015). Furthermore, the temperature indicated the role of controlling the trace metal (Cd, Cu, Rb, B and Li) mobility and presence in the groundwater. The strong factor loading of cadmium, rubidium, copper, boron and lithium indicated possible common source such as clay, shale or sulfide mineral-like pyrite (Snyder, 2004; Tostevin et al., 2016). Whereas, pH showed high negative loading with Fe, Ba, Cr and Sn, indicating that the acidic pH has released these trace metals in groundwater. The PC2 result showed that the contribution in well 2 has a moderate factor loading of 22.1 % of the variance for the temperature, K^{+}, Ca^{2+}, nutrients species (SO_4^{-2}, NH_4, NH_3 and NH_3N) and trace metals (Sc, Rb, B and Li). Similarly, with PC1, temperature played

an essential role in the mobility and presence of trace metal metals (Sc, Rb, B and Li) in the groundwater. Whereas, the nutrients species were controlled by calcium and potassium in the groundwater. For PC3, the turbidity, nutrients species (PO_4^{-3}, P, NO_3^- and NO_2^-) and trace metal (Zn and Rb) suggested that the groundwater turbidity depends on the concentration of the nutrient species (PO_4^{-3}, P, NO_3^- and NO_2^-), zinc and rubidium. The PC4 results showed that the NH_3 and NH_3N species is related to the iron, indicating the reducing environment which controlled these elements in the groundwater.

Table 5. 6 The correlation coefficient for saline groundwater samples in the POM season

		pH	Temp	TDS	EC	Salinity	Turbidity	SO4	PO4	P	NO3	NO2	NH4	NH3	NH3N	Na	K	Ca	Mg	Cl	HCO3	Mn	Fe	Ba	Zn	Sc	Co	Cd	Cu	Cr	Rb	Sn	B	Li
Correlation	pH	1.000																																
	Temp	-.810	1.000																															
	TDS	-.976	.667	1.000																														
	EC	-.945	.793	.898	1.000																													
	Salinity	-.967	.883	.902	.941	1.000																												
	Turbidity	-.108	-.375	.298	-.125	-.039	1.000																											
	SO4	-.353	.521	.295	.174	.261	-.042	1.000																										
	PO4	-.414	.005	.556	.133	.266	.913	.301	1.000																									
	P	-.410	-.086	.579	.184	.206	.888	.287	.943	1.000																								
	NO3	.347	-.686	-.166	-.563	-.470	.890	-.122	.695	.656	1.000																							
	NO2	.362	-.689	-.183	-.579	-.484	.881	-.110	.687	.647	1.000	1.000																						
	NH4	-.792	.727	.763	.581	.804	.321	.476	.635	.451	-.012	-.018	1.000																					
	NH3	-.752	.740	.709	.542	.784	.271	.481	.588	.382	-.037	-.042	.996	1.000																				
	NH3N	-.728	.763	.668	.529	.780	.203	.472	.523	.303	-.088	-.093	.985	.996	1.000																			
	Na	-.979	.881	.926	.910	.990	.046	.368	.373	.307	-.387	-.399	.864	.841	.831	1.000																		
	K	-.706	.704	.674	.475	.641	.235	.839	.609	.511	-.033	-.032	.871	.862	.842	.740	1.000																	
	Ca	-.924	.930	.837	.907	.910	-.207	.557	.162	.175	-.593	-.601	.692	.671	.666	.922	.738	1.000																
	Mg	-1.000	.802	.977	.953	.965	.103	.333	.402	.406	-.354	-.369	.775	.734	.709	.975	.686	.921	1.000															
	Cl	-.991	.872	.941	.942	.990	.024	.353	.345	.308	-.418	-.431	.818	.790	.777	.996	.709	.937	.989	1.000														
	HCO3	-.957	.852	.911	.863	.977	.118	.336	.434	.333	-.306	-.319	.909	.890	.880	.992	.747	.870	.951	.978	1.000													
	Mn	.106	.050	-.199	.199	.057	-.666	-.677	-.803	-.759	-.640	-.648	-.436	-.416	-.368	-.086	-.671	-.057	-.085	-.051	-.124	1.000												
	Fe	.646	-.118	-.776	-.615	-.459	-.506	-.080	-.567	-.761	-.147	-.129	-.273	-.184	-.110	-.486	-.299	-.455	-.658	-.538	-.448	.239	1.000											
	Ba	.880	-.596	-.888	-.867	-.899	-.228	.107	-.387	-.342	.210	.232	-.695	-.656	-.635	-.871	-.392	-.670	-.885	-.876	-.883	-.137	.598	1.000										
	Zn	.302	-.641	-.122	-.468	-.522	.710	.190	.580	.708	.812	.816	-.206	-.252	-.319	-.420	.044	-.410	-.304	-.412	-.409	-.723	-.364	.393	1.000									
	Sc	-.444	.685	.351	.233	.441	-.035	.901	.338	.189	-.150	-.139	.727	.754	.763	.534	.911	.598	.420	.488	.543	-.599	.098	-.089	-.080	1.000								
	Co	.925	-.892	-.866	-.796	-.904	-.060	-.634	-.442	-.372	.324	.331	-.895	-.879	-.866	-.951	-.903	-.934	-.914	-.939	-.939	.322	.424	.691	.270	-.751	1.000							
	Cd	-.730	.378	.796	.575	.716	.612	-.037	.734	.613	.240	.222	.810	.774	.739	.740	.506	.438	.726	.714	.801	-.245	-.539	-.875	-.070	.201	-.627	1.000						
	Cu	-.890	.668	.874	.891	.930	.129	-.079	.310	.254	-.305	-.325	.705	.673	.661	.895	.405	.714	.895	.900	.903	.188	-.533	-.994	-.484	.133	-.718	.837	1.000					
	Cr	.787	-.858	-.711	-.643	-.745	.041	-.838	-.369	-.317	.338	.337	-.795	-.788	-.780	-.814	-.948	-.893	-.772	-.802	-.788	.444	.303	.435	.165	-.880	.950	-.389	-.472	1.000				
	Rb	-.724	.425	.795	.505	.557	.550	.663	.816	.844	.222	.216	.720	.668	.608	.661	.860	.634	.714	.660	.657	-.737	-.709	-.472	.385	.600	-.779	.606	.434	-.773	1.000			
	Sn	.975	-.737	-.980	-.869	-.895	-.247	-.476	-.559	-.572	.197	.209	-.807	-.760	-.722	-.937	-.794	-.894	-.972	-.947	-.916	.308	.715	.801	.098	-.516	.934	-.725	-.797	.832	-.858	1.000		
	B	-.871	.978	.752	.860	.896	-.320	.566	.062	.035	-.668	-.673	.694	.689	.699	.901	.727	.985	.866	.907	.855	-.001	-.294	-.617	-.524	.652	-.919	.377	.677	-.893	.535	-.821	1.000	
	Li	-.754	.979	.607	.736	.801	-.430	.649	-.033	-.089	-.704	-.704	.652	.665	.687	.811	.731	.931	.745	.808	.766	-.022	-.107	-.458	-.553	.743	-.872	.234	.532	-.898	.451	-.706	.977	1.000

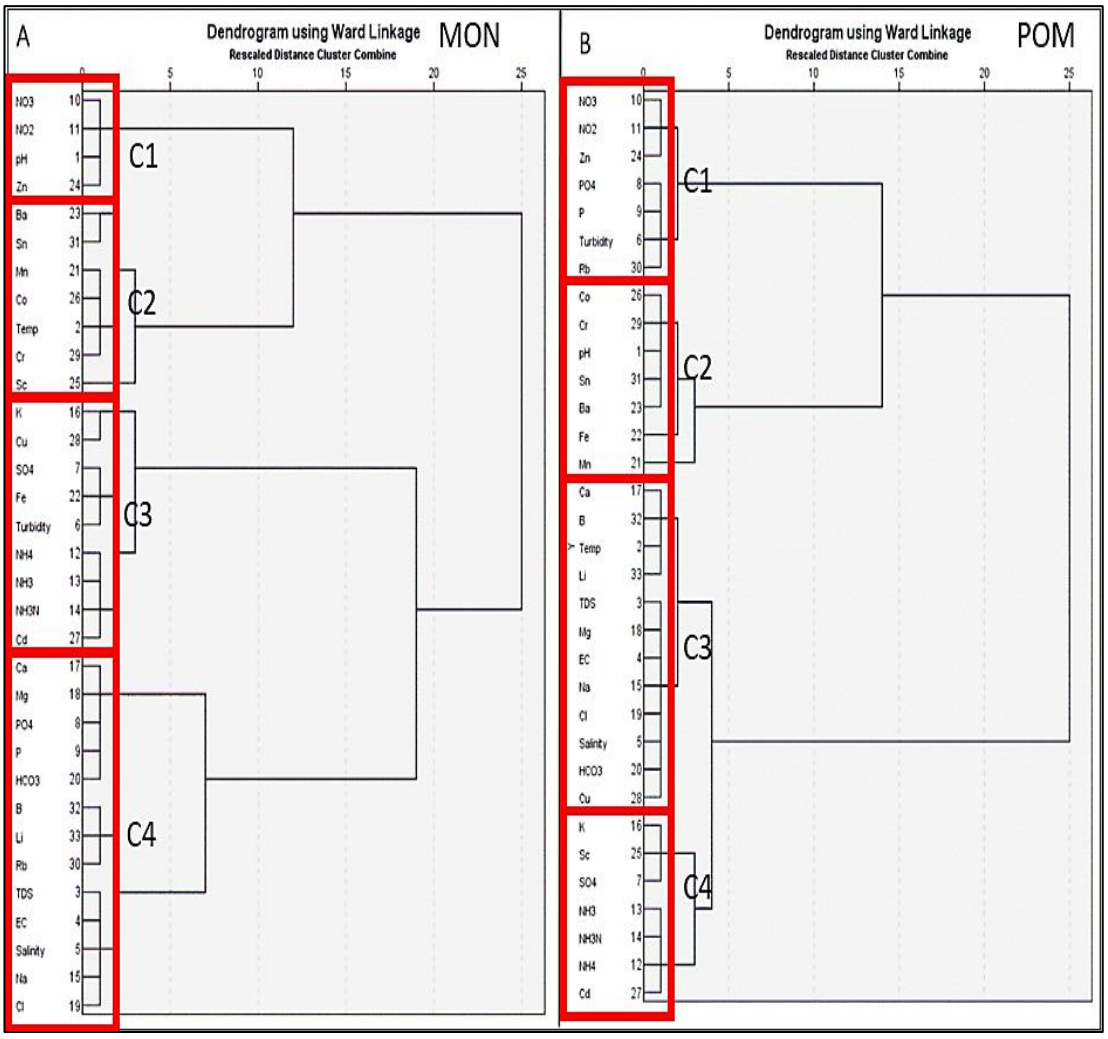

Figure 5. 6 (A) The Dendrogram for the MON season showing the division into four clusters. (B) The Dendrogram for the POM season showing the division into four clusters.

Table 5. 7 The rotated component matrix and factor score for saline groundwater during MON and POM seasons

MON Rotated Component Matrix					**POM Rotated Component Matrix**			
	Component				**Component**			
	1	**2**	**3**	**4**	**1**	**2**	**3**	**4**
pH	.098	-.924	-.369	-.001	-.938	-.345	-.004	.021
Temperature	-.691	.101	-.031	.715	.655	.583	-.441	.190
TDS	.961	.155	.058	-.223	.941	.262	.195	-.087
EC	.963	.146	.057	-.217	.945	.163	-.242	-.146

Salinity	.963	.160	.057	-.207	.927	.293	-.167	.164
Turbidity	.093	.166	.980	-.056	.151	-.102	.979	.093
SO_4	.339	.063	.937	-.053	.010	.986	.073	-.149
PO_4	.521	.816	.035	-.248	.346	.255	.894	.127
P	.541	.806	.033	-.238	.358	.192	.891	-.203
NO_3	.350	-.882	-.316	.008	-.309	-.169	.927	.130
NO_2	.350	-.882	-.315	.009	-.330	-.156	.922	.132
NH_4	-.204	.266	.942	-.012	.658	.531	.237	.479
NH_3	-.205	.265	.942	-.013	.610	.550	.188	.539
NH_3N	-.198	.277	.940	-.019	.585	.552	.119	.582
Na	.908	.042	.178	-.378	.903	.393	-.067	.160
K	-.705	.530	.449	-.141	.442	.850	.247	.147
Ca	.497	.616	.560	-.245	.778	.560	-.263	-.114
Mg	.390	.760	.493	.165	.946	.323	-.003	-.038
Cl	.952	.011	.094	-.291	.923	.367	-.087	.078
HCO_3	.814	.569	.101	-.057	.889	.372	-.003	.266
Mn	-.496	.129	-.047	.857	.123	-.632	-.765	-.001
Fe	.414	.264	.871	-.016	-.690	.044	-.459	.557
Ba	-.814	-.438	-.054	.377	-.976	.094	-.055	-.188
Zn	-.044	-.954	-.251	-.158	-.361	.071	.828	-.422
Sc	.074	.582	-.521	.621	.129	.953	.017	.275
Co	-.519	.036	-.018	.854	-.748	-.653	-.003	-.116
Cd	-.173	.083	.823	-.535	.792	-.019	.464	.397
Cu	-.786	.166	.582	-.125	.974	-.054	-.045	.217
Cr	-.287	-.321	-.154	.890	-.527	-.849	.036	-.013
Rb	.814	-.564	-.119	-.075	.545	.599	.557	-.184
Sn	-.890	-.339	-.027	.304	-.872	-.447	-.174	.095
B	.892	-.406	-.176	-.094	.711	.595	-.375	-.002

Li	.903	-.379	-.193	-.060	.551	.696	-.457	.060
Eigen values	14.37	11.49	4.72	2.41	20.10	7.26	3.817	1.81
% of Variance	43.54	34.82	14.32	7.30	60.92	22.01	11.56	5.49

	MON				**POM**			
Factors	**1**	**2**	**3**	**4**	**1**	**2**	**3**	**4**
Well 1	0.96	1.18	-0.92	-0.19	1.43	-0.30	-0.25	1.01
Well 2	0.61	0.11	1.68	-0.09	0.02	1.76	0.13	-0.27
Well 3	0.58	-1.59	-0.58	0.02	0.33	-0.66	-0.46	-1.57
Well 4	-1.26	0.07	-0.10	-1.27	-0.50	-0.54	1.62	0.16
Well 5	-0.89	0.23	-0.08	1.53	-1.27	-0.26	-1.04	0.66

CHAPTER 6. Hydrogeochemical Processes

6.1 Introduction

The major ion chemistry of groundwater is a powerful tool in determining solute sources and for describing groundwater evolution that is generally controlled by natural and anthropogenic factors. Natural processes include water-rock-soil interaction, precipitation, evaporation/ crystallization, oxidation or reduction reaction, groundwater flow and velocity, and local hydrology (Redwan et al., 2016; Barzegar et al., 2018; Ibrahim et al., 2019). Analysis of the hydrogeochemical processes and mechanism occurring in the study area was conducted for evaluation purposes and it was suggested that different conventional graphical plot on the hydrochemical data should be used (Kumar et al., 2009). The variation of geochemical data can be implicit by plotting ionic concentration (Guler et al., 2002; Okiongbo, 2015; Barzegar et al., 2018). The results from the cation concentration and ratios are used to identify the geochemical processes and mechanism input that may affect the groundwater quality (Barzegar et al., 2018). For instance, the key processes that increase groundwater salinity depend on reaction with host rocks (water-rock interaction) which are restrained by the network of the flow path and the time each path spends in contact with various minerals and mixing with connate water at depth (Marandi and Shand, 2018).

During water-rock interaction, different chemical processes and chemical constituent changes could occur in the groundwater derived from dissolution/ precipitation, oxidation/ reduction and ion exchange (Redwan et al., 2016; Mossad et al., 2019). In the process, minerals present from different rock types may partially or completely be dissolved when in contact with water, corresponding to different resistance of chemical weathering (Table 6.1). Generally, silicate rocks are less soluble compared to these common rocks that are most soluble, including halite (NaCl), sylvite (KCl), gypsum ($CaSO_4$), dolomite ($CaMgCO_3$) and limestone or calcite ($CaCO_3$), as they provide the principal source for major ions such Na^+, Ca^{2+}, Mg^{2+}, Cl^-, K^+, CO_3 and SO_4^{2-} (Hem, 1989). Weathering of parent rocks in one of the major mechanisms controls the concentration of the chemical constituent in the groundwater and helps researchers to understand the weathering processes of rocks that control the

groundwater chemistry (Liu et al., 2016). Groundwater is classified into different types according to the percentage of chemical constituents present due to different types of rock-water interaction (Figure 6.1). For instance, dissolution of calcite, dolomite, gypsum and halite give rise to Ca^{2+}-HCO_3^-, Ca^{2+}-Mg^{2+}-HCO_3^-, Ca^{2+}-SO_4^{2-} and Na^+-Cl^- type of groundwater, respectively (Kloppmann et al., 2001). Furthermore, due to cation exchange process, Na^+-HCO_3^-, Ca^{2+}-Cl^- and Na^+-SO_4^{2-} water types may form according to cation exchange capacity of the matrix and this is a vice versa reaction (Zaidi et al., 2018). Moreover, sulphate reduction may also occur and give rise to Na^+-Cl^-, Ca^{2+}-Cl^-, Ca^{2+}-HCO_3^- and Na^+-HCO_3^- type of groundwater (Elango and Kannan, 2007). The chemical analysis and composition of groundwater can serve as evidence and can be used to identify the water-rock interaction and chemical processes (Jalali and Khanlari, 2008; Redwan et al., 2016). Marandi et al. (2019) stated that along the groundwater flow path with increasing time, the groundwater tends to change from HCO_3^--type to Cl^--type water with increasing salinity, which is often associated by a change in the dominant cation from Ca^{2+} to Na^+ (Figure 6.1). The chemical composition of the analysed groundwater samples is characterized by the predominance of Na^+ and Cl^-, which generally represent more than 85 to 96 equivalent.mol% of the cation and anions in Table 6.2 and the ionic ratio shown in Table 6.3.

Table 6. 1 Common minerals and chemical processes during water-rock interaction. Adapted from Elango and Kannan, (2007)

Mineral	Chemical formula	Relative resistance	Chemical weathering processes
Halite	$NaCl$	Very low	Dissolution
Gypsum	$CaSO_4.2H_2O$	Very low	Dissolution
Pyrite	FeS_2	Low	Dissolution and oxidation
Calcite	$CaCO_3$	Low	Dissolution
Dolomite	$CaMg(CO_3)_2$	Low	Dissolution
Plagioclase	$CaAl_2Si_2O_8$	Moderate	Hydrolysis

K-feldspar	$KAlSi_3O_8$	Moderately high	Hydrolysis
Quartz	SiO_2	Very high	Dissolves very slowly
Clays	Al silicates	Very high	Hydrolysis

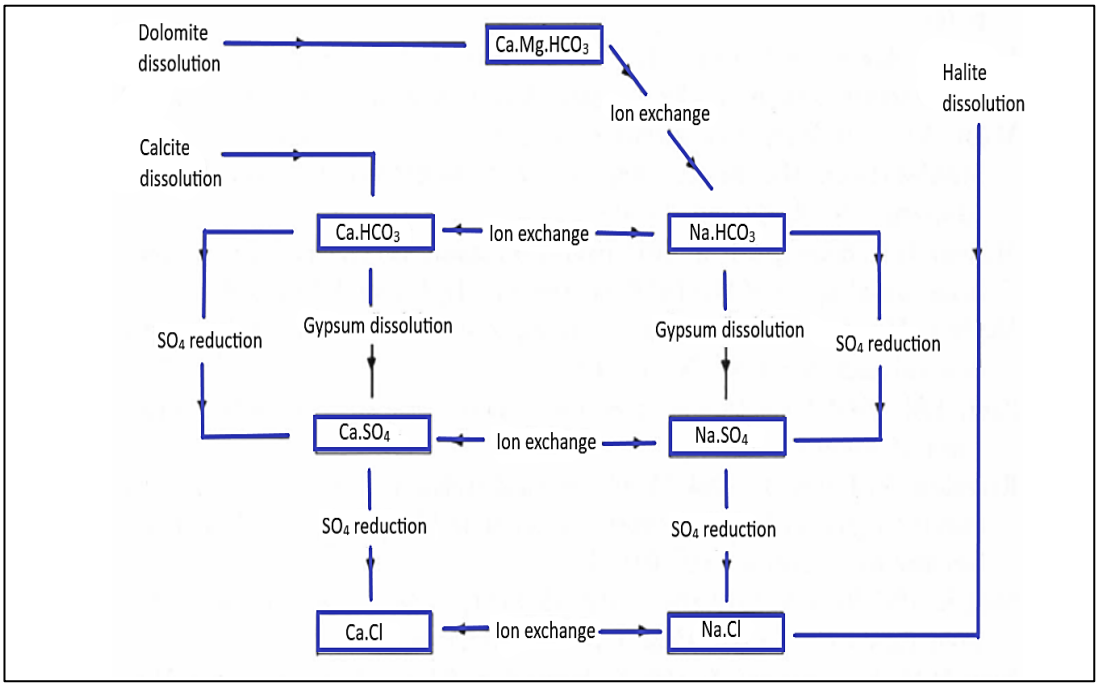

Figure 6. 1 The water-rock interaction, resultant groundwater chemical composition and water type. Adapted from Elango and Kannan, (2007); Boschetti et al. (2011); Esmaeli et al. (2018).

Table 6. 2 Molar percentages of major cation and anions (Seawater value adapted from Drever, 1988)

Sample	Cation (equivalent.mol%)				Anion (equivalent.mol%)		
	Na	K	Ca	Mg	Cl	SO_4	HCO_3^-
Well 1 S1	86.8	0.2	8.3	4.6	93.8	0.08	5.8
Well 2 S1	85.2	0.2	9.3	4.9	94.5	0.08	5.2
Well 3 S1	89.9	0.1	7.7	2.1	95.2	0.08	4.2
Well 4 S1	88.4	0.3	7.4	3.2	95.5	0.08	4.4
Well 5 S1	88.1	0.3	7.0	4.6	94.8	0.08	4.8

Well 1 S2	96.2	0.1	1.8	1.7	96.2	0.02	3.7
Well 2 S2	95.9	0.1	2.2	1.8	96.0	0.02	3.8
Well 3 S2	95.9	0.1	2.1	1.8	95.9	0.02	3.9
Well 4 S2	95.7	0.1	1.9	1.9	94.9	0.02	4.9
Well 5 S2	95.7	0.1	2.4	1.6	94.7	0.02	5.1
Seawater	77.4	1.69	3.39	17.55	90.2	9.34	0.39

Table 6. 3 The ionic ratio from major ions (Seawater value adapted from Drever, 1988)

Sample	Ratio (meq/L)/(meq/L)									
	Na^+/Cl^-	K^+/Na^+	Ca^{2+}/Mg^{2+}	K^+/Cl^-	SO_4^{2-}/Cl^-	Ca^{2+}/Cl^-	Ca^{2+}/HCO_3^-	Ca^{2+}/Na^+	Mg^{2+}/Cl^-	Cl^-/HCO_3^-
Well 1 S1	0.85	0.002	1.8	0.002	0.000043	0.08	1.3	0.10	0.05	16
Well 2 S1	0.87	0.003	1.8	0.003	0.00018	0.09	1.7	0.11	0.05	18.2
Well 3 S1	0.85	0.001	3.6	0.001	0.000045	0.07	1.6	0.09	0.02	22.3
Well 4 S1	0.87	0.004	2.3	0.004	0.000052	0.07	1.5	0.08	0.03	21.5
Well 5 S1	0.84	0.004	1.5	0.004	0.000054	0.07	1.3	0.08	0.04	19.4
Well 1 S2	0.86	0.001	1	0.001	0.000014	0.02	0.4	0.02	0.02	25.6
Well 2 S2	0.86	0.001	1.2	0.001	0.000034	0.02	0.5	0.02	0.02	24.7
Well 3 S2	0.88	0.001	1.1	0.001	0.000020	0.02	0.4	0.02	0.02	24.4
Well 4 S2	0.89	0.002	1	0.002	0.000026	0.02	0.3	0.02	0.02	19.3
Well 5 S2	0.90	0.002	1.4	0.002	0.000031	0.02	0.4	0.03	0.02	18.2
Seawater	0.86	0.03	0.18	0.01	0.1	0.04	8.7	0.04	0.2	231.1

6.2 Results

6.2.1 Gibbs diagram and Evaporation

The recommended diagram (Gibbs diagram) was used to differentiate the influence of water-rock interaction, evaporation and precipitation on water chemistry by using TDS against the ratio of $Na^+ + K^+/ (Na^+ + Ca^{2+})$ and $Cl^-/ (Cl^- + HCO_3^-)$ scatter diagram (Gibbs, 1970). Figure

6.2a shows the river water and rainwater samples fell on precipitation dominance, meanwhile, all saline groundwater sample fell on evaporation dominance. Additionally, the Mg^{2+}/Na^{+} versus Mg^{2+}/Ca^{2+} ratios can also be used to determine whether the groundwater quality is influenced by evaporation, rock interaction or human activities (Li et al., 2019; Liu et al., 2019). Zhu et al. (2011) stated that the use of Mg^{2+}/Ca^{2+} and Mg^{2+}/Na^{+} are to determine the process of evaporation (low Mg^{2+}/Ca^{2+} and Mg^{2+}/Na^{+}), rock interaction (low Mg^{2+}/Ca^{2+} and high Mg^{2+}/Na^{+}) and precipitation (high Mg^{2+}/Ca^{2+} and Mg^{2+}/Na^{+}). In Figure 6.2c, the groundwater data shows low Mg^{2+}/Na^{+} (0.02) ratio and the relatively moderate Mg^{2+}/Ca^{2+} (0.9) ratio indicates that the groundwater was governed by dissolution of evaporite mineral, whereas river water samples that have high Mg^{2+}/Ca^{2+} (8.4) ratio and high Mg^{2+}/Ca^{2+} (17.6) ratio show that it is controlled by precipitation dominance (Li et al., 2019a; Liu et al., 2019).

Based on Fisher and Mullican (1997), the plot of Na^{+}/Cl^{-} versus EC could indicate the influence of evaporation on the overall groundwater chemistry. A plot in Figure 6.2d shows the Na^{+}/Cl^{-} ratio represented by a horizontal line on the Na^{+}/Cl^{-} versus EC plot indicates a constant Na^{+}/Cl^{-} ratio with increasing salinity (EC) (Kumar et al., 2009; Farid et al., 2015; Zaidi et al., 2015; Redwan, 2016; Mgbenu and Egbueri, 2019).

The plots between HCO_3^{-}/Na^{+} and Mg^{2+}/Na^{+} versus Ca^{2+}/Na^{+} are an effective tool used to determine the relationship and effect of weathering or dissolution of silicates and carbonates or evaporation in the groundwater (Halim et al., 2010; Monjerezi et al., 2011; Singh et al., 2017; Mallick et al., 2018). Figure 6.2e and Figure 6.2f show the most dominant process affecting the groundwater quality and refer to dissolution of evaporites as the major hydrochemical process for all the groundwater samples (Fakharian and Narany, 2016).

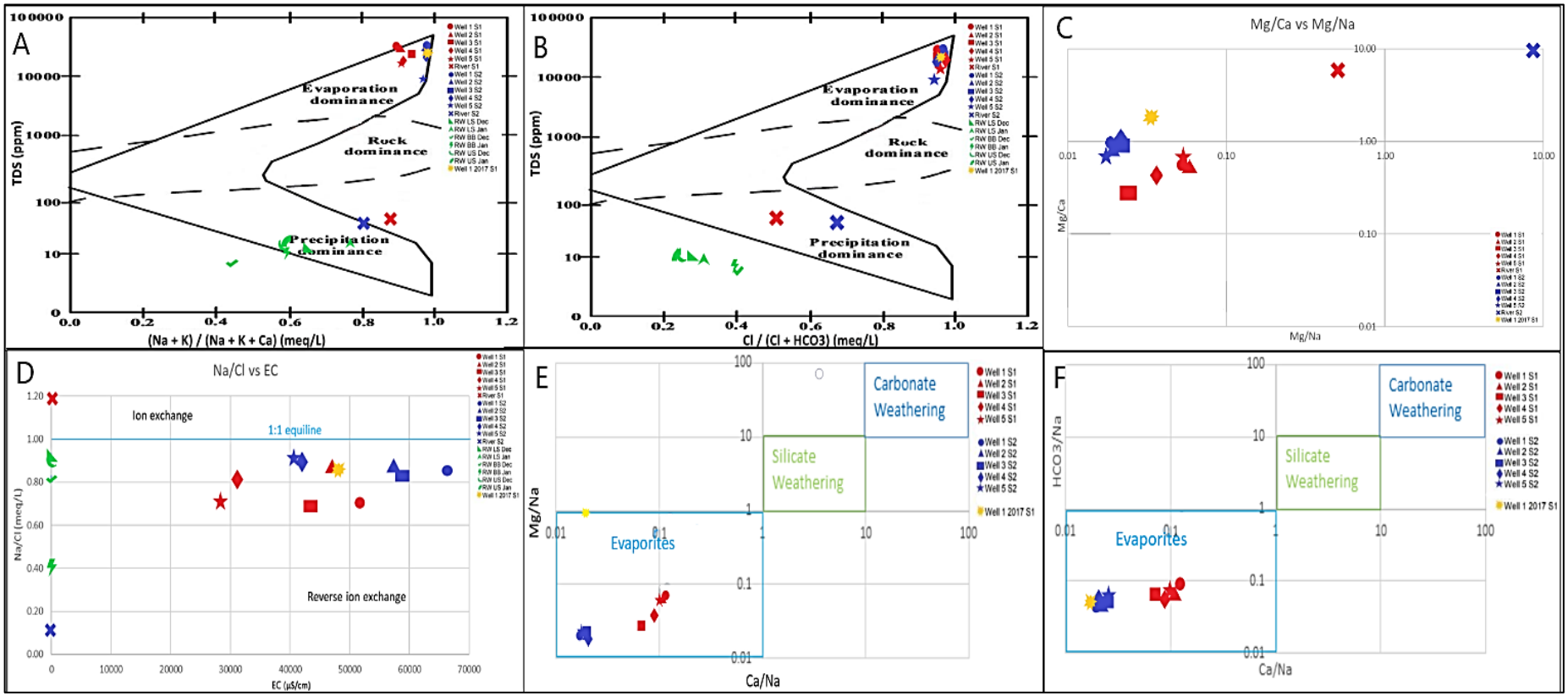

Figure 6. 2 (A and B) Gibbs diagram of the groundwater, river water and rainwater samples in the study area (Gibbs, 1970). (C) The plot ratio of Mg^{2+}/Na^{+} versus Mg^{2+}/Ca^{2+} (Li et al., 2019a; Liu et al., 2019). (D) The plot of Na^{+}/Cl^{-} versus EC (Mgbenu and Egbueri, 2019 (E) The plot of Mg^{2+}/Na^{+} versus Ca^{2+}/Na^{+} (Fakharian and Narany, 2016; Mallick et al., 2018). (F) The plot of HCO_3^{-}/Na^{+} versus Ca^{2+}/Na^{+} (Halim et al., 2010; Fakharian and Narany, 2016; Mallick et al., 2018).

6.2.2 Ion-exchange and Mineral Dissolution

Ion exchange is one of the most important processes responsible for the concentration of ions in groundwater. Ion exchange and sorption control the transport of pollutants in aquifers and soils (Appelo and Postma, 2005; Kumar et al., 2009; Ibrahim et al., 2019). If there is reverse ion exchange between Na^+ and K^+ in the groundwater with Mg^{2+} and Ca^{2+} attached to a solid surface, such as clay material, both of above indices would be positive and the concentration of Ca^{2+} and Mg^{2+} will increase in the groundwater. When ion-exchange occurs to Na^+ and K^+ attached to the aquifer material and Ca^{2+} and Mg^{2+} in the water, then these indices would be negative and the concentration of Na^+ or K^+ will increase in the groundwater (Schoeller, 1977; Zaidi et al., 2015; Ibrahim et al., 2019). The bar diagram of CAI 1 and CAI 2 for groundwater (Figure 6.3a) shows positive average value of 0.20 for both seasons. Whereas, the river samples have values ranging from -0.20 for MON and 0.50 for POM.

In Figure 6.3b, the plot of Na^+ versus Cl^- is used to create a distinction between the difference of geochemical mechanism for acquiring salinization processes (Vengosh, 2003; Zarei et al., 2013; Walter et al., 2018). Alternatively, according to many authors, it was stated that Na^+ versus Cl^- greater than 1 generally indicates that sodium ions were derived from silicate weathering or ion exchange process (Kumar et al., 2009; Zarei et al., 2013; Barzegar et al., 2018; Mgbenu and Egbueri, 2019). Whereas, Na^+ versus Cl^- ratio of 1:1 often indicates the dissolution of halite (Richter and Kreitler, 1993; Barzegar et al., 2018). The Na^+/Cl^- molar ratio of saline groundwater samples varied from 0.84 to 0.90 and its average value was 0.87, falling close and below to equiline 1:1. For well 1 (2017) sample, the Na^+/Cl^- ratio value was 0.86.

The plot of $Ca^{2+} + Mg^{2+}$ versus $SO_4^{2-} + HCO_3^-$ (Figure 6.3c) can be used to determine ion exchange and dissolution process in the groundwater samples, where data fall to 1:1 equiline indicates dissolution of calcite, dolomite and gypsum are the dominant reaction to supply Ca^{2+}, Mg^{2+}, SO_4^{2-} and HCO_3^- in the aquifer system (Aghazadeh et al., 2011; Fijani et al., 2017; Sefie et al., 2018; Ibrahim et al., 2019;). If ion exchange is the dominant process, the data tends to shift the points to the right due to an excess of $SO_4^{2-} + HCO_3^-$. If reverse ion exchange is the

process, the graph would shift to the left due to increase in the excess of Ca^{2+} + Mg^{2+} over SO_4^{2-}+ HCO_3^- (Fisher and Mullican, 1997; Kumar et al., 2009; Barzegar et al., 2018; Ibrahim et al., 2019). The plot of Ca^{2+} + Mg^{2+} versus SO_4^{2-} + HCO_3^- shows that all the saline groundwater samples for the MON fell above the 1:1 line, whereas, POM and well 1 (2017) samples fell close and below the 1:1 dissolution line of gypsum, calcite and dolomite (Rajmohan and Elango, 2004; Narany et al., 2014).

6.4 Discussion

6.4.1 Water-rock Interaction Processes

The plot of Mg^{2+}/Ca^{2+} versus Mg^{2+}/Na^+, HCO_3^-/Na^+ versus Ca^{2+}/Na^+ and Mg^{2+}/Na^+ versus Ca^{2+}/Na^+ shows the most dominant process affecting the groundwater quality and refers to the dissolution of evaporites as the major hydrochemical process for all the groundwater samples probably in deeper reservoir (Fakharian and Narany, 2016). Thus, the MON season samples show the influence of evaporite minerals with high rainfall, indicating water-rock interaction processes. Thus, the POM season showed a more intense evaporation processes compared to MON season where there is more dilution by rainwater.

Based on Gibbs diagram, it was suggested that the MON season samples showed less ionic concentration due to dilution by rainwater, whereas the POM and well 1 (2017) illustrated higher ionic concentration (evapo-concentrates) from monsoonal recharge in which the plot shifts to the upper right. This indicated the potential of dissolution of deposited evaporites in adjacent or underlying deeper aquifers (Haile, 1962). The groundwater is influenced by dissolution of evaporite minerals with presence of dilution due to infiltration of rainwater, whereby the processes might occur from deeper aquifer with the help of fault or fracture to passage of the saline groundwater to the surface wells or springs (Marandi et al., 2019). Meanwhile, the Na^+/Cl^- versus EC plot shows a horizontal trend in this which indicates that the dissolution of evaporites might be the major process in controlling the chemistry of the groundwater in the study area, whereas the Na^+/Cl^- ratio almost remained unchanged (Jankoswki and Acworth, 1997). Meanwhile, the dissolution of evaporite minerals such as

halite is in deeper confined aquifer and is channelled to the unconfined zone or spring (Haile, 1962).

If halite dissolution is the major attribution to Cl^- in the groundwater system, the increase in Cl^- concentration would correspond to an increase in TDS, salinity and all individual chemical constituents (Richter and Kreitler, 1993; Zaidi et al., 2015). Furthermore, the common halite dissolution brines have Na^+/Cl^- molar ratio = 1 as brines derived from halite dissolution in shallow fresh groundwater flow system revealed a similar ratio. If concentrations are high and not affected particularly by ion-exchange of calcium and magnesium for sodium on clay mineral surfaces and alteration of feldspar, this could affect the lower ratios (Kumar et al., 2009; Zarei et al., 2013; Gil-Marquez, 2017; Barzegar et al., 2018). However, deep-basin brines exhibited Na^+/Cl^- molar ratios lower than 0.95 due to the reaction of sodium with the aquifer rock material by ion exchange or albitization processes with a high concentration of magnesium, potassium and calcium (Richter and Kreitler, 1993). Compared with halite solution brine, the Na^+/Cl^- ratio for seawater was much lower = 0.86 (Richter and Kreitler, 1993; Ammar et al., 2020). The variation between the seasons was distinctive, whereas in the MON season, Na^+/Cl^- ratio was observed to have less ionic concentration due to more dilution compared to the POM season, indicating more ionic concentration due to the intense mineral dissolution during water-rock interaction. The variation of Na^+/Cl^- ratio less than 1 is an indicator of depletion of Na^+ ions and can be attributed to reverse ion exchange, leading to Na^+ adsorption on clay minerals and simultaneously releasing Ca^{2+} in groundwater (Mejri et al., 2018). Besides, a high concentration of Cl^- may originate from the dissolution of chloride-rich minerals such as halite or connate marine water entrapped in sediments (Vengosh, 2003; Edmund et al., 2003; Zaidi et al., 2015; Ammar et al., 2020). This suggests that the source of salt was likely to be dominated by the dissolution of halite and other geochemical processes that should be responsible for the deviation from the 1:1 dissolution line.

The positive value of diagram CAI 1 and CAI 2 for groundwater sample indicates a reverse ion exchange process for both seasons. Thus, the plot of $Ca^{2+} + Mg^{2+}$ versus $SO_4^{2-} + HCO_3^-$

shows that all the saline groundwater samples for the MON fell above the 1:1 line, indicating that excessive of Ca^{2+} and Mg^{2+} originated from other processes such as reverse ion exchange (Zaidi et al., 2015). Whereas, the POM and well 1 (2017) samples were scattered close and below the 1:1 dissolution line, indicating an excess of SO_4^{2-} + HCO_3^- that can be attributed to ion exchange process or dissolution of gypsum, calcite and dolomite (Rajmohan and Elango, 2004; Narany et al., 2014).

6.4.2 Saturation Index

Saturation index (SI) which evaluates the level of equilibrium between mineral and water is calculated by comparing the chemical activities of the dissolved ions on the minerals with their solubility (Mejri et al., 2018). The SI of carbonate minerals (anhydrite, aragonite, calcite, dolomite and magnesite), sulphate minerals (barite and gypsum) and halite were calculated using the PHREEQC and plot as a function of pH (Parkhurst and Appelo, 1999). Saturation or oversaturation in saline water could be explained by an increase of HCO_3^- concentration due to SO_4^{2-} reduction, Ca^{2+} release from cation exchange, as well as Mg^{2+} increase due to the incongruent dissolution of dolomite (Appelo and Postma, 2005; De Montety et al., 2008; Farid et al., 2015). The SI of minerals > 0 indicates an oversaturated condition with respect to respective minerals reaction (mineral precipitation). Where SI value < 0, this indicates the groundwater is undersaturated, resulting in mineral dissolution condition. When SI value equals to zero, this indicates that the groundwater is at an equilibrium state.

The SI versus HCO_3 in MON season showed that the carbonate minerals (aragonite, dolomite and calcite) were saturated to oversaturated irrespective of seasons, whereas, for the POM season, these minerals tend to form more saturated state probably due to less recharge and precipitation (Figure 6.4). The pH showed a slight increase in the saturation trend with increasing pH value for both MON and POM season (dolomite, aragonite and calcite), indicating that the minerals were precipitated in higher pH condition. Magnesite and barite were undersaturated and close to an equilibrium state (SI = 0) for both seasons, however, the SI of minerals for halite, anhydrite and gypsum were shown to be undersaturated. The SI for

halite dissolution showed a distinct difference between MON (-3 to -4) with more dissolution, while POM (-2 to -3) has comparatively less dissolution (Appendix I).

6.4.3 Potential Redox Reaction

A substantial amount of reaction is involved in groundwater, such as the transfer of electrons between dissolved and solid constituents, leading to electron loss in oxidation and electron gain in reduction (Elango and Kanna, 2007). The most significant oxidizing agents in groundwater are dissolved oxygen, and oxo-anions such as nitrate, sulfate and water (Farid et al., 2015). Meanwhile, the reducing agents include organic compounds and inorganic sulfides such as pyrite. The common constituents in soil and groundwater associated with the oxidation and reduction reactions are sulphate and iron (Edmunds et al., 2003), although the attempt of measuring redox potential and dissolved oxygen was not employed in this study and no reported data is available. Nevertheless, in this present study, NO_3, Ba, SO_4 and Fe may be used to define redox status in the aquifer (Edmunds et al., 2003). For instance, nitrate is stable in the presence of dissolved O_2 and may remain in groundwater for a very long time (Elango and Kannan, 2007). Once the redox reaction occurs, as O_2 has been consumed by the reaction of iron reduction or organic matter, subsequently, the next electron acceptor would be NO_3^-. This causes NO_3^- concentration to rapidly decrease in the aquifer, thus producing N_2 gas (Edmunds et al., 2003).

In the study area, the nitrite concentration decreased in the POM compared to the MON season, suggesting that nitrate has been consumed during the reduction processes that occurred in the groundwater system. In Figure 6.3d, the concentration of iron has reduced slightly during the POM season, indicating the possibility of a redox reaction in the groundwater system affecting the iron concentration. If the concentrations of sulphate and iron in groundwater are very low and Eh of the groundwater is in a reduced condition, thus, the ions might have been reduced due to reduction processes (Elango and Kannan, 2007). The abundance of sulphur in groundwater has significant implications to the redox and pH balance, since sulphur is intimately linked with the recycling of organic matter, such as sulfate-reducing

bacteria that respire sulphate in the absence of oxygen, and producing sulfide (Jorgensen, 1982; Tostevin et al., 2016). The low concentration of SO_4 (< 1 mg/L) and increase in Ba concentration in the groundwater can be explained with the solubility of barite (Farid et al., 2015; Bozau et al., 2015). Barite's solubility increases with depth and TDS content of the water due to the common ion effect as Ba's concentration decreases when sulphate from dissolution is released into water (Bozau et al., 2015). Groundwater under an anoxic condition in deep reservoirs is often associated with sulphate reduction, increase in Ba concentration or long groundwater residence time (Farid et al., 2015).

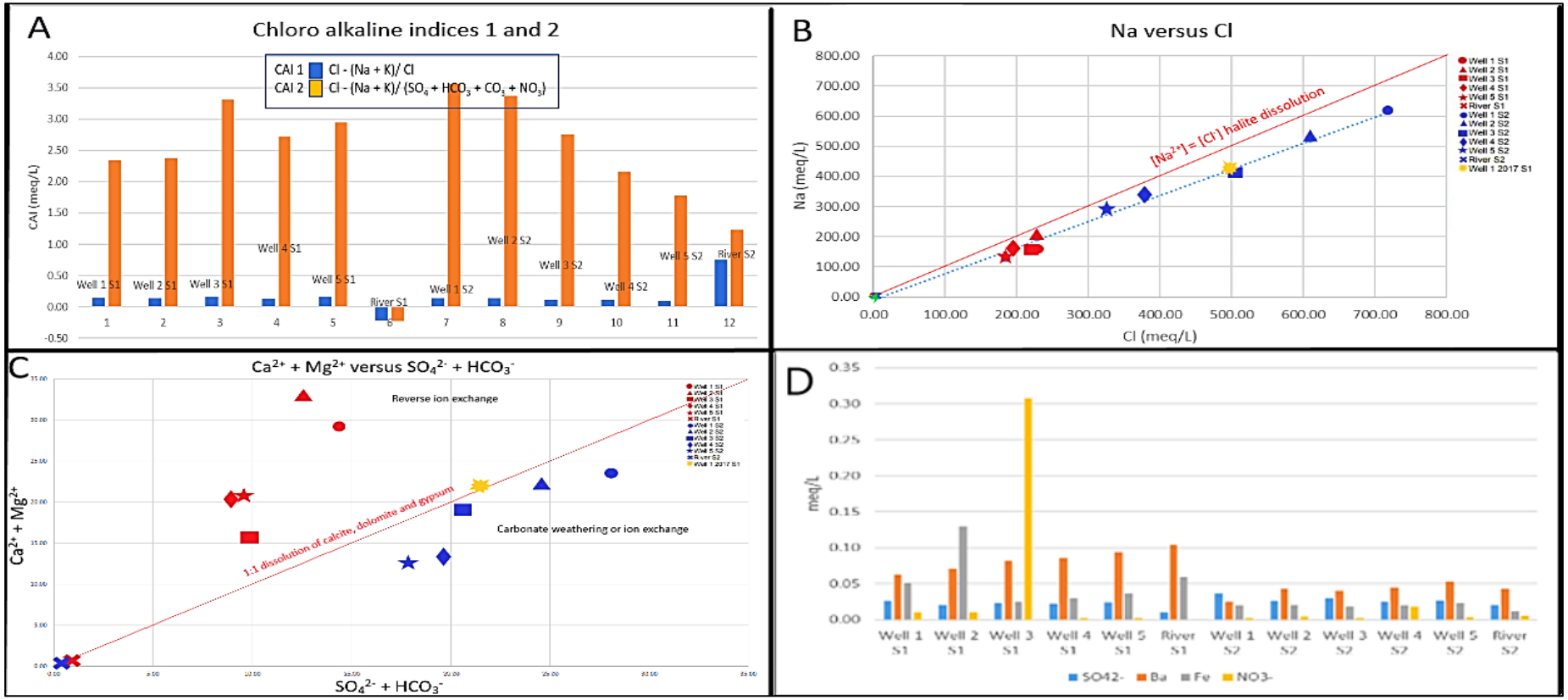

Figure 6. 3 (A) The bar diagram of Chloro-alkaline indices (CAI) 1 and 2 for MON and POM seasons. (B) The Na+ versus Cl- ratio. (C) The Ca^{2+} + Mg^{2+} versus SO_4^{2-} + HCO_3^-. (D) The graph of NO_3^-, Fe, Ba and SO_4^{2-} concentration in mg/L for groundwater and river samples.

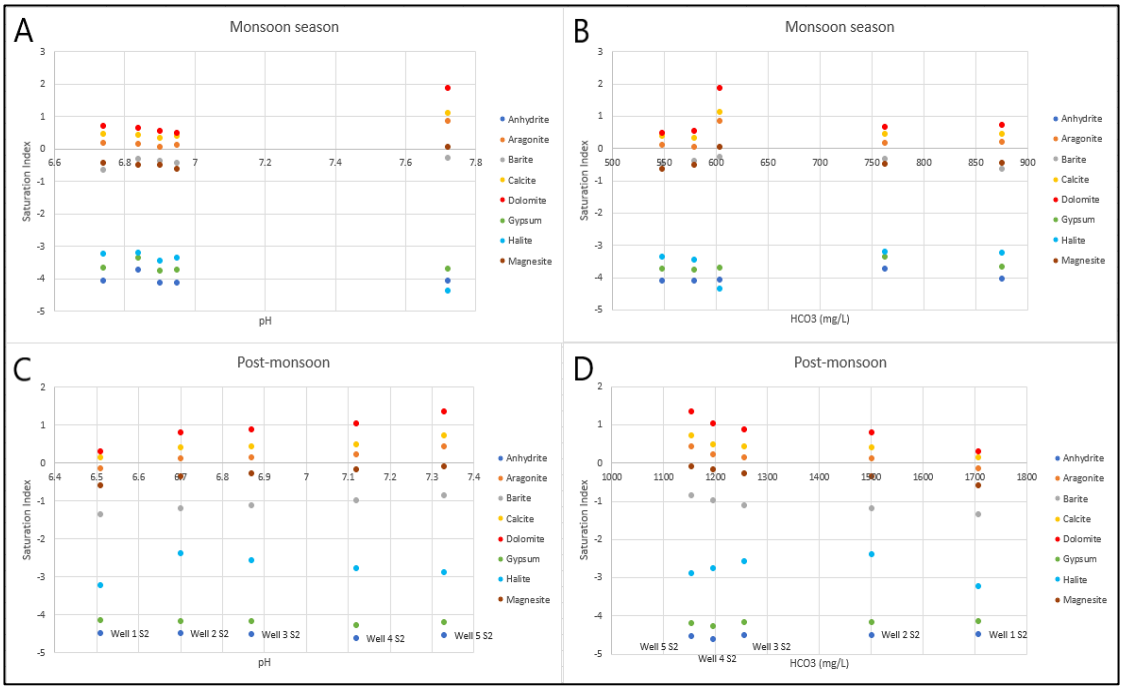

Figure 6. 4 (A and B) The bivariate plot between saturation index with pH and HCO_3 for MON season. (C and D) The bivariate plot between saturation index with pH and HCO_3 for the POM season.

CHAPTER 7. Source of Salinity

7.1 Introduction

Elucidating salinity source in water resources often employs assemblages of diagnostic chemical and isotopic tracers to accurately define the salinity sources, beside to obtain a more robust and reliable evaluation of salinization processes (Boschetti, 2011; Zarei et al., 2013; Dezayes et al., 2015; Han et al., 2018). A summary of the typical geochemical characteristic of different sources is listed in Table 7.1 (Vengosh, 2014). Often, the chemical composition of salinized water does not reveal single salinization source and the geochemical characteristic may be modified due to water-rock interaction, for instance, the Na^+/Cl^- ratio can be a good tracer for distinguishing marine (seawater intrusion = 0.86) to non-marine or anthropogenic (≥1). Thus, the Na^+ ion in the unsaturated zone can reduce the Na^+/Cl^- ratio even in a non-marine environment (Kass et al., 2005). In Table 7.1, Ba'kelalan samples were categorized as relics of evaporated seawater (brines) based on TDS values, Na^+/Cl^-, SO_4^{2-}/Cl^- and B/Cl^- molar ratio. However, based on ^{11}B and ^{34}S isotope signatures, it is classified as either deep water or dissolution of evaporite mineral as the source of water. Nevertheless, further analysis and interpretation of stable isotopes are required to justify the findings and sources.

Table 7. 1 Typical chemical and isotopic characteristic of major saline sources compared to samples from the study area (Vengosh, 2014)

Source	TDS (mg/L)	Na^+/Cl^- (molar ratio)	SO_4^{2-}/Cl^- (molar ratio)	B/Cl^- ($x10^{-3}$) (molar ratio)	$\delta^{34}S$ (‰)	$\delta^{11}B$ (‰)
Seawater	35,000	0.86	0.05	0.8	21	39
Relics of evaporated seawater (brines)	> 35,000	< 0.86	< 0.05	< 0.8	> 21	> 39

Evaporite dissolution	> 1,000	1	>> 0.05	< 0.8	<21	20 – 30
Hydrothermal water	> 1,000 to 2,000	> 1	>> 0.05	> 5	<< 21	0 ± 5
Domestic wastewater	~ 1,000	> 1	> 0.05	5	6 – 10	0 – 10
Agriculture return flow	500 to 5,000	>1	>> 0.05	> 0.8	-	20 – 30
Ba'kelalan	**32,700 – 33,300**	**0.84 – 0.91**	**< 0.05**	**0.2 – 0.6**	**1**	**18.2**

7.2 Results

7.2.1 Langelier and Ludwig Diagram

Langelier and Ludwig (1942) have proposed a diagram using 4 different major constituents to further evaluate the mechanism controlling the groundwater chemistry and quality by using a plot where they divide 50 % of total ions, such as $Na^+ + K^+$, $HCO_3^- + CO_3$, $SO_4^{2-} + Cl^-$ and $Ca^{2+} + Mg^{2+}$. The Langelier -Ludwig diagram provides a subtle subdivision and classification of 3 hydrocarbon-bearing water type in sedimentary basins such as Ca^{2+}-Cl^- brine, over-pressured/ mud volcanoes and Na^+-HCO_3^- waters. According to Boschetti et al. (2016), the fluid from mud volcanoes consists of formation of water diluted by clay dewatering due to overpressure that produces deep fluids with Na^+ excess ($Na^+/Cl^- > 0.86$) combined with calcite precipitation or silicate weathering and shallow groundwater (Lavrushin et al., 2003). In Figure 7.1, the saline groundwater samples fell on the Na^+-Cl^- brine zone near to overpressure waters for POM and well 1 (2017), whereas, the MON samples were more shifted to Ca^{2+}-Cl^- oil field's brine zone (Awaleh et al., 2018).

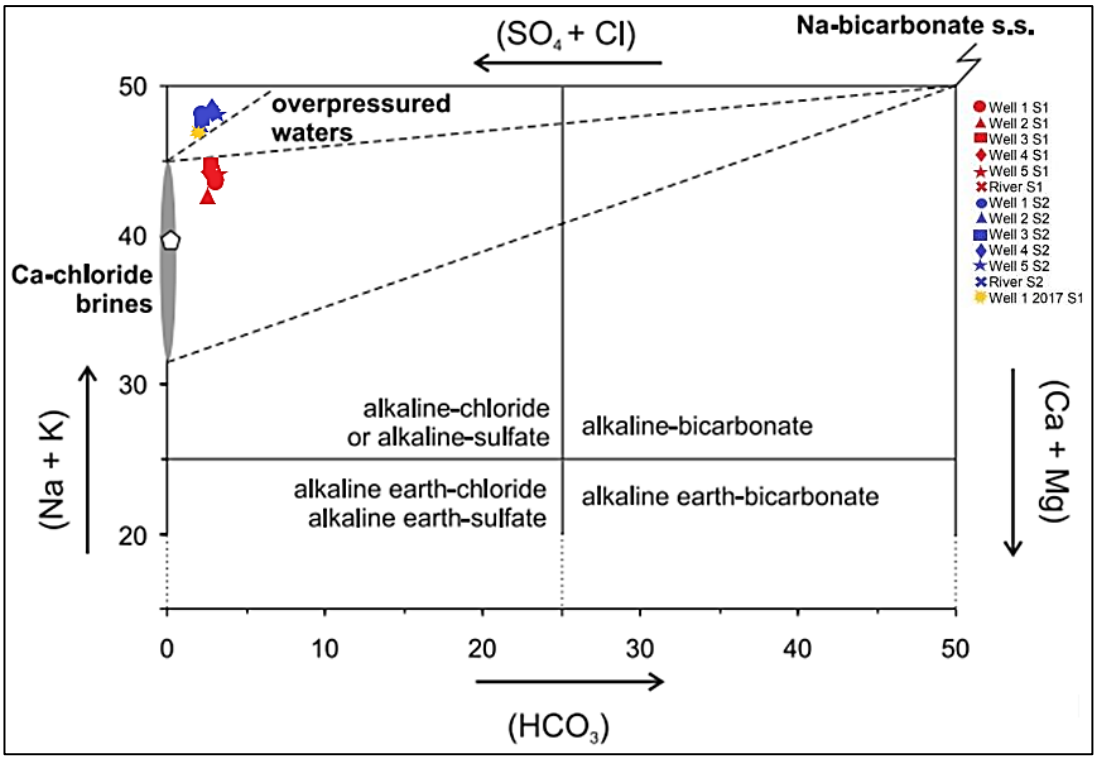

Figure 7. 1 The Langelier-Ludwig plot for monsoon and post-monsoon saline groundwater (Awaleh et al., 2018).

7.2.2 Brine Differentiation Plot

Hounslow (1995) proposed a plot to distinguish between different brine origins called Brine Differentiation Plot (BPS). The plot uses molar ratio of $Ca^{2+}/ (Ca^{2+}+ SO_4^{2-})$ versus $Na^{+}/ (Na^{+}+ Cl^{-})$ on x and y-axis, respectively. In BPS diagram, the field characteristics are divided into oil field brines, Na^{+}-HCO_3 water, terrestrial mud volcanoes, alkali lakes, evaporate solution and seawater that are separated and distinct. In Figure 7.2, the seawater has $Ca^{2+}/ (Ca^{2+}+ SO_4^{2-}) = 0.26$ and $Na^{+}/ (Na^{+}+ Cl^{-}) = 0.46$ and gypsum and halite dissolution after evaporation of seawater (Boschetti et al., 2016; Awaleh et al., 2020). Meanwhile, Na^{+}-Cl^{-} water from dissolution of evaporite was aligned in the middle of the plot because the dissolution of gypsum, anhydrite and halite were the main sources (Awaleh et al., 2018). For Ca^{2+}-Cl^{-} brine, the water has $Ca^{2+}/ (Ca^{2+}+ SO_4^{2-}) = 0.9 – 1$ and $Na^{+}/ (Na^{+}+ Cl^{-}) = 0.38 – 0.46$, thus falling on oil-brine zone. Oil field brines were correlated with the area of evaporation

dissolution but far from seawater zone, while Ca^{2+}-Cl^- brine showed no evaporite contribution, instead the evolution upwards from evaporated seawater, ion exchange, gypsum and halite dissolution (Boschetti et al., 2016; Awaleh et al., 2018). Vengosh et al. (2000) stated that the Mediterranean basin hypersaline groundwater has Ca^{2+}-Cl^- brines with a ratio of $Ca^{2+}/ (Ca^{2+}+ SO_4^{2-}) = 0.55 – 0.95$ and $Na^+/ (Na^+ + Cl^-) < 0.46$ and suggested that the groundwater evolved from seawater towards typical oil-field brines because of sulfate reduction (loss) and Ca^{2+} increase is related to early burial diagenesis. For mud volcanoes and Na^+-HCO_3^- water, there are characteristics of *m*Na/*m*Cl >> 0.86 which is plotted on the right side with $Na^+/ (Na^+ + Cl^-) = 0.50 – 1$ and spanning the $Ca^{2+}/ (Ca^{2+}+ SO_4^{2-})$ due to calcite precipitation and sulfate reduction (Boschetti et al., 2016). In Figure 7.2, the saline groundwater samples for MON and POM have $Ca^{2+}/ (Ca^{2+}+ SO_4^{2-}) = 0.90 – 0.98$ and $Na^+/ (Na^+ + Cl^-) = 0.46 – 0.47$, indicating saline groundwater samples falling on Ca^{2+}-Cl^- oil-field brine zone for MON season. Meanwhile, in the POM season, the samples fell on Ca^{2+}-Cl^- oil-field brine, but towards Na^+-Cl^- water from dissolution of evaporite minerals.

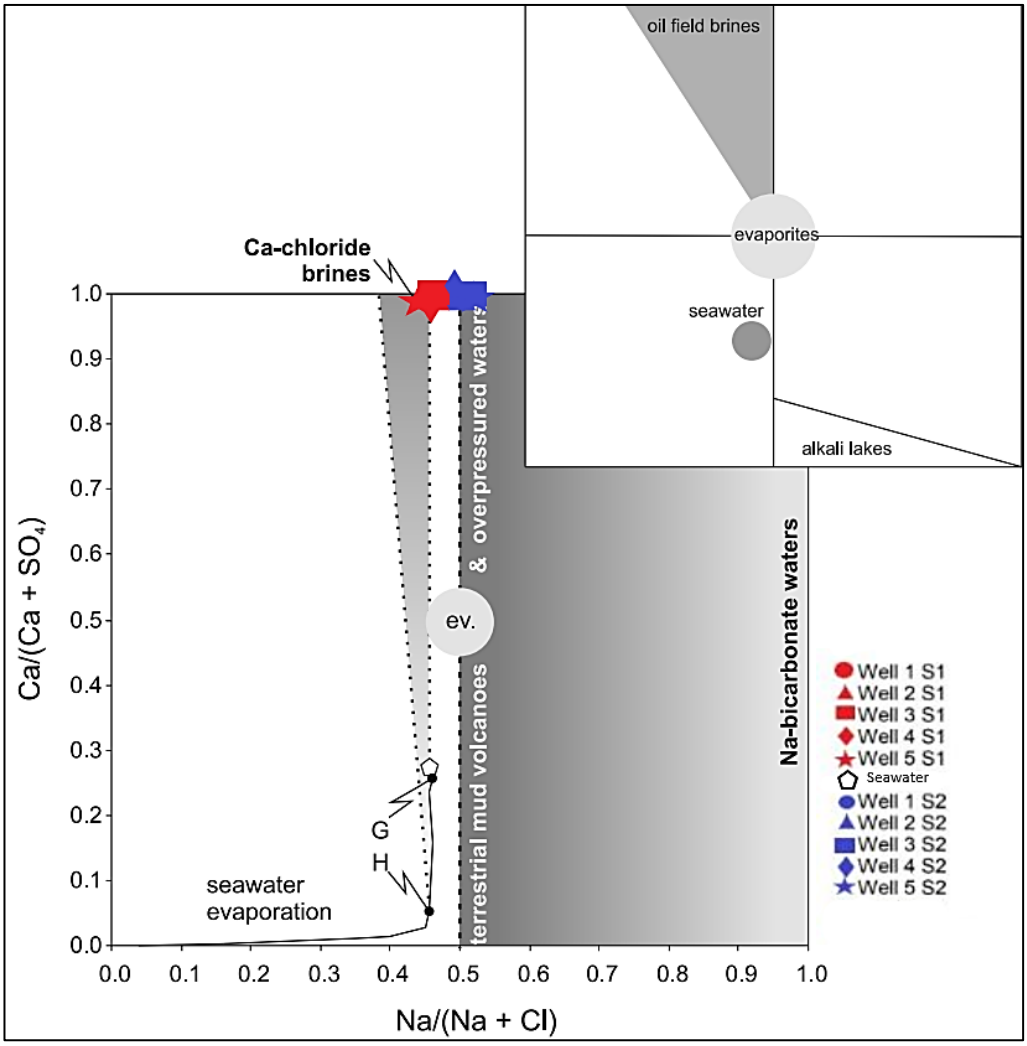

Figure 7. 2 The Brine Differentiation Plot (BPS), where $Ca^{2+}/(Ca^{2+}+SO_4^{2-})$ versus $Na^{+}/(Na^{+}+Cl^{-})$ molar ratio is the constituents; G and H are gypsum and halite dissolution after seawater evaporation compared to samples from the study area (Boschetti et al., 2016).

7.2.3 Na^{+}/Li Plot

The binary plot of sodium-lithium can be used to distinguish the end-member of mixed Na^{+}-Cl^{-} brackish groundwater (Vengosh et al., 2000; Fontes and Matray, 1993; Kloppmann et al., 2001; Lu et al., 2008; Boschetti, 2011; Zarei et al., 2013; Dezayes et al., 2014; Han et al., 2018; Kessler et al., 2019). Lithium's presence in water can be a good indication of geothermal mobility from volcanic or plutonic sources and has been linked to evaporitic materials (Sanchez-Martos et al., 2002; Monjerezi et al., 2012). Based on Dezayes et al. (2015), the plot

of Na^+/Li (Figure 7.3) could provide information regarding geothermal brines and oilfield brines in Rhine Graben, France by using sodium and lithium relationship with temperature for each brine. The highest concentrations of lithium (210 mg/L) are related to its high geothermal activity (240 ^{0}C), whilst lower temperature such as oil-field brines contributes to lower lithium content. The groundwater lithium concentration ranged from 0.10 to 0.32 mg/L for MON and 0.11 to 0.35 mg/L for POM season, respectively. The groundwater samples and well 1 (2017) in Li/Na^+ ratio and the cool temperature of 27.5 ^{0}C fell on the oil-field brine zone (Dezayes et al., 2015).

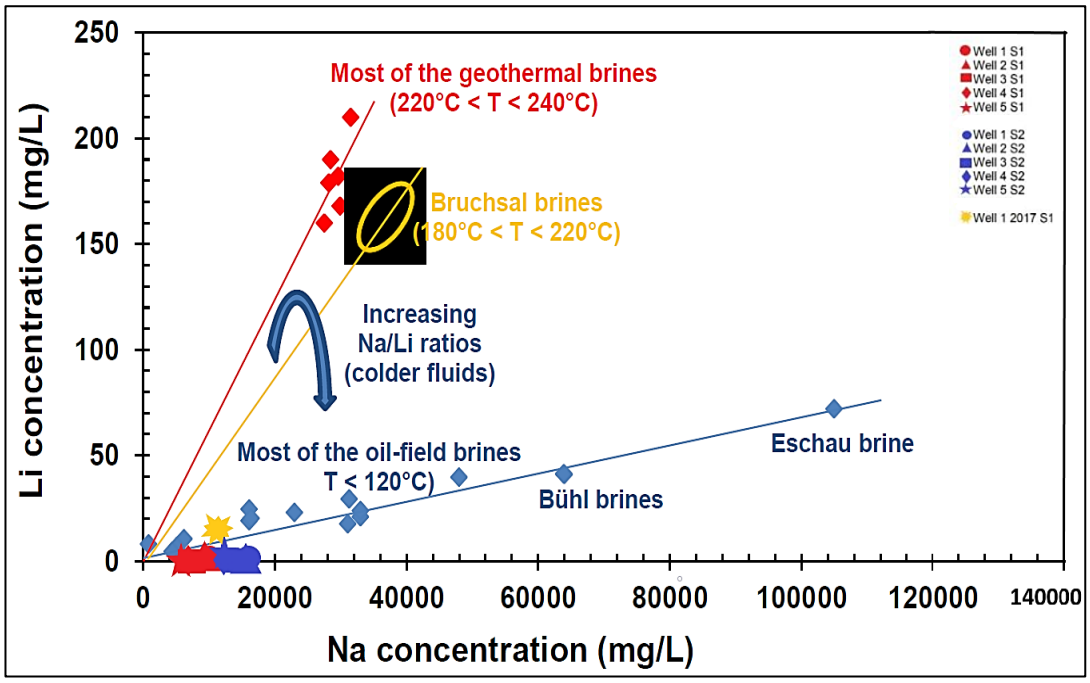

Figure 7. 3 The plot of Na^+ versus Li in mg/L compared to samples from the study area (Dezayes et al., 2015).

7.3 Stable isotope

7.3.1 Results

Table 7.2 shows the salinization from different sources around the world to compare with the study area. Awaleh et al. (2020) stated that the studies of isotopes ($\delta^{18}O$, δD, $\delta^{11}B$ and $\delta^{34}S$) in geothermal springs in Africa showed a shift of $\delta^{18}O$, δD and $\delta^{11}B$ towards higher values

during the evaporation path. The study of Na^+/Cl^- ratio and $\delta^{37}Cl$ of saline groundwater in Mongolia by Liu et al. (2016) indicated that salinity was from halite dissolution and other salts containing Cl concentration in the deeper aquifer. The salt dome investigation study in Northern Germany by Kloppmann et al. (2001) using B, O and H isotopes suggested that the $\delta^{11}B$ composition and $\delta^{18}O$ enrichment were compatible with halite dissolution and water-rock interaction. A study on oil-fields in Paris Basin by Fontes and Matray (1993) stated that the stable isotopes ($\delta^{18}O$, δD and $\delta^{34}S$) indicated the mixing with primary brine from the carbonate dissolution (halite, sylvite, gypsum and anhydrite) and features of deep formation and oil-field brines. The study of deep groundwater (100 m to 4000 m) in Russia by Stash et al. (2007) indicated that the $\delta^{18}O$ and δD values were enriched progressively during evaporation and the $\delta^{37}Cl$ value was reported within the range of halite. Han et al. (2018) stated that the studies of stable isotopes ($\delta^{18}O$, δD and $\delta^{37}B$) in Tibetan Plateau (Mongolia) indicated the types of leached brine with typical geothermal water of crustal origin (marine carbonate rocks and volcanic rocks). The study of brine water in Iran by Bagheri et al. (2014a) stated that the Kangan aquifer salinity was through the evaporated seawater and water-rock interaction. Whereas, the study of Kangan gasfield brine in Iran by Bagheri et al. (2014b) stated that the stable isotopes ($\delta^{18}O$, δD and $\delta^{37}Cl$) in Kangan gasfield brine indicated the source of salinization due to evaporation of brine and halite dissolution. The salt water of the foredeep basin in Italy by Boschetti et al. (2011) stated that the stable isotope values ($\delta^{18}O$, δD, $\delta^{34}S$ and $\delta^{37}Cl$) indicated the source of salinization by dissolution evaporites (gypsum and halite). The study area's saline groundwater samples that were high in $\delta^{18}O$, δD and d-excess values indicated the intensity of evaporation water sources, whereas the $\delta^{37}B$ value suggested dissolution of marine evaporites. Meanwhile, $\delta^{34}S$ and $\delta^{37}Cl$ values indicated oxidation of pyrite and dissolution of halite, respectively.

Table 7. 2 Comparison of Ba'kelalan groundwater stable isotopic compositions and d-excess value with other location in the world.

Sample	TDS (mg/L)	Na (mg/L)	Cl (mg/L)	B (mg/L)	$\delta^{18}O$ (‰)	δD (‰)	d-excess (‰)	$\delta^{37}Cl$ (‰)	$\delta^{11}B$ (‰)	$\delta^{34}S$ (‰)
Well 1	32,700	14,184	25,450	4.12	6.11	-17.85	-66.73	0.82	18.9	1
Well 2	30,100	12,064	21,584	-	5.06	-20.32	-60.80	-	-	-
Well 3	27,000	10,248	17,859	-	3.60	-24.70	-53.50	-	-	-
Geothermal Spring, East Africa (Awaleh et al., 2020)	2,160	802	1,083	10.50	-1.96	-14.3	1.38	-	21.68	12.73
Saline groundwater, Mongolia (Liu et al., 2016)	32,200	9,921	18,083	-	-7.5	-71	-11	2.13	-	-
Salt dome saline groundwater, Germany (Kloppmann et al., 2001)	292,500	87,800	138,000	5.56	-10.4	-73.10	10.10	-	33.51	-
Oil-field brine, France (Fontes and Mantray, 1993)	67,600	885	1,176	-	-4.2	-38	-4.40	-	-	12

Deep saline groundwater Siberia, Russia (Stash et al., 2007)	44,000	27,191	3,571	-	-0.5	-94	-90	1.54	-	-
Saline spring, Tibetan Plateau (Han et al., 2018)	332,390	126.73	174,410	14.70	-12.88	-100.90	2.14	-	3.55	-
Salt Diapir Spring, Iran (Bagheri et al., 2014a)	299,813	116,956	181,937	-	-2.49	-5.40	14.52	0.19	-	-
Kangan gas-field brine, Iran (Bagheri et al., 2014b)	334,000	70300	177,500	-	4.82	-19.60	-58.16	-0.10	-	-
Brine water, Italy (Boschetti et al., 2011)	131,000	41,900	83,403	-	10.6	-14.80	-99.60	0.18	-	37.60

7.3.2 $\delta^{18}O$ and δD

The studies of $\delta^{18}O$ and δD stable isotopes are proven to be suitable tracers in determining the origin of groundwater, paleoclimatic implication, natural water circulation and groundwater movement (Liu et al., 2016; Awaleh et al., 2017; Barzegar et al., 2018; Li et al., 2019b). The $\delta^{18}O$ and deuterium isotopes in waters initiate the meteoric processes from infiltration into sediments that change the isotopic signature of the groundwater as a result of rock-groundwater interaction (Chelnokov et al., 2013; Thivya et al., 2016; Awaleh et al., 2020). Prior to interpreting such tracers, a meteoric water line is constructed to provide a reference regarding fractionation and mixing processes (Alexeev et al., 2020). Since there were no systematic rainfall isotopic data available in the Ba'kelalan region, this study complied with the local meteoric water line (LMWL) from a nearby location Limbang river basin rainfall data (Ninu Krishnan, 2019). The stable isotopic composition of Ba'kelalan groundwater is shown in Table 4.15.

In Figure 7.4, all the data are compared with the Global Meteoric Water Line (GMWL) $\delta D = 8\ \delta^{18}O + 10$, as defined by Craig (1961), and the Local Meteoric Water Line (LMWL) $\delta D = 7.64\ \delta^{18}O + 10$, as defined by Ninu Krishnan (2019). The slope of GMWL and LMWL is close to each other due to the effects of local climatic factors including air, temperature, evaporation, seasonal precipitation and moisture source (Deshpande and Gupta, 2012; Thivya et al., 2016; Disli and Gulyuz, 2020). The $\delta^{18}O$ values (Table 7.2) of the saline groundwater fell in the range of 6.11 ‰, 5.06 ‰, and 3.6 ‰, for well 1, 2 and 3, respectively, with a mean value of 4.92 ‰. Meanwhile, the δD value ranged from -17.85 ‰, -20.32 ‰ and -24.70 ‰, with a mean value of -20.95 ‰.

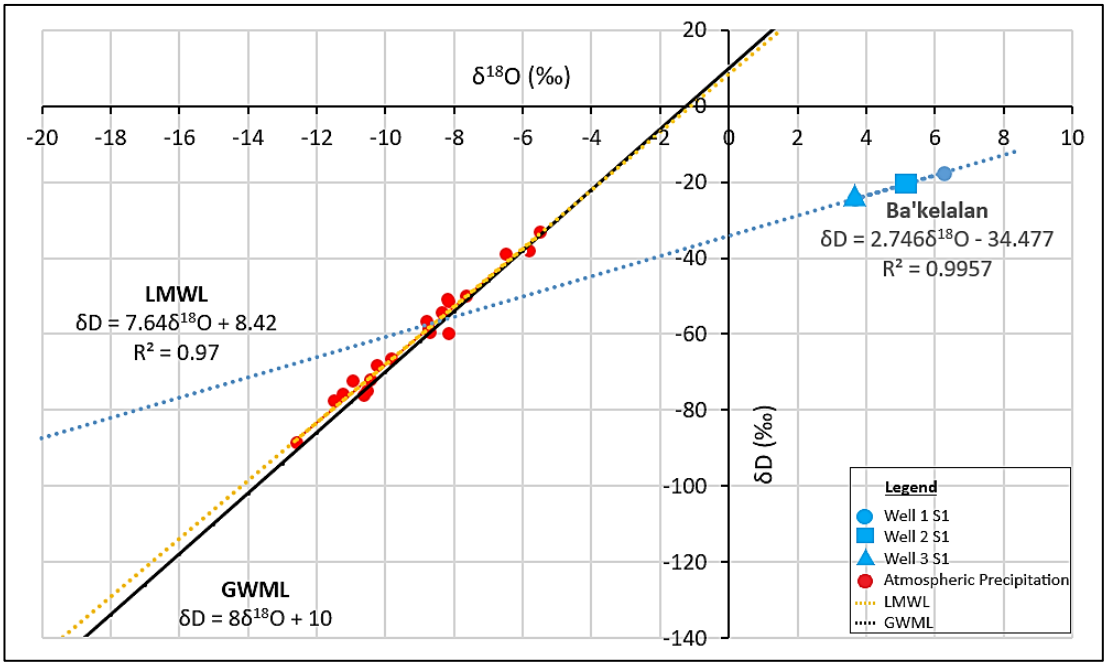

Figure 7. 4 Stable isotope composition plot of δD versus $\delta^{18}O$ of Ba'kelalan groundwater samples compared with the LMWL and GWML.

7.3.3 D-excess

The d-excess value is a useful approach in delineation secondary processes affecting the vapour content in the evaporation – condensation process in the atmosphere (Thivya et al., 2016; Bershaw, 2018; Mirzavand et al., 2020b). The comparison of the local meteoric line from precipitation with the obtained groundwater samples can provide insight as d-excess tends to decrease with evaporative intensity (Gautam et al., 2017). Deuterium excess (*d*) is a function of the isotopic composition of $\delta^{18}O$ and δD in water and is calculated in the following as: $d = \delta D - 8 \times \delta^{18}O$ (Dansgaard, 1964) to determine the relation between evaporation and salinity (Ninu Krishnan, 2019). High d-excess (> 10) is examined as a footprint of recycled moisture and lower d-excess (<10) is suggested as evaporated rainfall (Thivya et al., 2016). Figure 7.5 shows that the groundwater samples were negative and have very low d-excess values ranging from -66.73 ‰, -60.8 ‰ and -53.5 ‰, for well 1, 2 and 3, respectively. The plot of d-excess versus TDS (Figure 7.6) shows an increasing trend in TDS which leads to decreasing in d-excess.

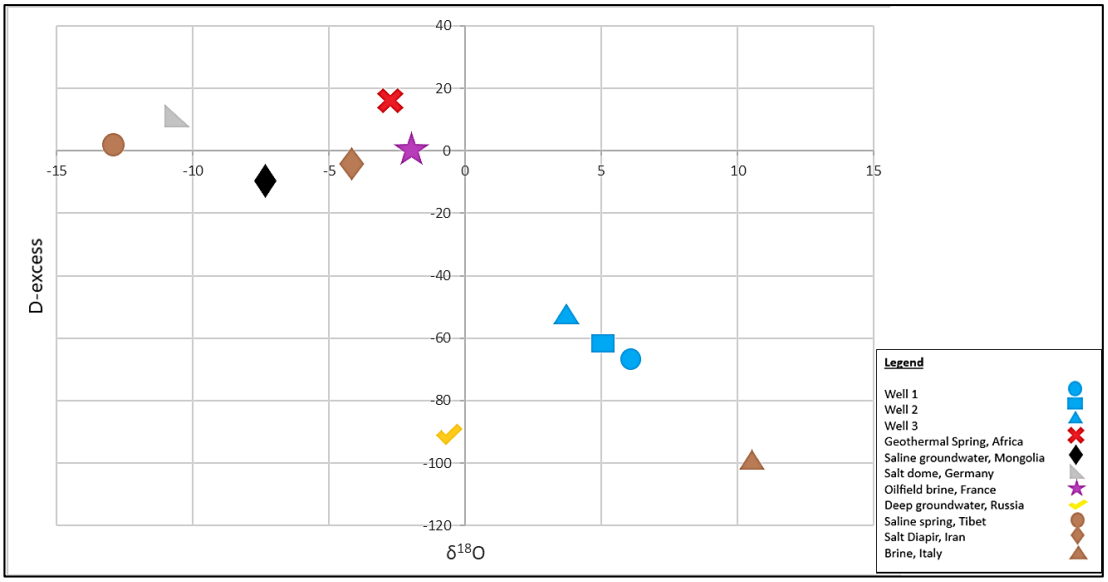

Figure 7. 5 The plot of d-excess versus $\delta^{18}O$ compared to samples from the study area (Thivya et al., 2016).

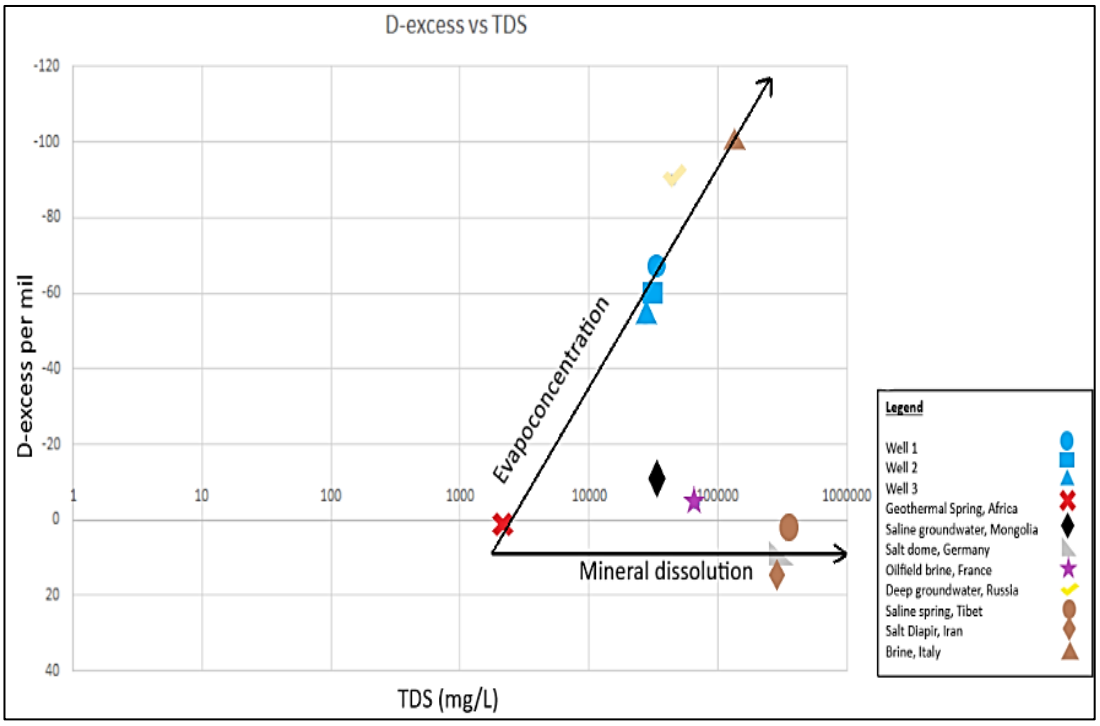

Figure 7. 6 The plot of d-excess versus TDS compared to samples from the study area (Huang and Pang, 2012).

7.3.4 $\delta^{34}S$

$\delta^{34}S$ isotope is generally used as a tracer in the interpretation of evaporative depositional environment (Karakaya et al., 2019). The $\delta^{34}S$ value of the seawater and magmatic sulfide ranged from 15 ‰ to 25 ‰ and –10 ‰ to 10 ‰, respectively (Paytan et al., 2004; Tostevin et al., 2016), whereas, the $\delta^{34}S$ values for evaporites and pyrite varied from 15 ‰ to 23 ‰ and from –15 ‰ to 4 ‰, respectively (Evans et al., 2015; Wang and Zhang, 2019; Zhang et al., 2020). Factors influencing $\delta^{34}S$ values of evaporative sulfates are marine and non-marine contribution, reservoir and redox reaction (Torfstein et al., 2005; Li et al., 2019b). For instance, bacterial sulfate reduction preferentially enriches in lighter ^{32}S, therefore, the residual sulphate minerals (gypsum) will enrich in heavier ^{34}S (Liu et al., 2016; Li et al., 2019b). The $\delta^{34}S$ in the study area was close to oxidative weathering of metamorphic pyrite with a value of – 1.8 ‰ to 2.4 ‰ (Toestevin et al., 2016). The study area sample has a value of $\delta^{34}S$ at 1 ‰, which fell on the oxidation sulfide zone (Figure 7.7).

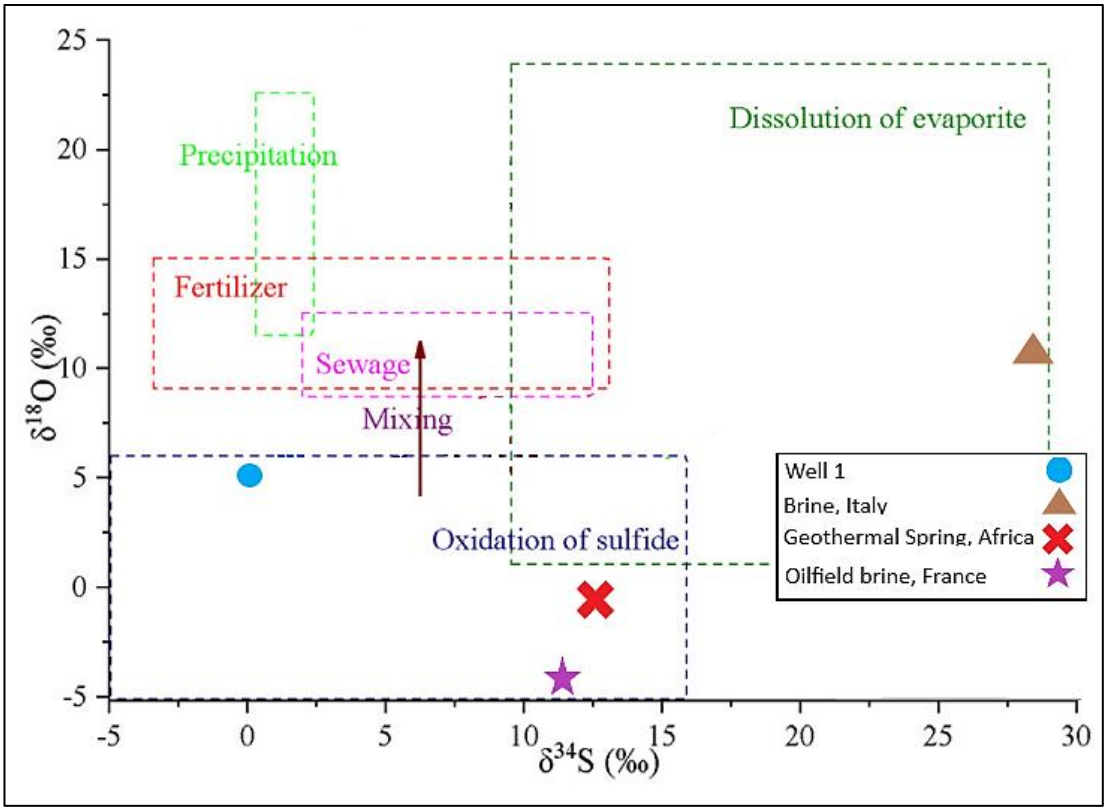

Figure 7. 7 The plot of $\delta^{34}S$ versus $\delta^{18}O$ values compared to samples from the study area (Zhang et al., 2020).

7.3.5 $\delta^{11}B$

The use of boron isotope is constrained by the reactivity in the hydrological system where boron tends to be absorbed on clay minerals and oxides, particularly under highly saline condition (Vengosh, 2005). Additionally, the boron isotope is used as a geochemical tracer due to its high mobility in processes involving high and low-temperature fluids (Ercan et al., 2019). The boron isotope composition of seawater ranged from 39.60 ‰ to 45.74 ‰ (Figure 7.8), whereas marine carbonates and continental crust were recorded approximately as 30 ‰ and – 10 ‰ to – 7 ‰, respectively (Hoefs, 2015; Han et al., 2018; Ercan et al., 2019). The $\delta^{11}B$ values for geothermal system ranged from – 16 ‰ to 13.1 ‰, indicating an origin from magmatic rocks (B concentration > 360 ppm) and marine carbonate (B concentration < 100 ppm) (Lu et al., 2014; Purnomo et al., 2016; Han et al., 2018). The $\delta^{11}B$ values for marine evaporites and non-marine evaporites ranged from 18.2 ‰ to 31.7 ‰ and – 30.1 ‰ to 10.2 ‰, respectively (Du et al., 2019). Factors influencing $\delta^{11}B$ values were the distribution of boron species, temperature and pH (Li et al., 2019b). In Figure 7.8, the plot for study area groundwater falls on dissolution of marine carbonate rocks zone with $\delta^{11}B$ value of 18.2 ‰. In Figure 7.9, the study area sample falls on the dissolution of marine evaporites zone and is witnessed by the $\delta^{11}B$ versus B (ppm).

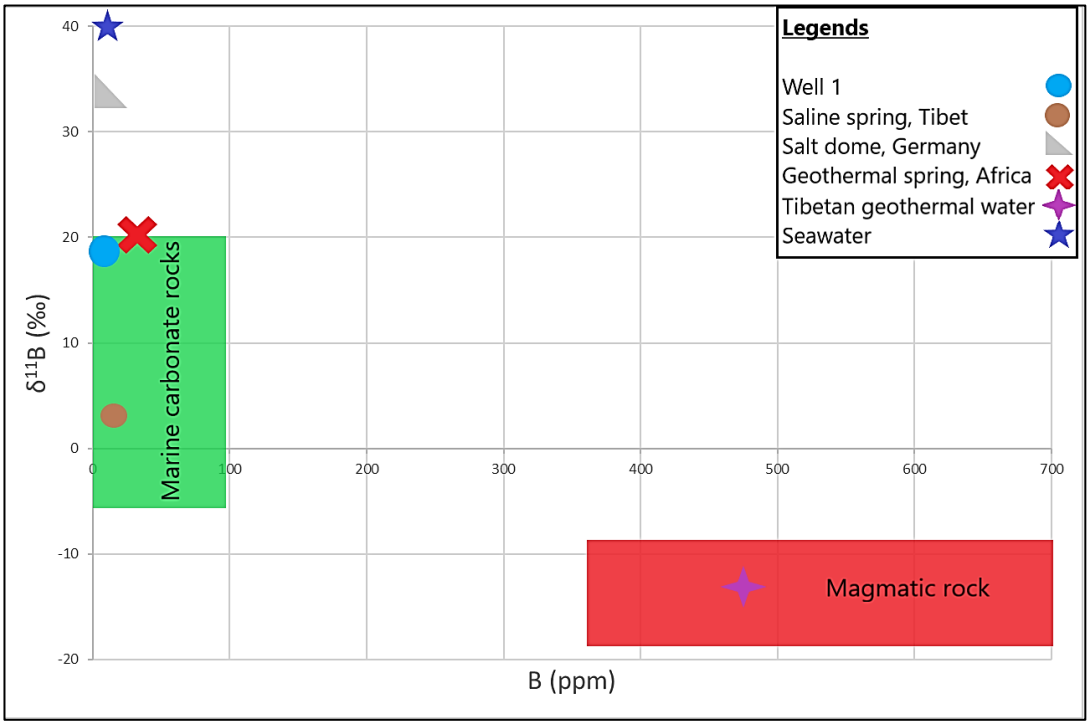

Figure 7. 8 The plot of $\delta^{11}B$ versus B (ppm) compared to samples from the study area (Lu et al., 2014; Han et al., 2018; Awaleh et al., 2020).

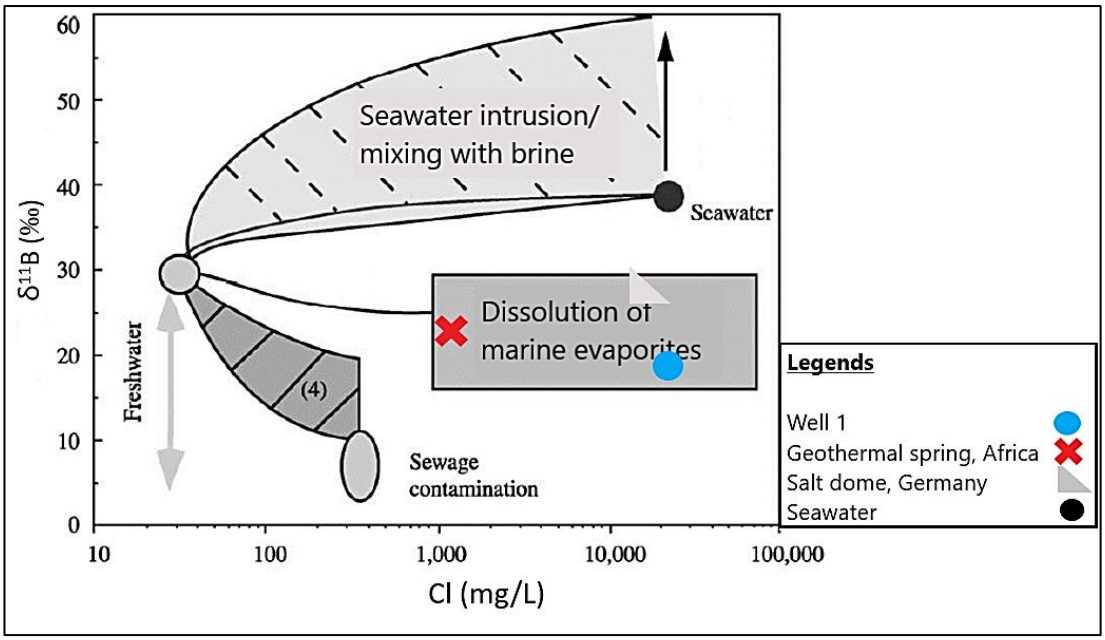

Figure 7. 9 The plot of $\delta^{11}B$ versus Cl (mg/L) compared to samples from the study area (Vengosh, 2005).

7.3.6 $\delta^{37}Cl$

Chloride isotope $\delta^{37}Cl$ is mainly used to define salinity sources, mixing of different sources of waters and water-rock interaction (Eggenkamp et al., 1994; Bagheri et al., 2014; Zhang et al., 2020). There are various $\delta^{37}Cl$ values for different sources, for instance, the $\delta^{37}Cl$ values for aerosol ranged from 0.42 ‰ to 2.53 ‰, for river water -0.74 ‰ to 2.85 ‰, for halite -0.60 ‰ to 1.20, for salt lake -2.06 ‰ to 1.01 ‰, for seawater -0.9 ‰ to 0.0 ‰ and for groundwater, ranging from -0.50 ‰ to 0.69 ‰ (Eggenkamp et al., 1995; Eastoe et al., 2001; Bagheri et al., 2014a; Liu et al., 2016; Birks et al., 2019). Physical and chemical processes such as ion filtration, ion-exchange and diffusion may affect $\delta^{37}Cl$ fractionation (Eggenkamp et al., 1995; Sherif et al., 2019). In Figure 7.10, the saline groundwater sample falls above the evaporation line and has a $\delta^{37}Cl$ value of 0.82 ‰.

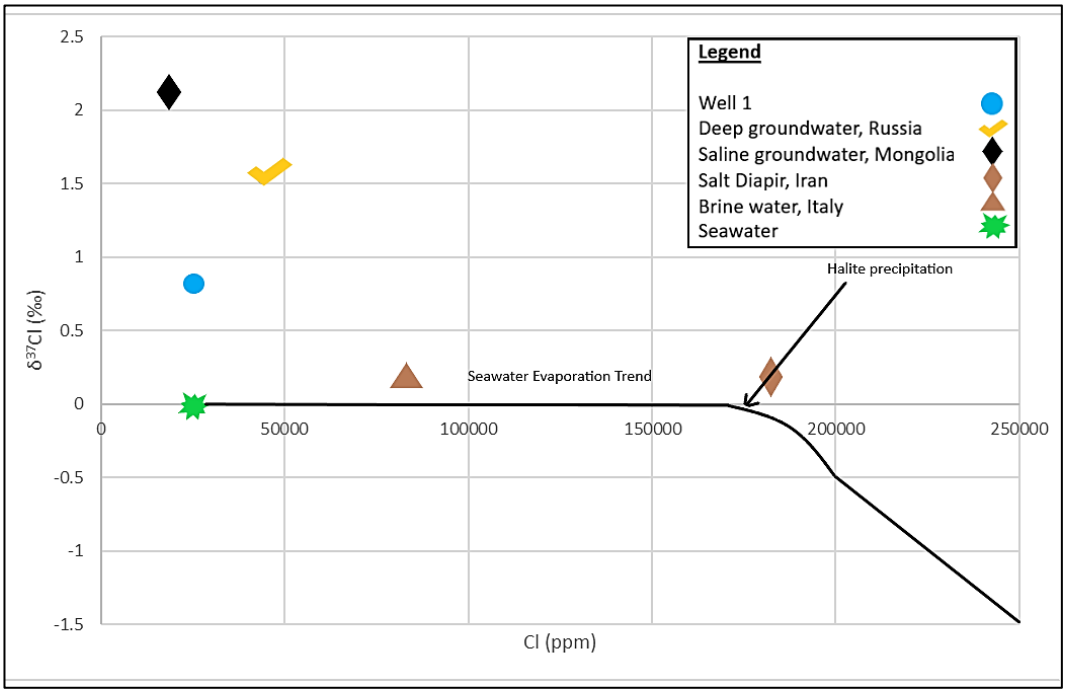

Figure 7. 10 The plot of $\delta^{37}Cl$ versus Cl (ppm) compared to samples from the study area (Bagheri et al., 2014; Sherif et al., 2019)

7.4 Discussion

7.4.1 Source of Salinity

Based on Na^+/Li plot, Brine Differentiation plot and Langlier-Ludwig diagram, the saline groundwater samples fell on the Na^+-Cl^- brine zone for POM season, indicating the longer residence time of water in deeper condition that resulted in higher salinity content. Whereas, the MON samples were more shifted to Ca^{2+}-Cl^- oil field brine zone. Based on Sulin (1946), the characteristic of Ca^{2+}-Cl^- brine can be defined by $Na^+/Cl^- < 1$ and $(Cl^- - Na^+)/ Mg^{2+} < 1$, whereas Ba'kelalan saline groundwater has a ratio of $Na^+/Cl = 0.86 – 0.91$ and $(Cl^- - Na^+)/ Mg^{2+} >1$, therefore, Ba'kelalan saline groundwater might have originated from Ca^{2+}-Cl^- oil-field brine zone (Boschetti et al., 2016; Ozdemir, 2018; Awaleh et al., 2020). All the saline groundwater sample data for both sources are plotted above the y-axis, suggesting that SO_4^{2-} reduction is an important process in the composition of the groundwater (Engle et al., 2016).

7.4.2 Stable Isotopes

Evaporation typically accumulates heavier isotopes in the brine but is dependent on the temperature and humidity of the environment (Regenspurg et al., 2016). During evaporation or water-rock interaction, the $\delta^{18}O$ and δD of water become enriched (Disli and Gulyuz, 2020). The $\delta^{18}O$ and δD values show that well 1 was more enriched in ^{18}O concentration compared to well 2 and well 3. The analysed saline groundwater samples plotted away from the GMWL and the LMWL with an enrichment isotopic concentration of $\delta^{18}O$ indicate that the meteoric water was not the main origin of the groundwater recharge in the study area (Coplen, 1994; Boschetti et al., 2011). The saline groundwater enriched value in $\delta^{18}O$ may be mainly due to the evaporation process, witnessed in the Gibbs plot and other geochemical plots (Mirzavand et al., 2020b). The enrichment in $\delta^{18}O$ of the groundwater may be due to a variety of processes, such as water-rock interaction, ancient seawater evaporation or mineral dehydration. The negative δ^2H values can be an indicator of ion hydration effects of mineral dissolution such as halite, which is witnessed by XRD salt sample data or isotope exchange during hydration and dehydration of minerals (Bagheri et al., 2014b). Figure 7.4 shows that the saline groundwater

sample trend line intersects the LMWL at a particular point, suggesting that the interconnection by a particular location and period might be the source of local precipitation (Liu et al., 2016). This suggests the recharge period might have occurred during January 2017 at Kampong Salidong, Limbang, Sarawak (Ninu Krishnan, 2019).

The groundwater samples' d-excess values were negative and very low, indicating that values less than 3 ‰ revealed the source as evaporative enrichment with certainty (Dansgaard, 1964; Harvey, 2005; Huang and Pang, 2012; Thivya et al., 2016). This suggests that the saline groundwater is attributed to the evaporation water source. The increasing trend in TDS led to decrease in d-excess, suggesting that intense evaporation process occurred in the deeper aquifer (Dansgaard, 1964; Huang and Pang, 2012; Krishnan et al., 2019; Torres-Martinez et al., 2020).

The $\delta^{34}S$ has a value which fell on the oxidation sulfide zone indicating oxidization by pyrite concentration as witnessed in geochemical plots and hand rock sample with pyrite grains identified in the study location (Tostevin et al., 2016; Wang and Zhang, 2019). Pyrite is commonly associated with the biogenic deposits of coal and indicator for a strong reducing environment (Hem, 1989). The following equation explains the chemical reaction for pyrite oxidation:

$$2FeS_2 + 7O_2 + 2H_2O \rightarrow 2Fe^{2+} + 4SO_4^{2-} + 4H^+ \quad (41)$$

The saline groundwater sample has $\delta^{11}B$ value of 18.2 ‰, which fell on dissolution of marine carbonate rocks zone, hence, dissolution of marine evaporites at the deeper circulation of groundwater through the infiltration of monsoonal rainwater was reflected in $\delta^{11}B$ value (Du et al., 2019; Ercan et al., 2019). The saline groundwater sample has a $\delta^{37}Cl$ value of 0.82 ‰, indicating that halite dissolution was the major process affecting the salinization in the study area which was justified by the XRD salt sample data (Eastoe et al., 2001; Liu et al., 2016; Birks et al., 2019). It is interesting to observe that the enrichment of $\delta^{37}Cl$ was around 25,000 ppm of Cl^-, which also indicated the intense evaporation process in deeper circulation of groundwater.

CHAPTER 8. Geophysical Survey

8.1 Results

8.1.1 2D Resistivity Survey

The purpose of conducting the preliminary field excursion in December 2018 was to investigate the study area and plan a suitable location to employ the geophysics survey. Figure 8.1 shows the aerial view of geophysical survey lines conducted across the study area. The 2D resistivity survey composed of 5 profiles across the Bang Main salt wells; profile R1, R2 and R3 successively transverse the perched aquifer as the main target for new potential saline groundwater. Meanwhile, profile R4 was located on the old wells that were dried up for the past decades and profile R5 was based on the existing 3 operative salt wells. This may act as the reference image for the findings of potential whereabouts of the saline groundwater in the region.

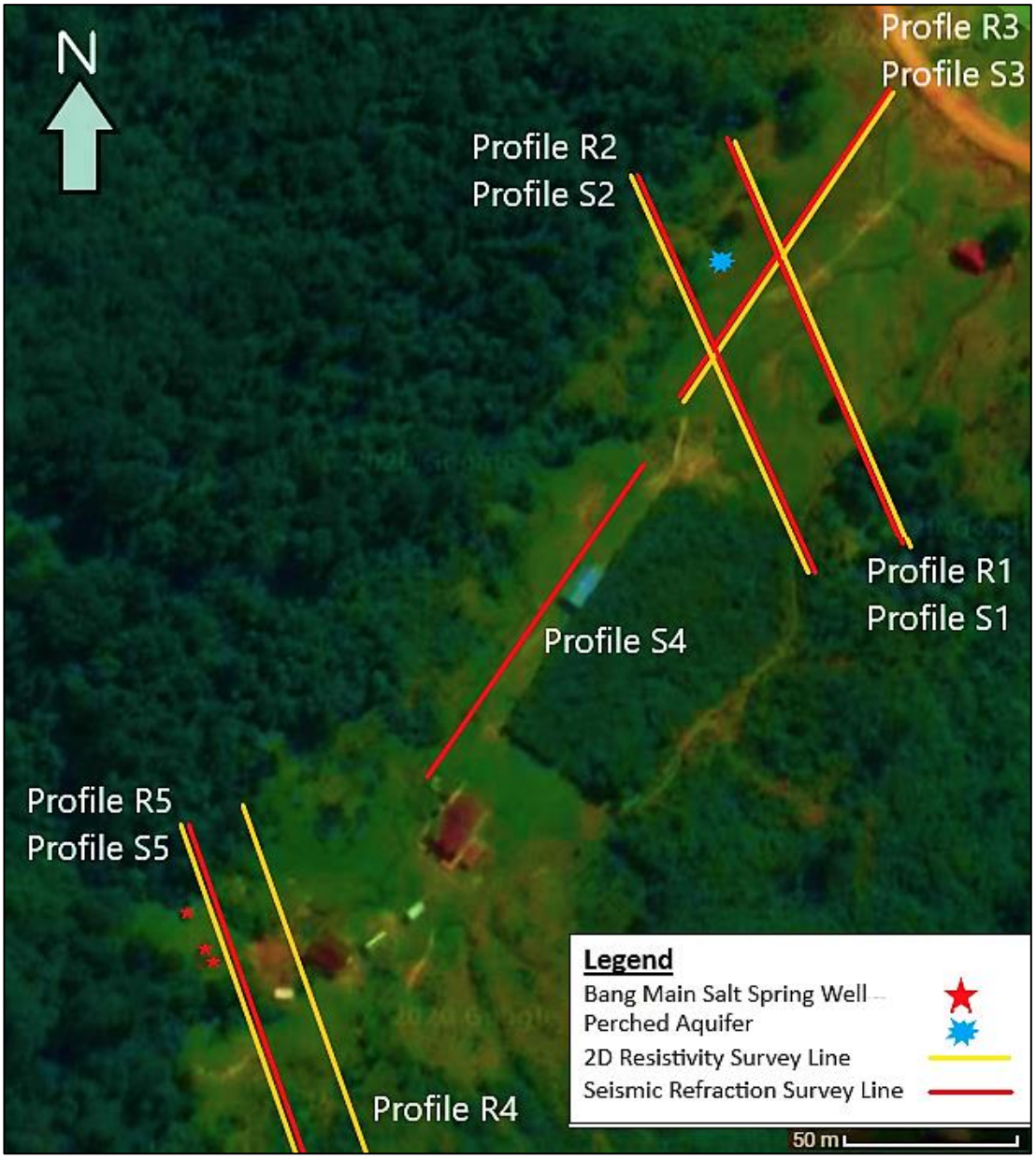

Figure 8. 1 The geophysical survey line for 2D resistivity and seismic refraction methods in the study area (Google Earth).

8.1.2 Profile R1

A Wenner array is known to have the highest signal-to-noise ratio and is used to eliminate any ambient noise with greatest horizontal data coverage and the sensitivity of the array to vertical and horizontal changes in subsurface resistivity (Loke, 2003). Profile R1 was located adjacent to the potential target of the perched aquifer and was marked near the midpoint with

a spreading length of 105 m at the orientation NW to SE (Figure 8.2). The resistivity was employed with Wenner array of 2.5 m electrode, spacing with a total of 42 electrodes across the straight line. The inverse model shows the resistivity value ranging from 120 Ω.m to 230 Ω.m at a depth of < 1 m to 4 m towards the NW part (Figure 8.2), indicating the weathered top soil layer. The moderate resistivity ranging between 45 Ω.m to 70 Ω.m suggested a sandy layer at a depth of 5 m to 15 m, separating the two groundwater plumes. The lowest resistivity value dominating the nearby perched aquifer (spring) with a value of 2.8 Ω.m to < 10 Ω.m at depth from 1 m to 14 m was suggested as the saline groundwater, as changes in salinity content lead to changes in resistivity. The saline water plume moved from higher to lower elevation (NW to SE), where perched aquifer water table intersected at a down valley (Figure 8.3) with the water discharging as a spring.

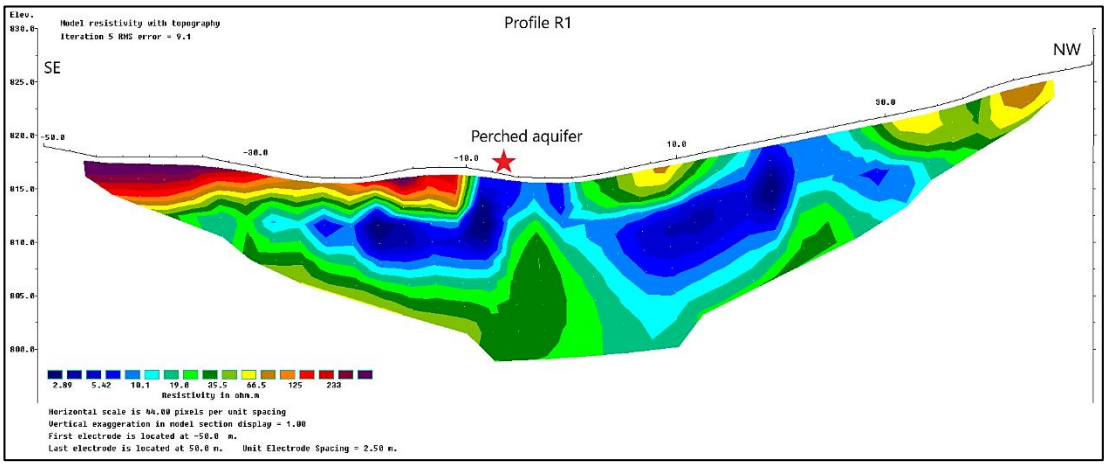

Figure 8. 2 Profile R1 - Inverse resistivity model.

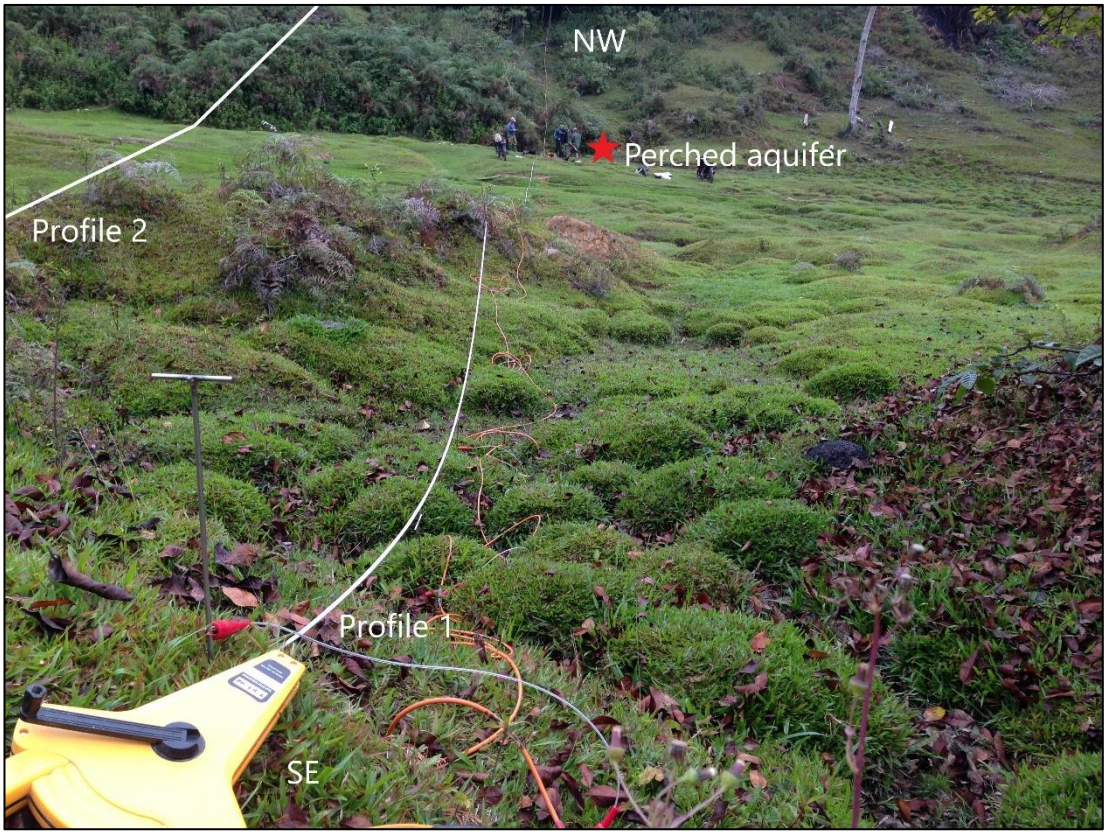

Figure 8. 3 Field photograph for profile R1 and R2, stretching from SE to NW with 105 m survey line spreading.

8.1.3 Profile R2

The traverse profile R2 located adjacent to profile R1 served to conduct a grid pattern for the target perched aquifer (spring) with spreading of 105 m and 2.5 m electrode spacing. The topsoil showed the highest resistivity value, ranging from 167 Ω.m to 505 Ω.m at depth from near-surface to 5 m mostly on the NW part. The yellow and green colour showed the resistivity value of ≈ 50 Ω.m, which could indicate a sandy layer at the depth of 10 m to 15 m. Towards the SE of the survey line, the lowest resistivity value from 0.2 Ω.m to 5.50 Ω.m at the depth of 3 m to 13 m indicated potential saline groundwater (Figure 8.4). The movement of the plume indicated the flow from NW to SE, whereby the perched water table intersected the ground surface at the middle of the section.

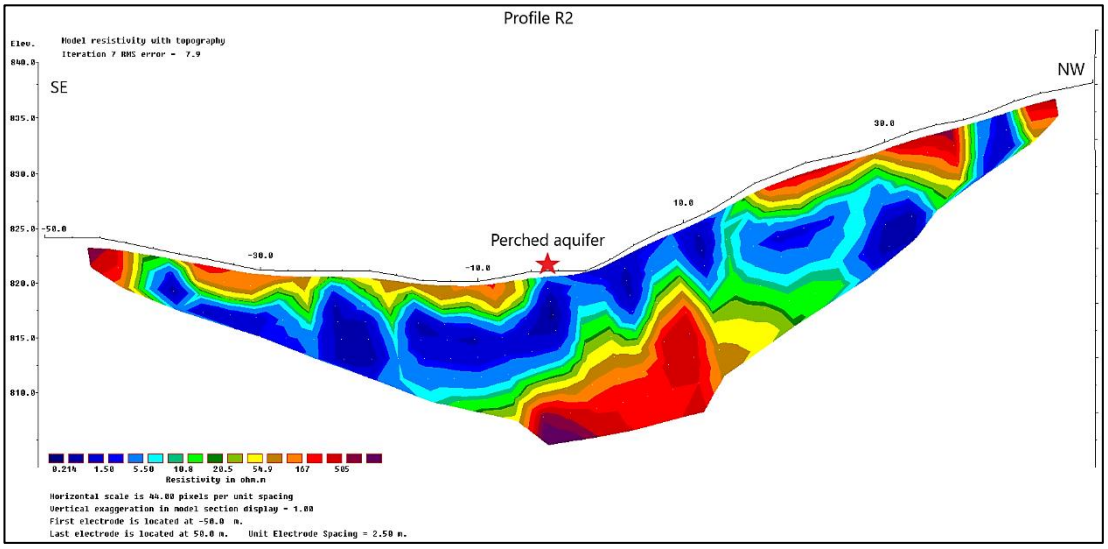

Figure 8. 4 Profile R2 - An inverse resistivity model orientation SE-NW.

8.1.4 Profile R3

Profile R3's survey line was stretched perpendicular across profile R1 and profile R2 like a grid pattern, with an intention to produce 3D concept view for the main target perched aquifer (Figure 8.6). The resistivity inverse model showed the highest value of 110 Ω.m to 300 Ω.m, suggesting topsoil at depth of 0.5 m to 5m, dominating most of the near-surface across profile R3. The resistivity value of ≈ 50 Ω.m could indicate the sandy layer between the two separated groundwater plumes. Nonetheless, the inverse resistivity model showed the lowest value of 0.3 Ω.m to < 5 Ω.m at a depth of 1 m to 8 m, indicating as groundwater potential corresponding to the targeted perched aquifer (spring), with approximately 5 m width. The resistivity model showed the groundwater plumes flowing from NE to SW due to the hydraulic pressure gradient, where the saline groundwater moved or upwelled to the surface as spring (Figure 8.5).

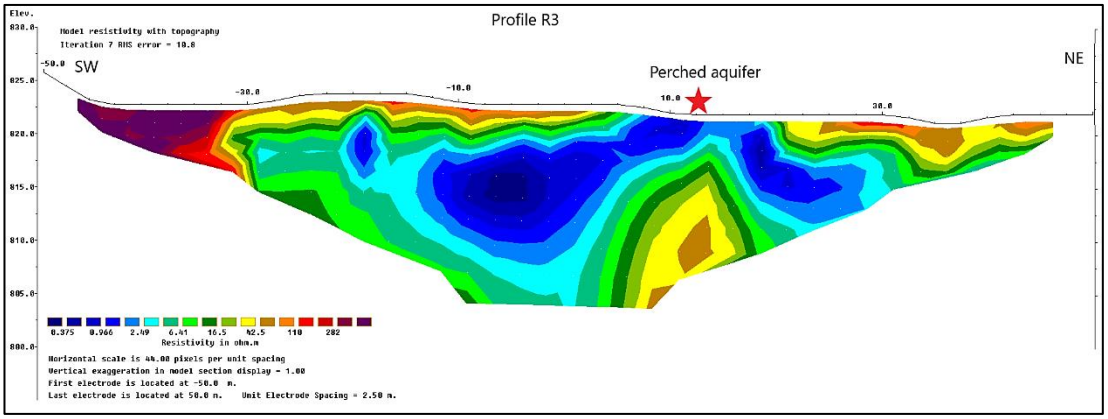

Figure 8. 5 Profile R3 - An inverse resistivity model cutting across profile R1 and profile R2 with orientation SW to NE.

Figure 8. 6 The field photography of profile R3 cut cross profile R1 and R2.

8.1.5 Profile R4

The survey line for profile R4 ran across the old well that has been depleted and dried throughout the decades which acted as the main source for the indigenous local salt production.

The above and adjacent to the traverse were the 3 existing wells, in which the reason for selecting this location is to determine the adjacent saline aquifer that acted as a reference to the targeted potential groundwater. Profile R4 was located at a lower altitude of 825 m to 830 m, whereas the existing wells were located adjacent at a higher altitude of 865 m to 870 m. The inverse resistivity model showed that the highest resistivity recorded started mostly near to the surface with a value ranging from 125 Ω.m to 233 Ω.m, indicating a layer of topsoil covering most of the entire survey line from depth < 1 m to 3.5 m. Whereas, the resistivity value of ≈ 60 Ω.m could indicate the sandy layer above the groundwater. The marked old well at a distance of 5 m from the mid-point showed very low resistivity value from 2.8 Ω.m to < 10 Ω.m, implying that the previous saline groundwater was at a depth from < 1 m to 15 m. The plume migrations clearly showed the hydraulic upwelling of saline water to the surface (Figure 8.7).

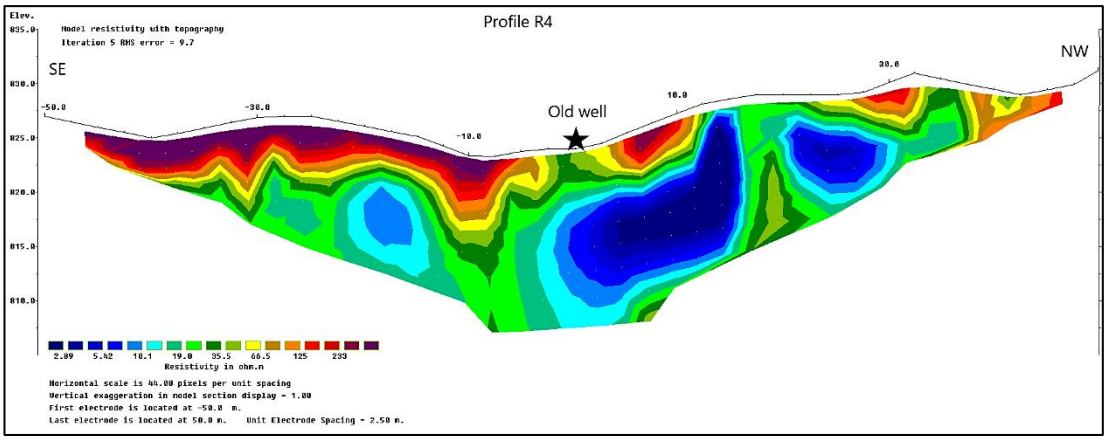

Figure 8. 7 Profile R4 - an inverse model for resistivity - orientation SE-NW.

Figure 8. 8 The field photography of profile R4 on the old existing well.

8.1.6 Profile R5

Profile R5 was located across all three existing wells in the study area. In understanding and determining the pattern and characteristic of saline groundwater, it was discovered that the wells were utilized and acted as a guide to locate and pinpoint other sources of saline groundwater on the study area site (Figure 8.10). The resistivity inverse model value showed that the highest value of 213 Ω.m to 480 Ω.m at a depth of < 1 m to 3.5 m located near the NW part could indicate the topsoil layer. Whereas, the resistivity value of ≈ 60 Ω.m could indicate the sandy layer above the saline groundwater. The three existing wells were marked at a distance location near the mid-point of 8 m, 12 m and 14 m. The inverse resistivity model value showed the lowest reading from 2.84 Ω.m to < 6 Ω.m at a depth from < 1 m to 15 m. The plume migration showed the hydraulic upwelling of saline groundwater from NW to SE orientation with a sandy layer in between and separating the plumes. Well 1 and 2 were located

below the saline plume, however, well 3 was disturbed by the sandy layer (Figure 8.9). This may be the reason that well 1 (TDS = 33,380 mg/L) and well 2 (TDS = 30,550 mg/L) gained more saline water and salt compared to well 3 (TDS = 27,440 mg/L).

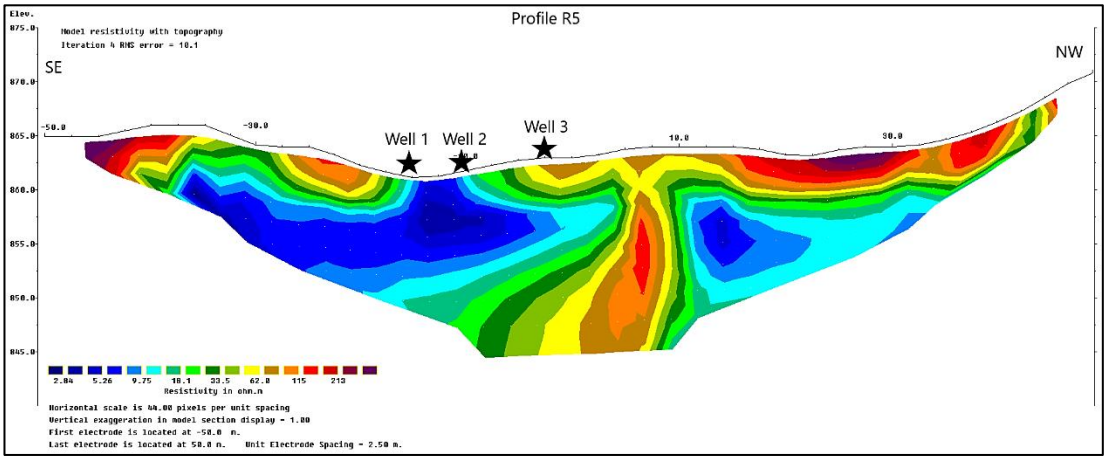

Figure 8. 9 The profile R5 showing both inverse resistivity model - orientation from SE to NW.

Figure 8. 10 The field photography of profile R5 on the well 1, 2 and 3.

The 2D resistivity survey across the study area has been a success in terms of quality of data and sufficiency in determining and locating the main target which is the potential saline groundwater. Thus, the potential sources of saline water can be explained with the 2D resistivity images. It is clear that near the perched aquifer, there will be a potential source of saline groundwater. Additionally, the groundwater flow was supported by the hydraulic gradient and topographic elevation to go for a new well.

8.2 Seismic Refraction

A total of 5 seismic refraction survey lines were conducted in Buduk Bui at the outcrop and is shown in Figure 8.1. Similar to 2D resistivity survey line, the seismic refraction survey line composed of 5 profiles with 120 m spreading length: profile S1, S2 and S3 successively transverse the perched aquifer. Furthermore, profile S4 was located between profile S3 and S5, whereas, profile S5 was situated on the existing 3 salt wells on top of the hills. The initial velocity model was created using the time-term technique (TTI), where uses a linear Least-Squares approach was used to determine the best discrete-layer. Subsequently, the refraction tomography (RT) technique was used to resolve lateral velocity and gradient changes and best applied in settings such as compaction, karst and faults zones (Jagadeshan et al., 2018; Al-Hetty, 2018). The compilation research of p-wave velocity values for fully saturated layers ranged between 1,200 m/s and 2,250 m/s (Desper et al., 2015; Araffa et al., 2017; Azhar et al., 2019).

8.2.1 Profile S1

The measurements of seismic refraction were conducted using seismograph ABEM TERRALOC PRO 2 with sampling interval set to 100 milliseconds, where the recording time was 1,024 milliseconds and the number of samples was 1,048. Profile S1 was located adjacent to the perched aquifer and was marked near the midpoint with a spreading length of 120 m and azimuth 140^0 towards NW-SE orientation. The lithology of the subsurface can be

identified by the change in travel-time slope and in seismic velocity. The primary wave velocity of the topmost layer (violet colour) where the lowest seismic velocities ranging from 727 m/s to 915 m/s was detected and corresponded to the area of topsoil which was mainly composed of unconsolidated alluvial sediments (Figure 8.12). Thickness of the first layer ranged between 1.5 m to 5 m. The second layer made up of seismic velocity ranging from 1,020 m/s to 1,900 m/s was distinguished and corresponded to a saturated layer at the depth of < 5 m (Azhar et al., 2019). The thickness of the second layer ranged between 2.5 m to 10 m. The third layer has velocity ranging between 2,050 m/s and 2,485 m/s, indicating partially saturated layer which could probably be a clayey sandy layer or a shale layer (Ibrahim, 2014; Desper et al., 2015). The model showed that at a distance of 40 m below the perched aquifer, there was a rapid lateral variation in the velocity. This variation can be interpreted as a local fault phenomenon (Ibrahim, 2018). The change of velocity has a value from 1,020 m/s to 1,900 m/s and displacement at depth of 5 m on the left-hand side (down thrown zone). Whereas, another displacement located at a distance of 90 m on the right-hand side (down thrown zone) has a velocity changing from 1,020 m/s to 2,193 m/s (Al-Hetty, 2018).

Figure 8. 11 The field photography of profile S1 stretching from SE to NW direction.

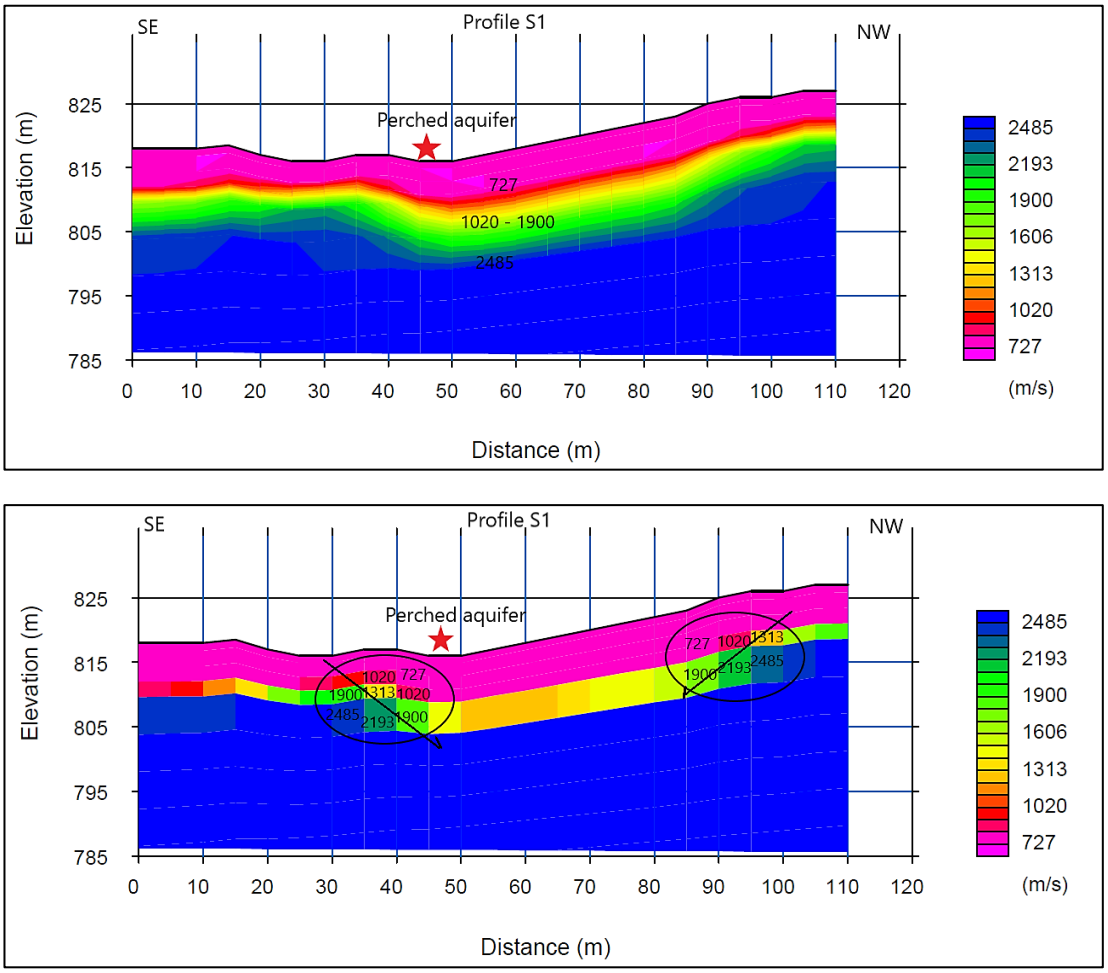

Figure 8. 12 The velocity models by tomographic method of profile S1.

8.2.2 Profile S2

The profile S2 located adjacent to profile S1 and profile S3 was used to conduct a 3D grid pattern for the target perched aquifer, with a spreading length of 120 m and 5 m geophone spacing. The first layer showed velocity value ranging from 997 m/s to 1,150 m/s, indicating unconsolidated topsoil (Figure 8.14). The thickness of the first layer was ranged from 1 m to 8 m. Whereas, the second layer showed velocity value ranging from 1,392 m/s to 2,579 m/s, indicating a fully saturated layer of sandstone from Meligan Formation (Pasquet et al., 2015; Abdullah et al., 2017). The saturated layer was estimated to be at depth of 5 m to 10 m below the surface. The third layer has a velocity ranging from 2,973 m/s to 3,370 m/s, and corresponded to the possibility of shale layer of Setap Formation (Ibrahim, 2014; Wang et al.,

2016). The shallow localized faults appeared below the perched aquifer at the distance of 50 m (down thrown zone) with rapid lateral velocity change from 1,200 m/s to 2,579 m/s and at the distance of 75 m (down thrown zone) with p-wave velocity changing from 1,300 m/s to 2,500 m/s. Meanwhile, additional location at distance of 95 m on the right-hand side (down thrown zone) has a change of velocity from 1,300 m/s to 2,100 m/s (Al-Hetty, 2018).

Figure 8. 13 The field photography of profile S2 stretching from SE to NW direction.

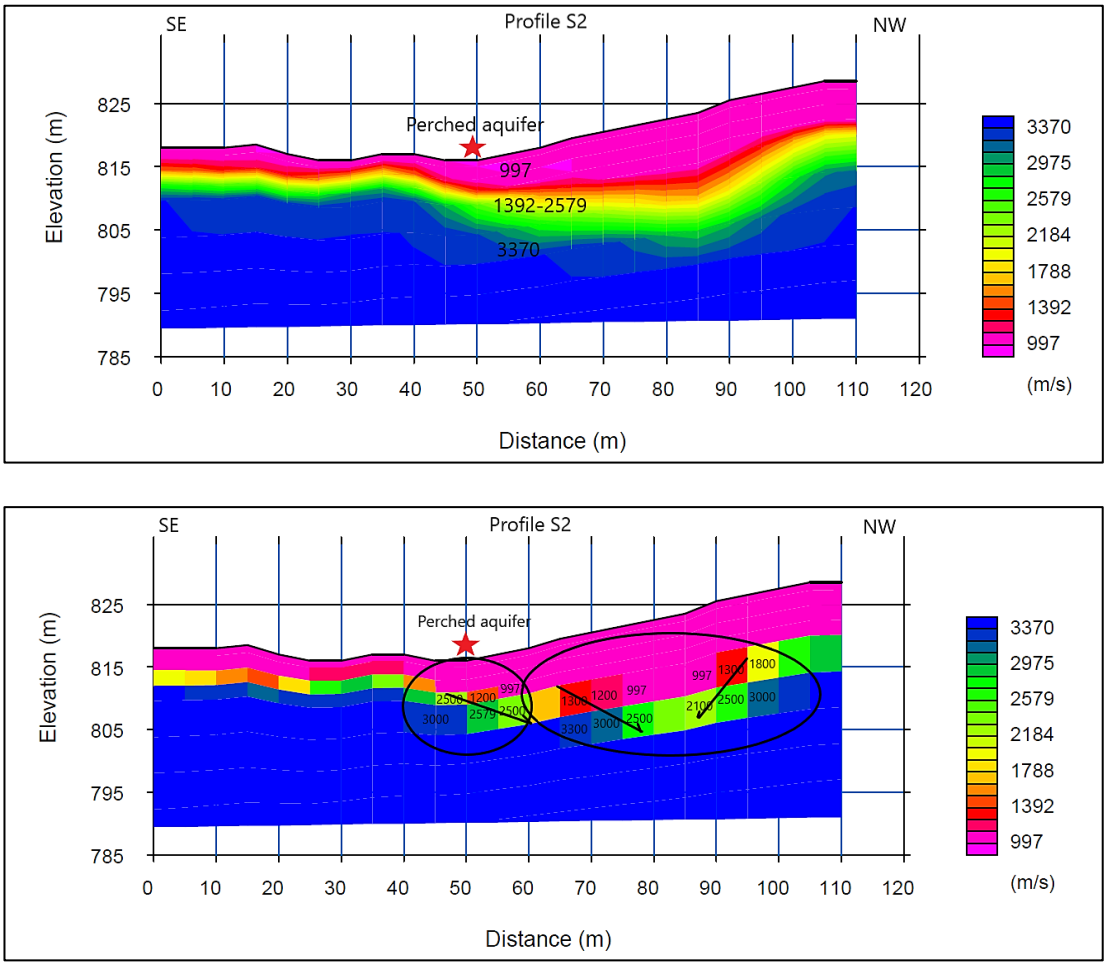

Figure 8. 14 The velocity models by tomographic method for profile S2.

8.2.3 Profile S3

The profile S3 survey line spreading almost perpendicular across profile S1 and profile S2 was used to conduct 3D concept view for the main target perched aquifer which was marked at the distance of 20 m towards NW. The first layer showing a velocity value ranging from 1,002 m/s to 1,150 m/s indicated partly saturated topsoil with thickness of 4 m to 6 m (Figure 8.16). The second layer showing a velocity value of 1,345 m/s to 2,375 m/s indicated a fully saturated layer (Pasquet et al., 2015) with thickness ranging between 1.5 m to 10 m. The third layer has velocity ranging between 2,718 m/s to 3,060 m/s, which probably indicated a shale layer at depth of 10 m to 25 m (Ibrahim, 2014). The localized faults were detected at a distance of 20 m with depth < 5 m, indicating rapid lateral change of velocity from 1,345 m/s to 2,375

m/s. Additionally, at distance 75 m below the marked perched aquifer, fault (stair step structure) was shown with a change in velocity from 1,700 m/s to 2,500 m/s (Al-Hetty, 2018).

Figure 8. 15 The field photography of profile S3 stretching from NE to SW direction.

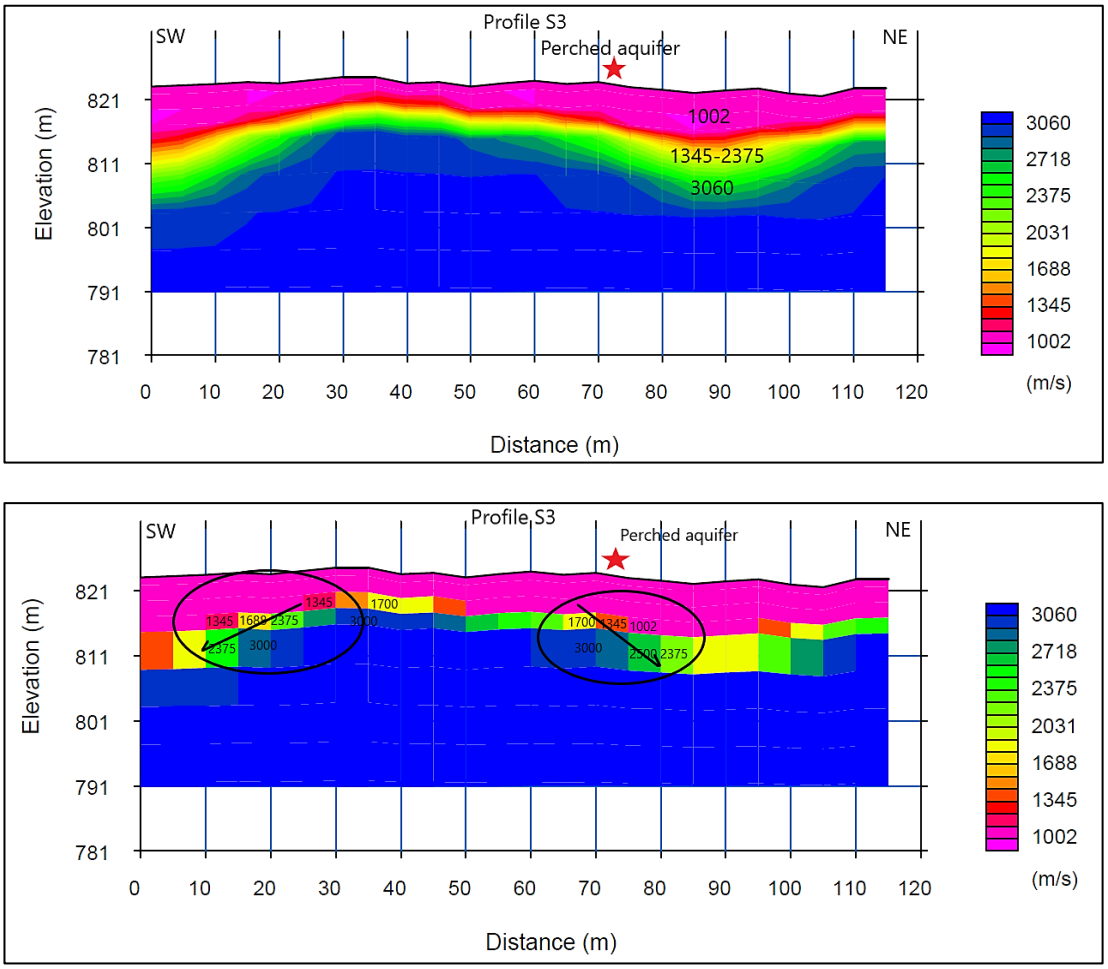

Figure 8. 16 The velocity models by tomographic method for profile S3.

8.2.4 Profile S4

Profile S4 located next to profile S3 with survey line extending towards SW was used to locate any possibility of extension of the perched aquifer. The first layer showed the velocity value of 209 m/s to 315 m/s, indicating a highly weathered soil layer with thickness ranging between 4 m to 15 m, with the center of the profile being thicker (Figure 8.18). The second layer showed the velocity value of 528 m/s to 846 m/s, indicating the partially weathered soil layer (Azhar et al., 2019). This location revealed no saturated layer of the extended potential perched aquifer towards the SW direction, however the velocity model showed a depression structure at distance of 40 m to 80 m.

Figure 8. 17 The field photography of profile S4 stretching from NE to SW direction.

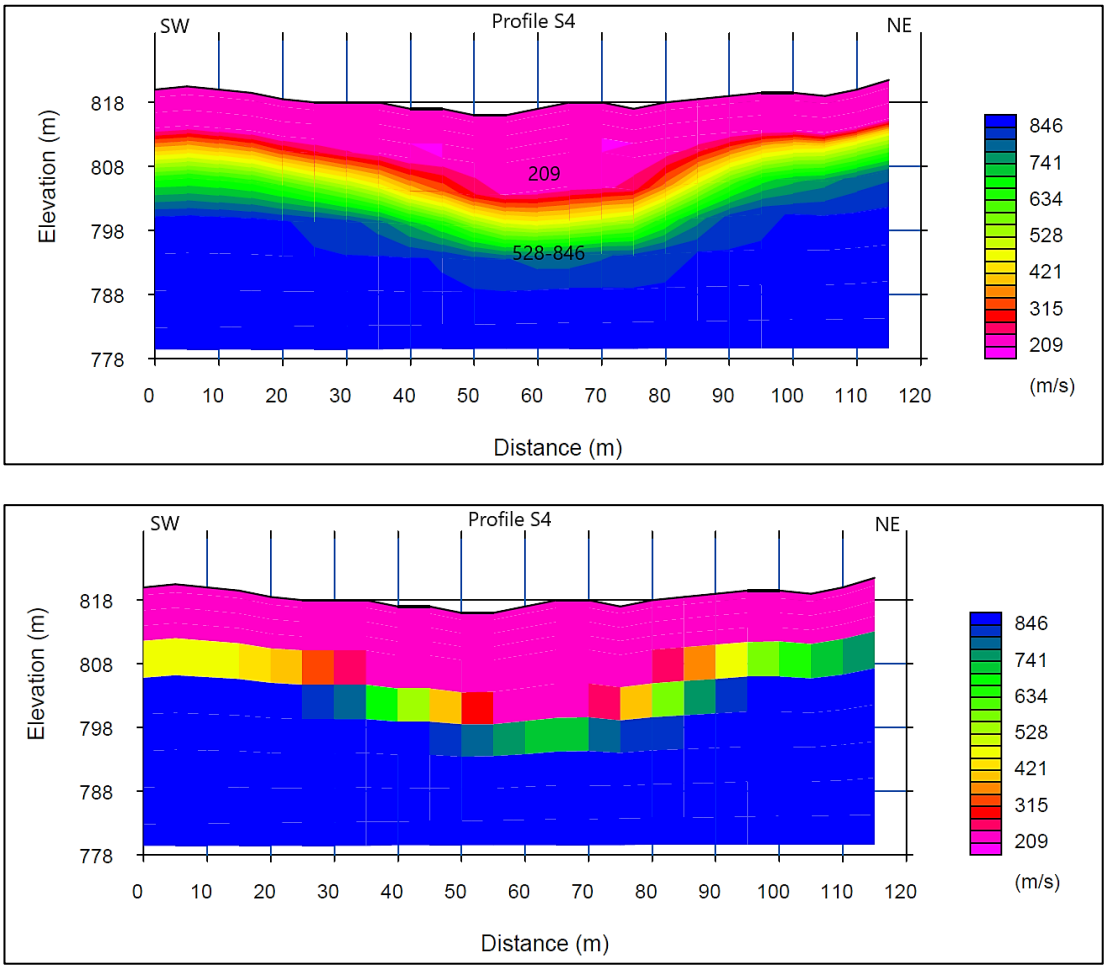

Figure 8. 18 The velocity models by tomographic method for profile S4

8.2.5 Profile S5

Profile S5 was located across all 3 existing wells in the study area. The first layer of the seismic velocity ranging from 524 m/s to 850 m/s indicated that the topsoil of the wells has thickness ranging between 2 m to 10 m (Figure 8.20). The second layer velocity ranging from 1,097 m/s to 2,091 m/s suggested the fully saturated zone (saline groundwater) with thickness ranging between 5 m to 9 m. For this location, the water table was estimated to be at a depth of < 10 m below the surface. The third layer has a velocity of 2,588 m/s, probably indicating the presence of fully saturated clayey sandy layer (Ibrahim, 2014). The fault was detected below well 3 at a depth of 10 m and at a distance of 80 m towards NW direction, with rapid lateral change of velocity from 1,097 m/s to 2,091 m/s (down thrown zone) (Al-Hetty, 2018).

Figure 8. 19 The field photography of profile S5 on the existing wells stretching from SE to NW direction.

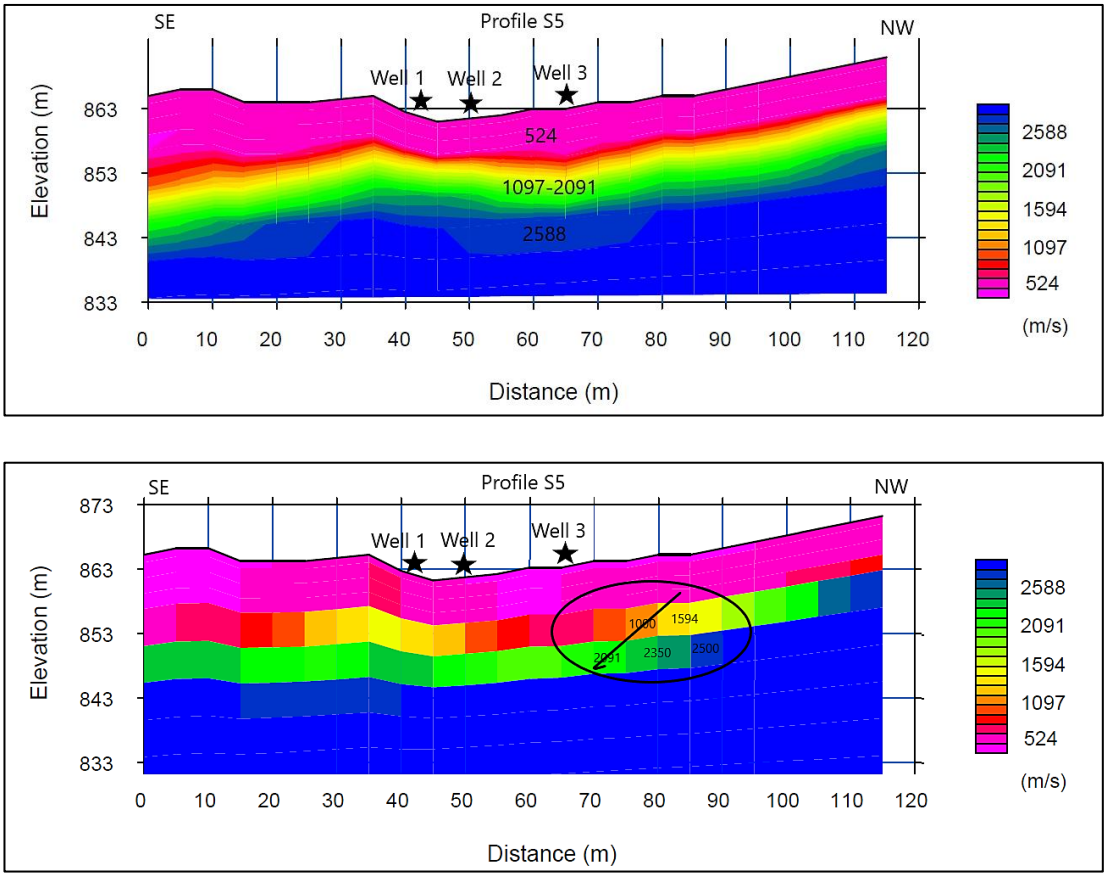

Figure 8. 20 The velocity models by tomographic method for profile S5

The seismic refraction survey across the study area has been a successful progress in terms of determining the subsurface lithologies and structures such as saturated layers and shallow localized faults, respectively. The seismic refraction penetration was shallow with a depth between 15 to 20 m, in which this indicated localized shallow faults in the study area. Nonetheless, there is no correlation or connection between the main target perched aquifer with the existing wells aquifer.

8.3 Discussion

8.3.1 Correlation of 2D Resistivity and Seismic Refraction in 3D Display

For profile R1 and S1, the 2D resistivity model showed that the high resistivity (in dark brown and red) was extended from SE to the midpoint direction at a distance of 40 m, where the resistivity was rapidly changing to lower values (in blue) (Figure 8.21). This rapid change in resistivity below the marked perched aquifer indicated the presence of shallow fault at a distance of 40 m and 60 m (Ibrahim, 2014). This corresponded with what was found during the seismic refraction survey, where velocity model showed the same (Figure 8.21) (Al-Hetty, 2018). At profile R2 and S2 (Figure 8.22), the seismic p-wave velocity model showed the presence of shallow fault at a distance of 25 m and 75 m, where resistivity model showed the rapid change in resistivity at depth of 5 m from 0.2 Ω.m to 500 Ω.m, therefore illustrating a similar fault pattern. Whereas, at profile R3 and S3, the resistivity model showed that the high resistivity value of 282 Ω.m was extended from SW's midpoint near the perched aquifer mark, where the resistivity was rapidly changing to lower values of 0.3 Ω.m (Figure 8.23). At the depth of 5 m to 10 m below, the perched aquifer mark showed two groundwater plumes with low resistivity values separated by rapid change due to high resistivity values, indicating the presence of shallow fault and similar fault pattern that was found in seismic refraction survey.

The 3D-like profiles were displayed by combining the 2D resistivity (Figure 8.24) and seismic profile images (Figure 8.25) from 3 survey profiles in the study area. This 3D profiles provided a clearer image of the subsurface and helped in better understanding of the groundwater structures and flow. In Figure 8.24, the 3D profile of 2D resistivity profile consisted of profile R1, R2 and R3 at the main target perched aquifer. The image showed that the groundwater was at the depth of 2 m to 15 m below the surface, whereas the groundwater plume flowed from SW to NE direction due to the hydraulic pressure gradient of the saline groundwater that moved from the higher elevation from NW to SE and upwelling to the surface as the perched water table intersected with the ground surface. Figure 8.25 shows the fault in the rapid lateral change in velocity of the second and third zones, and are marked in black circle. The localized fault profile 1 was detected at a distance of 30 m towards NW and 90 m

towards SE direction. Profile R2 was at a distance of 75 m dipping NW and 95 m dipping SE, thus, both profiles showed graben fault structure due to depression with the fact that it was in a valley. For profile R3, the fault was located at the perched aquifer at 75 m marked, illustrating normal fault structure (Ibrahim, 2014; Al-Hetty, 2018). The localized shallow faults detected were close to the perched aquifer, therefore suggesting that this not connected with the existing wells aquifer. However, it is clear that the perched aquifer has the potential to provide sufficient supply of saline groundwater for future drilling sites in the study area.

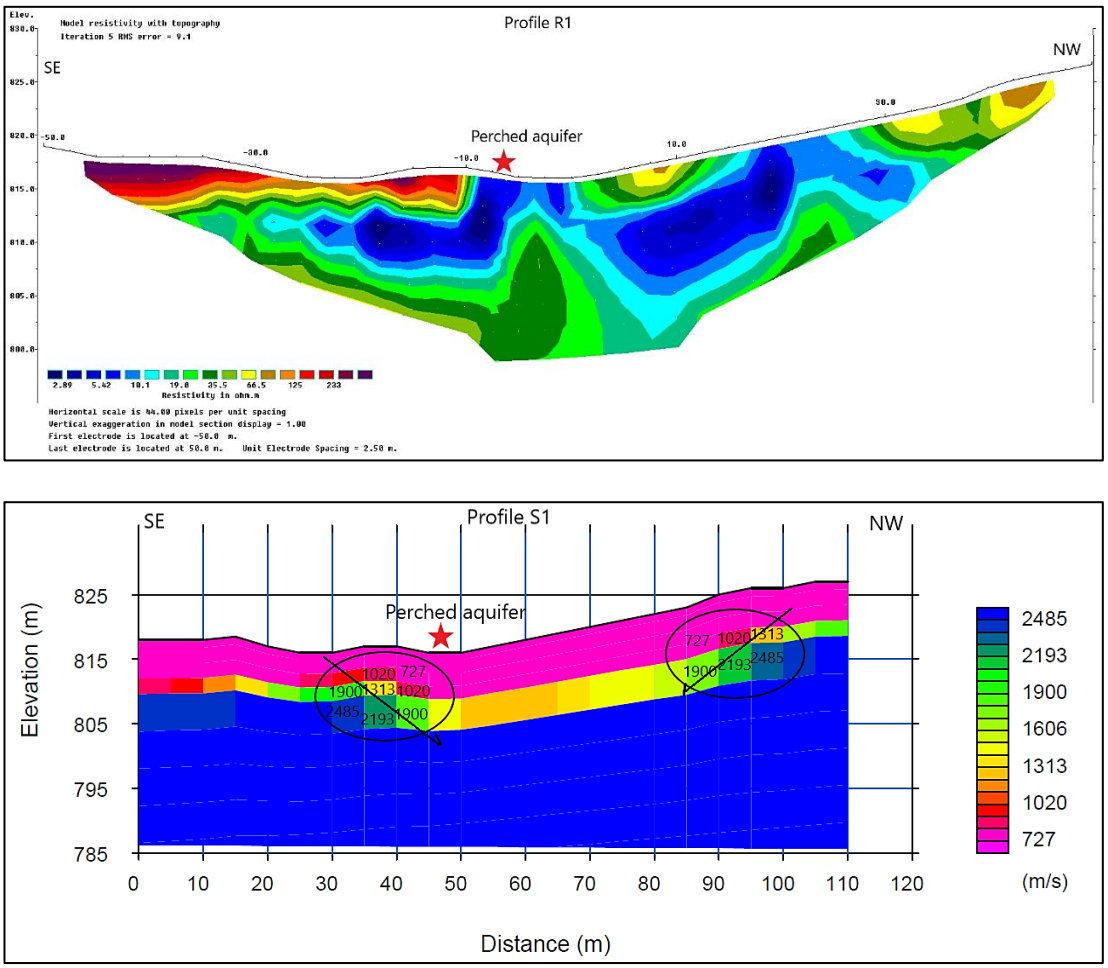

Figure 8. 21 The subsurface image of 2D resistivity and seismic refraction for profile 1.

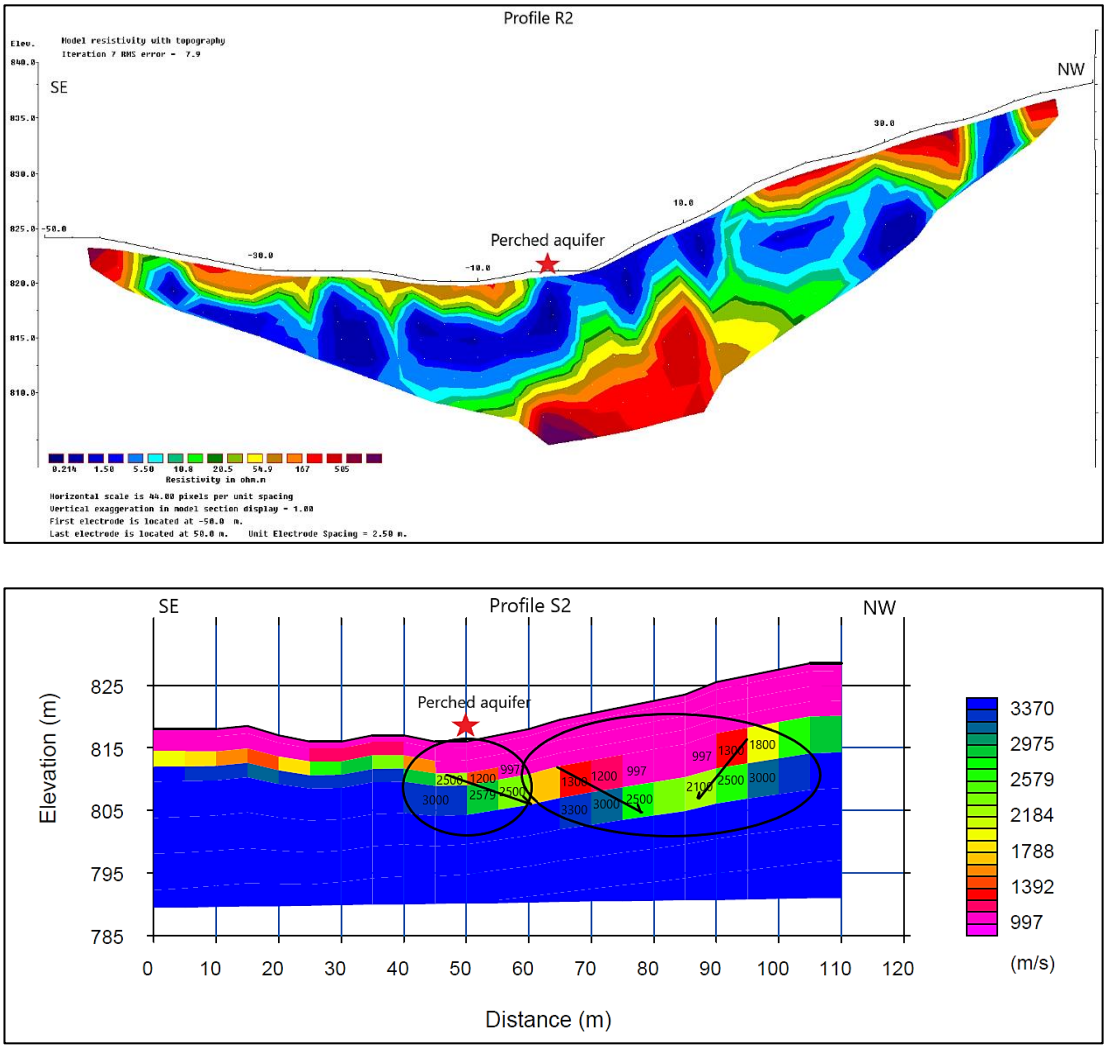

Figure 8. 22 The subsurface image of 2D resistivity and seismic refraction for profile 2.

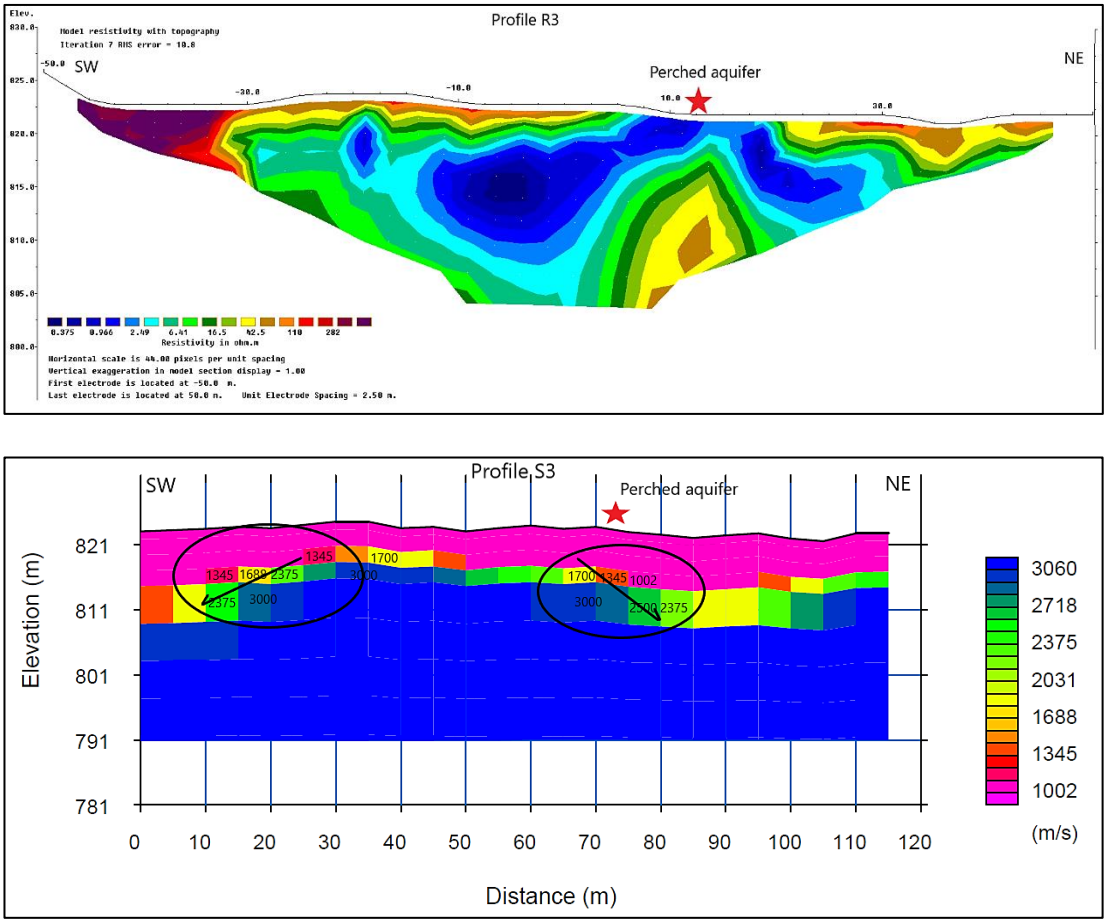

Figure 8. 23 The subsurface image of 2D resistivity and seismic refraction for profile 3.

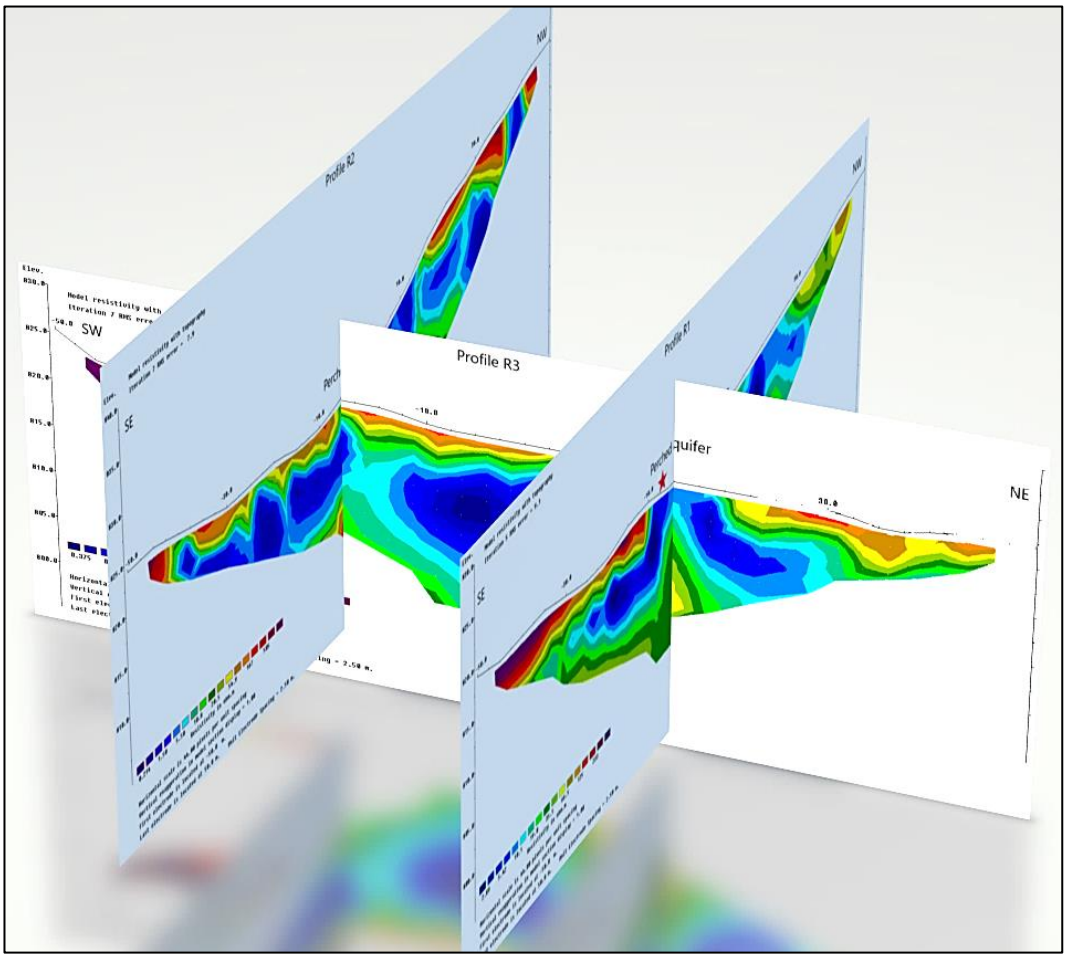

Figure 8. 24 The 3D profile for 2D resistivity of profile R1, R2 and R3.

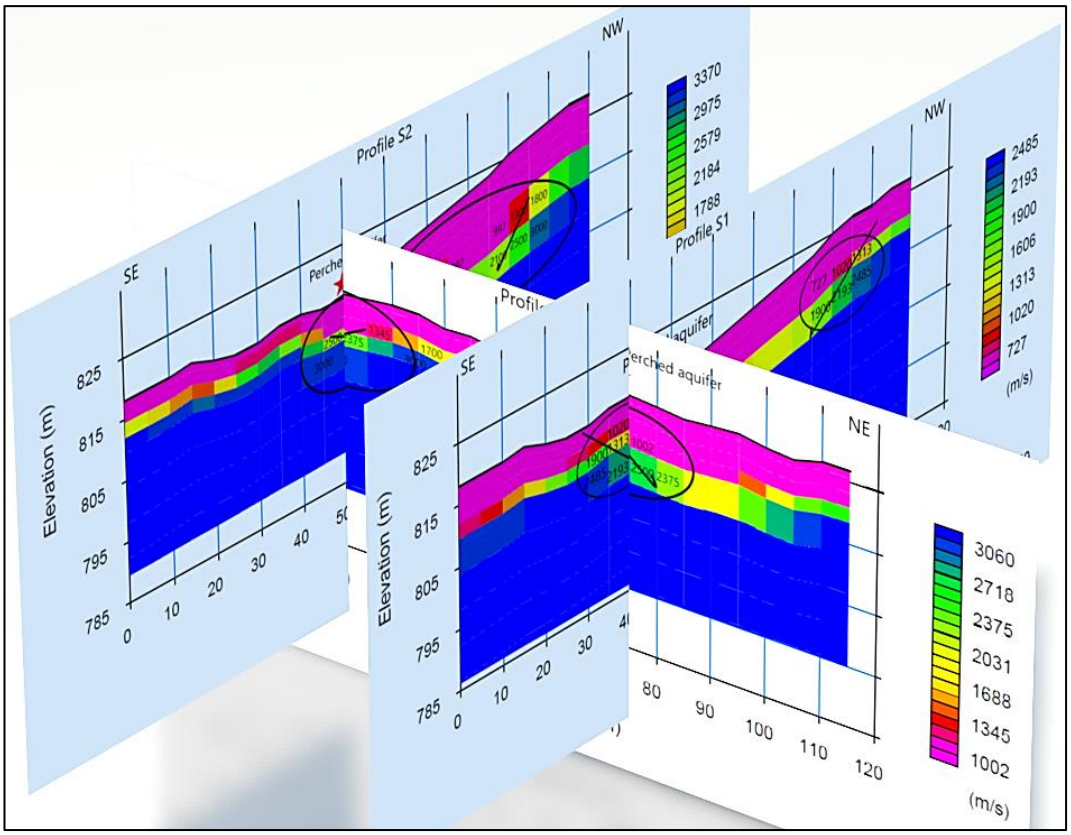

Figure 8. 25 The 3D profile for seismic refraction of profile S1, S2 and S3.

CHAPTER. 9 Conclusion

9.1 Conclusion

The main aim of this research is to locate the potential sources of saline groundwater to identify the lithological and structural controls on saline groundwater and to determine the evolution, origin and hydrochemical characteristic of saline groundwater. According to the results, the interpretation and discussion made in the previous chapters, the following conclusions are derived:

1. The physical and chemical measurement in well 1, 2 and 3 were categorized as highly saline to brine water (TDS = 10,000 – 100,000 mg/L and EC = > 45,000 µS/cm), whereas well 4 and 5 were highly saline (TDS = 10,000 – 100,000 mg/L and EC = 10,000 – 45,000 µS/cm).
2. The physical parameter measurement made from December 2018 to January 2019 reflected a significant increase in TDS, EC and salinity in all the wells due to seasonal variation with a trend along the topography gradient from downstream to upstream where: well 1 (913 m) > well 2 (913 m) > well 3 (914 m) > well 5 (948 m) > well 4 (967 m).
3. The hourly and daily observation on water level fluctuation reflected the changes in groundwater recharge.
4. The orders of dominance of ions in MON and POM are as follows: $Na^+ > Ca^{2+} > Mg^{2+} > K^+ = Cl^- > HCO_3^- > NO_3^- > SO_4^{2-}$, whereas for river samples, it is depicted as $Na^+ > Mg^{2+} > Ca^{2+} > K^+ = HCO_3 > Cl^- > NO_3^- > SO_4^{2-}$.
5. The groundwater samples are classified as Na^+-Cl^- type based on Piper, Durov and Van Wirdum's diagrams. Furthermore, according to Gibbs diagram and ionic ratios, the groundwater was inferred to be dominated by dissolution of evaporites. The scatter plot of Na/Cl ranged from 0.85 to 0.90, with an increasing ratio in the POM season, indicating halite dissolution and ion exchange processes responsible for the deviation of Na/Cl ratio.

6. The reverse ion exchange process was inferred to occur in the MON season, whereas the ion exchange and carbonate dissolution processes were predominant in the POM season.
7. The Brine Differentiation Plot (BPS), Langelier-Ludwig diagram and Na^{+}/Li plot indicated that the groundwater samples reflected similar groundwater composition to that of oil field Ca^{2+}-Cl^{-} brines.
8. Enriched $\delta^{18}O$, δD and low d-excess values of groundwater samples indicated its origin from high intense evaporation water source.
9. Stable isotope $\delta^{37}Cl$, $\delta^{11}B$ and $\delta^{34}S$ in groundwater samples indicated halite dissolution, marine evaporites dissolution and oxidation of sulfide (pyrite), respectively (Du et al., 2019; Ercan et al., 2019; Karakaya et al., 2019; Mirzavand et al., 2020b).
10. The XRD data of the produced salts from the study area indicated that halite is the dominant mineral with minor percentage of aragonite and orthoclase minerals (Lindholm, 2012). The saturation states of the groundwater also reflected oversaturation of aragonite, dolomite, calcite and undersaturation of halite, gypsum, anhydrite minerals.
11. The 2D resistivity method suggested that the lowest resistivity value of 0.2 Ω.m – 2.84 Ω.m indicated that the saline groundwater was located at the existing well sites and the perched aquifer with water source showed an upwelling structure. Nonetheless, there were no connections with each other. Whereas, the resistivity value of ≈ 60 Ω.m suggested a sandy layer and the highest resistivity value of 115 Ω.m – 505 Ω.m indicating the weathered topsoil layer.
12. The seismic refraction suggested the first layer velocity ranging between 209 m/s to 991 m/s indicating the unconsolidated weathered topsoil. The second layer velocity ranging between 1,329 m/s to 2,579 m/s indicated a fully saturated layer of saline groundwater. For the third layer with velocity ranging from 2,718 m/s to 3,370 m/s this indicated shale layer, which is correlated with the resistivity data.
13. The fault was detected in profile S1 and S2 at a distance of 45 m below the perched aquifer and 90 m on the foothill, illustrating graben fault structure. Whereas, the fault

detected in profile S3 at the distance of 75 m below the perched aquifer, illustrated the upwelling anticline structure. The presence of faults near to the perched aquifer has facilitated the groundwater movement from the saturated zone to the surface, however there was no connection with the existing wells. The rapid change in resistivity and velocity below the perched aquifer indicated the presence of localized shallow fault in the study area.

Hence, the study infers that there is an increase in salinity of groundwater with respect to season affecting the amount of salt production. Based on the results of the geochemical and geophysical studies, the source of the existing well water was mainly due to the dissolution of brine and they were connected through a fault system reaching the shallow levels. Nonetheless, the presence of the perched aquifer in the study area was not connected with the existing wells. But based on the geophysical studies, the perched aquifer indicated the most suitable and potential area to drill in getting more saline groundwater. Whereas, the saline groundwater chemistry would provide knowledge on the saline groundwater characteristics, which can be used for agriculture purposes especially for high salinity tolerant crops in near future. To obtain a more confirmative evidence on the origin and source of the well water, more rainwater, groundwater and surface water samples are to be collected throughout the study area. Furthermore, a regional pattern on the sedimentation and the structure of the basin are to be correlated with the aid of remote sensing techniques.

9.2 Limitation of the Study

1. Lack of details on depth-wise aquifer characteristics in the study area in order to correlate with the geophysical results.
2. The study area is located in a remote area with a limited number of existing wells located in inaccessible locations, which make it difficult to gather data for both water chemistry and geophysics.

3. Insufficient isotope data for water samples to justify more on the origin and sources of saline groundwater.

9.3 Future Recommendation

There are some recommendations that can be stated for further investigations:

1. To further study the aquifer characteristics of this region to delineate the occurrence of saline groundwater in more detail.
2. Remote sensing technique with GIS can be deployed to generate regional geomorphology and geology in order to trace the saline groundwater in regional scale.
3. Regional study for geophysical method such as seismic reflection would provide better image and deeper penetration for the geological structures in subsurface.

References (APA 6th Edition)

Abdullah, W. H., Togunwa, O. S., Makeen, Y. M., Hakimi, M. H., Mustapha, K. A., Baharuddin, M. H., & Tongkul, F. (2017). Hydrocarbon source potential of eocene-miocene sequence of western sabah, Malaysia. *Marine and Petroleum Geology*, *83*, 345-361.

Abdulrahman, A., Nawawi, M., Saad, R., Abu-Rizaiza, A. S., Yusoff, M. S., Khalil, A. E., & Ishola, K. S. (2016). Characterization of active and closed landfill sites using 2D resistivity/IP imaging: case studies in Penang, Malaysia. *Environmental Earth Sciences*, *75*(4), 347.

Abd-Razak, Y., & Abd-Karim, M. H. (2009). Groundwater colloquium: groundwater management in Malaysia—status and challenges. *Akademi Sains Malaysia, Putrajaya*.

Acosta, J. A., Jansen, B., Kalbitz, K., Faz, A., & Martínez-Martínez, S. (2011). Salinity increases mobility of heavy metals in soils. *Chemosphere*, *85*(8), 1318-1324.

Adelinet, M., Dominguez, C., Fortin, J., & Violette, S. (2018). Seismic-refraction field experiments on Galapagos Islands: A quantitative tool for hydrogeology. *Journal of Applied Geophysics*, *148*, 139-151.

Aghazadeh, N., & Mogaddam, A. A. (2011). Investigation of hydrochemical characteristics of groundwater in the Harzandat aquifer, Northwest of Iran. *Environmental monitoring and assessment*, *176*(1-4), 183-195.

Aghazadeh, N., Chitsazan, M., & Golestan, Y. (2017). Hydrochemistry and quality assessment of groundwater in the Ardabil area, Iran. *Applied Water Science*, *7*(7), 3599-3616. https://doi.org/10.1007/s13201-016-0498-9

Al-Bassam, A. M., & Khalil, A. R. (2012). DurovPwin: a new version to plot the expanded Durov diagram for hydro-chemical data analysis. *Computers & geosciences*, *42*, 1-6.

Alekseeva, L. P., & Alekseev, S. V. (2018). Geochemistry of ground ice, saline groundwater, and brines in the cryoartesian basins of the northeastern Siberian Platform. *Russian Geology and Geophysics*, *59*(2), 144-156. https://doi.org/10.1016/j.rgg.2018.01.012

Alexeev, S. V., Alexeeva, L. P., & Vakhromeev, A. G. (2020). Brines of the Siberian platform (Russia): Geochemistry and rocessing prospects. *Applied Geochemistry*, 104588.

Alhassan, D. U., Ugbor, D. O., Ejepu, S. J., Mufutau, O. J., & Mohammed, A. (2015). Seismic refraction survey for groundwater potentials of northern Paiko area, Niger State, Nigeria. *IOSR Journal Applied Geology and Geophysics*, *3*(2), 41-48. https://doi.org/10.9790/0990-03214148

Alhassan, D. U., Obiora, D. N., Okeke, F. N., & Ibuot, J. U. (2018). Investigation of groundwater potential of southern Paiko, northcentral Nigeria, using seismic refraction method. *Modeling Earth Systems and Environment*, *4*(2), 555-564. https://doi.org/10.1007/s40808-018-0452-y

Al-Heety, A. (2018). An Evaluation between Time-term, Reciprocal Time and Refraction Tomography Analysis Methods for obtaining 2-D shallow Seismic Velocity Models over Synthetic Traveltimes.

Al-Obaidy, A. H. M. J., & Joshi, H. (2006). Chemical composition of rainwater in a tropical urban area of northern India. *Atmospheric Environment*, *40*(35), 6886-6891.

Al-Shuhail, A. A., & Al-Shaibani, A. M. (2013). Characterization of Sabkha Jayb Uwayyid, eastern Saudi Arabia using seismic refraction profiling. *Arabian Journal of Geosciences*, *6*(3), 845-855. https://doi.org/10.1007/s12517-011-0366-8

Al-Zubedi, A. S., & Thabit, J. M. (2014). Comparison between 2D imaging and vertical electrical sounding in aquifer delineation: a case study of south and south west of Samawa City (IRAQ). *Arabian Journal of Geosciences*, *7*(1), 173-180. https://doi.org/10.1007/s12517-012-0788-y

Aizebeokhai, A. P., Oyeyemi, K. D., & Joel, E. S. (2016). Groundwater potential assessment in a sedimentary terrain, southwestern Nigeria. *Arabian Journal of Geosciences*, *9*(7), 496.

Akinbiyi, O. A., Oladunjoye, M. A., Sanuade, O. A., & Oyedeji, O. (2019). Geophysical characterization and hydraulic properties of unconsolidated floodplain aquifer system in Wamako area, Sokoto State, north-western Nigeria. *Applied Water Science*, *9*(8), 177.

Akoto, O., Teku, J. A., & Gasinu, D. (2019). Chemical characteristics and health hazards of heavy metals in shallow groundwater: case study Anloga community, Volta Region, Ghana. *Applied Water Science*, *9*(2), 36.

Ammar, S. B., Taupin, J. D., Alaya, M. B., Zouari, K., Patris, N., & Khouatmia, M. (2020). Using geochemical and isotopic tracers to characterize groundwater dynamics and salinity sources in the Wadi Guenniche coastal plain in northern Tunisia. *Journal of Arid Environments*, *178*, 104150.

APHA, A. (1998). Standard methods for the examination of water and wastewater, American Public Health Association. *Inc., Washington. DC*.

Anomohanran, O., Ofomola, M. O., & Okocha, F. O. (2017). Investigation of groundwater in parts of Ndokwa District in Nigeria using geophysical logging and electrical resistivity methods: Implications for groundwater exploration. *Journal of African Earth Sciences*, *129*, 108-116.

Appelo, C. A. J., & Postma, D. (1996). Ion exchange and sorption. *Geochemistry, Groundwater and Pollution*, 142-201.

Appelo, C. A. J., & Postma, D. (2005). Geochemistry, groundwater and pollution. 2nd. *Ed. Balkema, Rotterdam*.

Aquilano, D., Otálora, F., Pastero, L., & García-Ruiz, J. M. (2016). Three study cases of growth morphology in minerals: Halite, calcite and gypsum. *Progress in Crystal Growth and Characterization of Materials*, *62*(2), 227-251.

Araffa, S. A. S., Mohamed, A. M., & Santos, F. M. (2017). Geophysical investigation in the Northwestern part of the Gulf of Suez, Egypt. *Egyptian journal of petroleum*, *26*(2), 457-475. https://doi.org/10.1016/j.ejpe.2016.06.002

Asry, Z., Samsudin, A. R., Yaacob, W. Z., & Yaakub, J. (2012). Groundwater Exploration Using 2-D Geoelectrical Resistivity Imaging Technique at Sungai. Udang, Melaka. *Journal of Earth Science and Engineering*, *2*(10), 624.

Auge, M. (2016). *Hydrogeology of Plains* (1st ed., pp. 8-35). Springer International Publishing. https://doi.org/10.1007/978-3-319-31429-7

Awaleh, M. O., Baudron, P., Soubaneh, Y. D., Boschetti, T., Hoch, F. B., Egueh, N. M., ... & Gassani, J. (2017). Recharge, groundwater flow pattern and contamination processes in an arid volcanic area: insights from isotopic and geochemical tracers (Bara aquifer system, Republic of Djibouti). *Journal of Geochemical Exploration*, *175*, 82-98.

Awaleh, M. O., Boschetti, T., Soubaneh, Y. D., Kim, Y., Baudron, P., Kawalieh, A. D., ... & Adiyaman, Ö. (2018). Geochemical, multi-isotopic studies and geothermal potential evaluation of the complex Djibouti volcanic aquifer (Republic of Djibouti). *Applied geochemistry*, *97*, 301-321.

Awaleh, M. O., Boschetti, T., Adaneh, A. E., Daoud, M. A., Ahmed, M. M., Dabar, O. A., & Kadieh, I. H. (2020). Hydrochemistry and multi-isotope study of the waters from Hanlé-Gaggadé grabens (Republic of Djibouti, East African Rift System): A low-enthalpy geothermal resource from a transboundary aquifer. *Geothermics*, *86*, 101805.

Ayolabi, E. A., Adeoti, L., Oshinlaja, N. A., Adeosun, I. O., & Idowu, O. I. (2009). Seismic refraction and resistivity studies of part of Igbogbo township, south-west Nigeria.

Aziz, N. I. A., & Othman, N. (2017). Groundwater Quality and Soil Characterization: A Case Study at Bukit Tembaga, Kuala Nerang, Kedah. In *MATEC Web of Conferences* (Vol. 103, p. 05011). EDP Sciences. https://doi.org/10.1051/matecconf/201710305011

Azwin, I. N., Saad, R., & Nordiana, M. (2013). Applying the seismic refraction tomography for site characterization. *APCBEE procedia*, *5*, 227-231. https://doi.org/10.1016/j.apcbee.2013.05.039

Bagheri, R., Nadri, A., Raeisi, E., Eggenkamp, H. G. M., Kazemi, G. A., & Montaseri, A. (2014a). Hydrochemical and isotopic (δ18O, δ2H, 87Sr/86Sr, δ37Cl and δ81Br) evidence for the origin of saline formation water in a gas reservoir. *Chemical Geology*, *384*, 62-75.

Bagheri, R., Nadri, A., Raeisi, E., Kazemi, G. A., Eggenkamp, H. G. M., & Montaseri, A. (2014b). Origin of brine in the Kangan gasfield: isotopic and hydrogeochemical approaches. *Environmental earth sciences*, *72*(4), 1055-1072.

Bartolino, J. R., & Cole, J. C. (2002). *Ground-water resources of the middle Rio Grande basin, New Mexico* (No. 1222). US Geological survey.

Barzegar, R., Moghaddam, A. A., Nazemi, A. H., & Adamowski, J. (2018). Evidence for the occurrence of hydrogeochemical processes in the groundwater of Khoy plain, northwestern Iran, using ionic ratios and geochemical modeling. *Environmental Earth Sciences*, *77*(16), 597.

Beaty, B. E. (2002). Ground-water resource availability. West Fork and White River Basin, Indiana: Department of Natural Resources Report, 6, 119.

Birks, S. J., Fennell, J. W., Gibson, J. J., Yi, Y., Moncur, M. C., & Brewster, M. (2019). Using regional datasets of isotope geochemistry to resolve complex groundwater flow and formation connectivity in northeastern Alberta, Canada. *Applied Geochemistry*, *101*, 140-159.

Belkhiri, L., Mouni, L., Narany, T. S., & Tiri, A. (2017). Evaluation of potential health risk of heavy metals in groundwater using the integration of indicator kriging and multivariate statistical methods. *Groundwater for Sustainable Development*, *4*, 12-22.

Bershaw, J. (2018). Controls on deuterium excess across Asia. *Geosciences*, *8*(7), 257.

Bhandary, H., Sabarathinam, C., & Al-Khalid, A. (2018). Occurrence of hypersaline groundwater along the coastal aquifers of Kuwait. *Desalination*, *436*, 15-27. https://doi.org/10.1016/j.desal.2018.02.004

Bhattacharya, A. R. (2005). A classification of Folds: Role of Axial angle and Thickness Ratio. *Geoinformatics*, *16*(1), 27-34.

Biyada, S., Merzouki, M., Elkarrach, K., & Benlemlih, M. (2020). Spectroscopic characterization of organic matter transformation during composting of textile solid waste using UV-Visible spectroscopy, Infrared spectroscopy and X-ray diffraction (XRD). *Microchemical Journal*, 105314.

Boschetti, T., Cortecci, G., Barbieri, M., & Mussi, M. (2007). New and past geochemical data on fresh to brine waters of the Salar de Atacama and Andean Altiplano, northern Chile. *Geofluids*, *7*(1), 33-50.

Boschetti, T., Toscani, L., Shouakar-Stash, O., Iacumin, P., Venturelli, G., Mucchino, C., & Frape, S. K. (2011). Salt waters of the Northern Apennine Foredeep Basin (Italy): origin and evolution. *Aquatic Geochemistry*, *17*(1), 71-108.

Boschetti, T., Angulo, B., Cabrera, F., Vásquez, J., & Montero, R. L. (2016). Hydrogeochemical characterization of oilfield waters from southeast Maracaibo Basin (Venezuela): Diagenetic effects on chemical and isotopic composition. *Marine and Petroleum Geology*, *73*, 228-248.

Bourg, A. C. M., & Loch, J. G. (1995). Mobilization of heavy metals as affected by pH and redox conditions. In *Biogeodynamics of pollutants in soils and sediments* (pp. 87-102). Springer, Berlin, Heidelberg.

Bozau, E., Sattler, C. D., & van Berk, W. (2015). Hydrogeochemical classification of deep formation waters. *Applied Geochemistry*, *52*, 23-30.

Bragg, W. H., & Bragg, W. L. (1913). The reflection of X-rays by crystals. *Proceedings of the Royal Society of London. Series A, Containing Papers of a Mathematical and Physical Character*, *88*(605), 428-438.

Brodie, R., Sundaram, B., Tottenham, R., Hostetler, S., & Ransley, T. (2007). An overview of tools for assessing groundwater-surface water connectivity. *Bureau of Rural Sciences, Canberra, Australia*, *133*.

Busico, G., Cuoco, E., Kazakis, N., Colombani, N., Mastrocicco, M., Tedesco, D., & Voudouris, K. (2018). Multivariate statistical analysis to characterize/discriminate between anthropogenic and geogenic trace elements occurrence in the Campania Plain, Southern Italy. *Environmental pollution*, *234*, 260-269.

Cable Rains, M., Fogg, G. E., Harter, T., Dahlgren, R. A., & Williamson, R. J. (2006). The role of perched aquifers in hydrological connectivity and biogeochemical processes in vernal pool landscapes, Central Valley, California. *Hydrological Processes: An International Journal*, *20*(5), 1157-1175.

Canfield, D. E. (2001). Isotope fractionation by natural populations of sulfate-reducing bacteria. *Geochimica et Cosmochimica Acta*, *65*(7), 1117-1124.

Carroll, D. (1962). *Rainwater as a chemical agent of geologic processes: a review*. Washington, DC: US Government Printing Office.

Celico, F., Capuano, P., De Felice, V., & Naclerio, G. (2008). Hypersaline groundwater genesis assessment through a multidisciplinary approach: the case of Pozzo del Sale Spring (southern Italy). *Hydrogeology journal*, *16*(7), 1441-1451. https://doi.org/10.1007/s10040-008-0305-2

Chabaane, A., Redhaounia, B., & Gabtni, H. (2017). Combined application of vertical electrical sounding and 2D electrical resistivity imaging for geothermal groundwater characterization: Hammam Sayala hot spring case study (NW Tunisia). *Journal of African Earth Sciences*, *134*, 292-298. https://doi.org/10.1016/j.jafrearsci.2017.07.003

Chander, V., Tewari, D., Negi, V., Singh, R., Upadhyaya, K., & Aleya, L. (2020). Structural characterization of Himalayan black rock salt by SEM, XRD and in-vitro antioxidant activity. *Science of The Total Environment*, 141269.

Chandrasekhar, E., Ramesh, D., Gurav, T., & Biswal, T. K. (2014). Assessment of groundwater salinity in Nellore district using multi-electrode resistivity imaging technique. *Journal of earth system science*, *123*(8), 1809-1817. https://doi.org/10.1007/s12040-014-0506-0

Chen, J., & Zelt, C. A. (2016). Application of frequency-dependent travel time tomography and full waveform inversion to realistic near-surface seismic refraction data. *Journal of Environmental and Engineering Geophysics*, *21*(1), 1-11. https://doi.org/10.2113/JEEG21.1.1

Choudhury, K., Saha, D. K., & Chakraborty, P. (2001). Geophysical study for saline water intrusion in a coastal alluvial terrain. *Journal of Applied Geophysics*, *46*(3), 189-200. https://doi.org/10.1016/S0926-9851(01)00038-6

Christensen, T. H., Bjerg, P. L., Banwart, S. A., Jakobsen, R., Heron, G., & Albrechtsen, H. J. (2000). Characterization of redox conditions in groundwater contaminant plumes. *Journal of Contaminant Hydrology*, *45*(3-4), 165-241.

Clark, I. (2015). Groundwater geochemistry and isotopes. CRC press.

Cloutier, V., Lefebvre, R., Therrien, R., & Savard, M. M. (2008). Multivariate statistical analysis of geochemical data as indicative of the hydrogeochemical evolution of groundwater in a sedimentary rock aquifer system. *Journal of Hydrology*, *353*(3-4), 294-313.

Cullen, A. B. (2010). Transverse segmentation of the Baram-Balabac Basin, NW Borneo: refining the model of Borneo's tectonic evolution. *Petroleum Geoscience*, *16*(1), 3-29.

Curiale, J., Morelos, J., Lambiase, J., & Mueller, W. (2000). Brunei Darussalam: Characteristics of selected petroleums and source rocks. *Organic Geochemistry*, *31*(12), 1475-1493. https://doi.org/10.1016/S0146-6380(00)00084-X

Coetsiers, M., & Walraevens, K. (2006). Chemical characterization of the neogene aquifer, Belgium. *Hydrogeology Journal*, *14*(8), 1556-1568.

Coplen, T. B. (1994). Reporting of stable hydrogen, carbon, and oxygen isotopic abundances (technical report). *Pure and applied chemistry*, *66*(2), 273-276.

Dahlin, T., & Zhou, B. (2004). A numerical comparison of 2D resistivity imaging with 10 electrode arrays. *Geophysical prospecting*, *52*(5), 379-398. https://doi.org/10.1111/j.1365-2478.2004.00423.x

Dahlin, T., Rosqvist, H., & Leroux, V. (2010). Resistivity-IP mapping for landfill applications. *first break*, *28*(8).

Dansgaard, W. (1964). Stable isotopes in precipitation. *Tellus*, *16*(4), 436-468.

Daughney, C. J., Raiber, M., Moreau-Fournier, M., Morgenstern, U., & van der Raaij, R. (2012). Use of hierarchical cluster analysis to assess the representativeness of a baseline groundwater quality monitoring network: comparison of New Zealand's national and regional groundwater monitoring programs. *Hydrogeology journal*, *20*(1), 185-200. https://doi.org/10.1007/s10040-011-0786-2

Degen, T., Sadki, M., Bron, E., König, U., & Nénert, G. (2014). The highscore suite. *Powder Diffraction*, *29*(S2), S13-S18.

Deshpande, R. D., & Gupta, S. K. (2012). Oxygen and hydrogen isotopes in hydrological cycle: new data from IWIN national programme. *Proceedings of the Indian National Science Academy*, *78*(3), 321-331.

Desper, D. B., Link, C. A., & Nelson, P. N. (2015). Accurate water-table depth estimation using seismic refraction in areas of rapidly varying subsurface conditions. *Near Surface Geophysics*, *13*(5), 455-467.

Dillon, P., & Simmers, I. (Eds.). (1998). Shallow Groundwater Systems: IAH International Contributions to Hydrogeology 18. CRC Press.

Dinka, M. O. (2017). Hydrochemical composition and origin of surface water and groundwater in the Matahara area, Ethiopia. *Inland Waters*, *7*(3), 297-304.

Dişli, E., & Gülyüz, N. (2020). Hydrogeochemical investigation of an epithermal mineralization bearing basin using multivariate statistical techniques and isotopic evidence of groundwater: Kestanelik Sub-Basin, Lapseki, Turkey. *Geochemistry*, 125661.

Du, Y., Ma, T., Chen, L., Xiao, C., & Liu, C. (2016). Chlorine isotopic constraint on contrastive genesis of representative coastal and inland shallow brine in China. *Journal of Geochemical Exploration*, *170*, 21-29.

Du, Y., Fan, Q., Gao, D., Wei, H., Shan, F., Li, B., ... & Teng, X. (2019). Evaluation of boron isotopes in halite as an indicator of the salinity of Qarhan paleolake water in the eastern Qaidam Basin, western China. *Geoscience Frontiers*, *10*(1), 253-262.

Dupalová, T., Sracek, O., Vencelides, Z., & Žák, K. (2012). The origin of thermal waters in the northeastern part of the Eger Rift, Czech Republic. *Applied geochemistry*, *27*(3), 689-702.

Durov, S. A. (1948). Natural waters and graphic representation of their composition. In *Dokl Akad Nauk SSSR* (Vol. 59, No. 3, pp. 87-90).

De Montety, V., Radakovitch, O., Vallet-Coulomb, C., Blavoux, B., Hermitte, D., & Valles, V. (2008). Origin of groundwater salinity and hydrogeochemical processes in a confined coastal aquifer: case of the Rhône delta (Southern France). *Applied Geochemistry*, *23*(8), 2337-2349.

Devaraj, N., Chidambaram, S., Gantayat, R. R., Thivya, C., Thilagavathi, R., Prasanna, M. V., & Paramaguru, P. (2018). An insight on the speciation and genetical imprint of bicarbonate ion in the groundwater along K/T boundary, South India. *Arabian Journal of Geosciences*, *11*(12), 291.

Dezayes, C., Lerouge, C., Sanjuan, B., Ramboz, C., & Brach, M. (2015). Toward a better understanding of the fluid circulation in the Rhine Graben for a better geothermal exploration of the deep basins.

Domagalski, J. L., & Johnson, H. M. (2011). Subsurface transport of orthophosphate in five agricultural watersheds, USA. *Journal of Hydrology*, *409*(1-2), 157-171.

Dotsika, E., Poutoukis, D., Kloppmann, W., Raco, B., & Psomiadis, D. (2011). Distribution and Origin of Boron in Fresh and Thermal Waters in Different Areas of Greece. In *Water Security in the Mediterranean Region* (pp. 209-228). Springer, Dordrecht.

Drever, J. I. (1988). *The geochemistry of natural waters* (Vol. 437). Englewood Cliffs: prentice Hall.

Easley, R. A., & Byrne, R. H. (2011). The ionic strength dependence of lead (II) carbonate complexation in perchlorate media. *Geochimica et Cosmochimica Acta*, *75*(19), 5638-5647.

Eastoe, C. J., Long, A., Land, L. S., & Kyle, J. R. (2001). Stable chlorine isotopes in halite and brine from the Gulf Coast Basin: brine genesis and evolution. *Chemical Geology*, *176*(1-4), 343-360.

Edmunds, W. M., & Smedley, P. L. (2000). Residence time indicators in groundwater: The East Midlands Triassic sandstone aquifer. *Applied Geochemistry*, *15*(6), 737-752.

Edmunds, W. M., Guendouz, A. H., Mamou, A., Moulla, A., Shand, P., & Zouari, K. (2003). Groundwater evolution in the Continental Intercalaire aquifer of southern Algeria and Tunisia: trace element and isotopic indicators. *Applied geochemistry*, *18*(6), 805-822.

Eggenkamp, H. G. M., Kreulen, R., & Van Groos, A. K. (1995). Chlorine stable isotope fractionation in evaporites. *Geochimica et Cosmochimica Acta*, *59*(24), 5169-5175.

Ehya, F., & Marbouti, Z. (2016). Hydrochemistry and contamination of groundwater resources in the Behbahan plain, SW Iran. *Environmental Earth Sciences*, *75*(6), 455. https://doi.org/10.1007/s12665-016-5320-3

Engle, M. A., Reyes, F. R., Varonka, M. S., Orem, W. H., Ma, L., Ianno, A. J., ... & Carroll, K. C. (2016). Geochemistry of formation waters from the Wolfcamp and "Cline" shales: Insights into brine origin, reservoir connectivity, and fluid flow in the Permian Basin, USA. *Chemical Geology*, *425*, 76-92.

Ercan, H. Ü., Karakaya, M. Ç., Bozdağ, A., Karakaya, N., & Delikan, A. (2019). Origin and evolution of halite based on stable isotopes (δ37Cl, δ81Br, δ11B and δ7Li) and trace elements in Tuz Gölü Basin, Turkey. *Applied Geochemistry*, *105*, 17-30.

Esmaeili, S., Moghaddam, A. A., Barzegar, R., & Tziritis, E. (2018). Multivariate statistics and hydrogeochemical modeling for source identification of major elements and heavy metals in the groundwater of Qareh-Ziaeddin plain, NW Iran. *Arabian Journal of Geosciences*, *11*(1), 5.

Ettayfi, N., Bouchaou, L., Michelot, J. L., Tagma, T., Warner, N., Boutaleb, S., ... & Vengosh, A. (2012). Geochemical and isotopic (oxygen, hydrogen, carbon, strontium) constraints for the origin, salinity, and residence time of groundwater from a carbonate aquifer in the Western Anti-Atlas Mountains, Morocco. *Journal of hydrology*, *438*, 97-111. https://doi.org/10.1016/j.jhydrol.2012.03.003

Evans, N. P., Turchyn, A. V., Gázquez, F., Bontognali, T. R., Chapman, H. J., & Hodell, D. A. (2015). Coupled measurements of δ18O and δD of hydration water and salinity of fluid inclusions in gypsum from the Messinian Yesares Member, Sorbas Basin (SE Spain). *Earth and Planetary Science Letters*, *430*, 499-510.

Ezersky, M. (2005). The seismic velocities of Dead Sea salt applied to the sinkhole problem. *Journal of Applied Geophysics*, *58*(1), 45-58. https://doi.org/10.1016/j.jappgeo.2005.01.003

Fakharian, K., & Narany, T. S. (2016). Multidisciplinary approach to evaluate groundwater salinity in Saveh Plain, Iran. *Environmental Earth Sciences*, *75*(7), 624.

Fardousi, M. (2012). *Determination of iodine content in different brands table salt of Bangladesh* (Doctoral dissertation, East West University). http://hdl.handle.net/123456789/72

Farid, I., Zouari, K., Trabelsi, R., & Kallali, A. R. (2014). Application of environmental tracers to study groundwater recharge in a semi-arid area of Central Tunisia. *Hydrological Sciences Journal*, *59*(11), 2072-2085.

Farid, I., Zouari, K., Rigane, A., & Beji, R. (2015). Origin of the groundwater salinity and geochemical processes in detrital and carbonate aquifers: case of Chougafiya basin (Central Tunisia). *Journal of Hydrology*, *530*, 508-532. https://doi.org/10.1016/j.jhydrol.2015.10.009

Farid, A., Khalid, P., Jadoon, K. Z., Iqbal, M. A., & Shafique, M. (2017). Applications of variogram modeling to electrical resistivity data for the occurrence and distribution of saline groundwater in Domail Plain, northwestern Himalayan fold and thrust belt, Pakistan. *Journal of Mountain Science*, *14*(1), 158-174. https://doi.org/10.1007/s11629-015-3754-9

Fijani, E., Moghaddam, A. A., Tsai, F. T. C., & Tayfur, G. (2017). Analysis and assessment of hydrochemical characteristics of Maragheh-Bonab plain aquifer, northwest of Iran. *Water Resources Management*, *31*(3), 765-780.

Fisher, R. S., & Mullican III, W. F. (1997). Hydrochemical evolution of sodium-sulfate and sodium-chloride groundwater beneath the northern Chihuahuan Desert, Trans-Pecos, Texas, USA. *Hydrogeology journal*, *5*(2), 4-16.

Fontes, J. C., & Matray, J. M. (1993a). Geochemistry and origin of formation brines from the Paris Basin, France: 1. Brines associated with Triassic salts. *Chemical Geology*, *109*(1-4), 149-175.

Fontes, J. C., & Matray, J. M. (1993b). Geochemistry and origin of formation brines from the Paris Basin, France: 2. Saline solutions associated with oil fields. *Chemical Geology*, *109*(1-4), 177-200.

Fortin, J., Pimienta, L., Guéguen, Y., Schubnel, A., David, E. C., & Adelinet, M. (2014). Experimental results on the combined effects of frequency and pressure on the dispersion of elastic waves in porous rocks. *The Leading Edge*, *33*(6), 648-654.

Freeze, R. A., & Cherry, J. A. (1979). Groundwater: New Jersey. *Englewood Cliffs*.

Galin, T., Breitfeld, H. T., Hall, R., & Sevastjanova, I. (2017). Provenance of the Cretaceous–Eocene Rajang Group submarine fan, Sarawak, Malaysia from light and heavy mineral assemblages and U-Pb zircon geochronology. *Gondwana Research*, *51*, 209-233.

Gautam, M. K., Lee, K. S., Bong, Y. S., Song, B. Y., & Ryu, J. S. (2017). Oxygen and hydrogen isotopic characterization of rainfall and throughfall in four South Korean cool temperate forests. *Hydrological Sciences Journal*, *62*(12), 2025-2034.

Gao, J. P., Maguhn, J., Spitzauer, P., & Kettrup, A. (1998). Sorption of pesticides in the sediment of the Teufelsweiher pond (Southern Germany). I: Equilibrium assessments, effect of organic carbon content and pH. *Water Research*, *32*(5), 1662-1672.

Geometrics Inc. (2009). SeisImager/SWTM Manual.

Giang, N., Duan, N., Thanh, L., & Hida, N. (2013). Geophysical techniques to aquifer locating and monitoring for industrial zones in North Hanoi, Vietnam. *Acta Geophysica*, *61*(6), 1573-1597. https://doi.org/10.2478/s11600-013-0147-8

Gibbs, R. J. (1970). Mechanisms controlling world water chemistry. *Science*, *170*(3962), 1088-1090. https://doi.org/10.1126/science.170.3962.1088

Gil-Márquez, J. M., Barberá, J. A., Andreo, B., & Mudarra, M. (2017). Hydrological and geochemical processes constraining groundwater salinity in wetland areas related to evaporitic (karst) systems. A case study from Southern Spain. *Journal of Hydrology*, *544*, 538-554. https://doi.org/10.1016/j.jhydrol.2016.11.062

Glas, R., Lautz, L., McKenzie, J., Moucha, R., Chavez, D., Mark, B., & Lane, J. W. (2019). Hydrogeology of an alpine talus aquifer: Cordillera Blanca, Peru. *Hydrogeology Journal*, 1-18.

Gopinath, S., Srinivasamoorthy, K., Saravanan, K., & Prakash, R. (2019). Tracing groundwater salinization using geochemical and isotopic signature in Southeastern coastal Tamilnadu, India. *Chemosphere*, *236*, 124305.

Grundmann, J., Al-Khatri, A., & Schütze, N. (2016). Managing saltwater intrusion in coastal arid regions and its societal implications for agriculture. *Proc. IAHS*, *373*, 31-35.

Grelle, G., & Guadagno, F. M. (2009). Seismic refraction methodology for groundwater level determination: "Water seismic index". *Journal of Applied Geophysics*, *68*(3), 301-320. https://doi.org/10.1016/j.jappgeo.2009.02.001

Grobe, M., & Machel, H. G. (2002). Saline groundwater in the Münsterland Cretaceous Basin, Germany: clues to its origin and evolution. *Marine and petroleum Geology*, *19*(3), 307-322.

Guseva, N. V., Kopylova, Y. G., Oidup, C. K., Arakchaa, K. D., Rychkova, K. M., Khvashchevskaya, A. A., & Ayunova, O. D. (2018). Formation of the chemical composition of brackish and brine groundwater in the Tuva depression and surrounding areas. *Russian Geology and Geophysics*, *59*(2), 135-143. https://doi.org/10.1016/j.rgg.2018.01.011

Haeni, F. P. (1986). Application of seismic refraction methods in groundwater modeling studies in New England. *Geophysics*, *51*(2), 236-249. https://doi.org/10.1190/1.1442083

Haile, N. S. (1962). The geology and mineral resources of the Suai-Baram area. *Geological Survey Department British Territories in Borneo*.

Halim, M. A., Majumder, R. K., Nessa, S. A., Hiroshiro, Y., Sasaki, K., Saha, B. B., ... & Jinno, K. (2010). Evaluation of processes controlling the geochemical constituents in

deep groundwater in Bangladesh: spatial variability on arsenic and boron enrichment. *Journal of Hazardous Materials, 180*(1-3), 50-62.

Hall, R. (2013). Contraction and extension in northern Borneo driven by subduction rollback. *Journal of Asian Earth Sciences, 76*, 399-411. https://doi.org/10.1016/j.jseaes.2013.04.010

Hamdan, H., Kritikakis, G., Andronikidis, N., Economou, N., Manoutsoglou, E., & Vafidis, A. (2010). Integrated geophysical methods for imaging saline karst aquifers. A case study of Stylos, Chania, Greece. *Journal of the Balkan Geophysical Society*, *13*(1), 1-8.

Hamed, Y., & Dhahri, F. (2013). Hydro-geochemical and isotopic composition of groundwater, with emphasis on sources of salinity, in the aquifer system in Northwestern Tunisia. *Journal of African Earth Sciences, 83*, 10-24. https://doi.org/10.1016/j.jafrearsci.2013.02.004

Hamilton, W. B. (1979). *Tectonics of the Indonesian region* (No. 1078). US Govt. Print. Off..

Hamzah, U., Samsudin, A. R., & Malim, E. P. (2007). Groundwater investigation in Kuala Selangor using vertical electrical sounding (VES) surveys. *Environmental geology*, *51*(8), 1349-1359. https://doi.org/10.1007/s00254-006-0433-8

Hamzah, Z., Aris, A. Z., Ramli, M. F., Juahir, H., & Narany, T. S. (2017). Groundwater quality assessment using integrated geochemical methods, multivariate statistical analysis, and geostatistical technique in shallow coastal aquifer of Terengganu, Malaysia. *Arabian Journal of Geosciences*, *10*(2), 49. https://doi.org/10.1007/s12517-016-2828-5

Han, J. L., Han, F. Q., Hussain, S. A., Liu, W. Y., Nian, X. Q., & Mao, Q. F. (2018). Origin of boron and brine evolution in saline springs in the Nangqen Basin, Southern Tibetan Plateau. *Geofluids*, *2018*.

Hantzsche, N. N., & Finnemore, E. J. (1992). Predicting ground-water nitrate-nitrogen impacts. *Groundwater*, *30*(4), 490-499.

Hao, O. J., Chen, J. M., Huang, L., & Buglass, R. L. (1996). Sulfate-reducing bacteria. *Critical reviews in environmental science and technology*, *26*(2), 155-187.

Harrington, N. M., Herczeg, A. L., & La Salle, C. L. G. (2008). Hydrological and geochemical processes controlling variations in Na+–Mg2+–Cl−–SO42− groundwater brines, south-eastern Australia. *Chemical Geology*, *251*(1-4), 8-19. https://doi.org/10.1016/j.chemgeo.2008.02.007

Harvey, C. F., Swartz, C. H., Badruzzaman, A. B. M., Keon-Blute, N., Yu, W., Ali, M. A., ... & Oates, P. M. (2005). Groundwater arsenic contamination on the Ganges Delta: biogeochemistry, hydrology, human perturbations, and human suffering on a large scale. *Comptes Rendus Geoscience*, *337*(1-2), 285-296.

Hashim, M. A., Mukhopadhyay, S., Sahu, J. N., & Sengupta, B. (2011). Remediation technologies for heavy metal contaminated groundwater. *Journal of environmental management*, *92*(10), 2355-2388. https://doi.org/10.1016/j.jenvman.2011.06.009

Hiscock, K. M. & Bense V. F (2014). *Hydrogeology: principles and practice (second edition)*. John Wiley & Sons.

Huang, D. Y., Xu, Y. G., Zhang, H. H., & Lan, J. B. (2009). Chemical composition and seasonal variation of acid deposition in Guangzhou, South China: comparison with precipitation in other major Chinese cities. *Environmental Pollution*, *157*(1), 35-41.

Huang, T., & Pang, Z. (2012). The role of deuterium excess in determining the water salinisation mechanism: A case study of the arid Tarim River Basin, NW China. *Applied Geochemistry*, *27*(12), 2382-2388.

Hussin, N. H., Yusoff, I., Alias, Y., Mohamad, S., Rahim, N. Y., & Ashraf, M. A. (2014). Ionic liquid as a medium to remove iron and other metal ions: a case study of the North Kelantan Aquifer, Malaysia. *Environmental earth sciences*, *71*(5), 2105-2113. https://doi.org/10.1007/s12665-013-2615-5

Hutchison, C. S. (2005). Geology of North-West Borneo: Sarawak, Brunei and Sabah. Elsevier.

Hutchison, C. S. (2010). Oroclines and paleomagnetism in Borneo and south-east Asia. *Tectonophysics*, *496*(1-4), 53-67. https://doi.org/10.1016/j.tecto.2010.10.008

Healy, R. W. (2010). *Estimating groundwater recharge*. Cambridge University Press.

Hem, J. D. (1985). *Study and interpretation of the chemical characteristics of natural water* (Vol. 2254). Department of the Interior, US Geological Survey.

Hem, J. D., & Geological Survey (US). (1989). Study and interpretation of the chemical characteristics of natural water.

Hounslow, A. (1995). Water quality data: analysis and interpretation. CRC press.

Hodlur, G. K., Dhakate, R., Sirisha, T., & Panaskar, D. B. (2010). Resolution of freshwater and saline water aquifers by composite geophysical data analysis methods. *Hydrological Sciences Journal–Journal des Sciences Hydrologiques*, *55*(3), 414-434. https://doi.org/10.1080/02626661003738217

Horita, J. (2005). Saline waters. In *Isotopes in the water cycle* (pp. 271-287). Springer, Dordrecht.

Ibrahim, R. G. M., Korany, E. A., Tempel, R. N., & Gomaa, M. A. (2019). Processes of water–rock interactions and their impacts upon the groundwater composition in Assiut area, Egypt: Applications of hydrogeochemical and multivariate analysis. *Journal of African Earth Sciences*, *149*, 72-83.

Idris, A. N., Aris, A. Z., Suratman, S., & Tawnie, I. (2014). Preliminary Physicochemical Assessment of Groundwater in Kg. Salang, Pulau Tioman, Pahang, Malaysia. In *From Sources to Solution* (pp. 121-126). Springer, Singapore. https://doi.org/10.1007/978-981-4560-70-2_23

Isa, N. M., Aris, A. Z., & Sulaiman, W. N. A. W. (2012). Extent and severity of groundwater contamination based on hydrochemistry mechanism of sandy tropical coastal aquifer. *Science of the total Environment*, *438*, 414-425. https://doi.org/10.1016/j.scitotenv.2012.08.069

Isawi, H., El-Sayed, M. H., Eissa, M., Shouakar-Stash, O., Shawky, H., & Mottaleb, M. S. A. (2016). Integrated geochemistry, isotopes, and geostatistical techniques to investigate groundwater sources and salinization origin in the Sharm EL-Shiekh Area, South Sinia, Egypt. *Water, Air, & Soil Pollution*, *227*(5), 151.

Islam, A. T., Shen, S., Bodrud-Doza, M., Rahman, M. A., & Das, S. (2017). Assessment of trace elements of groundwater and their spatial distribution in Rangpur district, Bangladesh. *Arabian Journal of Geosciences*, *10*(4), 95.

Islami, N., Taib, S. H., Yusoff, I., & Ghani, A. A. (2018). Integrated geoelectrical resistivity and hydrogeochemical methods for delineating and mapping heavy metal zone in aquifer system. *Environmental Earth Sciences*, *77*(10), 383. https://doi.org/10.1007/s12665-018-7574-4

Jagadeshan, G., Gosaye, B., Zinabe, S., & Abeje, A. (2018). Assessment of Groundwater Potential Using Seismic Refraction Method in Secha, Arba Minch, Ethiopia. *IOSR J. Appl. Geol. Geophys.*, *6*(1), 18-24.

Jalali, M., & Khanlari, Z. V. (2008). Major ion chemistry of groundwaters in the Damagh area, Hamadan, western Iran. *Environmental geology*, *54*(1), 87-93.

Jankowski, J., & Acworth, R. I. (1997). Impact of debris-flow deposits on hydrogeochemical processes and the development of dryland salinity in the Yass River Catchment, New South Wales, Australia. *Hydrogeology journal*, *5*(4), 71-88.

Jia, Y., Guo, H., Xi, B., Jiang, Y., Zhang, Z., Yuan, R., ... & Xue, X. (2017). Sources of groundwater salinity and potential impact on arsenic mobility in the western Hetao Basin, Inner Mongolia. *Science of the Total Environment*, *601*, 691-702.

Jiráková, H., Huneau, F., Hrkal, Z., Celle-Jeanton, H., & Le Coustumer, P. (2010). Carbon isotopes to constrain the origin and circulation pattern of groundwater in the north-western part of the Bohemian Cretaceous Basin (Czech Republic). *Applied Geochemistry*, *25*(8), 1265-1279.

Jong, J., Idris, H. A. B. M., Barber, P., Kessler, F. L., Tan, T. Q., & Uchimura, R. (2017). Exploration history and petroleum systems of the onshore Baram Delta, northern Sarawak, Malaysia.

Joseph Mathew, M. (2016). *Geomorphology and Morphotectonic Analysis of north Borneo* (Doctoral dissertation, Lorient).

Juanah, M. S., Ibrahim, S., Sulaiman, W. N. A., & Latif, P. A. (2013). Groundwater resources assessment using integrated geophysical techniques in the southwestern region of Peninsular Malaysia. *Arabian Journal of Geosciences*, *6*(11), 4129-4144. https://doi.org/10.1007/s12517-012-0700-9

Kaiser, H. F. (1958). The varimax criterion for analytic rotation in factor analysis. *Psychometrika*, *23*(3), 187-200.

Kaufmann, R. S., Frape, S. K., McNutt, R., & Eastoe, C. (1993). Chlorine stable isotope distribution of Michigan Basin formation waters. *Applied geochemistry*, *8*(4), 403-407.

Karakaya, M. Ç., Bozdağ, A., Ercan, H. Ü., Karakaya, N., & Delikan, A. (2019). Origin of Miocene halite from Tuz Gölü basin in Central Anatolia, Turkey: Evidences from the pure halite and fluid inclusion geochemistry. *Journal of Geochemical Exploration*, *202*, 1-12.

Karamouz, M., Ahmadi, A., & Akhbari, M. (2020). *Groundwater hydrology: Engineering, planning, and management*. CRC press.

Kass, A., Gavrieli, I., Yechieli, Y., Vengosh, A., & Starinsky, A. (2005). The impact of freshwater and wastewater irrigation on the chemistry of shallow groundwater: a case study from the Israeli Coastal Aquifer. *Journal of Hydrology*, *300*(1-4), 314-331.

Katz, A., Starinsky, A., & Marion, G. M. (2011). Saline waters in basement rocks of the Kaapvaal Craton, South Africa. *Chemical Geology*, *289*(1-2), 163-170. https://doi.org/10.1016/j.chemgeo.2011.08.002

Kearey, P., Brooks, M., & Hill, I. (2013). *An introduction to geophysical exploration*. John Wiley & Sons.

Keys, W. S., & MacCary, L. M. (1971). *Application of borehole geophysics to water-resources investigations* (p. 126). Washington, DC: US Government Printing Office.

Khaki, M., Yusoff, I., Islami, N., & Saboohi, S. (2016). Integrated geoelectrical and hydrogeochemical investigation for mapping the aquifer at Langat Basin, Malaysia. *Environmental Earth Sciences*, *75*(4), 304. https://doi.org/10.1007/s12665-015-5182-0

Kloppmann, W., Négrel, P., Casanova, J., Klinge, H., Schelkes, K., & Guerrot, C. (2001). Halite dissolution derived brines in the vicinity of a Permian salt dome (N German Basin). Evidence from boron, strontium, oxygen, and hydrogen isotopes. *Geochimica et Cosmochimica Acta*, *65*(22), 4087-4101.

Kovač, N., Glavaš, N., Dolenec, M., Šmuc, N. R., & Šlejkovec, Z. (2013). Chemical composition of natural sea salt from the Sečovlje salina (Gulf of Trieste, northern Adriatic). *Acta chimica slovenica*, *60*(3), 706-714.

Krishnan, M. N., Prasanna, M. V., & Vijith, H. (2019). Statistical analysis of trends in monthly precipitation at the Limbang River Basin, Sarawak (NW Borneo), Malaysia. *Meteorology and Atmospheric Physics*, *131*(4), 883-896.

Krìstìansen, R. (2003). Scandium-mineraler i Norge. *Stein*, *30*, 14-23.

Kumar, M., Kumari, K., Singh, U. K., & Ramanathan, A. L. (2009). Hydrogeochemical processes in the groundwater environment of Muktsar, Punjab: conventional graphical and multivariate statistical approach. *Environmental Geology*, *57*(4), 873-884.

Kumar, D., Rao, V. A., & Sarma, V. S. (2014). Hydrogeological and geophysical study for deeper groundwater resource in quartzitic hard rock ridge region from 2D resistivity data. *Journal of Earth System Science*, *123*(3), 531-543.

Kumar, D., Mondal, S., Nandan, M. J., Harini, P., Sekhar, B. S., & Sen, M. K. (2016). Two-dimensional electrical resistivity tomography (ERT) and time-domain-induced polarization (TDIP) study in hard rock for groundwater investigation: a case study at Choutuppal Telangana, India. *Arabian Journal of Geosciences*, *9*(5), 355.

Kura, N. U., Ramli, M. F., Sulaiman, W. N. A., Ibrahim, S., & Aris, A. Z. (2018). An overview of groundwater chemistry studies in Malaysia. *Environmental Science and Pollution Research*, *25*(8), 7231-7249. https://doi.org/10.1007/s11356-015-5957-6

Ladd, M. F. C., Palmer, R. A., & Palmer, R. A. (2013). *Structure determination by X-ray crystallography*. New York: Plenum Press.

Lakshmanan, E., Kannan, R., & Kumar, M. S. (2003). Major ion chemistry and identification of hydrogeochemical processes of ground water in a part of Kancheepuram district, Tamil Nadu, India. *Environmental geosciences*, *10*(4), 157-166.

Lashkaripour, G. R., & Nakhaei, M. (2005). Geoelectrical investigation for the assessment of groundwater conditions: a case study. *Annals of Geophysics*, *48*(6). https://doi.org/10.4401/ag-3244

Langelier, W. F., & Ludwig, H. F. (1942). Graphical methods for indicating the mineral character of natural waters. *Journal (American water works association)*, *34*(3), 335-352.

Langmuir, D. (1997). Aqueous environmental. Geochemistry Prentice Hall: Upper Saddle River, NJ.

Lavrushin, V. Y., Kopf, A., Deyhle, A., & Stepanets, M. I. (2003). Formation of mud-volcanic fluids in Taman (Russia) and Kakhetia (Georgia): evidence from boron isotopes. *Lithology and Mineral Resources*, *38*(2), 120-153.

Leveille, J. P., Jones, I. F., Zhou, Z. Z., Wang, B., & Liu, F. (2011). Subsalt imaging for exploration, production, and development: A review. *Geophysics*, *76*(5), WB3-WB20.

Levy, D. B., & Amrhein, C. (2011). Geochemical evolution of hypersaline cave pools, Guadalupe Mountains, New Mexico. *Chemical Geology*, *290*(1-2), 60-66. https://doi.org/10.1016/j.chemgeo.2011.08.012

Li, P., Tian, R., & Liu, R. (2019a). Solute geochemistry and multivariate analysis of water quality in the Guohua phosphorite mine, Guizhou Province, China. *Exposure and Health*, *11*(2), 81-94.

Li, M., Fang, X., Li, J., Yan, M., Sun, S., & Zhu, L. (2019b). Isotopic Application in High Saline Conditions. In *Isotopes Applications in Earth Sciences*. IntechOpen.

Liechti, P., Roe, F. W., & Haile, N. S. (1960). The geology of Sarawak, Brunei, and the Western Part of North Borneo. British Borneo Geological Survey Bulletin 3, 358 pp. Geological Survey Department. *British Territories in Borneo, Kuching*.

Lim, W. Y., Aris, A. Z., Ismail, T. H. T., & Zakaria, M. P. (2013). Elemental hydrochemistry assessment on its variation and quality status in Langat River, Western Peninsular Malaysia. *Environmental earth sciences*, *70*(3), 993-1004. https://doi.org/10.1007/s12665-012-2189-7

Lin, C. Y., Abdullah, M. H., Musta, B., Praveena, S. M., & Aris, A. Z. (2011). Stability behavior and thermodynamic states of iron and manganese in sandy soil aquifer, Manukan Island, Malaysia. *Natural resources research*, *20*(1), 45-56. https://doi.org/10.1007/s11053-011-9136-2

Lindholm, R. (2012). *A practical approach to sedimentology*. Springer Science & Business Media.

Liu, C. W., Lu, K. L., Kao, Y. H., Wang, C. J., Maji, S. K., & Lee, J. F. (2014). Identifying sources and controlling factors of arsenic release in saline groundwater aquifers. *Hydrology and Earth System Sciences*, *18*(3), 1089-1103.

Liu, J., Chen, Z., Wang, L., Zhang, Y., Li, Z., Xu, J., & Peng, Y. (2016). Chemical and isotopic constrains on the origin of brine and saline groundwater in Hetao plain, Inner

Mongolia. *Environmental Science and Pollution Research*, *23*(15), 15003-15014. https://doi.org/10.1007/s11356-016-6617-1

Liu, J., Jin, D., Wang, T., Gao, M., Yang, J., & Wang, Q. (2019). Hydrogeochemical processes and quality assessment of shallow groundwater in Chenqi coalfield, Inner Mongolia, China. *Environmental Earth Sciences*, *78*(12), 347.

Lloyd, J. W., & Heathcote, J. A. A. (1985). Natural inorganic hydrochemistry in relation to ground water.

Lu, H. Y., Peng, T. R., & Liou, T. S. (2008). Identification of the origin of salinization in groundwater using multivariate statistical analysis and geochemical modeling: a case study of Kaohsiung, Southwest Taiwan. *Environmental geology*, *55*(2), 339-352.

Lü, Y., Zheng, M., Zhao, P., & Xu, R. (2014). Geochemical processes and origin of boron isotopes in geothermal water in the Yunnan-Tibet geothermal zone. *Science China Earth Sciences*, *57*(12), 2934-2944.

Loke, M. H. (2004). Tutorial: 2-D and 3-D electrical imaging surveys.

Loke, M. H. (2011). Electrical resistivity surveys and data interpretation. In *Encyclopedia of Solid Earth Geophysics* (pp. 276-283). Springer, Dordrecht. https://doi.org/10.1007/978-90-481-8702-7_46

Loke, M. H., Chambers, J. E., Rucker, D. F., Kuras, O., & Wilkinson, P. B. (2013). Recent developments in the direct-current geoelectrical imaging method. *Journal of Applied Geophysics*, *95*, 135-156. https://doi.org/10.1016/j.jappgeo.2013.02.017

Long, D. T., Lyons, W. B., & Hines, M. E. (2009). Influence of hydrogeology, microbiology and landscape history on the geochemistry of acid hypersaline waters, NW Victoria. *Applied Geochemistry*, *24*(2), 285-296. https://doi.org/10.1016/j.apgeochem.2008.11.012

Lower, S. K. (1999). Carbonate equilibria in natural waters. *Simon Fraser University*, *544*.

Lyu, M., Pang, Z., Yin, L., Zhang, J., Huang, T., Yang, S., ... & Gulbostan, T. (2019). The Control of Groundwater Flow Systems and Geochemical Processes on Groundwater Chemistry: A Case Study in Wushenzhao Basin, NW China. *Water*, *11*(4), 790.

Mace, R. E., Davidson, S. C., Angle, E. S., & Mullican, W. F. (2006). Aquifers of the Gulf coast of Texas. *Texas Water Development Board, USA Report*, *365*.

Machel, H. G. (1989). Relationships between sulphate reduction and oxidation of organic compounds to carbonate diagenesis, hydrocarbon accumulations, salt domes, and metal sulphide deposits. *Carbonates and Evaporites*, *4*(2), 137.

Mackenzie, F. T., & Garrels, R. M. (1971). *Evolution of sedimentary rocks*. New York: Norton.

Madzin, Z., Kusin, F. M., Yusof, F. M., & Muhammad, S. N. (2017). Assessment of water quality index and heavy metal contamination in active and abandoned iron ore mining sites in Pahang, Malaysia. In *MATEC Web of Conferences* (Vol. 103, p. 05010). EDP Sciences. https://doi.org/10.1051/matecconf/201710305010

Mahmoud, H. H., & Ghoubachi, S. Y. (2017). Geophysical and hydrogeological investigation to study groundwater occurrences in the Taref Formation, south Mut area–Dakhla Oasis-Egypt. *Journal of African Earth Sciences*, *129*, 610-622. https://doi.org/10.1016/j.jafrearsci.2017.02.009

Mainoo, P. A., Manu, E., Yidana, S. M., Agyekum, W. A., Stigter, T., Duah, A. A., & Preko, K. (2019). Application of 2D-Electrical resistivity tomography in delineating groundwater potential zones: Case study from the voltaian super group of Ghana. *Journal of African Earth Sciences*, *160*, 103618.

Mallick, J., Singh, C., AlMesfer, M., Kumar, A., Khan, R., Islam, S., & Rahman, A. (2018). Hydro-geochemical assessment of groundwater quality in Aseer Region, Saudi Arabia. *Water*, *10*(12), 1847.

Manap, M. A., Nampak, H., Pradhan, B., Lee, S., Sulaiman, W. N. A., & Ramli, M. F. (2014). Application of probabilistic-based frequency ratio model in groundwater potential

mapping using remote sensing data and GIS. *Arabian Journal of Geosciences*, *7*(2), 711-724.

Marandi, A., & Shand, P. (2018). Groundwater chemistry and the Gibbs Diagram. *Applied Geochemistry*, *97*, 209-212.

Marcovecchio, J. E., Botté, S. E., & Freije, R. H. (2007). Heavy metals, major metals, trace elements. *Handbook of water analysis*, *2*, 275-311.

Margat, J., & Van der Gun, J. (2013). Groundwater around the world: a geographic synopsis. Crc Press.

Martin, C., Flores, K. E., & Harlow, G. E. (2016). Boron isotopic discrimination for subduction-related serpentinites. *Geology*, *44*(11), 899-902.

Martínez, D., & Bocanegra, E. (2002). Hydrogeochemistry and cation-exchange processes in the coastal aquifer of Mar Del Plata, Argentina. *Hydrogeology Journal*, *10*(3), 393-408.

Mateo-Sagasta, J., Zadeh, S. M., Turral, H., & Burke, J. (2017). Water pollution from agriculture: a global review. *Food and Agriculture Organization of the United Nations and the International Water Management Institute, Rome*.

Mattos, J. B., Cruz, M. J. M., De Paula, F. C. F., & Sales, E. F. (2018a). Natural and anthropic processes controlling groundwater hydrogeochemistry in a tourist destination in northeastern Brazil. *Environmental monitoring and assessment*, *190*(7), 395. https://doi.org/10.1007/s10661-018-6765-5

Mattos, J. B., Cruz, M. J. M., De Paula, F. C. F., & Sales, E. F. (2018b). Spatio-seasonal changes in the hydrogeochemistry of groundwaters in a highland tropical zone. *Journal of South American Earth Sciences*, *88*, 275-286. https://doi.org/10.1016/j.jsames.2018.08.023

McHenry, L. J., Kodikara, G. L., Stanistreet, I. G., Stollhofen, H., Njau, J. K., Schick, K., & Toth, N. (2020). Lake conditions and detrital sources of Paleolake Olduvai, Tanzania,

reconstructed using X-ray Diffraction analysis of cores. *Palaeogeography, Palaeoclimatology, Palaeoecology*, 109855.

Musashi, M., Oi, T., & Kreulen, R. (2015). Chlorine isotopic compositions of deep saline fluids in Ibusuki coastal geothermal region, Japan: using B–Cl isotopes to interpret fluid sources. *Isotopes in Environmental and Health Studies*, *51*(2), 285-299.

Mejri, S., Chekirbene, A., Tsujimura, M., Boughdiri, M., & Mlayah, A. (2018). Tracing groundwater salinization processes in an inland aquifer: A hydrogeochemical and isotopic approach in Sminja aquifer (Zaghouan, northeast of Tunisia). *Journal of African Earth Sciences*, *147*, 511-522.

Mele, M., Bersezio, R., Giudici, M., Inzoli, S., Cavalli, E., & Zaja, A. (2013). Resistivity imaging of Pleistocene alluvial aquifers in a contractional tectonic setting: A case history from the Po plain (Northern Italy). *Journal of Applied Geophysics*, *93*, 114-126. https://doi.org/10.1016/j.jappgeo.2013.03.015

Merkel, B. J., Planer-Friedrich, B., & Nordstrom, D. K. (2005). Groundwater geochemistry. *A practical guide to modeling of natural and contaminated aquatic systems*, *2*.

Mgbenu, C. N., & Egbueri, J. C. (2019). The hydrogeochemical signatures, quality indices and health risk assessment of water resources in Umunya district, southeast Nigeria. *Applied Water Science*, *9*(1), 22.

Mhamdi, A., Dhahri, F., Gouasmia, M., Moumni, L., & Mohamed, S. (2015). Groundwater salinization survey of the Upper Cretaceous-Miocene Complexe terminal aquifer in the Sabaa Biar area of southwestern Tunisia. *Journal of African Earth Sciences*, *112*, 83-92. https://doi.org/10.1016/j.jafrearsci.2015.09.002

Miao, Z., Brusseau, M. L., Carroll, K. C., Carreón-Diazconti, C., & Johnson, B. (2012). Sulfate reduction in groundwater: characterization and applications for remediation. *Environmental geochemistry and health*, *34*(4), 539-550.

Michalowski, T., & Asuero, A. G. (2012). Thermodynamic modelling of dolomite behavior in aqueous media. *Journal of Thermodynamics*, *2012*. https://doi.org/10.1155/2012/723052

Mirzavand, M., Ghasemieh, H., Sadatinejad, S. J., & Bagheri, R. (2020a). An overview on source, mechanism and investigation approaches in groundwater salinization studies. *International Journal of Environmental Science and Technology*, 1-14.

Mirzavand, M., Ghasemieh, H., Sadatinejad, S. J., & Bagheri, R. (2020b). Delineating the source and mechanism of groundwater salinization in crucial declining aquifer using multi-chemo-isotopes approaches. *Journal of Hydrology*, 124877.

Mohamaden, M. I. I., Hamouda, A. Z., & Mansour, S. (2016). Application of electrical resistivity method for groundwater exploration at the Moghra area, Western Desert, Egypt. *The Egyptian Journal of Aquatic Research*, *42*(3), 261-268. https://doi.org/10.1016/j.ejar.2016.06.002

Mokrik, R., Karro, E., Savitskaja, L., & Drevalieneac, G. (2009). The origin of barium in the Cambrian-Vendian aquifer system, North Estonia. *Estonian Journal of Earth Sciences*, *58*(3).

Momodu, M. A., & Anyakora, C. A. (2010). Heavy metal contamination of ground water: The Surulere case study. *Research Journal Environmental and Earth Science*, *2*(1), 39-43.

Mondal, N. C., Singh, V. P., Singh, V. S., & Saxena, V. K. (2010). Determining the interaction between groundwater and saline water through groundwater major ions chemistry. *Journal of Hydrology*, *388*(1-2), 100-111. https://doi.org/10.1016/j.jhydrol.2010.04.032

Monjerezi, M., Vogt, R. D., Aagaard, P., & Saka, J. D. (2011). Hydro-geochemical processes in an area with saline groundwater in lower Shire River valley, Malawi: an integrated application of hierarchical cluster and principal component analyses. *Applied Geochemistry*, *26*(8), 1399-1413.

Monjerezi, M., Vogt, R. D., Gebru, A. G., Saka, J. D., & Aagaard, P. (2012). Minor element geochemistry of groundwater from an area with prevailing saline groundwater in Chikhwawa, lower Shire valley (Malawi). *Physics and Chemistry of the Earth, Parts A/B/C*, *50*, 52-63.

Montcoudiol, N., Molson, J., & Lemieux, J. M. (2015). Groundwater geochemistry of the Outaouais Region (Québec, Canada): a regional-scale study. *Hydrogeology Journal*, *23*(2), 377-396.

Morley, C. K., Back, S., Van Rensbergen, P., Crevello, P., & Lambiase, J. J. (2003). Characteristics of repeated, detached, Miocene–Pliocene tectonic inversion events, in a large delta province on an active margin, Brunei Darussalam, Borneo. *Journal of Structural Geology*, *25*(7), 1147-1169. https://doi.org/10.1016/S0191-8141(02)00130-X

Morley, C. K., Tingay, M., Hillis, R., & King, R. (2008). Relationship between structural style, overpressures, and modern stress, Baram Delta Province, northwest Borneo. *Journal of Geophysical Research: Solid Earth*, *113*(B9). https://doi.org/10.1029/2007JB005324

Mosaad, S., & Kehew, A. E. (2019). Integration of geochemical data to assess the groundwater quality in a carbonate aquifer in the southeast of Beni-Suef city, Egypt. *Journal of African Earth Sciences*, *158*, 103558.

Muchingami, I., Hlatywayo, D. J., Nel, J. M., & Chuma, C. (2012). Electrical resistivity survey for groundwater investigations and shallow subsurface evaluation of the basaltic-greenstone formation of the urban Bulawayo aquifer. *Physics and Chemistry of the Earth, Parts A/B/C*, *50*, 44-51. https://doi.org/10.1016/j.pce.2012.08.014

Naidu, L. S., VVS, G. R., Mahesh, J., Padalu, G., Sarma, V. S., Prasad, P. R., ... & Rao, R. (2013). An integrated approach to investigate saline water intrusion and to identify the salinity sources in the Central Godavari delta, Andhra Pradesh, India. *Arabian Journal of Geosciences*, *6*(10), 3709-3724.

Nampak, H., Pradhan, B., & Manap, M. A. (2014). Application of GIS based data driven evidential belief function model to predict groundwater potential zonation. *Journal of Hydrology*, *513*, 283-300.

Naseem, S., & McArthur, J. M. (2018). Arsenic and other water-quality issues affecting groundwater, I ndus alluvial plain, P akistan. *Hydrological Processes*, *32*(9), 1235-1253. https://doi.org/10.1002/hyp.11489

Nazaruddin, D. A., Amiruzan, Z. S., Hussin, H., & Jafar, M. T. M. (2017). Integrated geological and multi-electrode resistivity surveys for groundwater investigation in Kampung Rahmat village and its vicinity, Jeli district, Kelantan, Malaysia. *Journal of Applied Geophysics*, *138*, 23-32. https://doi.org/10.1016/j.jappgeo.2017.01.012

Nickel, B., Thallium, C., Vanadium, C., & Zinc, I. (1992). ACID DIGESTION OF WATERS FOR TOTAL RECOVERABLE OR DISSOLVED METALS FOR ANALYSIS BY FLAA OR ICP SPECTROSCOPY.

Ninu, K. M. V. (2019). Rainfall analysis and hydrochemical characterisation of the Limbang River Basin, Northern Borneo. Unpublished PhD Thesis. Curtin University, Malaysia.

Okiongbo, K. S., & Douglas, R. K. (2015). Evaluation of major factors influencing the geochemistry of groundwater using graphical and multivariate statistical methods in Yenagoa city, Southern Nigeria. *Applied Water Science*, *5*(1), 27-37.

Oliveira, P. L., Figueiredo, B. R., & Cardoso, A. A. (2012). Rainwater major and trace element contents in Southeastern Brazil: an assessment of a sugar cane region in dry and wet period. *Journal of the Brazilian Chemical Society*, *23*(12), 2258-2265.

Oskooi, B., Moradi, M., & Smirnov, M. (2019). Integrated interpretation of seismic and magnetotelluric data on Shurab diapirs in Qom basin, Central Iran. *Acta Geophysica*, 1-20.

Quattrini, S., Pampaloni, B., & Brandi, M. L. (2016). Natural mineral waters: chemical characteristics and health effects. *Clinical Cases in Mineral and Bone Metabolism*, *13*(3), 173. https://doi.org/10.11138/ccmbm/2016.13.3.173

Oyem, H. H., Oyem, I. M., & Obiwulu, E. N. (2017). Barium, Calcium and Sodium, Cyanide, Phosphate and Sulphate Contents of Groundwater in Some Ika Communities of Delta State, Nigeria. *Journal of Geoscience and Environment Protection*, *5*(8), 89-98.

Özdemir, A. (2018). Iodine-rich waters of Turkey and oil & gas potential of the onshore. *Journal of Sustainable Engineering*, *1*(2).

Palmer, D. (1980). *The generalized reciprocal method of seismic refraction interpretation*. Society of Exploration Geophysicists.

PANalytical, B. V. (2002). X'pert highscore plus. *X'Pert HighScore Plus, Lelyweg, Almelo, the Netherlands*, *2*.

Parkhurst, D. L., & Appelo, C. A. J. (1999). User's guide to PHREEQC (Version 2): A computer program for speciation, batch-reaction, one-dimensional transport, and inverse geochemical calculations. *Water-resources investigations report*, *99*(4259), 312.

Pasquet, S., Bodet, L., Dhemaied, A., Mouhri, A., Vitale, Q., Rejiba, F., ... & Guérin, R. (2015). Detecting different water table levels in a shallow aquifer with combined P-, surface and SH-wave surveys: Insights from VP/VS or Poisson's ratios. *Journal of Applied Geophysics*, *113*, 38-50. https://doi.org/10.1016/j.jappgeo.2014.12.005

Patra, H. P., Adhikari, S. K., & Kunar, S. (2016). *Groundwater prospecting and management*. Springer Singapore. https://doi.org/10.1007/978-981-10-1148-1_4

Paytan, A., Kastner, M., Campbell, D., & Thiemens, M. H. (2004). Seawater sulfur isotope fluctuations in the Cretaceous. *science*, *304*(5677), 1663-1665.

Picotti, V., Capozzi, R., Bertozzi, G., Mosca, F., Sitta, A., & Tornaghi, M. (2007). The Miocene petroleum system of the Northern Apennines in the central Po Plain (Italy). In *Thrust Belts and Foreland Basins* (pp. 117-131). Springer, Berlin, Heidelberg.

Piper, A. M. (1944). A graphic procedure in the geochemical interpretation of water-analyses. *Eos, Transactions American Geophysical Union*, *25*(6), 914-928. https://doi.org/10.1029/TR025i006p00914

Pisciotta, A., Tiwari, A. K., & De Maio, M. (2019). An integrated multivariate statistical analysis and hydrogeochemical approaches to identify the major factors governing the chemistry of water resources in a mountain region of northwest Italy. *Carbonates and Evaporites*, *34*(3), 955-973.

Pitzer, K. S. (1973). Thermodynamics of electrolytes. I. Theoretical basis and general equations. *The Journal of Physical Chemistry*, *77*(2), 268-277.

Prasanna, M. V., Praveena, S. M., Chidambaram, S., Nagarajan, R., & Elayaraja, A. (2012). Evaluation of water quality pollution indices for heavy metal contamination monitoring: a case study from Curtin Lake, Miri City, East Malaysia. *Environmental Earth Sciences*, *67*(7), 1987-2001.

Purnomo, B. J., Pichler, T., & You, C. F. (2016). Boron isotope variations in geothermal systems on Java, Indonesia. *Journal of Volcanology and Geothermal Research*, *311*, 1-8.

Pussi, K., Gallo, J., Ohara, K., Carbo-Argibay, E., Kolen'ko, Y. V., Barbiellini, B., ... & Kamali, S. (2020). Structure of Manganese Oxide Nanoparticles Extracted via Pair Distribution Functions. *Condensed Matter*, *5*(1), 19.

Rankama, K., & Sahama, T. G. (1950). Geochemistry.

Rajmohan, N., & Elango, L. (2004). Identification and evolution of hydrogeochemical processes in the groundwater environment in an area of the Palar and Cheyyar River Basins, Southern India. *Environmental Geology*, *46*(1), 47-61.

Rajmohan, N., & Elango, L. (2005). Nutrient chemistry of groundwater in an intensively irrigated region of southern India. *Environmental Geology*, *47*(6), 820-830.

Ramasamy, N., Franz L, K., Jong, J., Muthuvairavasamy, R., Muhammad, A. A., Dayong, V., ... & Kinanthi, D. (2020). Geochemistry of the Palaeocene-Eocene Upper Kelalan

Formation, NW Borneo: Implications on palaeoweathering, tectonic setting, and provenance. *Geological Journal*. 10.1002/gj.3950.

Ramesh, R., & Anbu, M. (1996). Chemical methods for environmental analysis: water and sediment. Macmillan India.

Razowska-Jaworek, L., & Sadurski, A. (Eds.). (2014). *Nitrates in Groundwater: IAH Selected Papers on Hydrogeology 5*. CRC Press.

Ravikumar, P., Somashekar, R. K., & Prakash, K. L. (2015). A comparative study on usage of Durov and Piper diagrams to interpret hydrochemical processes in groundwater from SRLIS river basin, Karnataka, India. *Elixir International Journal*, *80*, 31073-31077.

Richter, B. C., & Kreitler, C. W. (1993). Geochemical techniques for identifying sources of groundwater salinization: Boca Katon. *FL, CK Smoley*, *258*.

Rucker, M. L., Meyers, R. A., & Lommler, J. C. (2012). Assessing shallow rock conditions over a brine cavern using seismic methods. *Carbonates and evaporites*, *27*(2), 199-205. https://doi.org/10.1007/s13146-012-0108-3

Rusydi, A. F. (2018, February). Correlation between conductivity and total dissolved solid in various type of water: A review. In *IOP Conference Series: Earth and Environmental Science* (Vol. 118, No. 1, p. 012019). IOP Publishing.

Rebeix, R., La Salle, C. L. G., Michelot, J. L., Verdoux, P., Noret, A., Monvoisin, G., ... & Simler, R. (2011). Tracing the origin of water and solute transfers in deep groundwater from Oxfordian, Dogger and Trias formations in the east of the Paris Basin–France. *Physics and Chemistry of the Earth, Parts A/B/C*, *36*(17-18), 1496-1510.

Redwan, M., Moneim, A. A. A., & Amra, M. A. (2016). Effect of water–rock interaction processes on the hydrogeochemistry of groundwater west of Sohag area, Egypt. *Arabian Journal of Geosciences*, *9*(2), 111.

Regenspurg, S., Feldbusch, E., Norden, B., & Tichomirowa, M. (2016). Fluid-rock interactions in a geothermal Rotliegend/Permo-Carboniferous reservoir (north German basin). *Applied Geochemistry*, *69*, 12-27.

Rehman, F., Abuelnaga, H. S., Harbi, H. M., Cheema, T., & Atef, A. H. (2016). Using a combined electrical resistivity imaging and induced polarization techniques with the chemical analysis in determining of groundwater pollution at Al Misk Lake, Eastern Jeddah, Saudi Arabia. *Arabian Journal of Geosciences*, *9*(4), 286.

Revil, A., Karaoulis, M., Johnson, T., & Kemna, A. (2012). Some low-frequency electrical methods for subsurface characterization and monitoring in hydrogeology. *Hydrogeology Journal*, *20*(4), 617-658.

Reynolds, J. M. (2011). An introduction to applied and environmental geophysics. John Wiley & Sons.

Rezaeia, K., Amirib, V., & Beitollahic, A. (2013). The contribution of electrical resistivity and seismic refraction techniques to Site characterization and earthquake risk assessment, a case study: IKIA airport, Iran.

Sánchez-Martos, F., & Pulido-Bosch, A. (1999). Boron and the origin of salinization in an aquifer in southeast Spain. *COMPTES RENDUS-ACADEMIE DES SCIENCES PARIS SERIE 2 SCIENCES DE LA TERRE ET DES PLANETES FASCICULE A*, *328*, 751-758.

Sánchez-Martos, F., Pulido-Bosch, A., Molina-Sánchez, L., & Vallejos-Izquierdo, A. (2002). Identification of the origin of salinization in groundwater using minor ions (Lower Andarax, Southeast Spain). *Science of the Total Environment*, *297*(1-3), 43-58.

Samantara, M. K., Padhi, R. K., Sowmya, M., Kumaran, P., & Satpathy, K. K. (2017). Heavy metal contamination, major ion chemistry and appraisal of the groundwater status in coastal aquifer, Kalpakkam, Tamil Nadu, India. *Groundwater for Sustainable Development*, *5*, 49-58. https://doi.org/10.1016/j.gsd.2017.04.001

Samsudin, A. R., Haryono, A., Hamzah, U., & Rafek, A. G. (2008). Salinity mapping of coastal groundwater aquifers using hydrogeochemical and geophysical methods: a case study from north Kelantan, Malaysia. *Environmental Geology*, *55*(8), 1737-1743. https://doi.org/10.1007/s00254-007-1124-9

Saribudak, M., & Hauwert, N. M. (2017). Integrated geophysical investigations of Main Barton Springs, Austin, Texas, USA. *Journal of Applied Geophysics*, *138*, 114-126. https://doi.org/10.1016/j.jappgeo.2017.01.004

Sarikhani, R., Dehnavi, A. G., Ahmadnejad, Z., & Kalantari, N. (2015). Hydrochemical characteristics and groundwater quality assessment in Bushehr Province, SW Iran. *Environmental earth sciences*, *74*(7), 6265-6281.

Saw, B. B., Schlaich, M., Pöppelreiter, M. C., Ramkumar, M., Lunt, P., Vintaned, J. A. G., & Ali, S. H. (2019). Facies, depositional environments, and anatomy of the Subis build-up in Sarawak, Malaysia: implications on other Miocene isolated carbonate build-ups. *Facies*, *65*(3), 28.

Schoeller, H. (1977). Geochemistry of groundwater. Groundwater studies—an international guide for research and practice, 15, 1-18.

Sefie, A., Aris, A. Z., Ramli, M. F., Narany, T. S., Shamsuddin, M. K. N., Saadudin, S. B., & Zali, M. A. (2018). Hydrogeochemistry and groundwater quality assessment of the multilayered aquifer in Lower Kelantan Basin, Kelantan, Malaysia. *Environmental Earth Sciences*, *77*(10), 397. https://doi.org/10.1007/s12665-018-7561-9

Seinfeld, J. H., & Pandis, S. N. (2016). Atmospheric chemistry and physics: from air pollution to climate change. John Wiley & Sons.

Sellato, B. (1993). Salt in Borneo. *Le Sel de la vie en Asie du Sud-Est*, (4), 263-284.

Şeren, A., Babacan, A. E., Gelişli, K., Öğretmen, Z., & Kandemir, R. (2012). An investigation for potential extensions of the Karaca Cavern using geophysical methods. *Carbonates and evaporites*, *27*(3-4), 321-329. https://doi.org/10.1007/s13146-012-0115-4

Shamsuddin, M. K. N., Sulaiman, W. N. A., Ramli, M. F. B., & Kusin, F. M. (2019). Geochemical characteristic and water quality index of groundwater and surface water at Lower River Muda Basin, Malaysia. *Arabian Journal of Geosciences*, *12*(9), 309.

Sheikhy Narany, T., Ramli, M. F., Aris, A. Z., Sulaiman, W. N. A., Juahir, H., & Fakharian, K. (2014). Identification of the hydrogeochemical processes in groundwater using classic integrated geochemical methods and geostatistical techniques, in Amol-Babol Plain, Iran. *The Scientific World Journal*, *2014*.

Sherif, M. I., Sultan, M., & Sturchio, N. C. (2019). Chlorine isotopes as tracers of solute origin and age of groundwaters from the Eastern Desert of Egypt. *Earth and Planetary Science Letters*, *510*, 37-44.

Singh, C. K., Rina, K., Singh, R. P., & Mukherjee, S. (2014). Geochemical characterization and heavy metal contamination of groundwater in Satluj River Basin. *Environmental Earth Sciences*, *71*(1), 201-216. https://doi.org/10.1007/s12665-013-2424-x

Singh, C. K., Kumar, A., Shashtri, S., Kumar, A., Kumar, P., & Mallick, J. (2017). Multivariate statistical analysis and geochemical modeling for geochemical assessment of groundwater of Delhi, India. *Journal of Geochemical Exploration*, *175*, 59-71.

Singhal, B. B. S., & Gupta, R. P. (2010). *Applied hydrogeology of fractured rocks*. Springer Science & Business Media.

Snyder, M., Taillefert, M., & Ruppel, C. (2004). Redox zonation at the saline-influenced boundaries of a permeable surficial aquifer: effects of physical forcing on the biogeochemical cycling of iron and manganese. *Journal of Hydrology*, *296*(1-4), 164-178.

Shouakar-Stash, O., Alexeev, S. V., Frape, S. K., Alexeeva, L. P., & Drimmie, R. J. (2007). Geochemistry and stable isotopic signatures, including chlorine and bromine isotopes, of the deep groundwaters of the Siberian Platform, Russia. *Applied geochemistry*, *22*(3), 589-605.

Steen, A. K., Nunn, J. A., & Hanor, J. S. (2011). Indications of formation water flow and compartmentalization on the flank of a salt structure derived from salinity and seismic data. *Geofluids*, *11*(2), 199-208. https://doi.org/10.1111/j.1468-8123.2011.00330.x

Suastika, K. G., Karelius, K., & Sudyana, I. N. (2018). Characterization of natural puya sand extract of Central Kalimantan by using X-Ray Diffraction. *JPhCS*, *997*(1), 012038.

Sulin, V. A. (1946). Waters of petroleum formations in the system of natural water. *Gostoptekhiz-dat, Moscow (in Russian)*, *3596*.

Sun, Z., Ma, R., Wang, Y., Hu, Y., & Sun, L. (2016). Hydrogeological and hydrogeochemical control of groundwater salinity in an arid inland basin: Dunhuang Basin, northwestern China. *Hydrological Processes*, *30*(12), 1884-1902. https://doi.org/10.1002/hyp.10760

Syukri, M., & Saad, R. (2017). Seulimeum segment characteristic indicated by 2-D resistivity imaging method. *NRIAG Journal of Astronomy and Geophysics*, *6*(1), 210-217. https://doi.org/10.1016/j.nrjag.2017.04.001

Szynkiewicz, A., Olichwer, T., & Tarka, R. (2020). Delineation of groundwater provenance in Arctic environment using isotopic compositions of water and sulphate. *Journal of Hydrology*, *580*, 124232.

Tanasković, I., Golobocanin, D., & Miljević, N. (2012). Multivariate statistical analysis of hydrochemical and radiological data of Serbian spa waters. *Journal of Geochemical Exploration*, *112*, 226-234.

Taylor, B. E., Wheeler, M. C., & Nordstrom, D. K. (1984). Stable isotope geochemistry of acid mine drainage: Experimental oxidation of pyrite. *Geochimica et Cosmochimica Acta*, *48*(12), 2669-2678.

Tellam, J. H. (1995). Hydrochemistry of the saline groundwaters of the lower Mersey Basin Permo-Triassic sandstone aquifer, UK. *Journal of Hydrology*, *165*(1-4), 45-84. https://doi.org/10.1016/0022-1694(94)02583-W

Tesoriero, A. J., Liebscher, H., & Cox, S. E. (2000). Mechanism and rate of denitrification in an agricultural watershed: Electron and mass balance along groundwater flow paths. *Water Resources Research*, *36*(6), 1545-1559.

Thapa, B. R., Shrestha, S. R., Okwany, R. O., & Neupane, M. (2019). Shallow aquifer potential mapping in the foothills of Churia in Eastern Gangetic Plain of Saptari District, Nepal. *Applied Water Science*, *9*(4), 92.

Thivya, C., Chidambaram, S., Rao, M. S., Gopalakrishnan, M., Thilagavathi, R., Prasanna, M. V., & Nepolian, M. (2016). Identification of recharge processes in groundwater in hard rock aquifers of Madurai District using stable isotopes. *Environmental Processes*, *3*(2), 463-477.

Torres-Martínez, J. A., Mora, A., Knappett, P. S., Ornelas-Soto, N., & Mahlknecht, J. (2020). Tracking nitrate and sulfate sources in groundwater of an urbanized valley using a multi-tracer approach combined with a Bayesian isotope mixing model. *Water Research*, 115962.

Torfstein, A., Gavrieli, I., & Stein, M. (2005). The sources and evolution of sulfur in the hypersaline Lake Lisan (paleo-Dead Sea). *Earth and Planetary Science Letters*, *236*(1-2), 61-77.

Tostevin, R., Craw, D., Van Hale, R., & Vaughan, M. (2016). Sources of environmental sulfur in the groundwater system, southern New Zealand. *Applied Geochemistry*, *70*, 1-16.

Usunoff, E. J., & Guzmán-Guzmán, A. (1989). Multivariate analysis in hydrochemistry: an example of the use of factor and correspondence analyses. *Groundwater*, *27*(1), 27-34.

Van Engelen, J., Essink, G. H. O., Kooi, H., & Bierkens, M. F. (2018). On the origins of hypersaline groundwater in the Nile Delta aquifer. *Journal of Hydrology*, *560*, 301-317. https://doi.org/10.1016/j.jhydrol.2018.03.029

Van Hattum, M. W. A., Hall, R., Pickard, A. L., & Nichols, G. J. (2013). Provenance and geochronology of Cenozoic sandstones of northern Borneo. *Journal of Asian Earth Sciences*, *76*, 266-282. https://doi.org/10.1016/j.jseaes.2013.02.033

Van Wirdum, G. (1980). Description of water-quality changes in a hydrological cycle, for the purpose of nature conservation. *Waterquality in groundwater-flow systems*, *5*, 118-143.

Van Weert, F., Van der Gun, J., & Reckman, J. (2009). Global overview of saline groundwater occurrence and genesis. *International Groundwater Resources Assessment Centre*, *105*.

Vishwakarma, C. A., Sen, R., Singh, N., Singh, P., Rena, V., Rina, K., & Mukherjee, S. (2018). Geochemical characterization and controlling factors of chemical composition of spring water in a part of Eastern Himalaya. *Journal of the Geological Society of India*, *92*(6), 753-763.

Vengosh, A., Gieskes, J., & Mahn, C. (2000). New evidence for the origin of hypersaline pore fluids in the Mediterranean basin. *Chemical Geology*, *163*(1-4), 287-298.

Vengosh, A. (2003). Salinization and saline environments. *Treatise on geochemistry*, *9*, 612.

Vengosh, A. (2014). Treatise on Geochemistry. Volume 11: Environmental Geochemistry, 11.9 Salinization and Saline Environments, 325-378 p, doi: 10.1016. B978-0-08-095975-7. 00909-8.

Vespasiano, G., Apollaro, C., Muto, F., Dotsika, E., De Rosa, R., & Marini, L. (2014). Chemical and isotopic characteristics of the warm and cold waters of the Luigiane Spa near Guardia Piemontese (Calabria, Italy) in a complex faulted geological framework. *Applied Geochemistry*, *41*, 73-88.

Wannier, M. (2009). Carbonate platforms in wedge-top basins: an example from the Gunung Mulu National Park, Northern Sarawak (Malaysia). *Marine and Petroleum Geology*, *26*(2), 177-207. https://doi.org/10.1016/j.marpetgeo.2007.12.004

Walter, J., Chesnaux, R., Cloutier, V., & Gaboury, D. (2017). The influence of water/rock−water/clay interactions and mixing in the salinization processes of groundwater. *Journal of Hydrology: Regional Studies, 13*, 168-188. https://doi.org/10.1016/j.ejrh.2017.07.004

Wang, P. C., Li, S. Z., Guo, L. L., Jiang, S. H., Somerville, I. D., Zhao, S. J., & Han, B. (2016). Mesozoic and Cenozoic accretionary orogenic processes in Borneo and their mechanisms. *Geological Journal, 51*, 464-489. https://doi.org/10.1002/gj.2835

Wang, H., & Zhang, Q. (2019). Research Advances in Identifying Sulfate Contamination Sources of Water Environment by Using Stable Isotopes. *International journal of environmental research and public health*, *16*(11), 1914.

Ward Jr, J. H. (1963). Hierarchical grouping to optimize an objective function. *Journal of the American statistical association*, *58*(301), 236-244.

Warren, J. K. (2016). Depositional chemistry and hydrology. In *Evaporites* (pp. 85-205). Springer, Cham.

Whittemore, D. O. (1995). Geochemical differentiation of oil and gas brine from other saltwater sources contaminating water resources: Case studies from Kansas and Oklahoma. *Environmental Geosciences*, *2*(1), 15-31.

Weight, W. D., & Sonderegger, J. L. (2001). *Manual of applied field hydrogeology*. McGraw-Hill.

World Health Organization. (2008). Guidelines for drinking-water quality: second addendum. Vol. 1, Recommendations. World Health Organization.

World Wildlife Fund Malaysia. (2005). *The Conservation and Sustainable Use of the Highlands of Sabah & Sarawak Preliminary Report*. Issue 1.0. Retrieved from https://repository.wwf.org.my/technical_reports/P/PolicyStrategiesForTheConservationAndSustainableUseOfTheHighlandsOfSabahAndSarawakPreliminaryReport.pdf

Yousif, M., Oguchi, T., Anazawa, K., & Ohba, T. (2015). Framework for investigation of karst aquifer in an arid zone, using isotopes, remote sensing and GIS applications: the Northwestern Coast of Egypt. *Environmental Processes*, *2*(1), 37-60.

Zaidi, F. K., Nazzal, Y., Jafri, M. K., Naeem, M., & Ahmed, I. (2015). Reverse ion exchange as a major process controlling the groundwater chemistry in an arid environment: a case study from northwestern Saudi Arabia. *Environmental monitoring and assessment*, *187*(10), 607.

Zhang, J., & Toksöz, M. N. (1998). Nonlinear refraction traveltime tomography. *Geophysics*, *63*(5), 1726-1737.

Zhang, Q., Wang, H., & Lu, C. (2020). Tracing sulfate origin and transformation in an area with multiple sources of pollution in northern China by using environmental isotopes and Bayesian isotope mixing model. *Environmental Pollution*, *265*, 115105.

Zakhem, B. A., & Hafez, R. (2015). Heavy metal pollution index for groundwater quality assessment in Damascus Oasis, Syria. *Environmental Earth Sciences*, *73*(10), 6591-6600. https://doi.org/10.1007/s12665-014-3882-5

Zaporozec, A. (1972). Graphical interpretation of water-quality data. *Groundwater*, *10*(2), 32-43.

Zarei, M., Raeisi, E., Merkel, B. J., & Kummer, N. A. (2013). Identifying sources of salinization using hydrochemical and isotopic techniques, Konarsiah, Iran. *Environmental earth sciences*, *70*(2), 587-604.

Zunckel, M., Saizar, C., & Zarauz, J. (2003). Rainwater composition in northeast Uruguay. *Atmospheric Environment*, *37*(12), 1601-1611.

Appendix 1: The mineral saturation indices of the analysed groundwater samples.

Saturation Indices	Monsoon					Post-monsoon				
	Well 1	Well 2	Well 3	Well 4	Well 5	Well 1	Well 2	Well 3	Well 4	Well 5
pH	6.74	6.84	7.72	6.95	6.9	6.51	6.7	6.87	7.12	7.33
HCO_3 (mg/L)	875.5	762.5	603.9	548	578.9	1708	1500	1256	1195	11547
Anhydrite	-4.06	-3.73	-4.08	-4.12	-4.12	-4.48	-4.5	-4.52	-4.63	-4.54
Aragonite	0.18	0.16	0.84	0.11	0.05	-0.15	0.12	0.15	0.21	0.43
Barite	-0.65	-0.33	-0.28	-0.45	-0.39	-1.35	-1.19	-1.12	-0.99	-0.86
Borax	-14.44	-14.52	-12.29	-15.32	-15.57	-13.58	-13.09	-13.61	-14.89	-13.68
Brucite	-6.61	-6.59	-5.04	-6.39	-6.26	-7.1	-6.58	-6.33	-5.99	-5.65
Calcite	0.45	0.43	1.11	0.38	0.32	0.14	0.41	0.43	0.48	0.71
Carnallite	-13.03	-12.91	-16.94	-13.24	-13.22	-14.68	-11.78	-12.13	-12.55	-12.88
Dolomite	0.71	0.65	1.88	0.48	0.54	0.29	0.8	0.87	1.03	1.34
Epsomite	-6.67	-6.37	-6.84	-6.84	-6.69	-6.98	-7.05	-7.01	-7.04	-7.11
Gypsum	-3.67	-3.35	-3.7	-3.74	-3.76	-4.14	-4.17	-4.17	-4.27	-4.19
Halite	-3.25	-3.2	-4.37	-3.35	-3.45	-3.23	-2.39	-2.57	-2.77	-2.89
Hexanhydrite	-6.98	-6.68	-7.16	-7.15	-6.98	-7.29	-7.33	-7.3	-7.33	-7.4
Magnesite	-0.45	-0.49	0.05	-0.63	-0.51	-0.59	-0.35	-0.29	-0.18	-0.11
Polyhalite	-23.98	-22.49	-24.45	-23.82	-23.80	-24.87	-25.13	-25.25	-25.34	-25.29
Sylvite	-5.11	-5	-6.44	-4.97	-5.07	-5.49	-4.56	-4.72	-4.8	-4.9